U.S. Department
of Transportation

**Federal Railroad
Administration**

Aerodynamic Forces on Maglev Vehicles

National Maglev
Initiative
Washington, D.C. 20590

DOT/FRA/NMI-92/21

December 1992

This document is available to the
U.S. public throught the National
Technical Information Service,
Springfield, Virginia 22161

REPRODUCED BY
U.S. DEPARTMENT OF COMMERCE
NATIONAL TECHNICAL INFORMATION SERVICE
SPRINGFIELD, VA 22161

Technical Report Documentation Page

1. Report No.
DOT/FRA/NMI-92/21

PB93-154813

3. Recipient's Catalog No.

4. Title and Subtitle
AERODYNAMIC FORCES ON MAGLEV VEHICLES

5. Report Date
December 1992

6. Performing Organization Code

7. Author(s)
T. Barrows, D. McCullum, S. Mark, R.C. Castellino

8. Performing Organization Report No.
CSDL-R-2463

9. Performing Organization Name and Address
The Charles Stark Draper Laboratory, Inc.
555 Technology Square
Cambridge, Massachusetts 02139-3563

10. Work Unit No. (TRAIS)

11. Contract or Grant No.
DTFR53-91-C-00072

12. Sponsoring Agency Name and Address
U.S. Department of Transportation
Federal Railroad Administration
Office of Research and Development
Washington, D.C. 20590

13. Type of Report and Period Covered
Final Report
July 1991 - November 1992

14. Sponsoring Agency Code

15. Supplementary Notes
Contracting Officer Technical Representative: Mr. Thomas D. Schultz

16. Abstract

The results of four separate tasks are documented: (1) minimization of front-end drag, (2) effect of fineness ratio (ratio of length to diameter) on drag, (3) design of aerosurfaces for control purposes, and (4) control and dynamics of maglev vehicles with aerodynamic control surfaces. Task 1 examines the flow disturbances near the nose of a high speed channel vehicle which cause vortices to form near the tops of the guidewalls. These vortices are a major source of drag. The nose of the train can be idealized as a source flow, and the walls of the channel guideway are represented as two vertical flat plates. A numerical solution of the two-dimensional unsteady problem is presented. Using a representative design example, the nose shape which provides the minimum drag is derived from this solution. Under task 2, drag data is presented from the automotive industry, the Japanese National Railway, Krauss-Maffei, and Tracked Hovercraft Limited. An empirical formula is used to estimate the drag of vehicles designed for channel and box beam guideways. The optimum width for these cases is derived. Under task 3, a simple numerical scheme is described for computing the lift and drag on an aerosurface with a control flap operating in close proximity to a guideway surface. It is shown that large variations in lift can be produced using very small flap angles. Task 4 examines the improvement in ride quality (or conversely the increase in allowable guideway roughness for a given ride quality) which is possible through the use of aerodynamic control surfaces. Comparisons are made between vehicles with active and passive secondary suspensions with aerodynamic control surfaces mounted on the vehicle body or control flaps on the vehicle bogies.

17. Key Words
Nose Drag
Aerodynamic Control
Ground Effect
Optimal suspension
Active suspension

18. Distribution Statement
This document is available to the U.S. public through the National Technical Information Service, Springfield, Virginia 22161

19. Security Classif. (of this report)
Unclassified

20. Security Classif. (of this page)
Unclassified

21. No. of Pages
[illegible]

22. Price

Form DOT F 1700.7 (8-72) Reproduction of completed page authorized

METRIC / ENGLISH CONVERSION FACTORS

ENGLISH TO METRIC

LENGTH (APPROXIMATE)

1 inch (in) = 2.5 centimeters (cm)
1 foot (ft) = 30 centimeters (cm)
1 yard (yd) = 0.9 meter (m)
1 mile (mi) = 1.6 kilometers (km)

AREA (APPROXIMATE)

1 square inch (sq in, in²) = 6.5 square centimeters (cm²)
1 square foot (sq ft, ft²) = 0.09 square meter (m²)
1 square yard (sq yd, yd²) = 0.8 square meter (m²)
1 square mile (sq mi, mi²) = 2.6 square kilometers (km²)
1 acre = 0.4 hectares (he) = 4,000 square meters (m²)

MASS - WEIGHT (APPROXIMATE)

1 ounce (oz) = 28 grams (gr)
1 pound (lb) = .45 kilogram (kg)
1 short ton = 2,000 pounds (lb) = 0.9 tonne (t)

VOLUME (APPROXIMATE)

1 teaspoon (tsp) = 5 milliliters (ml)
1 tablespoon (tbsp) = 15 milliliters (ml)
1 fluid ounce (fl oz) = 30 milliliters (ml)
1 cup (c) = 0.24 liter (l)
1 pint (pt) = 0.47 liter (l)
1 quart (qt) = 0.96 liter (l)
1 gallon (gal) = 3.8 liters (l)
1 cubic foot (cu ft, ft³) = 0.03 cubic meter (m³)
1 cubic yard (cu yd, yd³) = 0.76 cubic meter (m³)

TEMPERATURE (EXACT)

[(x - 32) (5/9)] °F = y °C

METRIC TO ENGLISH

LENGTH (APPROXIMATE)

1 millimeter (mm) = 0.04 inch (in)
1 centimeter (cm) = 0.4 inch (in)
1 meter (m) = 3.3 feet (ft)
1 meter (m) = 1.1 yards (yd)
1 kilometer (km) = 0.6 mile (mi)

AREA (APPROXIMATE)

1 square centimeter (cm²) = 0.16 square inch (sq in, in²)
1 square meter (m²) = 1.2 square yards (sq yd, yd²)
1 square kilometer (km²) = 0.4 square mile (sq mi, mi²)
1 hectare (he) = 10,000 square meters (m²) = 2.5 acres

MASS - WEIGHT (APPROXIMATE)

1 gram (gr) = 0.036 ounce (oz)
1 kilogram (kg) = 2.2 pounds (lb)
1 tonne (t) = 1,000 kilograms (kg) = 1.1 short tons

VOLUME (APPROXIMATE)

1 milliliter (ml) = 0.03 fluid ounce (fl oz)
1 liter (l) = 2.1 pints (pt)
1 liter (l) = 1.06 quarts (qt)
1 liter (l) = 0.26 gallon (gal)
1 cubic meter (m³) = 36 cubic feet (cu ft, ft³)
1 cubic meter (m³) = 1.3 cubic yards (cu yd, yd³)

TEMPERATURE (EXACT)

[(9/5) y + 32] °C = x °F

QUICK INCH-CENTIMETER LENGTH CONVERSION

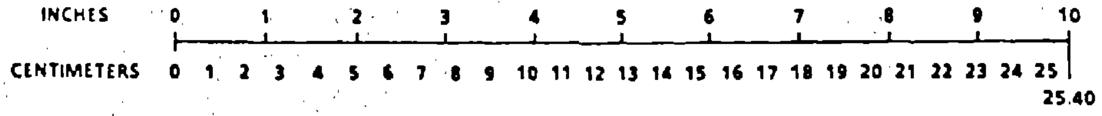

QUICK FAHRENHEIT-CELCIUS TEMPERATURE CONVERSION

°F	-40°	-22°	-4°	14°	32°	50°	68°	86°	104°	122°	140°	158°	176°	194°	212°
°C	-40°	-30°	-20°	-10°	0°	10°	20°	30°	40°	50°	60°	70°	80°	90°	100°

For more exact and/or other conversion factors, see NBS Miscellaneous Publication 286, Units of Weights and Measures. Price $2.50. SD Catalog No. C13 10 286.

TABLE OF CONTENTS

TABLE OF CONTENTS (Continued)

TABLE OF CONTENTS (Continued)

LIST OF FIGURES

LIST OF FIGURES (Continued)

LIST OF FIGURES (Continued)

LIST OF FIGURES (Continued)

LIST OF FIGURES (Continued)

LIST OF FIGURES (Continued)

LIST OF FIGURES (Continued)

LIST OF FIGURES (Continued)

LIST OF TABLES

EXECUTIVE SUMMARY

There are two main purposes to this work. The first is to minimize the aerodynamic drag of high speed ground transportation vehicles. The second is to examine in quantitative terms the potential improvements in design and performance which are possible through the use of aerodynamic control surfaces. This improvement can be manifested through a more favorable tradeoff between allowable guideway roughness and ride quality. For a given ride quality criteria, aerodynamic control surfaces may allow a rougher, and hence less expensive, guideway.

The specific objective for each section follows:

Section 1.	For vehicles which are designed to travel in a channel guideway, understand the relationship between the shape of the front of the vehicle and the resulting drag.
Section 2.	Determine the potential for reducing the energy per passenger by adjusting various shape parameters, such as the fineness ratio (ratio of length to diameter), or varying the interface with the guideway.
Section 3.	Review existing literature on aerodynamic surfaces in ground effect and develop a simple method for predicting the performance of control flaps.
Section 4.	Quantify the improvement in ride quality (or conversely the increase in allowable guideway roughness for a given ride quality) which is possible through the use of aerodynamic control surfaces.

The motivation for Section 1 came from the observation that the flow disturbances near the nose of a high speed channel vehicle cause vortices to form near the tops of the guidewalls, and these vortices are a major source of drag. The nose of the train can be idealized as a source flow, and the walls of the channel guideway are represented as two vertical flat plates. A numerical solution of the two-dimensional unsteady problem is presented. Using a representative design example, the nose shape which provides the minimum drag is derived from this solution. This nose is considerably more elongated than that of a typical subsonic aircraft.

In Section 2, a discussion is presented of the relationship between the fineness ratio and the drag of streamlined axisymmetric bodies in a free stream. The effect of placing such bodies near a ground plane is discussed. Data is presented from the automotive industry, the Japanese National Railway, Krauss-Maffei, and Tracked Hovercraft Limited. A simple empirical formula is developed for the drag of vehicles designed for channel and box beam guideways. The optimum width for these cases is derived. It is found that for a vehicle carrying 120 passengers the optimum width allows 7 abreast seating in the case of a box guideway and 6 abreast seating for the channel guideway.

One of the problems with persistent mode superconducting magnets is that their fields cannot be varied for control purposes. Aerodynamic surfaces are a relatively simple way to produce a controllable force. A small flap at the trailing edge of some part of the vehicle such as a magnet bogie can control the aerodynamic pressure between this part and the guideway. Section 3 is essentially a review of previously derived theories for the lift on a wing in ground effect. There is one theory due to Boccadoro which is particularly simple and useful. Based on this theory, some new numerical results are presented for a wing with a flap at the trailing edge. When this wing is in close proximity to a flat surface such as the floor or side of a guideway, very large variations in the lift force can be produced by small flap angles. Thus, the power required to operate such a flap is very small.

In order to evaluate the feasibility and benefits of aerodynamic control surfaces, a dynamics and control analysis was conducted as described in Section 4. Using internal Corporate Sponsored Research funding, Draper Laboratory has developed a five-degree-of-freedom dynamic model which is described in some detail in Section 4.1. The present research effort, however, calls for generic results which are applicable to a range of vehicle concepts. For this purpose a reduced, three-degree-of-freedom model is appropriate, which limits the vehicle motion to that in a cross-sectional plane (heave, roll, and sway). A typical vehicle consisting of a passenger compartment, an electro-dynamic (EDS) primary suspension, magnetic bogies, and secondary suspensions with both active and passive elements was analyzed.

It is apparent that a controllable lateral aerodynamic force applied directly to the vehicle would be able to improve the ride quality. Actively controlled vertical fins mounted above the front and rear of the passenger compartment could do this. *A key assumption of the study is that this is impractical.* The disadvantage of such a configuration is that makes the vehicle vulnerable to crosswinds in the event of a failure of the active control system for the fins. There may also be practical problems at stations and tunnels. On the other hand, aerosurfaces mounted on the bogies which produce lateral forces were considered perfectly feasible.

It is worth noting that two of the Maglev system concept definition teams (Bechtel and Magneplane) came up with horizontal aerodynamic surfaces mounted on the passenger compartment for producing controllable vertical forces. This arrangement is apparently feasible. It is not expected that vertical wind variations (updrafts and downdrafts) on the vehicle will be nearly as strong as crosswinds, so the consequences of a failure of the active control are not as serious in this case. Thus, the two major configurations chosen for the present study were (1) ground-effect flaps on the suspension bogies which produce both horizontal and vertical forces, and (2) aerodynamic control surfaces (i.e. wings) mounted on the passenger compartment which produce only vertical forces. The results of the study are summarized in Table EX-1 and EX-2 below. In these tables, a guideway roughness equivalent to welded rail is assumed. An rms wind variation of plus or minus 4.5 m/s is also assumed. It is hypothesized that such variations would be encountered when the steady component of the wind is 13.5 m/s (30 mph).

Table EX-1. Aero-surfaces in ground-effect on bogies, vehicle velocity = 150 m/s (Both Guideway and Crosswind Disturbances)

V = 150 m/s Welded Rail RMS Wind = 10 mph	Passive Secondary	Active Hydraulic Secondary	Active Ground-Effect Aero-surfaces	Active Aero & Hydraulic Secondary
Pepler Index	3.49	1.54	2.87	1.07
Z RMS Air Gap Variation	0.6034 cm	1.5671 cm	0.3342 cm	0.2337 cm
Z RMS Sec. Stroke	1.3121 cm	3.4256 cm	1.1561 cm	3.0028 cm
Roll Rate (RMS)	1.04 deg/s	0.13 deg/s	0.79 deg/s	0.09 deg/s

Table EX-2. Wings on train, vehicle velocity = 150 m/s (Both Guideway and Crosswind Disturbances)

V = 150 m/s Welded Rail RMS Wind = 10 mph	Passive Secondary	Active Hydraulic Secondary	Active Aero-surfaces	Active Aero & Hydraulic Secondary
Pepler Index	3.49	1.54	2.23	1.28
Z RMS Air Gap Variation	0.6034 cm	1.5671 cm	0.6133 cm	0.8488 cm
Z RMS Sec. Stroke	1.3121 cm	3.4256 cm	3.7041 cm	3.1559 cm
Roll Rate (RMS)	1.04 deg/s	0.13 deg/s	0.19 deg/s	0.07 deg/s

Discussion of RMS Results

Without the active hydraulic suspension, the Pepler Ride Comfort Index is reduced more by wings mounted on the vehicle body than it is by aerosurfaces in ground-effect acting on the bogies. This is despite the assumptions that the wings on the vehicle body cannot produce lateral forces while the aerosurfaces in ground-effect can. A contributing factor to this is that the aerosurfaces on the bogies cannot reduce the roll rate as significantly as wings which are mounted directly to the vehicle body (the roll rate has a significant contribution to the Pepler Index).

When active secondary elements are added to the aerosurfaces in ground-effect, the above conclusion is reversed. It is evident from comparing the Pepler Index for both combined systems that the aerosurfaces in ground-effect with hydraulic secondary suspension actuators configuration has the advantage of being able to exert forces in both the lateral and the vertical directions. This explains why it has the lowest Pepler Index. The roll rate is less than 10% of the roll rate of the optimized passive suspension, and the Pepler Index is very close to its minimum of 1, which represents excellent ride quality. (A Pepler Index of 1 is equivalent to sitting in a stationary chair.)

If the above arguments against vertical fins above the vehicle body could be refuted, one could exert lateral forces on the passenger compartment, whose effect on roll could be canceled by the vertical force wings. The resulting configuration would have an advantage over all of the others. This advantage is contingent on there being sufficient wing area available to produce forces of the required magnitude. This was the case for the vertical force wings at a vehicle speed of 150 m/s, but wing area was the limiting factor at 100 m/s.

Another significant conclusion is that the ride quality in the vertical direction for the wings-alone configuration is almost as good as the combined wing and hydraulic secondary suspension configuration, without a significant increase in the air gap variations. (Vertical RMS acceleration is given in Table 4.5.2.) In other words, an active secondary does not produce a large improvement in this case. With ground-effect flaps mounted on the bogies, there is a dramatic improvement from the addition of an active hydraulic secondary.

Once again, intuitively, the primary advantage of the wings mounted to the vehicle body is that forces can be exerted directly on the passenger compartment, making them more effective in controlling passenger acceleration. These forces are exerted with respect to an earth-fixed reference frame, and are not affected by guideway irregularities, as are the aerosurfaces in ground-effect.

SECTION 1

MINIMIZATION OF FRONT-END DRAG

1.1 Introduction

In the 1960's the Office of High Speed Ground Transportation sponsored a study by Tracked Hovercraft Limited [ref. 78] to conduct wind tunnel tests of three guideway configurations:

1. The inverted T
2. The channel
3. The box beam

This study showed that the channel guideway had more drag than either of the other configurations. However, the researchers who conducted this study did not have any systematic method for selecting the vehicle configurations which were used in these tests. The result was that the vehicle shapes were chosen rather arbitrarily. It is quite possible that different vehicle shapes would have resulted in different results. It appears that no one asked the simple question "Why is the drag of the channel configuration greater than that of the others?". Since drag is associated with flow over the surface of the vehicle and the channel vehicle had less surface than either the inverted T or the box beam vehicle, one might have expected the opposite result. This question will be answered in the discussion which follows.

The channel guideway offers certain advantages, and in fact researchers at the Japanese National Railroad (JNR) have selected this configuration for their maglev vehicle. Thus an understanding of the fundamental reason for this extra drag would be very useful, especially if it provided insight into ways to reduce this effect. If the drag difference could be narrowed, designers could feel free to choose the channel guideway configuration without incurring a burdensome energy penalty.

It appears that the Japanese and all previous designers of high speed channel guideway vehicles have not thought about the fundamentals of the flow in the front region. The result is that the front end of these vehicles all have conventional streamlining, i.e. they end up looking like the nose of a subsonic passenger airliner.

The speed regime in which a maglev vehicle would operate can be described using incompressible aerodynamics. That is, flow speeds relative to the vehicle body are not expected to approach the speed of sound, with the result that the air density can be considered to be constant. Another important simplification is to assume that the effects of viscosity can be neglected. If this assumption is valid we have what is known as inviscid flow. If the flow is truly inviscid, there can be no aerodynamic drag. In fact, Kelvin's Theorem states that in steady inviscid flow no aerodynamic forces of any kind can be generated. Pressures can be produced on the body, but they act in such a way as to produce no net force. Thus, it might seem that nothing could be learned about aerodynamic forces from inviscid flow theory. One of the great breakthroughs in aerodynamics was the realization that if we have two-dimensional flow over an airfoil with a sharp trailing edge, the effect of viscosity will produce a net circulation such that the streams above and below the airfoil flow smoothly off the trailing edge. This is known as the Kutta condition. The lift is directly proportional to this circulation. The important point is that a method was developed to compute the lift on an airfoil without going into the details of the boundary layer. More advanced theories were able to compute the induced drag, or drag due to lift, associated with the three-dimensional flow over a wing, while still avoiding direct computation of the effects of viscosity. The research reported herein accomplishes a similar result; namely, inviscid flow theory has been used to compute an important component of the drag. The remainder of the drag would best be determined empirically.

For inviscid flow, an easy way to represent the flow around an object traveling near a ground plane is to imagine that there is a mirror image of the object below the ground plane, and both objects are traveling through unrestricted air. The resulting symmetry means that there is no flow across the ground plane, as required. In this situation, one can obtain good streamlining if the object plus its image form a shape which would be well-streamlined in the absence of the ground plane. In other words, take a conventional streamlined body like an airplane fuselage and cut it in half to form a good shape for operation near a ground plane, as shown in Fig. 1.1. This line of thinking is apparently what has motivated maglev researchers at the JNR, judging by the design shown in Fig. 1.2. It represents the state of the art for this particular niche of aerodynamics, which apparently has not advanced in the last 15 years, in either the U.S. or Japan. To summarize, the effect of the horizontal plane of the channel is taken into account, but no recognition is given to the presence of the guidewalls.

When viscosity is introduced, the image method is only partially valid. This method only produces a condition of zero flow across the plane of symmetry, it does nothing to establish the true condition of viscous flow which requires that the velocity be zero both normal and tangential to the ground. Let us divide the flow in Fig. 1.1 into the "outer" flow which goes over the vehicle and the "channel" flow between the vehicle and the ground plane. In the outer region it is valid to assume that the flow is basically the same as inviscid flow plus a thin boundary layer on the surface, so that the outer flow will be well-represented by the image method. However,

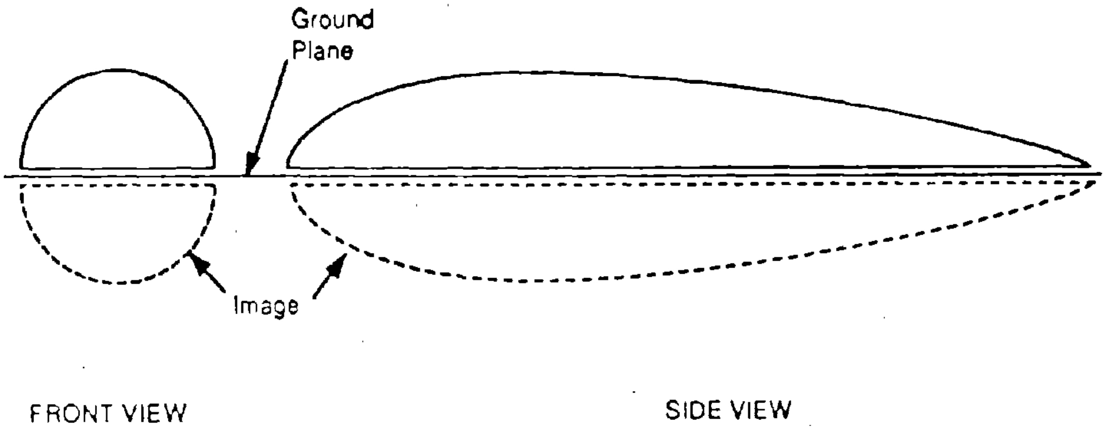

Figure 1.1 A body plus its mirror image can be used to represent a ground Plane

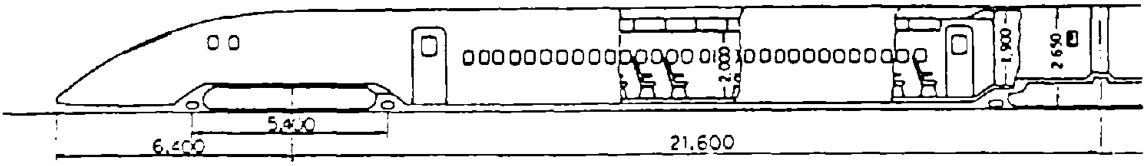

Figure 1.2 The JNR maglev Vehicle

the channel flow will show some differences from the real situation in which the vehicle travels over the ground, because of the presence of the ground boundary layer. If the height of the channel is comparable to the boundary layer thickness, the channel flow will be quite different.

Let us pursue the simple flow situation shown in Fig. 1.1. In this figure the outer flow is radially outward near the front of the vehicle and radially inward near the back. If sidewalls are added, we obtain the flow situation shown in Fig. 1.3. We can easily perceive that the flow will not be able to go around the sharp turns at the top of the guidewalls, in other words the flow on each guidewall will separate and form a "bow vortex". These vortices contain energy, and all this energy is directly related to the front-end drag. This is the answer to the question posed at the beginning of this section. The drag of a vehicle in a channel is greater than that of a vehicle in an inverted T guideway because of these vortices.

An important point is that the strength of the bow vortices can be calculated from slender body theory [3]. This is in contrast to the drag due to the boundary layer on the surface of the vehicle, which is so hard to calculate that researchers universally resort to wind tunnel measurements if an accurate value is required. It is this empirical nature of the subject of drag which has caused previous researchers to overlook the fact that for the front-end problem, a valuable theoretical advance is still possible without going into the details of the boundary layer. The separation of the flow off the top edges of the guidewalls is analogous to the Kutta condition for an airfoil. In both cases, the fact that the flow cannot be expected to turn around a sharp corner is used in conjunction with inviscid aerodynamic theory to produce a relatively simple result. The crucial advantage of using the relatively simple inviscid theory is that the relationship between the vehicle shape and the front-end drag can be established, and an optimized nose shape can be derived.

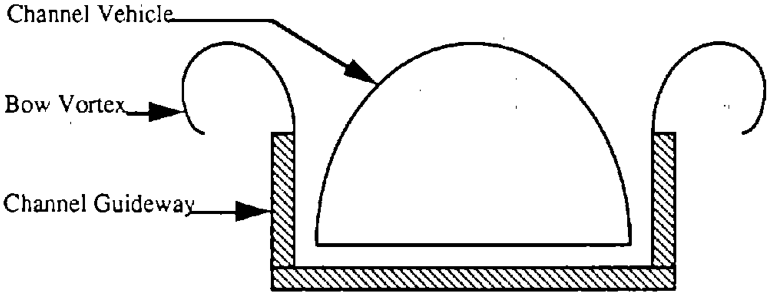

Figure 1.3. Cross-Section of Vortex Shedding in a Channel Guideway

Estimating the energy in the bow vortices is accomplished numerically using a technique based on slender body theory along with a type of paneling method which employs discrete point singularities in an inviscid, incompressible flow [ref 1]. In order to establish the method, two simpler and more elementary problems are first attacked: 1. the problem of the flow about a circular cylinder in a free stream flow and 2. the problem of vortex shedding off a flat plate oriented perpendicular to a free stream flow. The numerical methods used for each of these problems are then superimposed to solve the problem of vortex shedding due to the existence of a point source of known strength between two parallel plates. It is this final model that provides an estimate for the vortex drag of a maglev vehicle in a channel guideway.

1.2 Modeling Strategy for Flow Problems

The numerical method chosen to model the three flow problems is a fairly standard one used by fluid dynamicists to simulate flows for which an analytical solution is either extremely difficult or practically impossible. It superimposes a series of so called elementary flows to obtain a desired complex flow field. The first of these elementary flows is a uniform flow, shown below.

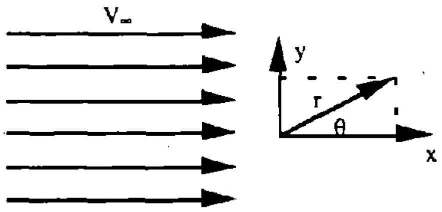

Figure 1.4. A Uniform Flow.

The straight arrows represent velocity vectors, each of magnitude 'V_∞' in the x-direction. The uniform flow alone does not yield an interesting solution; however, it may be superimposed with other elementary flows such as a source flow, to simulate various interesting types of real flows.

The source flow only has a velocity component in the radial direction,

$$V_r = \Lambda/(2\,\pi\,r),\ \Lambda = \text{source strength.} \qquad (1.1)$$

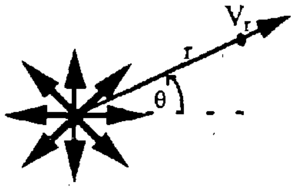

Figure 1.5. A Source Flow.

It can either be a source or a sink depending on the sign of the strength; a sink has all the radial arrows in Figure 1.5 pointing inward. Finally, the last and most important elementary flow of interest in the drag model is the vortex flow.

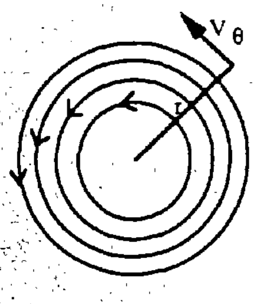

Figure 1.6. A Vortex Flow

The vortex flow only has a velocity component in the tangential direction,

$$V_\theta = \Gamma/(2\,\pi\,r),\ \Gamma = \text{vortex strength}. \qquad (1.2)$$

The reason that this elementary flow is so important is because it is the one of the three elementary flows shown above that simulates the important aerodynamic quantity, lift, in a numerical simulation.. It will be superimposed with the other elementary flow to obtain an estimate of the vortex drag of a vehicle in a channel.

In the three numerical simulations which will be discussed below, the three elementary flows are employed to simulate a particular flow situation using the following methodology. Vortices are first fixed in space in such a way so that they form the shapes of all solid surfaces such as the maglev vehicle fuselage and channel walls in the flow problem. In the problem of a circular cylinder in a free stream, for example, vortices are first arranged in the form of a circle of nondimensional radius, R=1. Then, in this problem as in all the other problems, a flow tangency condition is satisfied halfway in between each of the fixed vortices around the perimeter of a cross section of the cylinder.

$$\overline{V}*\hat{n} = 0$$

$\overline{V}$ ≡ velocity vector from fixed vortex to a collocation point. (1.3)

$\hat{n}$ ≡ normal vector to simulated surface at a collocation point.

This ensures that the air flow in the numerical simulation does not cross (that is, penetrate) any simulated solid surface (... formed by the fixed vortices). Once this is done at each location called a collocation point, it is then possible to form a matrix of flow tangency conditions of the form: $A\Gamma = b$.

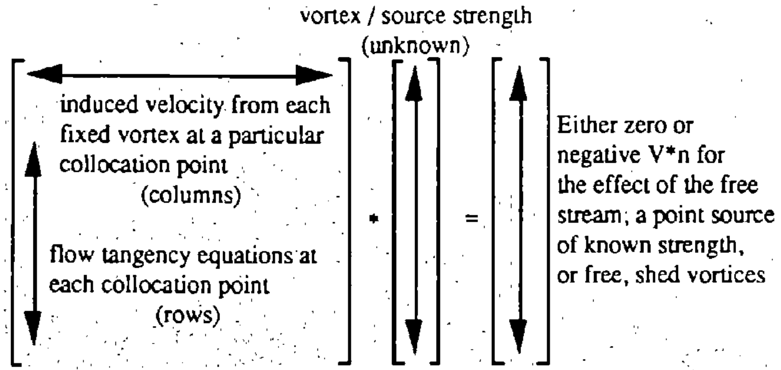

Figure 1.7. Solution Matrix for Flow Simulations.

The matrix shown in Fig. 1.7 is solved for the unknown strengths, Γ, and those strengths are used to compute other important quantities such as induced velocity and eventually drag, depending on the problem.

1.3 Circular Cylinder in a Free Stream

Using the general solution method outlined in the paragraph above, it is now possible to discuss the individual flow problems, starting with the problem of a circular cylinder in a free stream. On the surface it seems that this should be a fairly simple and straight forward problem to solve numerically. After all, the velocity field around a circular cylinder in a free stream is solved easily using complex variables. See, for example, the book by Anderson [1] for this analytical solution.

$$V(r,\theta) = V_\theta = \text{tangential surface velocity} = -2V_\infty \sin(\theta) \qquad (1.4)$$

However, there are some problems with the numerical method which, if not properly addressed, yield an answer with only half the magnitude of the expression in Eq. 1.4.

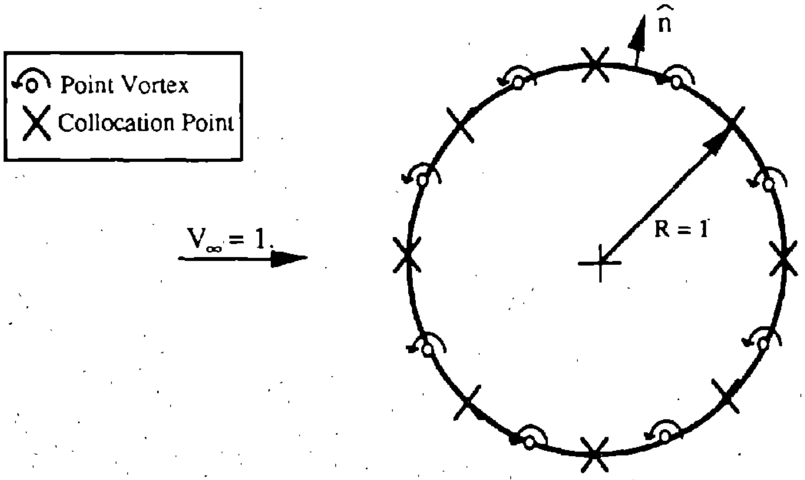

Figure 1.8. Numerical Model for Simulated Flow over a Cylinder.

The simulation is set up, for the most part, as outlined above. Discrete point vortices are first arranged in the form of a circle of nondimensional radius, R=1. Each point vortex induces a velocity at a particular collocation point, and the sum of each of those induced velocities constitutes a row of the solution matrix, A. Flow tangency equations are then written into the solution matrix, giving a system of 'N' point vortices of unknown strength and 'N' equations written at each collocation point (∴ an NxN system). Unfortunately, the problem, which is not obvious, with this set up is that the flow tangency equations at one of the collocation points is redundant[1]. One more unknown and equation are required to close the system of equations and solve for the vector 'Γ'. A point source of unknown strength is placed at the center of the cylinder to bring the total number of unknowns to 'N+1'(see footnote[2]). The Kutta Condition, which says that flow must leave smoothly off the end of the cylinder, is used as the final, 'N+1'th equation to close the system of (N+1)x(N+1) equations.

Having constructed the vector equation it is now possible to solve for the vortex and point source strengths and to use these strengths to determine the velocity profile of air flow around the cylinder. The strength of the point source comes out, as expected, to be very small (essentially zero) when the solution matrix is inverted, but it still must be used to close the system of equations. It is then possible to compute the fluid velocity on the surface of the cylinder to check the accuracy of the numerical scheme. The numerical answer should be close to the answer in Eq. 1.4. Unfortunately, the numerical scheme encounters problems when trying to evaluate fluid velocities close to the surface of the cylinder. The solution obtained is half the answer determined by the analytical solution.

As it turns out, the trick is to use an analytic velocity correction near the cylinder surface (i.e. in the near-field) instead of the velocity induced by point vortices. The near-field correction is set up by considering a small section of cylinder and smearing the vorticity, Γ, contained within a near-by point vortex over this section. See Fig. 1.9 below for the model for this type of technique.

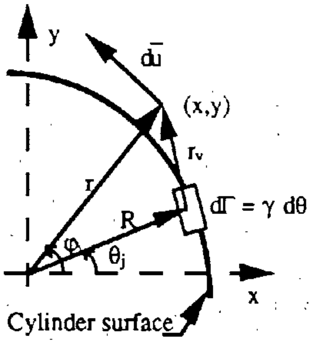

$$\bar{r_v} = (x_v, y_v) \qquad \begin{aligned} x_v &= r\cos(\varphi) - R\cos(\theta) \\ y_v &= r\sin(\varphi) - R\sin(\theta) \\ r_v^2 &= x_v^2 + y_v^2 \\ &= S + P\cos(\varphi - \theta) \\ &: S = r^2 + R^2,\ P = -2\,r\,R \end{aligned}$$

$$\bar{du} = (du, dv) \qquad du = -\frac{d\Gamma}{2\pi}\frac{\cos(\theta)}{r_v},\ dv = \frac{d\Gamma}{2\pi}\frac{\sin(\theta)}{r_v}.$$

$$: \theta_j - \Delta\theta < \theta < \theta_j + \Delta\theta$$

Figure 1.9 Model for Numerical Smoothing Technique

The vertical, near-field velocity induced by the boxed section of vorticity in Fig. 1.9 at point (x,y) is:

---

[1] Private communication with Prof. Donald B. Bliss, Prof. of Mech. Engineering, Duke University, Durham, N.C., November 1989.

[2] Private communication with Prof. Mark Drela, Prof. of Aeronautics and Astronautics, M.I.T., Cambridge, Ma., July 1991.

$$dv = \frac{\gamma}{2\pi}\frac{x_v}{r_v^2} = \frac{\gamma}{2\pi}\left[\frac{r\cos\varphi}{S + P\cos(\varphi - \theta)} - \frac{R\cos\varphi}{S + P\cos(\varphi - \theta)}\right] d\theta \qquad (1.5)$$

Using the dummy variable, Ψ, so that $\Psi = \theta - \varphi$ and $d\Psi = d\theta$,

$$dv = \frac{\gamma}{2\pi}\left[\frac{r\cos\varphi}{S + P\cos\Psi} - \frac{R\cos\Psi\cos\varphi}{S + P\cos\Psi} + \frac{R\sin\Psi\sin\varphi}{S + P\cos\Psi}\right] d\Psi \qquad (1.6)$$

Finally, an integration of Eq. 1.6 between $\theta_j - \Delta\theta - \varphi$ and $\theta_j + \Delta\theta - \varphi$ gives the following expression for the vertical near-field velocity, v.

$$\begin{aligned} v = \frac{\gamma}{2\pi}\Bigg[& -2\frac{R\cos\varphi}{P}(\Delta\theta) + \frac{\cos\varphi}{P}(rP + RS)\frac{2}{\sqrt{S^2 - P^2}}\Bigg[\\ & \mathrm{Arctan}\left(\frac{\sqrt{S^2 - P^2}\,\mathrm{Tan}((\theta_j + \Delta\theta - \varphi)/2)}{S+P}\right) - \\ & \mathrm{Arctan}\left(\frac{\sqrt{S^2 - P^2}\,\mathrm{Tan}((\theta_j - \Delta\theta - \varphi)/2)}{S+P}\right)\Bigg] - \\ & \frac{R\sin\varphi}{P}\ln\left(\frac{S + P\cos(\theta_j + \Delta\theta - \varphi)}{S + P\cos(\theta_j - \Delta\theta - \varphi)}\right)\Bigg]. \end{aligned} \qquad (1.7)$$

A similar expression is obtained for the horizontal near-field velocity, u.

$$\begin{aligned} u = \frac{\gamma}{2\pi}\Bigg[& -2\frac{R\sin\varphi}{P}(\Delta\theta) + \frac{\sin\varphi}{P}(rP + RS)\frac{2}{\sqrt{S^2 - P^2}}\Bigg[\\ & \mathrm{Arctan}\left(\frac{\sqrt{S^2 - P^2}\,\mathrm{Tan}((\theta_j + \Delta\theta - \varphi)/2)}{S+P}\right) - \\ & \mathrm{Arctan}\left(\frac{\sqrt{S^2 - P^2}\,\mathrm{Tan}((\theta_j - \Delta\theta - \varphi)/2)}{S+P}\right)\Bigg] - \\ & \frac{R\sin\varphi}{P}\ln\left(\frac{S + P\cos(\theta_j + \Delta\theta - \varphi)}{S + P\cos(\theta_j - \Delta\theta - \varphi)}\right)\Bigg]. \end{aligned} \qquad (1.8)$$

Using these near-field corrections, it is possible to match the numerical to the analytical fluid velocity profile around the cylinder as shown below in Fig. 1.10.

In this graph, r = 1 represents the nondimensional radius of the cylinder, R, and the data shown is with and without smoothing. The data at 81 degrees represents the velocity profile right at a point vortex and the data at 90 degrees is half-way in between vortices. Notice that the rippled data, or data without smoothing, is good far away from the surface of the cylinder (i.e. in the far-field), but not near or on the surface of the cylinder. As mentioned before, the data in between

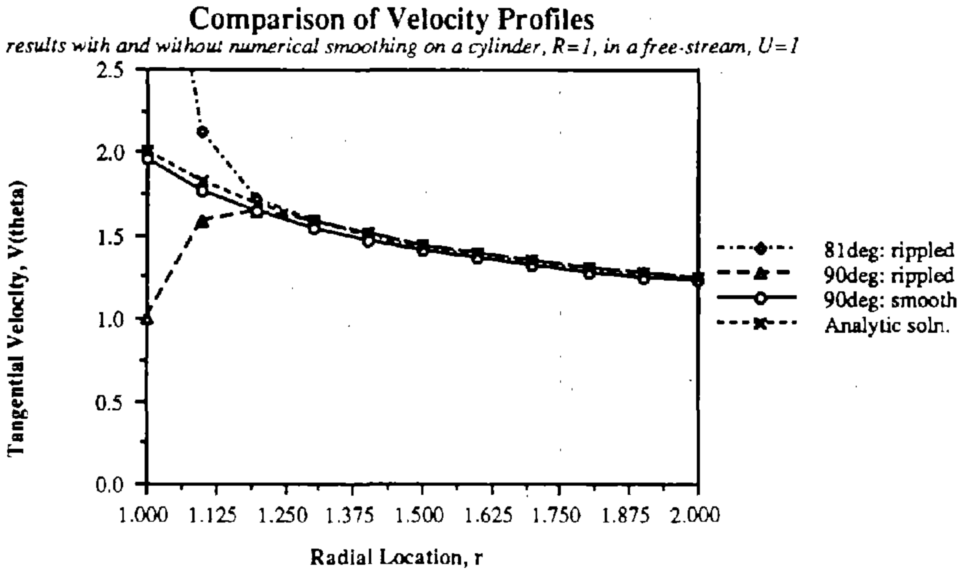
Comparison of Velocity Profiles

results with and without numerical smoothing on a cylinder, R=1, in a free-stream, U=1

Figure 1.10. Comparison of Velocity Profiles to Analytical Solution.

vortices (at 90 degrees) is half the expected value without smoothing, but is effectively equal to the analytical solution when numerical smoothing is performed. Consequently, the numerical scheme with an analytical correction routine produces the correct flow field for flow about a circular cylinder in a free stream. It can now be inserted into the overall numerical scheme to simulate the cross-section of a maglev vehicle nose in a channel guideway, which is modeled in the next section using an appropriate numerical scheme.

1.4 Vortex Shedding off a Flat Plate in a Free Stream

The second flow simulation of interest is the simulation of vortex shedding off a flat plate normal to a free stream. The problem involving the motion of a flat plate through a fluid medium prior to the onset of flow separation off the tips of the plate has been solved analytically using complex variables. However, this problem gets a little more complicated with the introduction of shed vorticity into the flow, necessitating the use of numerical methods for a solution. The problem is constructed initially just like the problem of a cylinder in a free stream; fixed point vortices are arranged in such a manner (i.e. in a straight line) that they simulate the surface of a flat plate, perpendicular to a free stream of nondimensional velocity, $V_\infty = 1$.

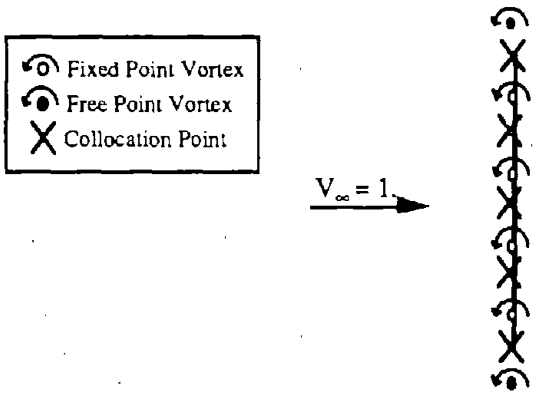

Figure 1.11. Numerical Model for Simulated Flow over a Flat Plate.

Initially, all vortices are positioned as shown in Fig. 1.11. A number, N, of fixed vortices are used to simulate the surface of the flat plate while two free vortices lie juxtapositioned to the tips of the plate. Altogether, the 'N+2' vortices, all of unknown strength, simulate a so-called 'extended' flat plate. The 'extended' flat plate, a plate slightly longer than the actual flat plate in the simulation, is a tool which is used to determine the proper location of the two free, near-tip vortices while conserving energy in the flow. This is done by first determining the circulation distribution on the extended flat plate, using the matrix equation $A\Gamma = b$ (see Fig. 1.7).

The circulation distribution is determined using the 'N+2' vortices along with their corresponding 'N+1' collocation points (... and thus 'N+1' equations) halfway in between the vortices and at the plate tips, as shown in Fig. 1.11. The Kutta Condition, which mandates smooth flow off the plate tips, constitutes the N+2nd and final equation. Now, the (N+2)x(N+2) system of equations may be solved for the 'N' unknown fixed vortex strengths and 2 unknown near-tip vortex strengths, Γ. These strengths represent the strengths of the vortices at the initial time step. The important portion of this circulation distribution is the portion beyond the last collocation point on each end of the flat plate; it is the portion beyond each tip of the flat plate, as shown in Fig. 1.12. It is important because it locates the appropriate position for each near-tip free vortex by integrating for the 'y' centroid of the portion of the circulation distribution near each plate tip.

So far, everything that has been said about the flat plate model has applied only to the initial time step in which there are two free, shed vortices in the flow. However, the same ideas apply to later time steps; the only difference is the existence of more than two free vortices in the flow. Yet, the matrix, A, does not grow in size as additional vortices are shed off the plate tips. It remains a (N+2)x(N+2) matrix. The influence of the so called previously shed vortices, seen in Fig. 1.13, on the solution matrix is seen only in the form of the 'b' vector. The velocities induced

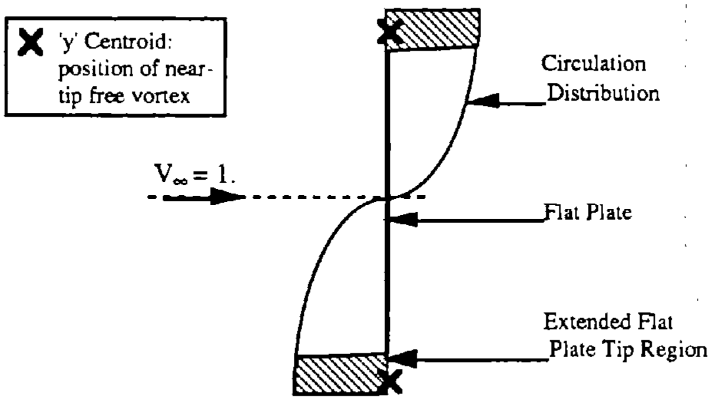

Figure 1.12. Position of Near-Tip Free Vortices

at a particular collocation point by all the previously shed vortices are summed and appear in the form '-V*n' on the right-hand side of the solution matrix, $A\Gamma = b$, where Γ is now a vector of unknown fixed and near-tip, shed vortex strengths. In addition, once free vortices closest to the plate tips are shed into the fluid medium, they retain their same strength but just change their locations in space during successive shedding iterations. The first pair of shed vortices, for example, retains its same strength throughout further shedding iterations. The only free vortices of unknown strength are the near-tip free vortices.

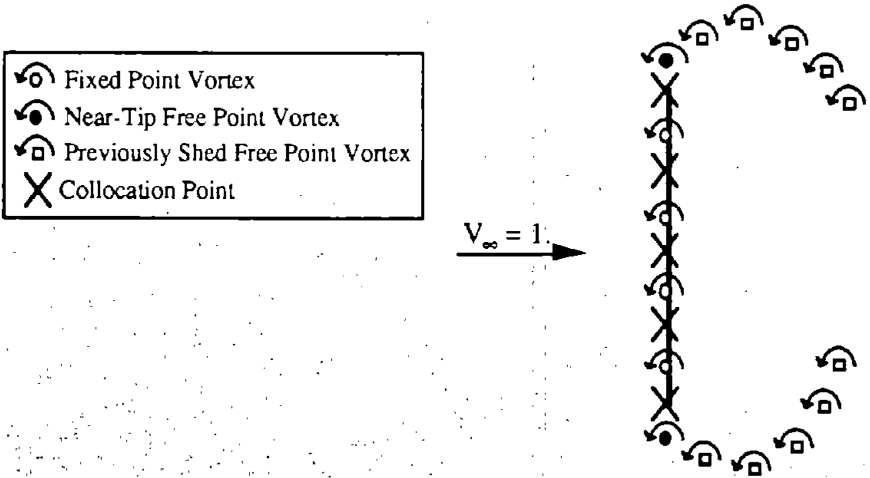

Figure 1.13. Schematic of Vortex Shedding off a Flat Plate.

Once all vortex strengths are known, the induced velocity from all vortices, fixed and free, is computed on each of the free vortices and a new position for each of the free vortices is computed according to the integral of the induced velocity. Using a Kutta Condition formulated to produce symmetric vortex shedding and adjusting the time scale, the result looks as follows.

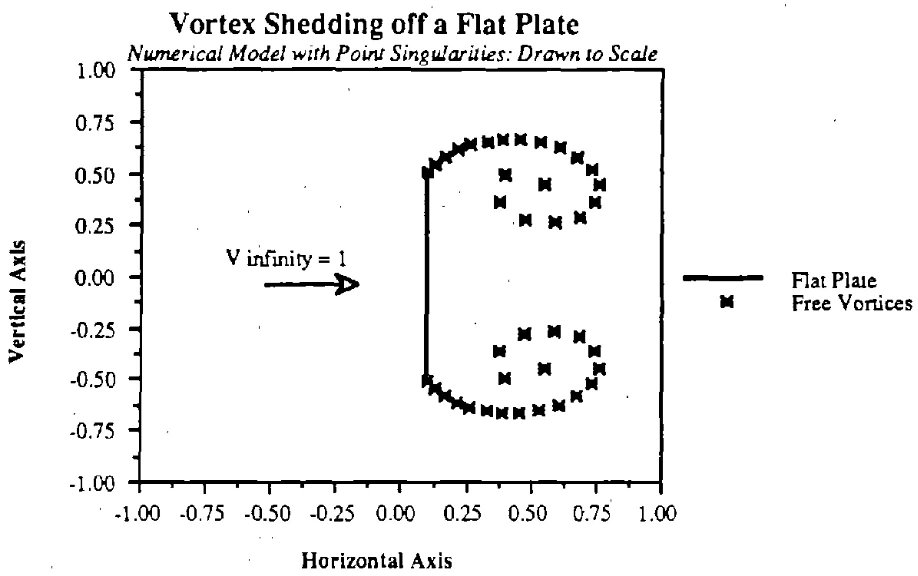

Figure 1.14. Numerical Results of Vortex Shedding off a Flat Plate

A few problems had to be resolved before obtaining the desired solution. First, it was hard to enforce the Kutta condition at both plate tips and still obtain a solution with the geometry shown in Fig. 1.14. The condition of zero circulation, $\Sigma \Gamma_i = 0$, which in this case is identical to the Kutta Condition, kept giving a solution with undesired periodic shedding. However, this type of solution is not useful in the larger problem of a maglev vehicle moving through a channel guideway. The larger problem must be able to take advantage of various symmetries in order for it to be tractable. Consequently, the problem of vortex shedding off a flat plate must display some symmetry. This problem was corrected by enforcing top-to-bottom symmetry, via a modified Kutta Condition, in the model shown in Fig. 1.13. When the strengths of the free, shed vortices are set to be equal in magnitude and opposite in sign, the resultant solution is symmetric, as seen in Fig. 1.14.

The most time-consuming issue involved a determination of the form of the free vortices. The primary objective of this section of the overall report is to provide an estimate for drag of the nose of a maglev vehicle. As will be demonstrated near the end of this specific report, drag is directly related to the amount of kinetic energy in the flow. It turns out that the form of the free vortices directly affects the calculation of kinetic energy in the flow; thus, it is important to select the correct form for the free vortices. One method of calculating energy employs vortices of finite size, that is, vortices with cores. When a system of vortices can be simplified down to a pair of vortices with cores, it is possible to derive an analytical expression for the kinetic energy in the flow, as shown below.

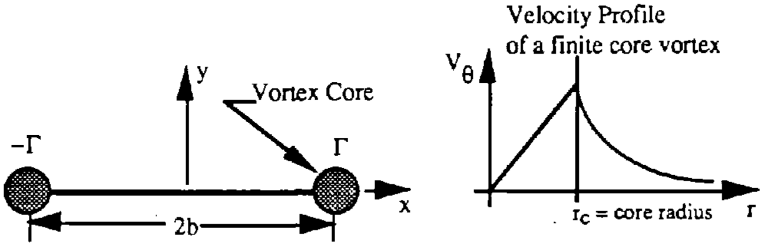

Figure 1.15. Vortex Pair with Cores.

$$V_\theta = \begin{cases} \dfrac{\Gamma}{2\pi r_c^2} r, & 0 \le r \le r_c \\ \dfrac{\Gamma}{2\pi r}, & r_c \le r \le \infty \end{cases} \tag{1.9}$$

Using the integral equation for energy, T:

$$T = \frac{\rho}{2}\int \Gamma\, \overline{V} * \hat{n}\, dS \tag{1.10}$$

The integral in (1.10) is evaluated along a line connecting the centers of the two vortex cores in Fig. 1.3 so that along with the velocity field for a vortex with a finite core, it is possible to express the energy of a vortex pair as

$$T = \frac{\rho\, \Gamma^2}{2\pi}\left\{\ln\left(\frac{2b - r_c}{r_c}\right) + \frac{1}{4}\right\}. \tag{1.11}$$

The size of the core can now be determined by setting the analytical solution for the energy equal to Eq. 1.11.

$$\frac{\pi\rho}{2} b^2 U^2 = \frac{\rho\, \Gamma^2}{2\pi}\left\{\ln\left(\frac{2b - r_c}{r_c}\right) + \frac{1}{4}\right\}. \tag{1.12}$$

However, when this is done the core size, r_c, is minuscule and the energy computed using this method for successive shedding iterations does not exactly match the expected energy.

The alternate, much simpler method for computing kinetic energy in a flow due to the shedding of vorticity off a flat plate is to use the formula for kinetic energy of a collection of discrete point vortices (i.e. without cores) in space, given by Batchelor [9]:

$$T = -\frac{\rho}{4\pi} \sum_i \sum_j \Gamma_i \Gamma_j \ln r_{ij} \ ,(i \neq j) \ ; \ r_{ij}^2 = (x_i - x_j)^2 + (y_i - y_j)^2 \qquad (1.13)$$

where Γ_i is the strength of vortex 'i' in the numerical solution.

When this formula is evaluated in the first time step (corresponding to kinetic energy in the flow prior to any shedding of vortices), it gives a value of $T/\rho = 1.3 \ m^4/sec^2$ for 40 point vortices fixed to a flat plate and $T/\rho = 1.5 \ m^4/sec^2$ for 80 vortices fixed to the flat plate. This compares fairly well against a value of $T/\rho = 1.7 \ m^4/sec^2$ from the analytical solution, also shown in Batchelor. That is, one would expect that as the number of fixed vortices becomes infinite the correct result from the analytical solution is approached asymptotically. This model will now be superimposed onto the model of a cylinder in a free stream to obtain an estimate for the drag of a maglev vehicle nose in a channel guideway.

1.5 Maglev Model: Point Source between two Parallel Walls

The problem of vortex shedding due to the passage of the nose of a maglev vehicle through a channel guideway can be simulated using an expanding cylinder between two parallel walls, with only the upper-half of the model (which will be referred to as the half-model) simulating the actual movement of a maglev vehicle nose through a channel guideway.

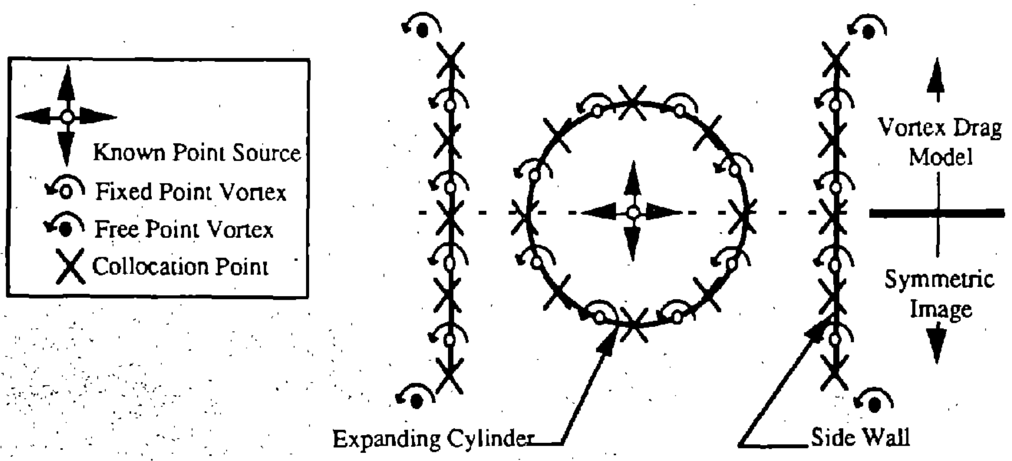

Figure 1.16. Schematic of Maglev Nose Vortex Drag Model.

That much should be fairly obvious considering the general maglev nose geometry, shown schematically in Fig. 1.3, and the model shown above in Fig. 1.16. What is not obvious is the numerical scheme needed to simulate the real channel flow. In particular, the form of the matrix, A, in the matrix equation $A\Gamma = b$ is not immediately apparent.

The simulation is set up, for the most part, in a manner similar to the general set up outlined in section 1.2. Discrete point vortices are first fixed in the form of a circle of nondimensional radius, $R = 1$. In general, there are 'Ncyl' of these vortices with 'Ncyl' collocation points halfway in between each pair of vortices. The vortices simulate the cross-section of a maglev vehicle nose and its image in the channel guideway, as shown in Fig. 1.16. Next, a number, Nwall, of fixed vortices, on each side of the cylinder, are used to simulate the sidewalls of the channel guideway and their images, see Fig. 1.16. Each sidewall, with its image, has 'Nwall+1' collocation points between each pair of fixed vortices and at the tips of the side wall and its image. All vortices in the simulation mentioned thus far are fixed in space and are of unknown strength. There is also one free vortex of unknown strength which lies juxtapositioned to the tip of each side wall and its image, for a total of four near-tip free vortices of unknown strength.

Unfortunately, the simulation of this channel flow cannot be constructed using a direct superposition of the two numerical schemes used in sections 1.3 and 1.4 (i.e. simulations of a cylinder in a free stream and a flat plate in a free stream). This is due primarily to the absence of a free stream which was present in the other two flow simulations but does not exist in this case. Instead, the energy source in this simulation is a point source within the cylinder. To first order, the energy of the bow vortices is determined by the source strength, and the effect of the vortices fixed to the cylinder has only a second order effect. The main function of these vortices is to preserve the exact shape of the cylinder in the presence of the vortices associated with the side walls. Therefore, the problem of the expanding cylinder can be replaced by that of a source between two walls, while still maintaining an excellent approximation to the nose drag.

For the sake of completeness, however, the computation of strength of the vortices on the cylinder shown in Fig. 1.17 is outlined below, even though these vortices are not included in the actual simulation which follows. One immediately encounters the same problem with closure that was encountered for the cylinder in a free stream. The problem can be simplified by introducing symmetry about both the horizontal and vertical axes, i.e. recognize that there is no flow about either the ground plane or the vertical mid-plane. To do this, assume that for each vortex in the first quadrant, there is one of opposite sign in the second quadrant, of the same sign in the third, and of opposite sign in the fourth, all strengths being equal.

The introduction of symmetry eliminates the problem of redundant equations, i.e. the flow-tangency equations satisfy the boundary conditions on the surface of the cylinder and are linearly

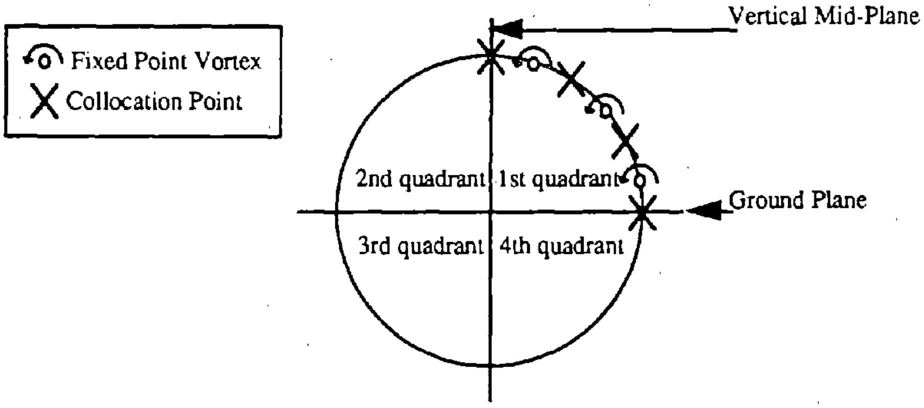

Figure 1.17. Schematic of Cylinder Construction.

independent. However, there is still one more collocation point than vortex, since the boundary conditions must be satisfied at both ends of the quadrant (i.e., there are four X's in Fig. 1.17 and only three O's). This problem is solved by letting the strength of the source at the center be the remaining unknown. Recall that in the case of the cylinder in a free stream, a source was arbitrarily introduced at the center of the cylinder as an unknown and the strength of the source from the numerical solution automatically "came out" to be the right answer, namely zero. Similarly, in the present case, the strength of the source will "come out" to be equal to the rate of change of nose cross-sectional area. To see this, consider the following formula for the source strength.

$$\Lambda = \int V_r \, r \, d\theta = 4 \int_0^{\pi/2} V_r \, r \, d\theta \qquad (1.14)$$

The second integral in Eq. 1.14 is taken along the arc of one quadrant of the cylinder. Now imagine that one wishes to build up the required flow one piece at a time, starting with the expanding cylinder without the plates. We prescribe a velocity V_r at each collocation point. In that case one finds, obviously, that the strength of all the vortices on the surface of the cylinder is zero and $\Lambda = dA/dt$ as required. When the vortices on the plates are introduced, they have the same double symmetry as vortices on the cylinder, i.e. no flow through the x-axis or the y-axis, and no net flow across the arc of any quadrant of the cylinder. That is, the local velocities, V_r, are affected by the vortices, but the integral is unaffected. Stated differently, we have the following system of equations.

$$A\Gamma + V_s = b \qquad (1.15)$$

In Eq. 1.15, V_s (the unknown velocities from the source) is a column vector, each of whose elements has the same value, $\Lambda/2\pi r$, and the elements of the column vector 'b' are the prescribed velocities V_r on the surface of the cylinder. Even though the flow field becomes complicated due to the growth of the perimeter of the cylinder in the course of the simulation, plate vortices will try to make some V_r's to go up and some to go down in such a way as to leave the average value unchanged. The vortices on the cylinder will counteract the plate vortices and restore the V_r's to the prescibed values. Furthermore, the source strength, Λ, emerging from the numerical solution depends only on the average value and so it is unaffected by any of these vortices.

Fortunately, since energy is the only real concern in this numerical simulation, the model in Fig. 1.16 can be simplified down to a point source of known strength, which simulates the maglev vehicle nose cross-section, between two parallel walls, which are simulated with a distribution of fixed vortices, as shown below in Fig. 1.18.

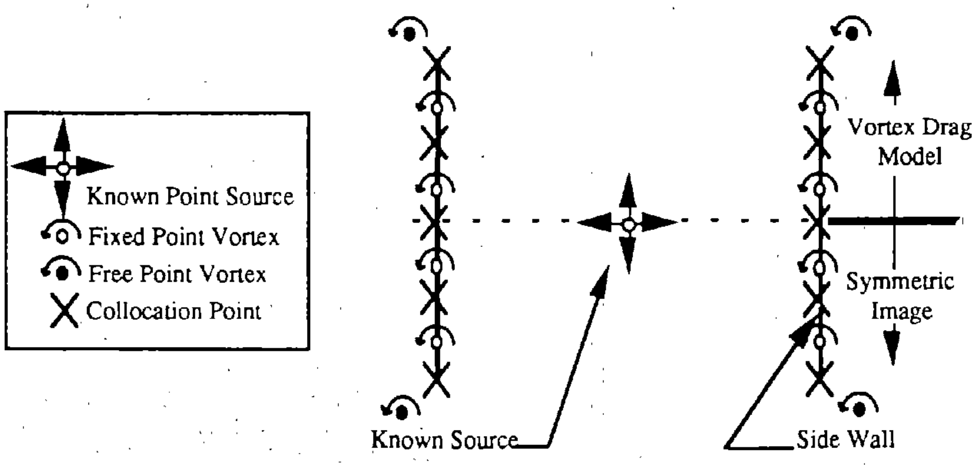

Figure 1.18. Numerical Vortex Drag Model without a Cylinder.

The result from this simulation, which uses the model in Fig. 1.18, should be very similar to the result using the model shown in Fig. 1.16. In both cases, the elementary flow which actually simulates the passage of a maglev vehicle nose through a channel guideway is the source flow. The strength of the discrete point source is adjusted so that it simulates the shape of the maglev vehicle nose. As an example, consider the cross-section shown in Fig. 1.3 and let 'x' represent a direction perpendicular to the page. This corresponds to a point source of constant strength, Λ, in 'x', where 'Λ' is equal to the rate of change in cross-sectional area, S'(x), of the maglev vehicle's nose. In this simulation, $\Lambda = 1$. Stated mathematically, the strength of the point source, Λ, and the nose cross-sectional area, S'(x), are related through Eq. 1.16, where R(x) is the radius of the nose cross-section.

$$R(x) = \text{cylinder (i.e. cross-sectional area) radius} = \sqrt{\frac{\Delta x}{\pi}} \qquad (1.16)$$

Now, before proceeding, it is important to discuss the crucial difference, alluded to in the previous paragraph, between this simulation and the other simulations discussed in sections 1.3 and 1.4. Whereas the other real flows, corresponding to the simulations in sections 1.3 and 1.4, were two-dimensional in nature, the real flow geometry of this channel-type flow is three dimensional; that is why the 'x' direction, perpendicular to the page, was only introduced in the previous paragraph. The link between two-dimensional flows and this three-dimensional flow is made through an analytical method called slender-body theory [3]. It permits the analysis of certain steady, three-dimensional flows as unsteady, two-dimensional flows. In three dimensions, it is possible to fix a frame of reference to a slab of fluid which is also fixed at some location along the channel guideway. The problem is thus reduced to a problem in two dimensions as the maglev vehicle's nose passes through the channel guideway, penetrating a fixed slab of fluid (see Fig. 1.19 below).

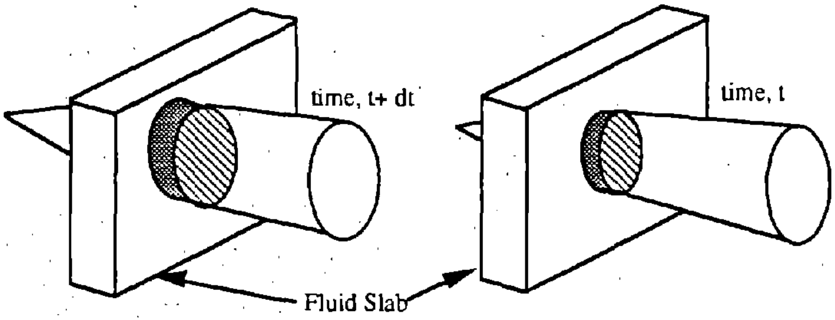

Figure 1.19. Vehicular Penetration of a Fluid Slab.

Actual vortex shedding off channel walls is performed, based on the slender-body analogy. Shed vorticity and energy of the vortices are tracked within the fluid slab at each iteration of time, as the maglev vehicle nose moves through the guideway and through the fluid slab. The result of such tracking is a description of the energy build-up in a flow with shed vorticity, and an estimation of the energy associated with the motion of a maglev vehicle nose through a channel guideway.

The numerical simulation of this flow begins with the geometry pictured in Fig. 1.18. There are 'Nwall' fixed vortices on each of the side walls and images, and initially four free vortices, one at each of the tips of the two walls and images. The energy source is the point source (...representing the nose of the vehicle) of known strength in between the two walls. To close the system of equations, left-to-right symmetry is assumed and the Kutta condition is enforced off the right and its image. Therefore, the solution matrix, A, has dimensions (Nwall + 2)x(Nwall + 2), corresponding only to the right-hand side of the model. It is solved for the strengths of all the fixed and the two free vortices on the right wall and image using the matrix equation $A\Gamma = b$. In the first time step, 'b' is composed of the induced component '-V*n' from the point source at a particular collocation point. The rest of the vortex strengths in the model in Fig. 1.18 are known because of symmetry.

The vortex strengths are used to compute an induced velocity on each of the four initial, shed vortices and these four free vortices are shed during the time interval, Δt. Subsequent iterations repeat the same type of steps for all free vortices; only the values in the 'b' vector change in the solution equation, $A\Gamma=b$. In subsequent iterations, the vorticity at each collocation point (i.e. associated with each row of 'A') contains the sum of the velocities induced by all free vortices which are not near-tip free vortices (... near-tip free vortices are the only free vortices whose strengths are initially unknown in each shedding iteration) plus the velocity induced by the point source. That is to say, the 'b' vector is made up of an appropriate sum of '-V*n' components at each collocation point. See Fig. 1.13 and 1.18 for a pictorial description of this scheme.

When this numerical sheme for vortex shedding is implemented and run through several iterations, it produces the flow shown below in Fig. 1.20.

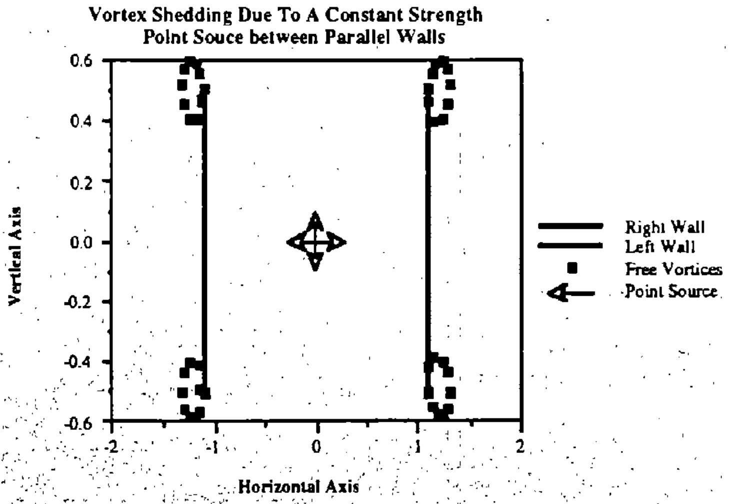

Figure 1.20. Vortex Shedding off Parallel Walls due to a Point Source

However, to represent the real flow, the geometry of Fig. 1.20 must be modified into the geometry shown below in Fig. 1.21, with only the top half of Fig. 1.20 shown, to represent vortex shedding due to the passage of a flat-bottomed nose of a maglev vehicle through a channel guideway. Recall that this modification is possible because of the use of an image technique to solve the flow problem. The lower half of Fig. 1.20 is simply the image of the upper half. It is used as a tool to obtain the geometry of large-scale bow vortices (see Fig. 1.3 for review of terminology) in the channel flow, and may be discarded for further calculations, such as for the calculation of kinetic energy and vortex drag.

But, before proceeding, it is worthwhile to examine the differences between the flow simulation in section 1.4 and the one shown below in Fig. 1.21. Notice that, compared to the result of the numerical simulation of vortex shedding off a flat plate in a free stream (Fig. 1.14), the free vortices shown in Fig. 1.21 form much tighter spirals which are much closer to the sidewalls. This is probably because the source, given its location, does not have as great an influence on the free vortices here as a free stream has on free vortices shed off a flat plate. The point source, in this case, is centralized, so the sidewalls tend to block its effect on the free vortices. Considering the simulation of a flat plate in a free stream, the full effect of the free stream is felt at the tips of the plate constantly, resulting in much greater convection of the free vortices and vortex spirals which are not wound as tightly as the bow vortices of the present case.

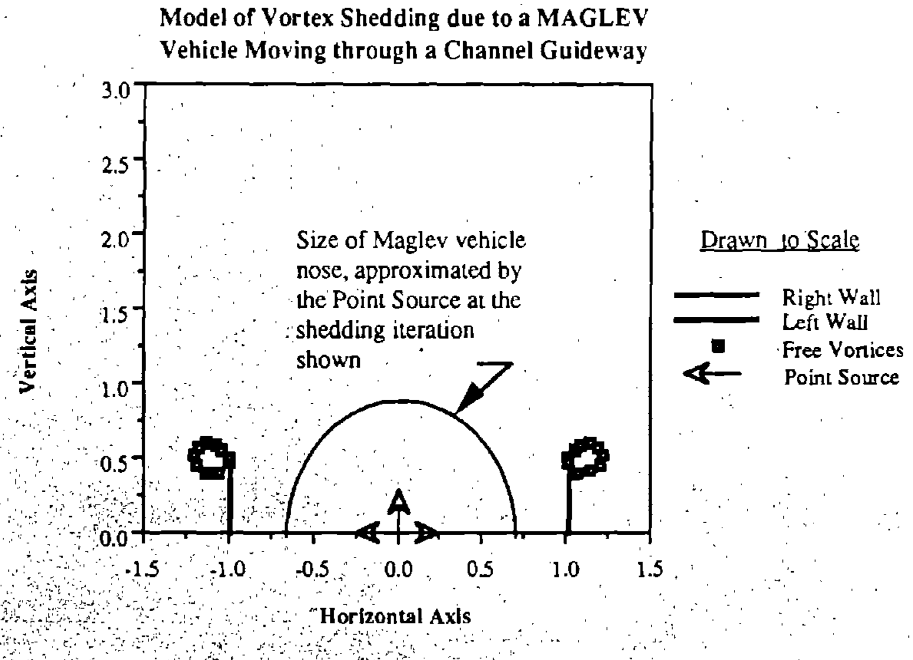

Figure 1.21. Maglev Nose Vortex Drag Model.

Getting back to the main purpose of this section, it is now possible to determine kinetic energy in this channel flow due to the passage of a maglev vehicle nose through the channel guideway using the geometry of the bow vortices shown in Fig. 1.21. The kinetic energy, per unit length of maglev vehicle nose, T, of the collection of free vortices which constitute the bow vortices in Fig. 1.21 is computed according to Batchelor's formula, which may be re-stated as follows:

$$T = -\frac{\rho}{4\pi}\sum_{i}\sum_{j}\Gamma_i\,\Gamma_j \ln r_{ij}\,,\ (i{\neq}j)\ \ ;\ \ r_{ij}^2 = (x_i - x_j)^2 + (y_i - y_j)^2 \qquad (1.13)$$

where Γ_i is the strength of vortex 'i' in the numerical solution.

When it is made dimensionless, the kinetic energy may be expressed in terms of an energy coefficient, C_T.

$$C_T = \frac{T}{\frac{1}{2}\,\rho\, A'^{2}_{ref}} = -\frac{1}{2\pi A'^{2}_{ref}}\Big[\sum_{i}\sum_{j}\Gamma_i\,\Gamma_j \ln r_{ij}\Big]\,,\ (i{\neq}j) \qquad (1.17)$$

Then, when Eq. 1.17 is incorporated into the numerical simulation of vortex shedding, it is possible to calculate kinetic energy in the channel flow for each iteration of vortex shedding, as shown below in Fig. 1.22.

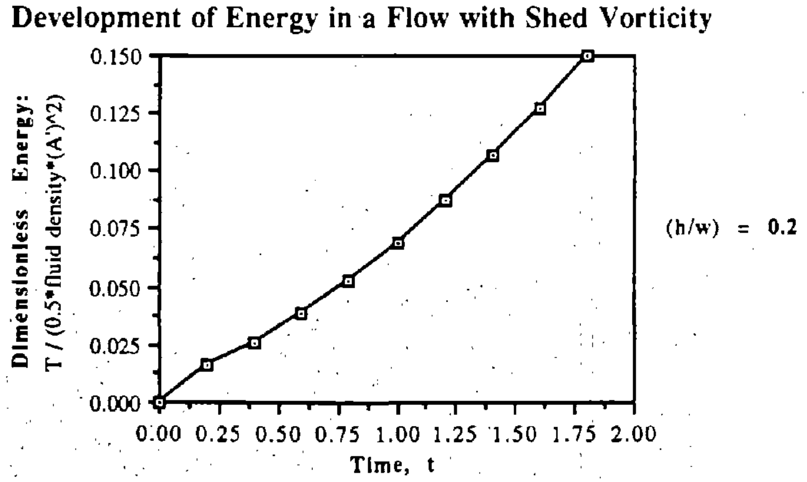

Figure 1.22. Energy Due to Passage of Maglev Vehicle Nose.

While this graph is interesting, it is not particularly useful in the form shown above. What is required is a reference which facilitates the computation of kinetic energy due to vortex shedding, based on channel and vehicle dimensions for a variety of nose and channel geometries. This reference is constructed most easily using the numerical scheme which was used to generate

Fig. 1.22. By simply varying parameters for channel dimensions and for the source strength in the numerical scheme, it is possible to generate multiple curves for kinetic energy in the flow.

The results in Fig. 1.22 are made more general by converting the time scale to a dimensionless area scale. This is accomplished by first selecting the reference length 'w/2', where 'w' is the width of the channel guideway, from the geometry in Fig. 1.21. The cross-sectional area of the nose, A, is also made dimensionless as follows.

$$A = \left(\frac{w}{2}\right)^2 \bar{A}, \quad \bar{A} \equiv \text{dimensionless area} \qquad (1.18)$$

When Eq. 1.18 is differentiated with respect to the dimensionless time, t, seen in Fig. 1.22, it assumes the following form.

$$\frac{dA}{dt} = \left(\frac{w}{2}\right)^2 \frac{d\bar{A}}{dt} \qquad (1.19)$$

In the simulation, $\Lambda = \frac{d\bar{A}}{dt}$ is set equal to 1, so when Eq. 1.19 is integrated with respect to the dimensionless time 't', the following relation is obtained to relate the nondimensional time scale 't' to the geometry in Fig. 1.21.

$$t = \frac{A_{max}}{\left(\frac{w}{2}\right)^2 \frac{d\bar{A}}{dt}} = \frac{A_{max}}{\left(\frac{w}{2}\right)^2} \qquad (1.20)$$

In this expression, A_{max} is the maximum cross-sectional area at the base of the nose, as shown in Fig. 1.23 below.

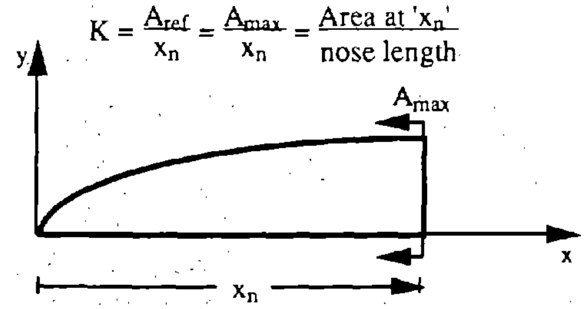

Figure 1.23. Schematic Representation of the Nose of a Maglev Vehicle.

When nondimensional kinetic energy due to vortex shedding is plotted against the dimensionless area ratio A_{max} / w^2 for a variety of channel guideway geometries, it is possible to obtain the graph shown below in Fig. 1.24.

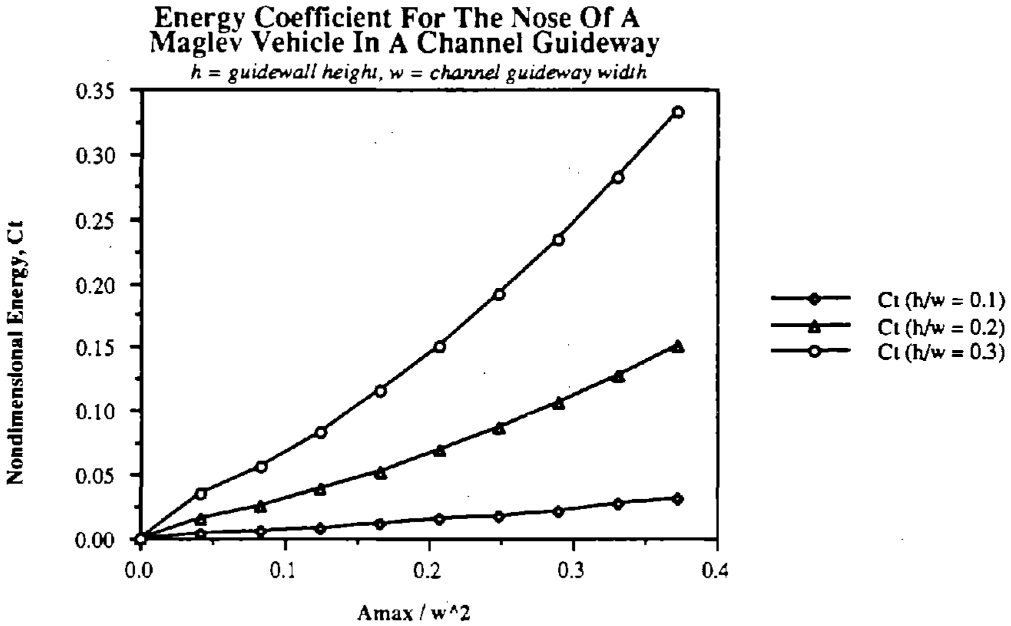

Figure 1.24. Nondimensional Energy for the Nose of a Maglev Vehicle

This graph now serves as a reference for the calculation of kinetic energy, for a specific nose shape and for a variety of channel geometries. In particular, the curves shown in Fig. 1.24 correspond to a point source of constant strength. This simulates a nose with a constant change in cross-sectional area, dA(x)/dx = K = constant (see Fig. 1.25). Kinetic energy is shown for a variety of channel geometries, h/w = channel guidewall height / channel width, as a function of the dimensionless length scale, Amax/w^2. Given a maximum cross-sectional area, Amax, and channel dimensions 'h' and 'w', Fig. 1.24 may be used to determine the amount of kinetic energy, due to vortex shedding, generated as a result of the passage of a maglev vehicle nose through a channel guideway.

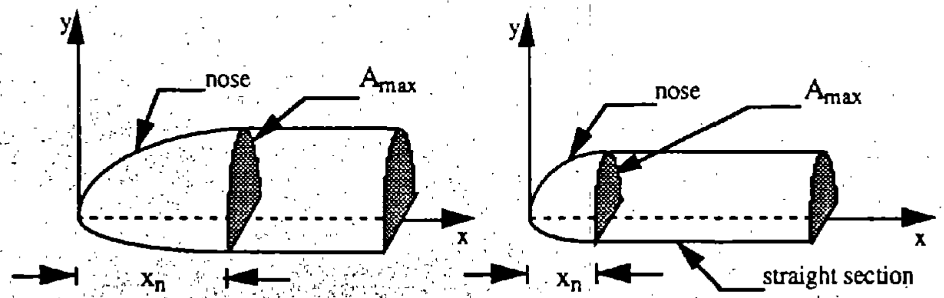

Figure 1.25. Maglev Nose Shapes for dA(x)/dx = Constant

Vortex drag may be calculated as follows, using the kinetic energy obtained from curves such as the ones shown above in Fig. 1.24. First, consider the form of the integral expression for vortex drag [ref 8 page 173-175]:

$$D_V = -\frac{\rho}{4\pi} \int_{-b/2}^{b/2} \int_{-b/2}^{b/2} \frac{d\Gamma}{dy} \frac{d\Gamma}{dy_1} \ln | y - y_1 | \, dy \, dy_1 \qquad (1.21)$$

where $\Gamma(y)$ is the distributed circulation on a wing of span 'b'.

This form can be made dimensionless and expressed as a vortex drag coefficient, C_{D_v}, as follows:

$$C_{D_v} = \frac{D_v}{\frac{1}{2} \rho_\infty U_\infty^2 A_{ref}} = - \frac{1}{2 \pi U_\infty^2 A_{ref}} \left[\int_{-b/2}^{b/2} \int_{-b/2}^{b/2} \frac{d\Gamma}{dy} \frac{d\Gamma}{dy_1} \ln | y - y_1 | \, dy \, dy_1 \right]. \qquad (1.22)$$

Notice the similarity between the expression in Eq. 1.22 and the expression for kinetic energy in Eq. 1.17. At least in form, Eq. 1.17 looks like the discretized version of the expression for vortex drag in Eq. 1.22. The relationship between these two quantities is better understood via a comparison such as the one shown below.

$$\frac{C_T}{C_{D_v}} = \frac{ - \frac{1}{2 \pi A'^2_{ref}} \left[\sum_i \sum_j \Gamma_i \Gamma_j \ln r_{ij} \right] }{ - \frac{1}{2 \pi U_\infty^2 A_{ref}} \left[\int \int \frac{d\Gamma}{dy} \frac{d\Gamma}{dy_1} \ln | y - y_1 | \, dy \, dy_1 \right] } \qquad (1.23)$$

Since the bracketed quantities are identical, the bracketed quantity in Eq. 1.17 simply being the discretized version of the bracketed quantity in Eq. 1.22, this ratio can be reduced to the following form.

$$C_{D_v} = C_T \frac{1}{U_\infty^2} \left[\frac{A'^2}{A} \right]_{ref} \qquad (1.24)$$

In Eq. 1.24, the variable ' A' ' is defined as

$$A' = \frac{dA}{dt} = \frac{dA}{dx} * \frac{dx}{dt} = U_\infty * \frac{dA}{dx} . \qquad (1.25)$$

Consequently, when dA/dx = const. (= K, as shown in Fig. 1.23), and setting $A_{max} = A_{ref}$, the coefficient of vortex drag for the nose of a maglev vehicle, in terms of kinetic energy in the flow, may be written as

$$C_{D_v} = C_T \frac{A_{max}}{x_n^2}. \qquad (1.26)$$

This result now permits an estimation of the total drag of the nose of a maglev vehicle moving through a channel guideway by considering both vortex drag (1.26) and viscous drag, that is, drag due to skin friction. In general, the expression for the total drag coefficient, Cd, may be written as follows:

$$C_d = C_T \frac{A_{max}}{x_n^2} + C_f \frac{A_w}{A_{max}}. \qquad (1.27)$$

In this expression (1.27), 'A_w' is the wetted surface area of the nose and 'C_f' is the coefficient of skin friction for the nose. The coefficient of skin friction is estimated, using Hoerner's experimental data [ref 38] to be $C_f = 0.002$. The wetted surface area of the nose, which is all the area touched (i.e. wetted) by air moving over the nose, must be determined analytically. It may be calculated according to the following integral formula.

$$A_w = \int_0^{x_n} p(x)\,dx, \quad p(x) = 2\pi R(x) \qquad (1.28)$$

Here, p(x) refers to the perimeter of a cross-section of the maglev vehicle nose at location 'x' and R(x) is the radius of the cross-section. This expression (1.28) is integrated with the expression for R(x) in Eq. 1.16 to obtain the following result.

$$A_w = \frac{4}{3} x_n^{3/2} \sqrt{\Lambda\pi} \qquad (1.29)$$

And, using Eq. 1.16, this result may be simplified into the following expression:

$$A_w = \frac{4}{3} x_n \sqrt{\pi A_{max}}. \qquad (1.30)$$

Once the expression in Eq. 1.30 is substituted into the formula for total drag (1.27), the total drag coefficient for the nose of a maglev vehicle can be expressed in the following simple form:

$$C_d = C_T \frac{A_{max}}{x_n^2} + C_f \frac{4}{3} x_n \sqrt{\frac{\pi}{A_{max}}}. \qquad (1.31)$$

Consider the following example of the calculation of drag due to the passage of a maglev vehicle nose through a channel guideway. For a nose of the shape shown in Fig. 1.23 and 1.25, the method outlined above (in the previous three pages) is used to obtain an estimate of drag. The method is implemented by first selecting a value for the cross-sectional area at the base of the nose, Amax. The region behind the maglev vehicle's nose is modeled simply as a semi-circular cylinder; so, the constant cross-sectional area of this region corresponds to the cross-sectional area Amax. If the semi-circular, cylindrical region behind the maglev vehicle's nose has a width, d = 3.0 m, then Amax has a radius, $R(x_n) = 1.5$ m, and a value of $\text{Amax} = \pi R^2(x_n)/2 = 1.125\pi$ m^2.

The next step in this method is to select several geometrical parameters which model the channel guideway and are crucial to the determination of nondimensional energy in the flow, C_T, from Fig. 1.24. For example, choose the value $\text{Amax}/w^2 = 0.30$ and the curve corresponding to the parameter $h/w = 0.2$. In physical terms, these parameters simulate a channel guideway width of 3.4 m, with sidewalls of a height which is approximately 20% the width of the maglev vehicle body. The energy coefficient, from Fig. 1.24, corresponding to these parameters is $C_T = 0.112$.

The calculation of drag is straight-forward if the nose length, x_n, is known for a specific maglev vehicle; however, when x_n is unknown, Eq. 1.31 can be used to determine the optimum nose shape for a maglev vehicle. The optimization itself is fairly simple. Each variable, except x_n, in Eq. 1.31 is first assigned a value so that it assumes the following form.

$$\begin{aligned} C_d &= (0.112)\,\frac{1.125\pi}{x_n^2} + (0.002)\,\frac{4}{3}\sqrt{\frac{\pi}{1.125\pi}}\,x_n \\ &= \frac{0.396}{x_n^2} + (0.00251)\,x_n \end{aligned} \tag{1.32}$$

Equation 1.32 is then evaluated and plotted within a range of values of x_n for the minimum C_d.

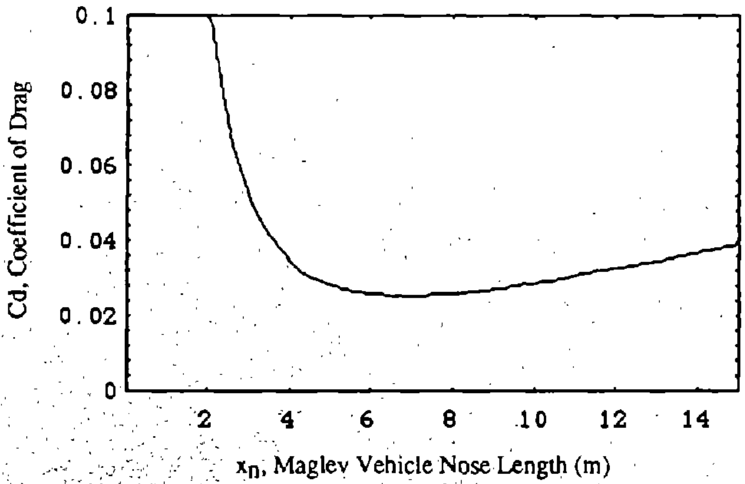

Figure 1.26. Nose Drag as a Function of Nose Length, for $\text{Amax} = 1.125\pi$ m^2.

Figure 1.26 implies that the nose of a maglev vehicle, with constant change in cross-sectional area, should have a length, $x_n \approx 7$ m, to have a minimum amount of drag. The ratio A_{max}/x_n^2 for this case is 0.072, which is more elongated than what one normally encounters on subsonic aircraft, for which A_{max}/x_n^2 is typically 0.4 or 0.5.

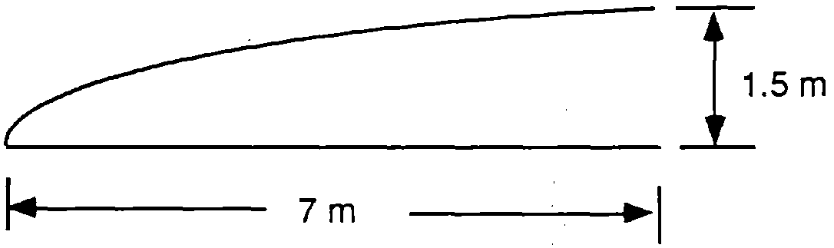

Figure 1.27. Side View of Optimum Maglev Vehicle Nose

1.6 Conclusions

1. The numerical simulation of a circular cylinder in a free stream works well, giving good agreement between the numerical and analytical solutions for the flow field. It was necessary to add an analytical correction to the solution in order to get accurate values for the surface velocities.

2. The numerical simulation of vortex shedding off a flat plate normal to the free stream also works well, giving good agreement with the analytical solution for the energy in the flow around a flat plate normal to the free stream. This numerical scheme was used in the energy calculation for the vortices shed off the tops of the channel walls.

3. Actually placing a cylinder between parallel walls results in complications which tend to obscure the nature of the solution. Consequently, a point source was used to simulate the nose of a maglev vehicle in a channel guideway. Assuming top to bottom symmetry, the flow tangency equations were solved and the geometry of the vortex shedding was determined (see Fig. 1.21).

4. The strength of the shed vortices were then used to calculate the energy in the flow. This energy is, in turn, related to vortex drag, which is related to overall drag of the maglev vehicle's nose via Eq. 1.27 and 1.32.

5. For the case of a maglev vehicle with a fuselage of semi-circular cross-section and width, d = 3.0 m, the methodology for calculating drag which was discussed at the end of section 1.5 may be implemented to find an optimal nose shape, with the length $x_{n,\,opt.} \approx 7$ m.

SECTION 2

EFFECT OF FINENESS RATIO ON DRAG

2.1 Introduction

In this section the energy penalty per passenger is computed for vehicles of various fineness ratio, using available assumptions about the relation between the number of passengers and the vehicle width. Tradeoffs between vehicle width and energy cost are derived for a box beam vehicle and a channel vehicle.

2.2 Aerodynamic Fundamentals

Aerodynamic theory and experimental data is commonly expressed in non-dimensional terms. Let us define

ρ = Air density
v = Vehicle velocity
q = Dynamic pressure
$q = \rho v^2/2$
A = Reference Area
D = Drag

The drag is non-dimensionalized as follows:

C_D = Drag Coefficient
$= D/qA$

There is sometimes confusion over just which area is being used to define the drag coefficient. This confusion can be bypassed by using the "equivalent flat plate area" f, sometimes called the drag area, where

$$f = \text{Drag}/q = C_D A$$

One can imagine a plate with an area f on which the difference in pressure acting against the two sides is equal to the dynamic pressure. The force on this plate is equal to the drag of the body. This is, incidentally, approximately the same drag as would be felt by a plate which is held perpendicular to the free stream. Instead of using f some authors simply use $C_D A$, without bothering to define A. This is particularly common with railroad aerodynamics because trains generally have the same frontal area and it is highly unlikely one would want to use the $C_D A$ obtained for one train to predict the drag on a train with the same shape and a smaller frontal area. As long as the two terms always appear together as a product it is not necessary to define them separately. On the other hand, the allowable width of maglev vehicles is not yet defined, so one might indeed want to know the effect of varying the vehicle size.

A word on commonly recognized aircraft notation may be in order. The uppercase "C" generally stands for a force coefficient of a three dimensional body, whereas the lowercase "c" is used for two-dimensional shapes. Thus we define

c_f = Surface friction drag coefficient

The quantity c_f is obtained by taking the force on a flat plate parallel to the airstream and dividing by the area times the dynamic pressure. Within a narrow range, the resulting value is independent of the area of the plate and the stream velocity. For large variations in the velocity or length scale, it is necessary to take into account the Reynolds Number, defined as

$R = \rho v l / \mu$

where μ is the viscosity. Hoerner [38] discusses the effect of Reynolds number on c_f.

2.3 Drag of Bodies in a Free Stream

Let us define the following coefficient:

C_{D_w}= Drag coefficient based on wetted area

It is very useful to begin a discussion of drag by first considering bodies in a free stream, i.e. without any effects due to the guideway. Hoerner provides an excellent discussion of shape effects; the reader is encouraged to review this material for a good introduction which does not require extensive familiarity with aerodynamic theory. A summary of his discussion is provided here as a point of departure. Hoerner gives the following formula for well-streamlined axisymmetric bodies:

$$\frac{C_{D_w}}{c_f} = 1 + 1.5\left(\frac{d}{l}\right)^{3/2} + 7\left(\frac{d}{l}\right)^4 \qquad (2.1)$$

where

d = Diameter
l = Length

If there were no effects of shape, this equation would have only the first term and C_{D_W} would be the same as the surface friction coefficient c_f. The middle term on the right hand side is called the form drag and is due to the fact that the flow must speed up as it goes around the body. The third term in this equation is called the pressure drag. It is due to the fact that the thickness of the boundary layer increases as one proceeds from the nose of the body to the rear, which causes the streamlines outside the boundary layer to be more crowded together at the rear than they are at the front. This in turn causes a slight decrease in pressure in the aft regions. For a flat plate this pressure change does not cause any additional drag, since the pressure is perpendicular to the freestream flow, but for any shape with thickness the decreased pressure in the rear will cause additional drag.

Drag is estimated in the aircraft industry using the "partial " drag method, i.e. the drag of each part is estimated and these estimates are then summed. Fig. 2.1, taken from Ref. [90], gives drag coefficients for aircraft fuselages and nacelles of different fineness ratios.

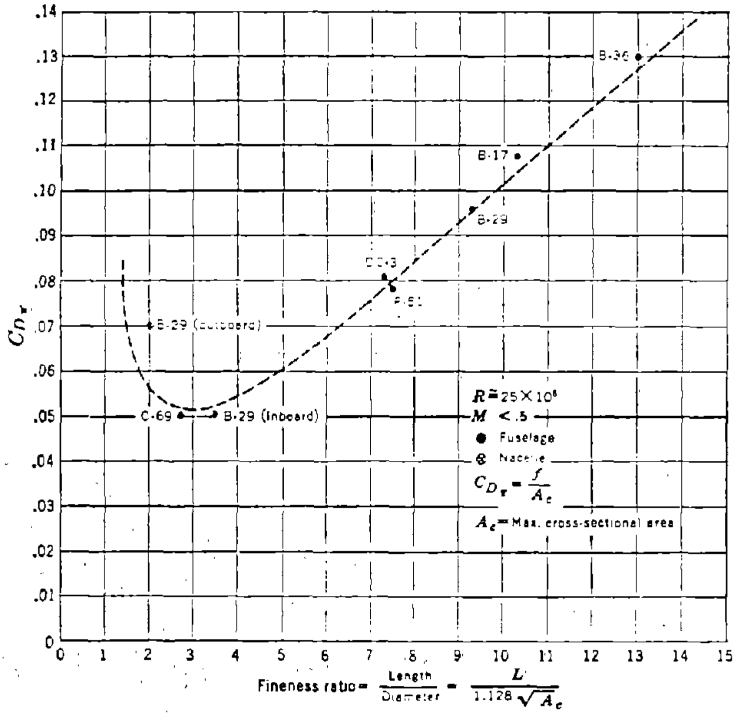

Figure 2.1 Drag based on frontal area for various fineness ratios

In this figure we have

$C_{d\pi}$ = "Partial" drag coefficient, i.e. the portion of the drag ascribed to each part

For our purposes the only "part" is the vehicle itself so that $C_{D\pi}$ is the same as C_D as given above. The data in this figure correlates well with (2.1) if we use a value for c_f of 0.0023.

For practical vehicles, it is very difficult to obtain attached flow all the way to the trailing edge. In other words, the body is not fully streamlined. In such cases there is an additional term called the base drag. Hoerner [38] gives the following formula for axisymmetric bodies which are simply cut off without any tapering at the rear end:

$$C_{DB} = \frac{0.029}{\sqrt{C_{Df}}} \tag{2.2}$$

where

$$C_{Df} = \frac{A_w}{A_C} c_f \approx \frac{4l}{d} c_f \tag{2.3}$$

The approximation that $A_w/A_c = 4\ l/d$ is exact for a uniform cylinder and approximately correct for typical streamlined bodies. C_{Df} is the same as the surface friction coefficient c_f except that it is based on the frontal area rather than the wetted area. The total drag of an axisymmetric body is thus

$$C_D = C_{Df} + C_{DB} \tag{2.4}$$

The base drag as computed from these formulas is a useful notion for idealized shapes in a free stream but it can be misleading for a real vehicle operating near the ground or a guideway. This can be illustrated by the following numbers which come from the automotive industry [70]:

$C_D = 0.04$	Body of revolution optimized for low drag (l/d = 3.3)
$C_D = 0.05$	Body of revolution (l/d = 3.3)
$C_D = 0.15$	Body near ground
$C_D = 0.46$	Actual Car

The "body near ground" is W. Klemperer's shape which is streamlined with a tapered tail that avoids separation. There are more refined formulas for the base drag than that given above, which account for tapering at the rear end in various ways, but the point is that they are not worth reproducing here because the drag values are affected so drastically by the presence of the ground or a guideway.

Figure 2.1 shows that for a given cross-sectional area, the minimum drag occurs at a fineness ratio of about 3. The data in this plot is not presented in the ideal form for purposes of the present discussion, since the number of passengers in a train is proportional to the planform area, not cross-sectional area. However, we can see that if the fineness ratio is increased to 12 (i.e. increased by a factor of 4), and the cross-sectional area is held constant, $C_{D\pi}$ is increased from .05 to .12, i.e. the drag only increases by a factor of 2.4. Further extrapolation of this data indicates that for aircraft type fuselages, the minimum drag for a given planform area (i.e. the area available for passengers) is obtained with the minimum cross-sectional area.

2.4 Drag of Maglev Vehicles

Matsunama et al [88] present the following formula for the drag of a train in open air:

$$D = q\,(C_{dp} + \lambda l/d)A_c \qquad (2.5)$$

where

D = Drag
C_{dp} = Form drag coefficient
λ = Hydraulic skin friction coefficient
d = Hydraulic diameter = $4A_c/p$
p = Peripheral length of the cross-section
l = Train length

This form of the equation is not convenient in the present context. Equation (2.5) can be approximated as follows:

$$D = q\,(C_{dp}A_c + C_{dw}A_w) \qquad (2.6)$$

where

$$C_{dw} = \lambda/4 \qquad (2.7)$$

This relation is derived from the same factor of 4 which went into (2.3). (There is a fine distinction between C_{dw} and the C_{Dw} defined previously in that the former does not represent the total drag.) In this form we see that there is a certain amount of drag due to the fact that the vehicle has a nose and a tail, plus a certain amount due to the product pl which is essentially the wetted area. The form drag coefficient and the drag coefficient are related as follows

$$C_D = C_{dp} + c_f \frac{4l}{d} \qquad (2.8)$$

The following values for the coefficients were given for the "commercial maglev vehicle" of the Japanese National Railway (JNR):

$C_{dp} = 0.15$
$\lambda = 0.016$ (i.e., $C_{dw} = 0.004$)

Two things are striking about this data. First, the value given for C_{dp} is exactly the same as the C_D given above for Klemperer's "body near the ground." In other words, the automotive industry and the railroad industry in Japan both seem to agree that there is, at a minimum, a factor of three increase in drag over that obtained from a streamlined axisymmetric body of the same cross-sectional area operating in a free stream. This is true even for smooth bodies without separation. The second striking thing is the value of 0.004 given for C_{dw}. This is more than twice what one would expect for a smooth surface operating at the Reynolds number of a maglev train. The extra drag is due to the flow between the vehicle and the guideway. This flow must contend with the guideway surface, which is rougher than the vehicle exterior surface. More important, it must also contend with the magnet bogies. It is difficult to streamline the bogies because of the fact that they are not fixed rigidly to the vehicle but must be mounted so as to allow relative motion. Thus there is an unavoidable amount of separated flow which occurs between the vehicle and the guideway.

If we temporarily assume a circular cross section, the diameter of this circle becomes the same as the hydraulic diameter d. Thus

$$A_w = \pi dl$$

so that

$$D = q(A_c C_{dp} + \pi C_{dw} dl) \qquad (2.8)$$

The product dl is the planform area available for seating. For a given planform area, the second term is independent of the way d and l are apportioned, but the first term will increase with d. This would indicate that we should minimize d, i.e. long skinny trains are a good idea. Interestingly enough, Matsunuma et. al. [88] took their formula and showed that if the width of the train were increased to seat five abreast rather than four abreast, and the train were shortened so as to maintain almost the same total seating capacity, the drag of the train would decrease by ten percent! The explanation for this apparent anomaly is very simple. Let us drop the assumption that the cross-section is circular, and use (2.5) rather than (2.8). They stipulated that the cross-sectional area would increase from 7.0m^2 to 8.3m^2. They did not actually provide a picture of the cross section, but if we assume that the 7.0m^2 cross-section is approximately square and the 8.3m^2 cross-section has the same height and a greater width, we find that the peripheral length only increases by 9 percent, whereas the number of seats per row increases by 25 percent. The proportionately greater increase in the seating capacity per unit length more than offsets the greater drag per unit length. We learn two lessons from this exercise: (1) the number of seats is not proportional to the planform area because the center aisle width and the thickness of the walls remain fixed, and (2) the effect of skin friction drag is easier to understand if we work with the peripheral length rather than other more obscure parameters like hydraulic diameter or planform area.

Even greater drag reductions can be obtained if we are willing to hypothesize a double deck arrangement for the seating. This will further shorten the train and reduce the wetted area.

Equation (2.5) is very handy for certain things but it leaves much to be desired. It shows the effect of varying the vehicle length and width but it does not show the effect of varying other important parameters such as the vehicle/guideway clearance. If one accepts the values of the coefficients as given then there is a very limited scope for reducing the drag. Real progress in the state of the art requires a fundamental investigation into how to decrease these coefficients.

J.L.Peters, aerodynamics project manager for Krauss-Maffei AG, provides the following comment on maglev vehicles [91]:

> "Drag of the complex maglev bogies can easily amount to 2/3 of the total drag."

He goes on to describe a number of steps which were taken in the design of the TR07 in order to reduce the drag. Among these were:

- Continuous disposition of the magnets along the whole length of the train instead of the conventional wheel/rail arrangement at the extremities of the cars.
- Smooth fairings on the guideway side of the underbelly and legs
- Front fairings of the leading magnets
- Separating the bogies (four per car) by walls perpendicular to the direction of motion.

All of the steps taken by Krauss-Maffei succeeded in cutting the bogie drag in half, and in decreasing the total drag by more than one third.

Peters [91] gives the following wind tunnel measurements for the drag coefficient of a "short stator" maglev configuration, which is a two-car consist 64m long:

Nose	0.06
Tail	0.14
Lead Car	0.19
Trailing Car	0.23
Total C_D	0.42

As can be seen, the lead car plus the trailing car add up to the total drag. One would conclude from adding the drag of the nose and the tail that C_{dp} = .20, but unfortunately Peter's did not specify exactly which configuration these numbers refer to. Since it is a "short stator" configuration, we have reason to believe the above numbers refer to an earlier configuration which did not benefit from the improvements made in the TR07. Furthermore, on all the German maglev vehicles the nose and the tail have the same shape, whereas a vehicle with a streamlined tail or proper boat-tailing can expect some improvement. We therefor conclude that this is a pessimistic number for C_{dp}. The above number for the total drag may be optimistic, particularly for a wind tunnel model which may not include all of the details of the bogies. Peters provides tantalizing hints about towing tank investigations which focused on the drag due the flow between the vehicle and the guideway, but not enough detail to know whether we should add some additional bogie drag to the wind tunnel numbers. The following value is given for the drag of the TR07 [ref.92]:

$C_D = 0.45$ (TR07)

As can be seen, this number is slightly higher than the above "total C_D" wind tunnel measurement. This tends to confirm our suspicion some additional drag must be added to the wind tunnel value to get a realistic measurement. This additional drag would be proportional to the length of the vehicle, i.e. it should be reflected in an increase in the coefficient C_{dw} rather than C_{dp}.

For Klemperer's "body near the ground", if we assume $C_{dw} = c_f = .0025$, which is appropriate for the Reynolds number of a car, we would obtain the following value using (2.8):

$C_{dp} = 0.12$

This is the best that can be expected for a body operating near a ground plane, barring some unforeseen and fundamental improvement in aerodynamics. For a vehicle designed for a channel guideway we expect a number larger than this, and for a vehicle on a box beam guideway it may be possible to get a number smaller than this.

For the sake of completeness, we provide the following values from Tracked Hovercraft Limited:

$C_D = 0.26$ (Box Beam)
$C_D = 0.32$ (Channel)

These numbers are for a single car with an l/d of about 8. Once again, the usefulness of these wind tunnel results for our immediate purpose is unclear due to uncertainties about the flow between vehicle and the guideway. Also, some interpretation of the relatively large difference between these values is in order. The channel vehicle configuration was chosen without any consideration of the front end drag analyzed in Section 1. In fact, it almost appears that the configuration was chosen to maximize the drag due to the bow vortices. Thus it is reasonable to expect that for a more enlightened design of the box beam vehicle, this source of drag could be reduced.

All things considered, the following values are proposed for the coefficients in (2.6)

$$C_{dp} = 0.11 \text{ (Box Beam)}$$
$$C_{dp} = 0.15 \text{ (Channel)} \qquad (2.10)$$
$$C_{dw} = .004 \text{ (box or channel)}$$

These numbers can be called state of the art values. There is some reason to hope for improvement for C_{dw} , since this value comes from the JNR experience with vehicles having bogies at the extremities of the cars rather than continuously distributed.

Let us now apply these numbers against the Transrapid experience. Their two-car consist is 51 m long with an L/D of 18. Inserting these values into (2.7) we obtain $C_D = 0.40$. This is below the value of 0.45 given previously, but in the right ballpark.

2.5 Determination of Optimum Width

Calculations to find the optimum widths, i.e. the width at which the drag force on the vehicle is a minimum, of two different concepts of maglev vehicles are presented here. To find this width, various seating configurations were defined. Configurations ranged from four to eight passengers per row.

Studies were made for two concepts of maglev vehicles; vehicles traveling on a box-beam and vehicles traveling in a channel. Figure 2.2 shows assumed cross-sections for each of the two vehicles. The channel vehicle is modeled as a rectangular area capped with a semi-circular area. The box-beam vehicle is slightly more complex and was modeled as a channel vehicle with two 'legs'. These are not the actual shapes of the vehicles, however, for our purposes, they will suffice. Note that the box-beam vehicle without the 'legs' is 4.33 meters high which is the same as the channel vehicle.

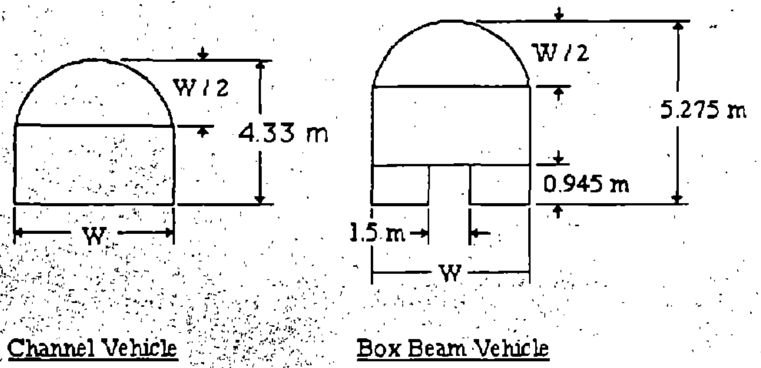

Figure 2.2. Cross section of channel and box beam vehicles.

Equation (2.6) is used to evaluate the drag of each vehicle, using the parameters given by (2.10). A_c and p are different for the channel and box-beam vehicles. The formulas are shown here as functions of vehicle width:

Channel Vehicle:

$$A_c = \frac{\pi\left(\frac{W}{2}\right)^2}{2} + \left(3.5 - \frac{W}{2}\right)W$$

$$p = \pi\frac{W}{2} + \left(3.5 - \frac{W}{2}\right)2 + W$$

Box-Beam Vehicle:

$$A_c = \frac{\pi\left(\frac{W}{2}\right)^2}{2} + \left(5.275 - 0.945 - \frac{W}{2}\right)W + (W - 1.5)0.945$$

$$p = \pi\frac{W}{2} + \left(5.275 - 0.945 - \frac{W}{2}\right)2 + W + (0.945)4$$

The heights for each train remain constant for different widths, but differ between configurations. The channel vehicle is given as 3.5 meters and the box-beam vehicle is given as 5.275 meters. The widths and lengths for the other configurations were computed using the following formulas:

$$W_{train} = n_{seats/row}w_{seat} + n_{aisles}w_{aisle} + 0.5$$

$$l_{train} = \frac{N_{pas.}}{n_{seats/row}}l_{seat}$$

where;

$w_{seat} = 0.5$ meter

$w_{aisle} = 0.6$ meter

$N_{pas} = 120$

$$l_{seat} = \frac{36.129 \times 6}{120} = 1.81 \text{ meter}$$

The configurations for the vehicle are as follows:

4 pas./row	2 seats - 1 aisle - 2 seats	W = 3.1 m
5 pas./row	2 seats - 1 aisle - 3 seats	W = 3.6 m
6 pas./row	3 seats - 1 aisle - 3 seats	W = 4.1 m
7 pas./row	3 seats - 1 aisle - 4 seats	W = 4.6 m
8 pas./row	4 seats - 1 aisle - 4 seats	W = 5.1 m

Calculations were made of the drag force on the vehicle versus the width of the train. The plots are shown in Figures 2.3 and 2.4. The optimum width of the train is 4.1 meters for the channel type and 4.6 meters for the box-beam type of maglev vehicles.

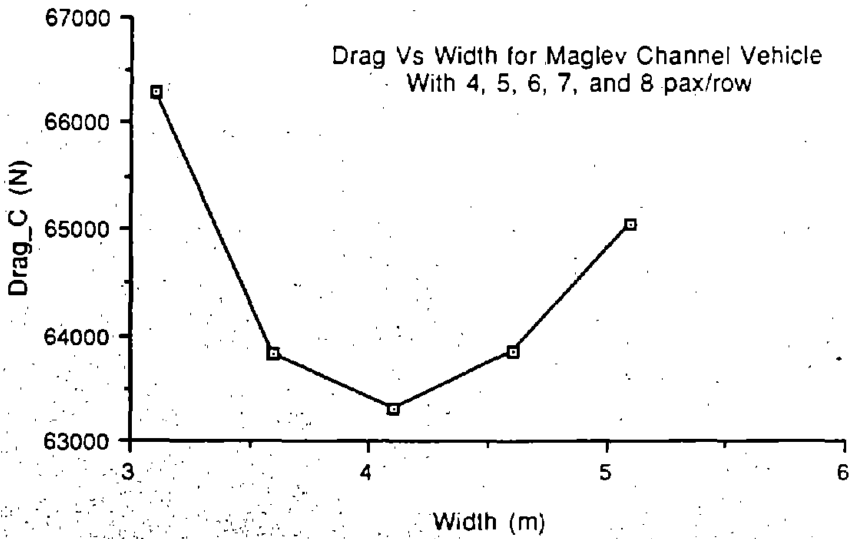

Figure 2.3 Drag vs width for Maglev channel vehicle.

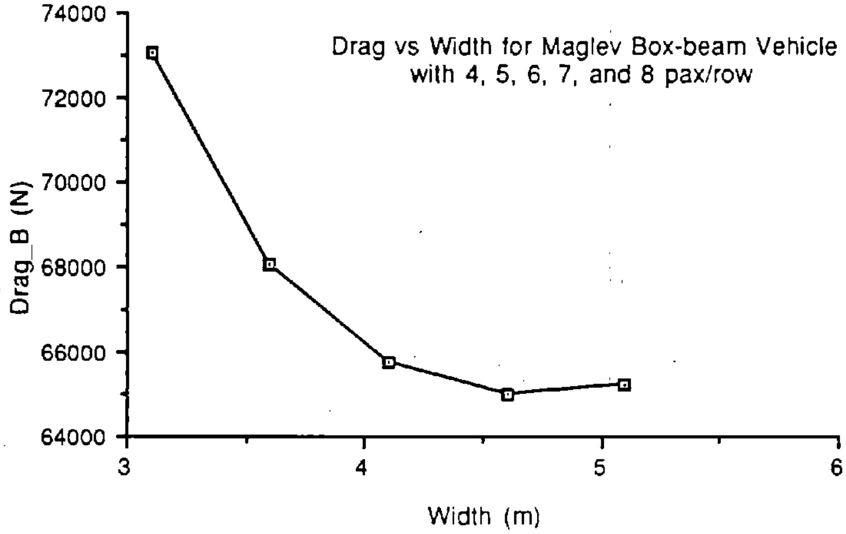

Figure 2.4 Drag vs width for Maglev box-beam vehicle.

2.6 Conclusions

The optimum width of a channel vehicle will generally be less than that of a box-beam vehicle. There are two reasons for this: (1) the channel vehicle has a higher penalty for frontal area as reflected in the higher value of the coefficient C_{dp}, and (2) the box-beam vehicle has a higher penalty on vehicle length due to the longer periphery around the cross-section.

SECTION 3

PERFORMANCE OF AERODYNAMIC CONTROL SURFACES

3.1 Introduction

One of the problems with persistent mode superconducting magnets is that their fields cannot be varied for control purposes. Aerodynamic surfaces are a relatively simple way to produce a controllable force. This is particularly true for vehicles which travel at high speeds in close proximity to guideway surfaces, since the presence of the guideway produces an amplifying effect, known as the ground effect, on the control forces. The result is that a small surface can produce a large effect. In fact, it is not even necessary to have a separate control surface. A small flap at the trailing edge of an existing structure can control the aerodynamic pressure between this structure and the guideway. For instance, the JNR design envisions magnet bogies which are suspended separately from the vehicle body. Small flaps at the trailing edges of these bogies would be very effective at producing control forces. .

A considerable amount of research on ground vehicle aerodynamics was performed at Princeton in the period prior to 1980 [17-20,37,48]. A basic theory was developed to predict the lift on aerodynamic surfaces in very close proximity to the ground. This was followed by a number of wind tunnel tests on simple configurations to confirm the basic theory. A great deal of attention was focused on the issue of the validity of using a wind tunnel, in which the ground is stationary relative to the vehicle, as opposed to the real situation in which the ground is stationary relative to the ambient air. To properly simulate the ground boundary condition, it is necessary to either have a moving model or a moving ground boundary. Tests have been conducted by other researchers using an endless, rotating belt to represent a moving ground plane, but this is not practical if the vehicle is moving in proximity to a guideway which is not a flat surface. The moving model approach was taken at MIT by building a guideway in the bottom of a ship model towing tank, towing a vehicle through it, and measuring the resulting forces [10]. The advantage of doing this underwater is that large forces can be generated at low speeds. Some useful information was obtained from these tests, but the underwater environment proved to be very inconvenient. Moving model tests in air were conducted at Princeton [20]. Ultimately it was concluded that as long as there is not an unfavorable pressure gradient which causes the ground boundary layer to separate, the wind tunnel produces results which are very close to what is obtained from a moving model test. More important, wind tunnel tests were used to refine and verify the theoretical results, which had advanced to include the effects of flaps at the side and trailing edges.

As discussed by Ashill [2] it is not possible to use conventional wing data to estimate the aerodynamic forces on wings in ground effect. This is because aerodynamic forces on a wing flying close to the ground are strongly influenced by the camber and thickness of the wing. One must resort to the asymptotic methods of Widnall and Barrows [82] to obtain correct values for the various aerodynamic coefficients of interest close to the ground. The first-order approximation to the flow solution, obtained from asymptotic methods, is one-dimensional channel flow under the ram-wing with an unperturbed free stream flow over the upper surface of the wing.

In the case of the maglev control surfaces, it is advantageous to apply the one-dimensional channel flow theory with leakage, presented by Gallington *et. al.* [29] and modified by Boccadoro [10], to obtain the lift as a function of dimensionless ground height clearance. Here it is important to remember that in the context of control surfaces the term 'ground' is relative. It can refer to either the side wall or the bottom of the channel guideway, depending on the function of the control surface. One-dimensional channel flow theory is the first-order solution to the more complicated asymptotic methods of Widnall and Barrows [82]. It compares well with experimental data, and its analytical formulation requires only slight alterations for variations in the geometry of the ram-wing.

3.2 Justification for One-Dimensional Flow Theory

One of the major areas of fluids research in the 1970s seems to have been in air cushion vehicles, both pressurized and dynamic, because the literature is extremely abundant. Maglev control surfaces fall into the category of what are termed "dynamic ram air cushion vehicles" [5]. In particular, the low aspect ratio "ram-wing" discussed here is a ground effect mechanism which uses only aerodynamic lift (as opposed to pressurized air used in air cushion vehicles such as hovercrafts) for suspension in a channel guideway. This means that the maglev vehicle must exhibit some forward motion for the control surfaces to operate.

When the maglev vehicle is moving forward, air moves over the upper and within the lower surface and side lips of the ram-wing creating a pressure differential between the upper and lower surfaces of the ram-wing. The physical, geometric analogy is the analogy to a leaky duct:

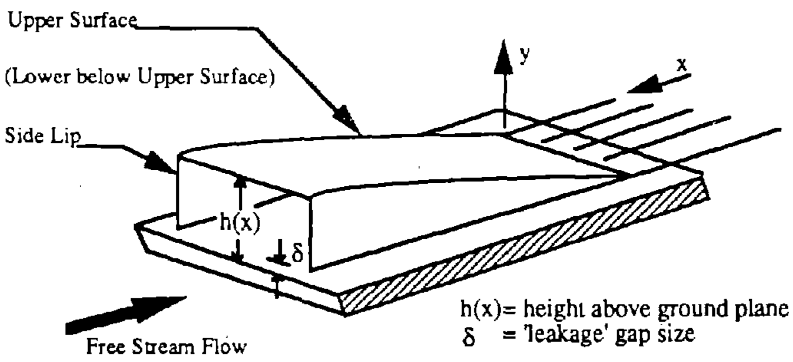

Figure 3.1. Schematic of a Ram-Wing.

The lower surface and sidewalls of the control surface form the 'leaky' duct through which air flows. The air flows along the length of the duct of height h(x) and simultaneously out of the side gaps of height δ, exiting smoothly, and for this model at atmospheric pressure, from the trailing edge. Consequently, a 'lifting' pressure is generated within the 'leaky' duct. See Gallington [29]. for excellent photographs of this type of mechanism. Depending on the orientation of the control surface, the pressure differential between the upper and lower surfaces results in either lift for a control surface parallel to the bottom of the channel guideway or side force for a control surface parallel to a side wall of the channel guideway.

3.3 One-Dimensional Flow Theory with Leakage

Simplification of the real flow around a ram-wing to the flow through a duct permits a subsequent simplification in the equations of motion. Since the variation in the cross-sectional area, A(x) (i.e. the area within the 'leaky' duct), may be assumed to be moderate, it is possible to write the equations of motion for the flow around the ram-wing in only one dimension. The only complications are: 1. the leakage of air through side gaps and 2. the existence of a flap at the rear portion of a control surface; however, both these problems can still be dealt with in one dimension. Before proceeding it is worth noting that thickness effects and the pressure field above a control surface are ignored in this model since Barrows [6] showed their effects to be small compared to the dominant effect of contraction of the area below the control surface.

Consider the following model of a maglev control surface:

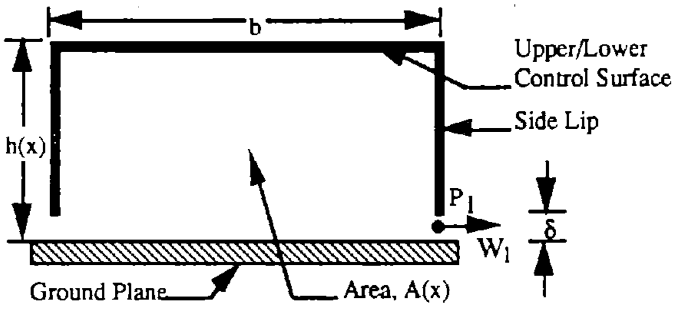

Figure 3.2. Cross Section of a Ram-Wing.

Using the appropriate nondimensionalizations, the following variables emerge:

W_l is the velocity of fluid squirting out of the side gap, made dimensionless with respect to the free stream velocity, U_∞.

U(x) is the nondimensional average velocity of air in area A(x).

Cp is the usual pressure coefficient for potential flow, $(P(x)-P_\infty)/((1/2)\rho U_\infty^2)$, P_∞ = atmospheric pressure.

x is the nondimensional (...with respect to the <u>control surface length, c</u>) trailing edge variable. This means that x=0 at the trailing edge and 1 at the leading edge of the control surface. The purpose of this coordinate system is to avoid complicated leading edge effects which alter the pitching moment, but do not alter the lift or drag significantly. This is discussed in [6].

The analytical approach to the one-dimensional flow with leakage essentially follows the method developed by Boccadoro [10] with a few changes. Since Boccadoro outlines the general method very well, only a few of the important steps will follow. The equation which is fundamental to his treatment of this flow is the equation of mass conservation. Simply put, the mass of fluid entering the area under the control surface must exit either through the side gaps or out from the trailing edge.

$$2c\int_x^1 W_l(x)\,\delta(x)\,dx + U(x)\,A(x) = \text{const.} \tag{3.1}$$

Using the nondimensionalizations

$$\hat{A}(x) = A(x)/c^2;\ \hat{H}(x) = \delta(x)/c,\ \delta(x) = \delta = \text{const.} \tag{3.2}$$

Eq. (3.1) can now be expressed in a more compact and useful form.

$$U'(x) = \frac{2\,W_l(x)\,\hat{H}(x)\ -\ U(x)\,\hat{A}'}{\hat{A}},\ \ (\,)' = d(\,)/dx \tag{3.3}$$

Equation (3.3) may be simplified even further by eliminating the variable W_l. This is accomplished using Bernoulli's equation along a streamline to write the pressure coefficient, Cp_l, just outside the side gap, δ.

$$Cp_l = 1\ -W_l^2\ -\ U_l^2 \tag{3.4}$$

In relation to the second figure, it is reasonable to assume: (1) the pressure, P_l, of air escaping through the side gap is equal to atmospheric pressure, P_∞, and (2) $U_l(x)$ is also equal to $U(x)$, where $U_l(x)$ is the velocity along the chord, c, of the ram-wing, just outside the side gap, δ. This implies that $Cp_l = 0$. Thus Eq. (3.3) may be written as follows:

$$U'(x) = \frac{\sqrt{1 - U^2(x)}\ \hat{H}(x)\ -\ U(x)\,\hat{A}'}{\hat{A}} \tag{3.5}$$

3.4 Solution Methodology for Aerodynamic Coefficients

Using the method of Boccadoro, all that remains to be done is to select a specific geometry for the control surfaces and solve Eq. (3.5) numerically to obtain the lift (... or side force, depending on the orientation) of the control surface. However, the numerical method was first checked for accuracy against a known analytical solution to an analogous problem. The problem was to determine the pressure distribution over a flat plate wing in ground effect, flying in a U-shaped trough at a given angle of attack, α. A schematic side view of this model is shown below in Figure 3.3.

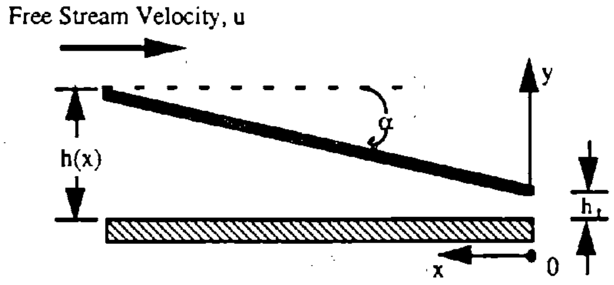

Figure 3.3. Flat Plate Wing in Ground Effect.

The cross-sectional area at location 'x' under this flat plate wing in ground effect is A(x) = b h(x), where the dimension 'b' represents the width of the flat plate. The dimension 'b' in this problem is identical to the 'b' of the upper and lower control surfaces in Figure 3.2. Then, using Eq. (3.5) and Bernoulli's equation it is possible to solve for Cp as shown below in Figure 3.4.

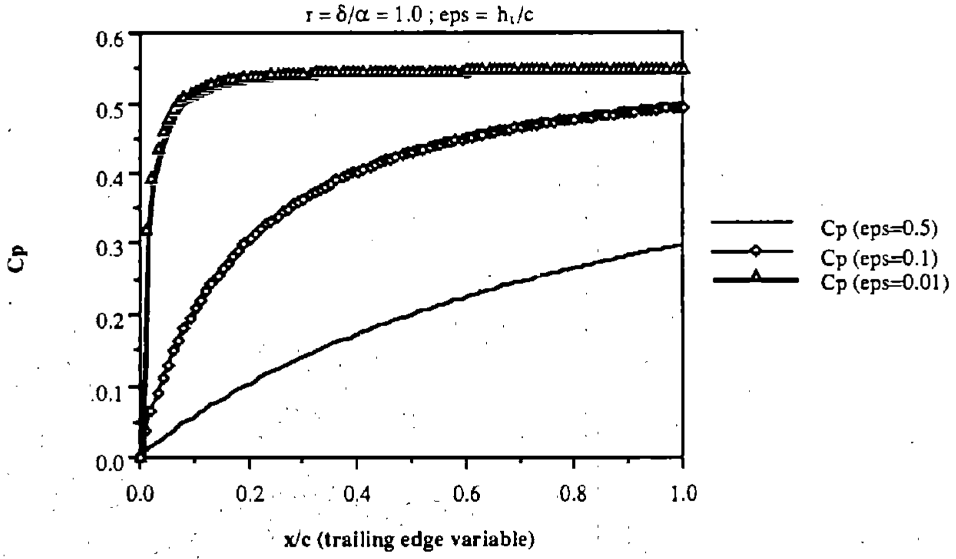

Figure 3.4. Cp(x) on a Flat Plate Wing in Ground Effect.

The solution in Figure 3.4 is obtained using Eq. (3.5) with the boundary condition U=1 when x=0 to solve for dU/dx, starting at the trailing edge(x=0). Incremental steps in 'x' between x=0 and x=1 determine U(x); and, Bernoulli's equation determines the pressure coefficient, Cp(x). Notice that the shape of the curves at the leading edge, x=1, are not quite correct; they show graphically the effect of ignoring leading edge effects, which is true of Boccadoro's model.

Having verified the accuracy of the numerical method, it is now possible to use the same numerical scheme for the control surfaces, but with a slightly different geometry (i.e., a different

A(x)). The new geometry consists of a wing with a flap near its trailing edge. A schematic side view of this configuration is shown below in Figure 3.5 (notice the dimensions given).

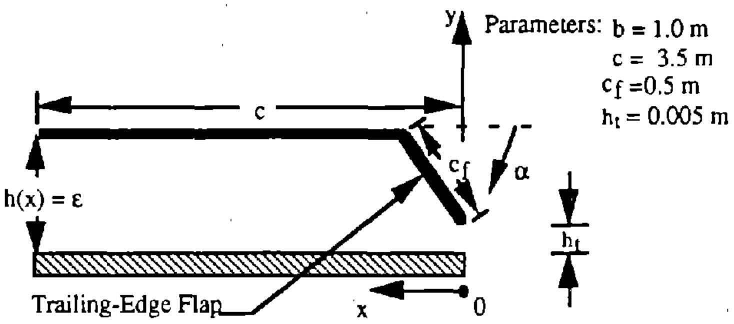

Figure 3.5. Ram-Wing Control Surface with a Flap.

The nondimensional area distribution and its derivative beneath this control surface are:

$$\hat{A}(x) = \begin{cases} (b/c)\left[\alpha x + \left(\frac{\varepsilon}{c} - \alpha \frac{c_f}{c}\right)\right], & 0 \le x \le \frac{c_f}{c} \\ \frac{b}{c}\frac{\varepsilon}{c}, & \frac{c_f}{c} \le x \le 1 \end{cases} \tag{3.6}$$

$$\hat{A}'(x) = \begin{cases} (b/c)\,\alpha, & 0 \le x \le \frac{c_f}{c} \\ 0, & \frac{c_f}{c} \le x \le 1 \end{cases} \tag{3.7}$$

Just as before, the numerical scheme uses Eq. (3.5) to find the speed and pressure distributions for each angle of attack, α, and a corresponding nondimensional altitude above the ground plane, ε/c. If one of these two variables is kept constant (i.e. α or ε/c) then it is possible to compute the Cp(x) as the other variable changes.

The result is a distribution of Cp(x)s for either α or ε/c held constant while the other variable changes. The coefficient of lift at a given α and ε/c is computed simply by summing Cp(x) over all values of x. Even though lift is usually computed by summing the change in the pressure across a lifting surface, a simple summation of the Cp(x)s on the lower surface is possible in this model because of the original assumption that the pressure coefficient on the upper surface of the ram-wing is zero. Lift is expressed as a function of α for ε = 0.05 and 0.10, and as a function of ε/c for α = 1.5 and 4.0 degrees. These values correspond to the values used in the maglev control algorithms in Section 4. Results are shown in figures 3.6 through 3.9.

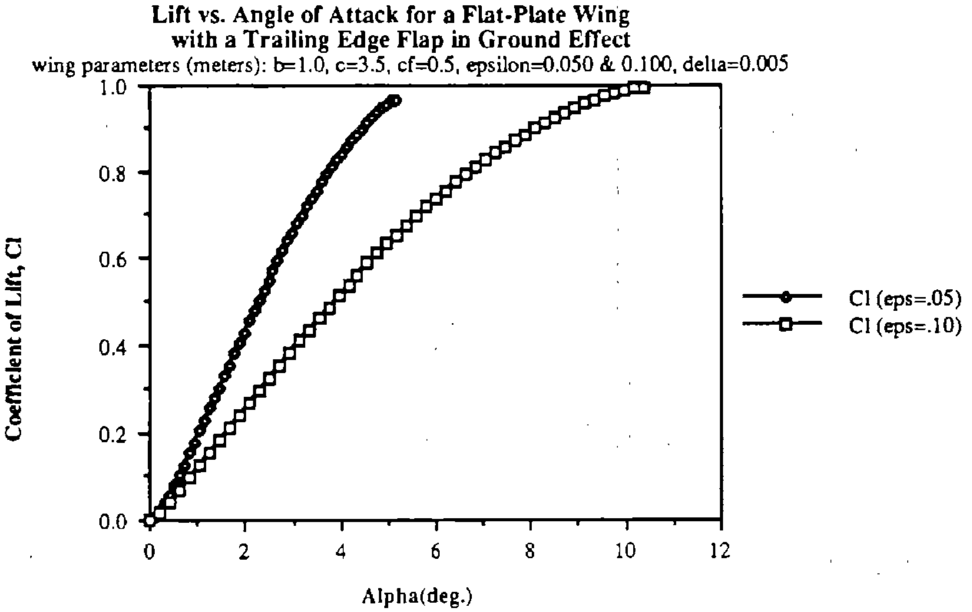

Figure 3.6. Cl versus α.

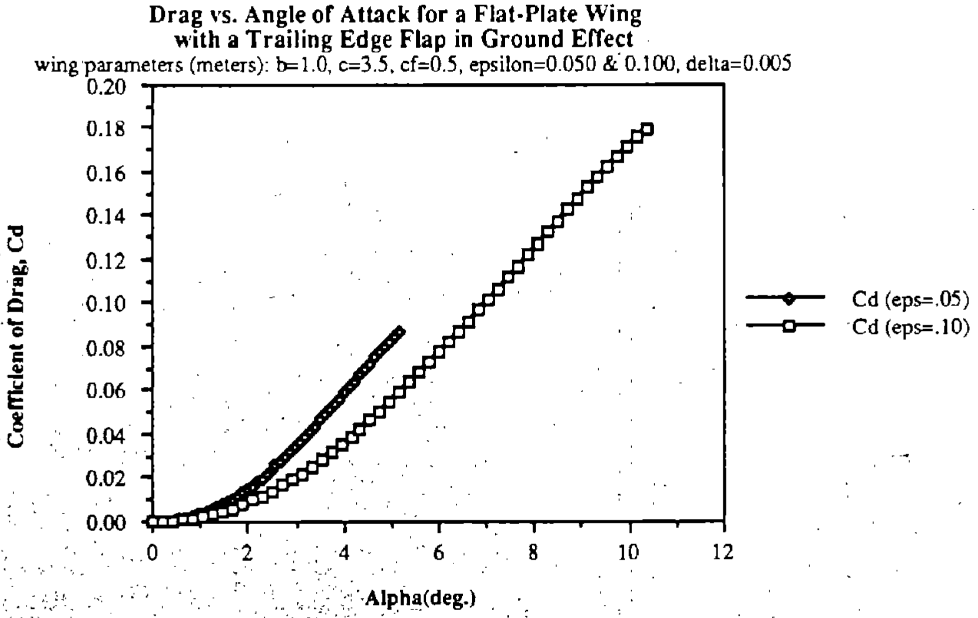

Figure 3.7. Cd versus α.

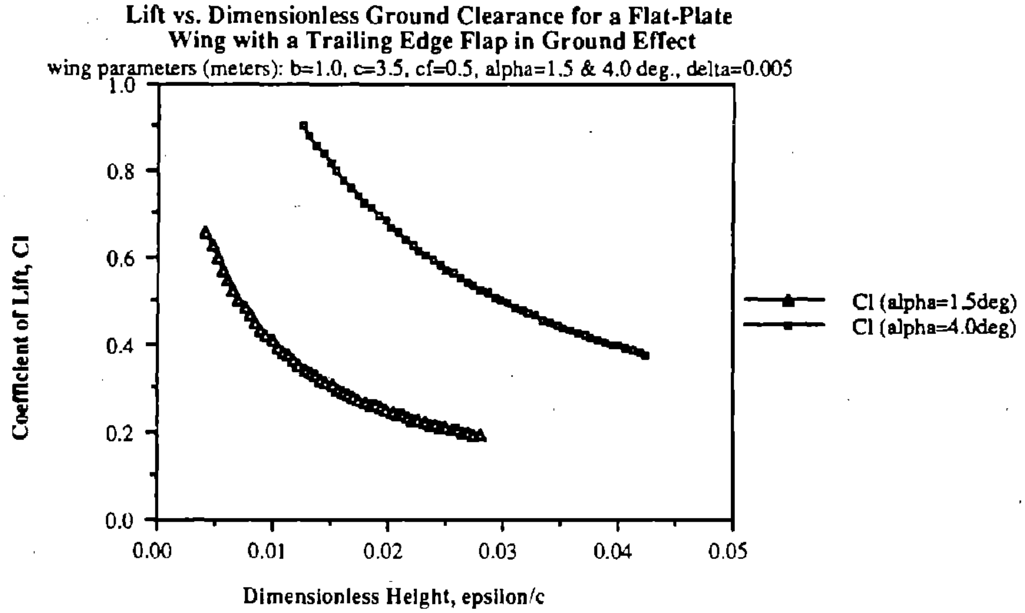

Figure 3.8. Cl versus ε/c.

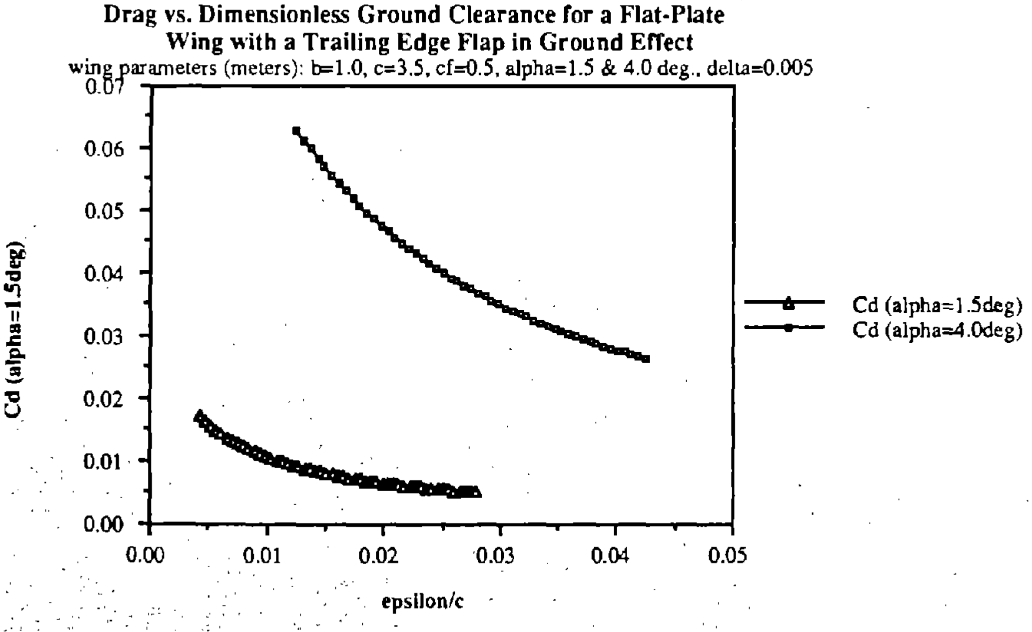

Figure 3.9. Cd versus ε/c.

3.5 Results and Conclusions

1. The graphs shown in Figures 3.6 to 3.9 represent the output of FORTRAN computer code which computed the lift and drag on a maglev control surface.
2. The application of these results may be seen in Section 4, where they are used for aerodynamic control of a maglev vehicle.
3. It is worth noting that the lift shown in Figures 3.6 to 3.9 is a nonlinear function of flap angle and height.
4. In addition, the lift to drag ratio, L/D, is good as long as the flap angle, α, is small. Large values of α yield a significant amount of drag with very little extra lift.

SECTION 4

SUSPENSION DYNAMICS AND CONTROL

The purpose of this section is to evaluate the feasibility and benefits of aerodynamic control. Using internal Corporate Sponsored Research funding, Draper Laboratory has developed a five-degree-of-freedom dynamic model, which is described in some detail in Section 4.1. The current research effort, however, calls for generic results that are applicable to a range of vehicle concepts. For this purpose, a reduced, three-degree-of-freedom model is appropriate, which includes the vehicle motion in a cross-sectional plane (heave, roll, and sway). Section 4.11 describes the subset of the five-degree-of-freedom model which was used.

Section 4.2 describes the criteria that were used to evaluate the performance of the suspension. Under crosswind conditions, there is both a steady state and a random component of the dynamic response. Limits for the maximum allowable stroke of both the primary and the secondary suspension are established. The methodology by which the guideway irregularities and crosswind forces are related to performance criteria such as ride quality and air gap variation is described.

In Section 4.3, a control law for the active elements of the suspension is derived using linear quadratic optimal control theory. Active elements may include a hydraulic secondary suspension, aerodynamic controls, or both. A control cost function is defined, and the choice of which output variables to penalize more heavily (passenger acceleration, control effort, gap variation, etc.) is discussed.

The performance benefits of active control can best be assessed through comparison with the performance of an optimized passive suspension. In Section 4.4, several issues are discussed that define what is meant by "optimized," and parameters are chosen for an appropriate passive suspension.

Results of all the analyses are presented in Section 4.5. Both tabular results and frequency response spectra are given.

4.1 Model Development

4.1.1. Introduction and Outline

We modeled the train as a two bogie vehicle with an Electro-Dynamic Suspension (EDS) primary suspension, active secondary suspension, and aerodynamic control surfaces mounted on the train and/or bogie. This chapter describes a general five degree-of-freedom model developed at Draper for Maglev vehicles.

Section 4.1 consists of 11 sections. The first 10 provide a description of the general model developed. A subset of this five degree-of-freedom model was used for the analysis discussed in this report. The final section describes how this subset of this model was obtained. The chapter begins with an overview of the model's assumptions and a description of the axis conventions. Detailed descriptions of the train, suspension, and disturbance models are presented subsequently.

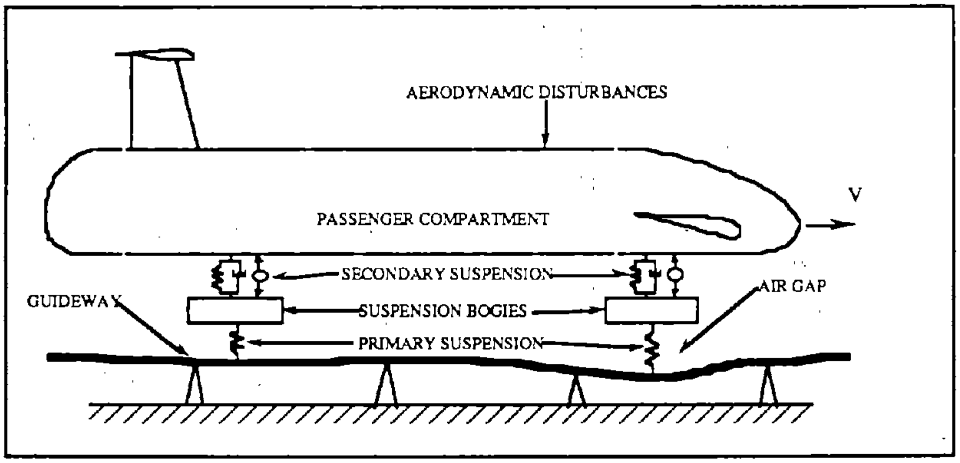

Figure 4.1.1. - Overview of train model with aero-surfaces - side view

The vehicle-suspension model includes the following components:

- the passenger compartment (train), including vehicle aerodynamic effects (wind, aerodynamic yaw-stability derivatives);
- the suspension bogies;
- the secondary suspension elements, including actuators used for active suspension control;
- the primary suspension elements (the magnetic suspension); and
- the aerodynamic control surfaces (wings or flaps).

Sections 4.1.3 through 4.1.7 follow this outline, presenting models for each of these components.

Equations describing train accelerations due to aerodynamic and secondary suspension forces are derived in Section 4.1.3. Included in this section is an aerodynamic model that includes aero-stability effects and forces on the train due to crosswinds. Section 4.1.4 presents the bogie model and equations for bogie acceleration due to forces from the primary and secondary suspension elements. Detailed equations for the forces due to the primary and secondary suspensions are described in Sections 4.1.5 and 4.1.6. Section 4.1.7 presents models of the aerodynamic control surfaces investigated.

The train-suspension system modeled in Sections 4.1.2 through 4.1.7 is driven by two types of inputs:

- controllable inputs due to the secondary suspension actuators and aerodynamic flaps; and
- disturbance inputs due to the guideway irregularities and crosswinds.

Models for the guideway position and wind velocity disturbances are derived in Sections 4.1.8 and 4.1.9, respectively. In Section 4.1.10, these disturbance models are combined with the train-suspension model – and, for the active secondary suspension, control laws for the secondary and aerodynamic flaps – to yield a complete model of the train-suspension system and its disturbances. This model takes the form of a linear system driven by white noise and constant terms. This form is desirable because it permits the development of closed-form analytic solutions for the system outputs. The constant wind force and torque inputs are ignored for the analysis of the RMS values of the outputs. However, the constant forces are considered when determining the aerodynamic stability derivatives and yaw angle about which the vehicle's non-linear aerodynamic response will be linearized.

4.1.2. Overview of Assumptions and Definition of Axes

4.1.2.1. Assumptions

The vehicle-suspension system is modeled as a two-bogie vehicle with an EDS primary suspension (see Figure 4.1.1). Linear lumped elements are used to model the train, bogies, and suspension elements. The model includes:

- train rotation and rotation rates in three dimensions
- train and bogie displacements and velocities perpendicular to the velocity vector
- rotation of the bogies about the velocity vector (roll)

Thus, the train has five degrees of freedom, while the bogies are each limited to three. The bogie yaw and pitch modes are omitted, since these modes can be made stable with a passive suspension system[1] and do not significantly impact the rigid train's dynamics.

We have made the following assumptions in developing the model:

General

- the train velocity changes slowly relative to the other dynamics of the system so that velocity can be modeled as constant.
- there is no coupling between propulsion and levitation (no time-varying lift contributed by the propulsion system)
- non-linear equations of motion are used to obtain a linear model, linearized appropriate operating points where necessary.
- although not inherent assumptions in the model, for this analysis both the primary and secondary suspension stiffnesses are the same at the front and rear, and the CG. (center of gravity) is located at the midpoint between the front and rear bogies.
- when active control is implemented, full state feedback is assumed

Train

- the train (including passengers and baggage) is completely rigid
- the train center of mass is in the vertical plane bisecting the train
- angular rotation rates of the train are small (Coriolis accelerations or gyroscopic effects are ignored)

Bogie

- the bogies have "zero length" (no guideway filtering, no bogie pitch or yaw dynamics)
- the bogies (including cryogenic subsystems) are perfectly rigid
- each bogie is axi-symmetric, with center of mass in the vertical plane bisecting the bogie
- the relative displacements of the bogies with respect to the train are small

Primary suspension

---

[1] Guenther, Christian R.; Leonides, Cornelius T., "Synthesis of a High-Speed Tracked Vehicle Suspension System - Part I: Problem Statement, Suspension Structure, and Decomposition" IEEE Transactions on Automatic Control, vol. AC-22, No. 2, April 1977.

- the primary suspension is an Electro-Dynamic Suspension (EDS), and has no damping
- crosswind forces act only on the train (no wind forces on bogies)

Hydraulic actuators

- the active secondary suspension forces are perfectly controllable without time delays

Aerodynamic actuators

- the flap angles are perfectly controllable without time delays

Guideway

- guideway roughness is a random process with zero mean and stationary statistics (*i.e.*, statistics do not vary with time or train location)

Wind

- the time-varying component of the wind is a random process with zero mean and stationary statistics

4.1.2.2. Definition of Axes

Displacements and rotations of the train and bogies are defined relative to a right-handed Cartesian coordinate system (see Figure 4.1.2). The frame conventions are:

- X-axis parallel to the vehicle's instantaneous Earth-relative velocity vector, and positive in the forward direction
- Z-axis vertical, positive upwards
- Y-axis perpendicular to X and Z, completing the right-handed coordinate frame
- ϕ (roll) is rotation about the +X axis
- θ (pitch) is rotation about the +Y axis
- ψ (yaw) is rotation about the +Z axis

In all cases, train and bogie displacements and rotations are measured from their no-load equilibrium positions.

4.1.3. Train

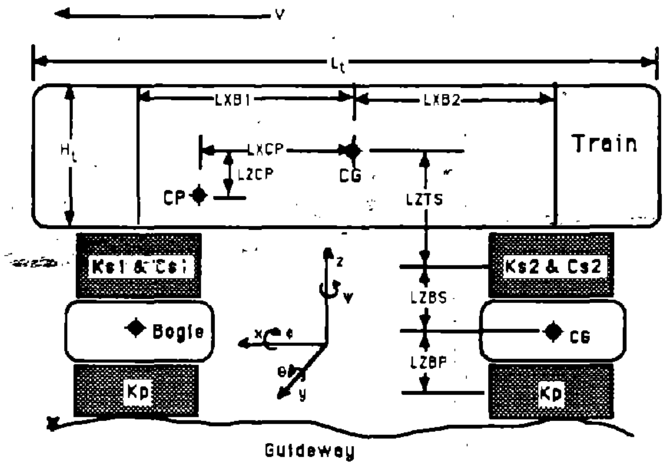

Figure 4.1.2. - Side view of train model

The train is modeled as a rigid mass, with a center of gravity in the vertical plane bisecting the vehicle (see Figure 4.1.3). The train is allowed to rotate about any axis and translate in the Y and Z directions, but is assumed to move at a constant velocity in the positive X direction. The train state is defined by a vector[2] of linear and angular train displacements

$$\mathbf{x}_t = \begin{bmatrix} y_t & z_t & \phi_t & \theta_t & \psi_t \end{bmatrix}^T \tag{4.1.1}$$

and their derivatives $\dot{\mathbf{x}}_t$.

The train is characterized in term of its length (L_t), width (W_t), height (H_t), cross-sectional area (A_t), mass (m_t), inertia matrix (I_{xx}, *etc.*) and aerodynamic force and torque coefficients (C_y, C_n). The train parameter values used in our study are listed in Appendix A.

Three sets of forces[3] act on the train: forces due to the secondary suspension elements (both active and passive); forces due to wind and aerodynamic stability effects; and forces due to aerodynamic actuators. Thus, under the assumption of very small train rotation rates, the train accelerations are given by:

---

[2] Vectors will be identified by **bold** face print.

[3] Throughout this chapter, "forces" refers to a vector of both forces and torques.

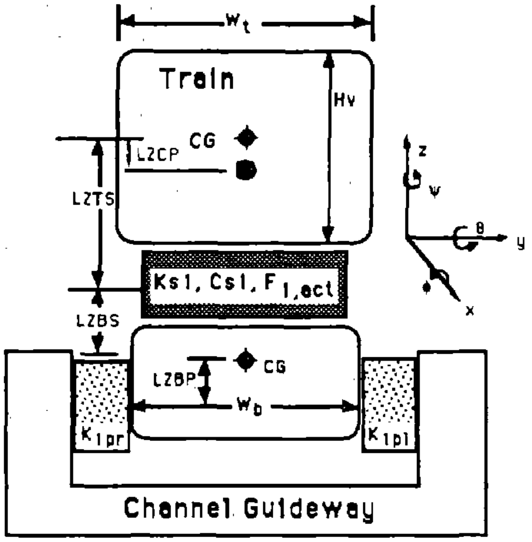

Figure 4.1.3. - Front view of train model

$$\ddot{\mathbf{x}}_t = \mathbf{I}_t^{-1} \cdot \left(\mathbf{T}^f_{s1\text{-}t} \cdot \mathbf{F}_{s1} + \mathbf{T}^f_{s2\text{-}t} \cdot \mathbf{F}_{s2} + \mathbf{T}^f_{aero\text{-}t} \cdot \mathbf{F}_{aero} + \mathbf{T}^f_{flap\text{-}t} \cdot \mathbf{F}_{flap} \right) \tag{4.1.2}$$

$$\mathbf{I}_t^{-1} = \begin{bmatrix} 1/m_t & 0 & 0 \\ 0 & 1/m_t & 0 \\ 0 & 0 & \begin{bmatrix} I_{xx} & I_{xy} & I_{xz} \\ I_{yx} & I_{yy} & I_{yz} \\ I_{zx} & I_{zy} & I_{zz} \end{bmatrix}^{-1} \end{bmatrix} \tag{4.1.3}$$

where

m_t = mass of train

$\mathbf{I}_{xy}$, etc. = moments of inertia for train (defined about the train CG)

$\mathbf{F}_{s1}$ = force across the front secondary suspension

$\mathbf{F}_{s2}$ = force across the rear secondary suspension

$\mathbf{F}_{aero}$ = force on the train due to wind and aero-stability effects

$\mathbf{F}_{flap}$ = force on the train due to aerodynamic flaps

$\mathbf{T}^f_{s1\text{-}t}$ = transformation from forces at front secondary suspension to forces at the train CG

$\mathbf{T}^{f}_{s2\text{-}t}$ = transformation from forces at rear secondary suspension to forces at the train CG

$\mathbf{T}^{f}_{aero\text{-}t}$ = transformation from forces at the aerodynamic center of pressure at the train CG

$\mathbf{T}^{f}_{flap\text{-}t}$ = transformation from forces at the aerodynamic flaps to forces at the train CG

The transformation matrices (T) are included to transform forces and torques from their points of application to forces and torques acting at the train center of mass[4].

4.1.3.1. Accelerations due to secondary suspension forces

Forces across each of the two secondary suspensions are given by a roll torque and vertical and lateral forces:

$$\mathbf{F}_{si} = \begin{bmatrix} F_y & F_z & T_\phi \end{bmatrix}_{si}^{T} \quad (i = 1,2) \tag{4.1.4}$$

These forces act at points LXB1 and LXB2 fore and aft, and LZTS below, the train center of mass, as shown in Figure 4.1.2. Thus, the transformation from forces at the front secondary suspension to the train's CG is given by:

$$\mathbf{T}^{f}_{s1-t} = \begin{bmatrix} 1 & 0 & 0 \\ 0 & 1 & 0 \\ \mathrm{LZTS} & 0 & 1 \\ 0 & -\mathrm{LXB1} & 0 \\ \mathrm{LXB1} & 0 & 0 \end{bmatrix} \tag{4.1.5}$$

so that

---

[4] We use transformation matrices so that the model can describe forces and torques acting at arbitrary points on the train and bogie. This approach allows the model to be modified quickly to reflect changes in vehicle configuration (vehicle dimensions, bogie locations, etc.) This also allows us to define the primary and secondary stiffness matrices at the roll center of the suspension, where they are diagonal. Inherent in assumption of a linear model is the assumption that the roll center will not move as the vehicle suspension does, since the transformation matrices are constant and independent of the state vector.

$$\begin{bmatrix} F_y \\ F_z \\ T_\phi \\ T_\theta \\ T_\psi \end{bmatrix}_{\text{train c.g.}} = \mathbf{T}^f_{s1-t} \begin{bmatrix} F_y \\ F_z \\ T_\phi \end{bmatrix}_{s1} \tag{4.1.6}$$

The transformation matrix $\mathbf{T}^f_{s2-t}$ is similar.

4.1.3.2. Wind and aerodynamic stability effects

Crosswind forces on the train are modeled as a side force[5] acting in the +Y direction (perpendicular to velocity) at the center of pressure, denoted CP. (see Figure 4.1.4). Since the center of pressure is LXCP ahead of, and LZCP above, the train's CG, the transformation from force at this point to force at the train CG is:

$$\mathbf{T}^f_{\text{aero}-t} = \begin{bmatrix} 1 \\ 0 \\ -\text{LZCP} \\ 0 \\ \text{LXCP} \end{bmatrix} \tag{4.1.7}$$

$$\begin{bmatrix} F_y \\ F_z \\ T_\phi \\ T_\theta \\ T_\psi \end{bmatrix}_{\text{train c.g.}} = T^f_{\text{aero}-t}\left[F_y\right]_{\text{aero}} \tag{4.1.8}$$

The aerodynamic side force is dependent on the wind and train velocities, train cross-sectional area, and aerodynamic side force coefficient:

$$\left[F_y\right]_{\text{aero}} = \frac{1}{2}\rho\ |V_{\text{air}}|^2 A_t\ C_y(\beta) \tag{4.1.9}$$

where

ρ = density of air

---

[5] Since drag acts parallel to the train's velocity, it can be excluded from our model. Lift forces are assumed small.

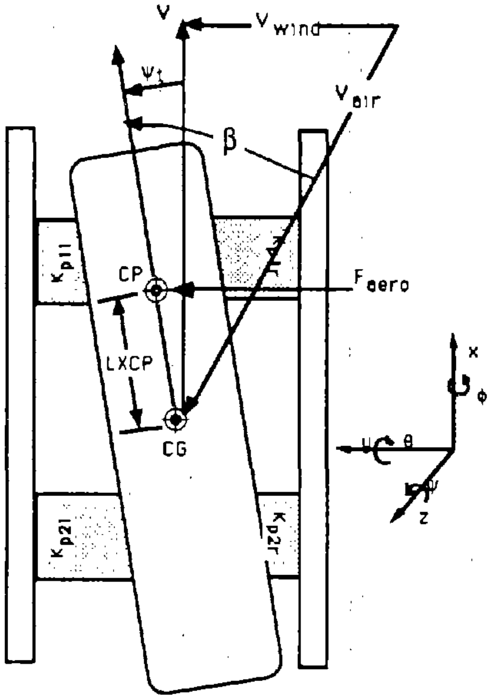

Figure 4.1.4. - Top view of train model showing aerodynamic effects

$|V_{air}|$ = magnitude of air-relative train velocity
A_t = cross-sectional area of the train
$C_y(\beta)$ = coefficient of side force

The air-relative train velocity is a vector sum of the train's earth-relative velocity and the applied wind. For our work, we model all winds as perpendicular to the vehicle's velocity, so:

$$|V_{air}|^2 = |V|^2 + |V_{wind}|^2 \tag{4.1.10}$$

The aerodynamic coefficient, $Cy(\beta)$, is non-linearly dependent on the sideslip angle, β:

$$\beta = \psi_t + \arctan\left(\frac{|V_{wind}|}{|V|}\right) \tag{4.1.11}$$

$Cy(\beta)$ is described by a polynomial curve fit:

$$Cy(\beta) = Cy0 + Cy1\,\beta + Cy2\,\beta^2 + Cy3\,\beta^3 \tag{4.1.12}$$

It is desirable to form a single linear state space representation describing the dynamics of the system. To do this, a linear model of the wind force is required. A state space description of this wind model may then be appended to the state space description of the train's dynamics.

We begin by noting that the wind model consists of two parts, a steady (DC) term and a random, time-varying component:

$$V_{wind} = \overline{V}_{wind} + V_{wind}(t) \tag{4.1.13}$$

Similarly, the train yaw angle will have two parts:

$$\psi_t = \overline{\psi}_t + \psi_t(t) \tag{4.1.14}$$

Thus, the sideslip angle consists of two components:

$$\beta = \beta_0 + \delta\beta(t) \tag{4.1.15}$$

We apply a first-order approximation to obtain a linear equation for $Cy(\beta)$:

$$Cy(\beta) \approx C_y(\beta_0) + \left(\frac{dC_y}{d\beta}\right)_{\beta_0} \delta\beta(t) \tag{4.1.16}$$

$$\left(\frac{dC_y}{d\beta}\right)_{\beta_0} = C_{y1} + 2C_{y2}\cdot\beta_0 + 3C_{y3}\cdot\beta_0{}^2$$

Note that $C_{y\beta}$ is calculated using β_0.

We continue the linearization by assuming that the $V_{wind}(t)$ is small relative to the vehicle's Earth-relative velocity. This assumption yields a small angle approximation for sideslip as:

$$\delta\beta(t) \approx \psi_t(t) + \frac{|V_{wind}(t)|}{|V|} \tag{4.1.17}$$

and an approximation for the air-relative vehicle velocity

$$|V_{air}|^2 \approx |V|^2 \tag{4.1.18}$$

Combining the equations above yields the desired linear approximation for aerodynamic side-force:

$$[F_y]_{aero} \approx \frac{1}{2}\rho\,|V|A_t\left(C_y(\beta_0) + \left(\frac{dC_y}{d\beta}\right)_{\beta_0}\left(V\psi_t(t) + V_{wind}(t)\right)\right) \tag{4.1.19}$$

We rewrite this equation in terms of the train state vector as:

$$\left[F_y\right]_{aero} \approx \frac{1}{2}\rho\ |V| A_t \left(C_y(\beta_0) + \left(\frac{dC_y}{d\beta}\right)_{\beta_0} \left(V \mathbf{T}^{\lambda}_{t-\psi_t} \mathbf{x}_t + V_{wind}(t) \right) \right) \qquad (4.1.20)$$

The location of the center of pressure, denoted by LZCP (distance from CG in the +Z direction) and LXCP (distance in the +X direction) must now be determined. Here we assume LZCP to be such that the CP is 0.24 meters below a point midway between the top and bottom of the vehicle (the assumed value of LZCP is listed in Appendix A). LXCP is calculated by noting that:

$$\left[T_\psi\right]_{aero} = \left[F_y\right]_{aero} LXCP \qquad (4.1.21)$$

$\left[T_\psi\right]_{aero}$ is also given by[6]:

$$\left[T_\psi\right]_{aero} = \frac{1}{2}\rho\ |V_{air}|^2 A_t\ L_t\ C_n(\beta) \qquad (4.1.22)$$

$$C_n(\beta) = C_{n0} + C_{n1}\,\beta + C_{n2}\,\beta^2 + C_{n3}\,\beta^3 \qquad (4.1.23)$$

Algebraic manipulation yields:

$$LXCP = L_t \frac{C_n(\beta)}{C_y(\beta)} \qquad (4.1.24)$$

Since C_{n0} and C_{y0} are zero for a symmetric train, equation 4.1.24 can be reduced to:

$$LXCP = L_t \frac{C_{n1} + C_{n2}\cdot\beta + C_{n3}\cdot\beta^2}{C_{y1} + C_{y2}\cdot\beta + C_{y3}\cdot\beta^2} \qquad (4.1.25)$$

which is non-singular for zero sideslip. To linearize the model, we calculate LXCP assuming:

$$\beta = \beta_0 \qquad (4.1.26)$$

---

[6] Again determined from a curve fit to data.

4.1.3.3. *Accelerations due to train-mounted aerodynamic actuators*

Aerodynamic actuators can be mounted in many places on the train. We describe the location of each actuator relative to the train CG via the parameters:

$$[\mathrm{LXF}i \;\; \mathrm{LYF}i \;\; \mathrm{LZF}i]^T$$

Note that these parameters may be positive or negative. Specified locations for each actuator assumed in our study are given in Appendix A.

A force is exerted on each aero-surface at its center of pressure; by definition there is no torque exerted on the control surface at this point. The force due to a flap on the train is described by the vector:

$$\mathbf{F}_{\mathrm{flap}i} = \begin{bmatrix} F_y \\ F_z \end{bmatrix}_{\mathrm{flap}i}$$

The transformation of a flap's forces to forces and torques at the train CG is given by:

$$\mathbf{T}^f_{\mathrm{flap}i-t} = \begin{bmatrix} 1 & 0 \\ 0 & 1 \\ -\mathrm{LZF}i & -\mathrm{LYF}i \\ 0 & -\mathrm{LXF}i \\ \mathrm{LXF}i & 0 \end{bmatrix} \tag{4.1.27}$$

$$\begin{bmatrix} F_y \\ F_z \\ T_\phi \\ T_\theta \\ T_\psi \end{bmatrix}_{\mathrm{train\ c.g.}} = \mathrm{T}^f_{\mathrm{flap}i-t}\mathbf{F}_{\mathrm{flap}i} \tag{4.1.28}$$

In these transformation matrices, the force of the wing naturally acts at the center of pressure of each aerodynamic control surface. It is this point from which the forces are converted to forces and torques about the CG of the train.

4.1.4. Suspension Bogies

Both suspension bogies in our two bogie vehicle are assumed to be identical. Each is modeled as a rigid mass, with a center of mass in the vertical plane bisecting the bogie (see Figure 4.1.2). The bogies are assumed to translate in the Y and Z directions and roll about the X axis – however, rotations about the Y axis (pitch) and Z axis (yaw) are neglected. Each bogie's state is defined by a vector of its positions

$$\mathbf{x}_{bi} = \begin{bmatrix} y_{bi} & z_{bi} & \phi_{bi} \end{bmatrix}^{T} \tag{4.1.29}$$

and their derivatives $\dot{\mathbf{x}}_{bi}$.

The bogies are characterized by their width (W_b), mass (m_b), and roll moment of inertia (I_{xx}). The bogie parameter values used in our study are listed in Appendix A.

The secondary suspension, primary suspension, and aerodynamic actuators all exert forces on each bogie (we assume that crosswind forces do not affect the bogie directly). Thus, under the assumption of small rotation rates and angles, the bogie accelerations are given by:

$$\ddot{\mathbf{x}}_{bi} = \mathbf{I}_b^{-1} \cdot \left(\mathbf{T}^{f}_{si\text{-}bi} \cdot \mathbf{F}_{si} + \mathbf{T}^{f}_{pil\text{-}bi} \cdot \mathbf{F}_{pil} + \mathbf{T}^{f}_{pir\text{-}bi} \cdot \mathbf{F}_{pir} + \mathbf{T}^{f}_{gef\text{-}bi} \cdot \mathbf{F}_{gef} \right) \tag{4.1.30}$$

$$\mathbf{I}_b^{-1} = \begin{bmatrix} 1/m_b & 0 & 0 \\ 0 & 1/m_b & 0 \\ 0 & 0 & I_{xx}^{-1} \end{bmatrix} \tag{4.1.31}$$

where

$\mathbf{I}_{xx}$ = roll moment of inertia for bogie (defined about bogie CG)

$\mathbf{F}_{pi\,l}$ = force across the left side of the primary suspension (at bogie *i*)

$\mathbf{F}_{pi\,r}$ = force across the right side primary suspension (at bogie *i*)

$\mathbf{F}_{si}$ = force across the secondary suspension (at bogie *i*)

$\mathbf{F}_{gef}$ = force due to ground-effect flaps mounted on the bogie

$\mathbf{T}^{f}_{pil\text{-}bi}$ = transformation from forces at left side of *i*-th primary suspension to bogie CG

$\mathbf{T}^{f}_{pir\text{-}bi}$ = transformation from forces at right side of *i*-th primary suspension to bogie CG

$\mathbf{T}^{f}_{si\text{-}bi}$ = transformation from forces at *i*-th secondary suspension to forces at bogie CG

$\mathbf{T}^{f}_{gef-bi}$ = transformation from forces at ground-effect flaps to forces at bogie CG

4.1.4.1. Accelerations due to secondary suspension forces

The secondary suspension force acts on each bogie at a point LZBS above the bogie's center of mass, as shown in Figure 4.1.2. Thus, for each bogie, the transformation from forces and torques at the secondary suspension elements to the bogie's CG is given by:

$$\mathbf{T}^{f}_{si-bi} = \begin{bmatrix} -1 & 0 & 0 \\ 0 & -1 & 0 \\ \mathrm{LZBS} & 0 & -1 \end{bmatrix} \tag{4.1.32}$$

so that

$$\begin{bmatrix} F_y \\ F_z \\ T_\phi \end{bmatrix}_{\text{bogie-}i\text{ c.g.}} = T^f_{si-bi} \begin{bmatrix} F_y \\ F_z \\ T_\phi \end{bmatrix}_{si} \tag{4.1.33}$$

4.1.4.2. *Accelerations due to primary suspension forces*

There are vertical and lateral forces at each of the four corners of the primary suspension. There is no roll stiffness of the primary suspension at each corner as it is defined, so any torques about each bogie's CG are due to the fact that the vertical and lateral forces do not act at the CG. These torques naturally arise from the application of transformation matrices described below. Nevertheless, the forces at each corner of the primary suspension can be described by:

$$\mathbf{F}_{pij} = \begin{bmatrix} F_y & F_z & T_\phi \end{bmatrix}_{pij}^T \quad (j = l, r) \tag{4.1.34}$$

These forces act at points LZBP below, and $\frac{W_b}{2}$ to the left or right of, the bogie center of mass (see Figure 4.1.2). The transformations from forces and torques at these points to forces and torques about the bogie's CG are given by:

$$T^f_{pil-bi} = \begin{bmatrix} -1 & 0 & 0 \\ 0 & 1 & 0 \\ -\text{LZBP} & \frac{W_b}{2} & 1 \end{bmatrix} \tag{4.1.35}$$

$$T^f_{pir-bi} = \begin{bmatrix} 1 & 0 & 0 \\ 0 & 1 & 0 \\ LZBP & -\frac{W_b}{2} & 1 \end{bmatrix} \tag{4.1.36}$$

4.1.4.3. *Accelerations due to bogie-mounted aerodynamic actuators*

Ground-effect aerodynamic actuators can be mounted in many places on each bogie. We describe the location of each actuator relative to the bogie CG via the parameters:

$$[\text{LYGEF}i \quad \text{LZGEF}i]^T$$

Note that these parameters may be positive or negative. Specified locations of each actuator assumed in our study are given in Appendix A.

A pure force (no moment) is exerted on each actuator at its center of pressure. The force on each actuator is described by:

$$\mathbf{F}_{\mathrm{gef}i} = \begin{bmatrix} \mathrm{F_y} \\ \mathrm{F_z} \end{bmatrix}_{\mathrm{gef}i}$$

The transformation of a flap's forces to forces and torques at the bogie CG is given by:

$$\mathbf{T}^{\mathrm{f}}_{\mathrm{gef}i-\mathrm{b}i} = \begin{bmatrix} 1 & 0 \\ 0 & 1 \\ -\mathrm{LZGEF}i & -\mathrm{LYGEF}i \end{bmatrix} \tag{4.1.37}$$

4.1.5. Secondary Suspension

Each secondary suspension (front and rear) is modeled as an element that exerts equal and opposite forces on the train and bogie (see Figure 4.1.5). These forces can be dependent on displacements, velocities, or a combination of the states, and so can represent springs, dampers, and active elements. The location of these "elements," as described in Sections 4.1.3 and 4.1.4, are shown in Figures 4.1.2 and 4.1.3. The forces across each secondary suspension are a combination of the forces due to its active and passive elements:

$$\mathbf{F}_{\mathrm{s}i} = \mathbf{F}_{\mathrm{s}i,\mathrm{act}} + \mathbf{F}_{\mathrm{s}i,\mathrm{pass}} \tag{4.1.38}$$

In this report, actuator dynamics are ignored, so $\mathbf{F}_{\mathrm{act}}$ is a perfectly controllable input (control laws are discussed in Chapter 3). Passive forces are given by a combination of linear stiffness and linear damping:

$$\mathbf{F}_{\mathrm{s}i,\mathrm{pass}} = \mathbf{K}_{\mathrm{s}i} \cdot \Delta\mathbf{x}_{\mathrm{s}i} + \mathbf{C}_{\mathrm{s}i} \cdot \Delta\dot{\mathbf{x}}_{\mathrm{s}i} \tag{4.1.39}$$

where

$$\mathbf{K}_{\mathrm{s}i} = \frac{\delta\mathbf{F}_{\mathrm{s}i}}{\delta\Delta\mathbf{x}_{\mathrm{s}i}} \text{ (negative for a stable spring)} \tag{4.1.40}$$

$$\mathbf{C}_{\mathrm{s}i} = \frac{\delta\mathbf{F}_{\mathrm{s}i}}{\delta\Delta\dot{\mathbf{x}}_{\mathrm{s}i}} \text{ (negative for a stable damper)} \tag{4.1.41}$$

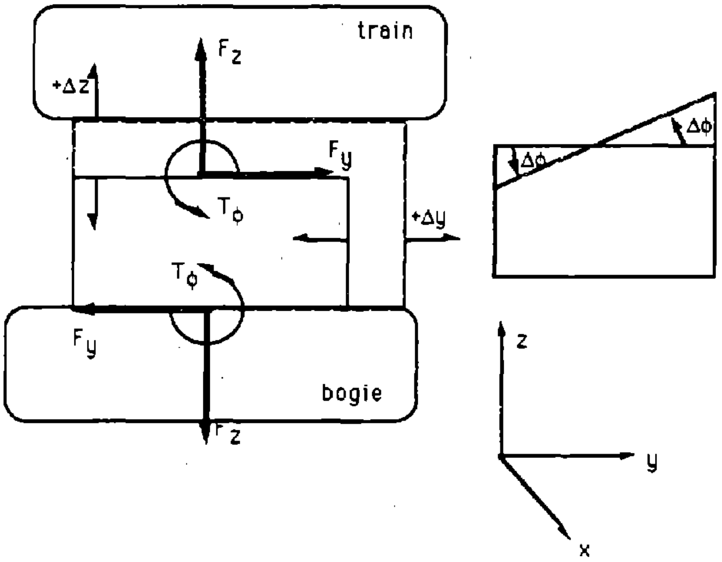

Figure 4.1.5 - Secondary suspension model

and $\Delta\mathbf{x}_{si}$ is the deflection across the secondary suspension element (positive when the deflection of the secondary increases):

$$\Delta\mathbf{x}_{si} = \begin{bmatrix} \Delta y \\ \Delta z \\ \Delta\phi \end{bmatrix}_{si} \tag{4.1.42}$$

$\Delta\mathbf{x}_{si}$, in terms of displacements of the train and bogie states is:

$$\begin{bmatrix} \Delta y \\ \Delta z \\ \Delta\phi \end{bmatrix}_{s1} = \begin{bmatrix} -y_{b1} + LZBS\cdot\phi_{b1} + y_t + LZTS\cdot\phi_t + LXB1\cdot\psi_t \\ -z_{b1} + z_t - LXB1\cdot\theta_t \\ -\phi_{b1} + \phi_t \end{bmatrix} \tag{4.1.43}$$

$$\begin{bmatrix} \Delta y \\ \Delta z \\ \Delta\phi \end{bmatrix}_{s2} = \begin{bmatrix} -y_{b2} + LZBS\cdot\phi_{b2} + y_t + LZTS\cdot\phi_t - LXB2\cdot\psi_t \\ -z_{b2} + z_t + LXB2\cdot\theta_t \\ -\phi_{b2} + \phi_t \end{bmatrix} \tag{4.1.44}$$

which can be written using transformation matrices:

$$\Delta\mathbf{x}_{si} = \mathbf{T}^{\mathbf{x}}_{t-si}\,\mathbf{x}_t + \mathbf{T}^{\mathbf{x}}_{bi-si}\,\mathbf{x}_{bi} \tag{4.1.45}$$

Similarly,

$$\Delta\dot{\mathbf{x}}_{si} = \mathbf{T}^{\mathbf{x}}_{t-si}\,\dot{\mathbf{x}}_t + \mathbf{T}^{\mathbf{x}}_{bi-si}\,\dot{\mathbf{x}}_{bi} \tag{4.1.46}$$

Combining the equations above yields an equation for secondary suspension force in terms of system states and control inputs:

$$\mathbf{F}_{si} = \mathbf{F}_{si,\mathrm{act}} + \mathbf{K}_{si}\left(\mathbf{T}^{x}_{t-si}\,\mathbf{x}_{t} + \mathbf{T}^{x}_{bi-si}\,\mathbf{x}_{bi}\right) + \mathbf{C}_{si}\left(\mathbf{T}^{x}_{t-si}\,\dot{\mathbf{x}}_{t} + \mathbf{T}^{x}_{bi-si}\,\dot{\mathbf{x}}_{bi}\right) \tag{4.1.47}$$

In this report, we assume that the secondary suspension stiffness ($\mathbf{K}_s$) and damping ($\mathbf{C}_s$) are free design parameters. Generally, we chose diagonal stiffness and damping matrices, thereby implying that we are defining these values at the roll center of the suspension (note that transformations yield off-diagonal terms). The non-zero terms in the stiffness matrix describing the stiffness in the vertical and lateral directions are determined by specifying a natural frequency:

$$\omega_n = \sqrt{\frac{2k_{si}}{m_t}} \tag{4.1.48}$$

or

$$\omega_n = \sqrt{\frac{2k_{si}}{I_t}} \tag{4.1.49}$$

Terms on the diagonal of the damping matrix are determined by specifying a damping ratio:

$$\xi = b_{si}\sqrt{\frac{1}{2k_{si}m_t}} \tag{4.1.50}$$

or

$$\xi = b_{si}\sqrt{\frac{1}{2k_{si}I_t}} \tag{4.1.51}$$

These frequencies and damping ratios are for mode shapes of pure train translation above fixed bogies. While these modes are not necessarily actual modes of the system, they are easy to visualize and therefore useful for communicating suspension parameter values. The roll stiffness and roll damping were determined by the particular vehicle geometry, with a provision for fine-tuning these parameters via the addition of extra stiffness and damping. This extra stiffness and damping would be provided in practice by additional suspension elements (such as a swaybar on an automobile). Chapter 4.4 describes how the secondary suspension parameters were chosen.

4.1.6. Primary suspensions

We assumed an electro-dynamic (EDS) primary suspension. Because damping is very low in this type of magnetic suspension, the primary suspension was modeled as a linear stiffness without damping.

We considered a channel guideway configuration, where the bogie is suspended between two guideway walls as shown in Figure 4.1.2 (the analysis is equally valid for a box-beam type guideway). In this configuration, the primary suspension at each of the two bogies is considered to consist of two box-shaped elements (left and right). Each element exerts equal forces at opposing sides in response to deflections across the element (see Figure 4.1.6). For our analysis, we assumed that the stiffness is the same in all the elements. These box-shaped elements are a representation of the primary suspension stiffness at each of the four corners of the vehicle. Thus this is how the primary suspension was modelled, as mentioned in Section 4.1.4.2.

The forces across a side of a primary suspension are given by the equation

$$\mathbf{F}_{pil} = \mathbf{K}_p \cdot \Delta\mathbf{x}_{pi,l} \tag{4.1.52}$$

$$\mathbf{F}_{pir} = \mathbf{K}_p \cdot \Delta\mathbf{x}_{pi,r} \tag{4.1.53}$$

where

$$\mathbf{K}_p = \frac{\delta\mathbf{F}_{pi(l,r)}}{\delta\Delta\mathbf{x}_{pi(l,r)}} \text{ (negative for a stable spring)} \tag{4.1.54}$$

and $\Delta\mathbf{x}_{pi(l,r)}$ are the deflections across the primary suspension elements:

$$\Delta\mathbf{x}_{pi(l,r)} = \begin{bmatrix} \Delta y \\ \Delta z \\ \Delta\phi \end{bmatrix}_{pi(l,r)} \tag{4.1.55}$$

The primary suspension deflections can be written in terms of guideway position and the displacement of the bogie center of mass:

$$\Delta\mathbf{x}_{pir} = \begin{bmatrix} y_{bi} + \phi_{bi}LZBP - y_{gi} \\ z_{bi} - z_{gi} - \frac{W_b}{2}\left(\phi_{bi} - \phi_{gi}\right) \\ \phi_{bi} - \phi_{gi} \end{bmatrix} \tag{4.1.56}$$

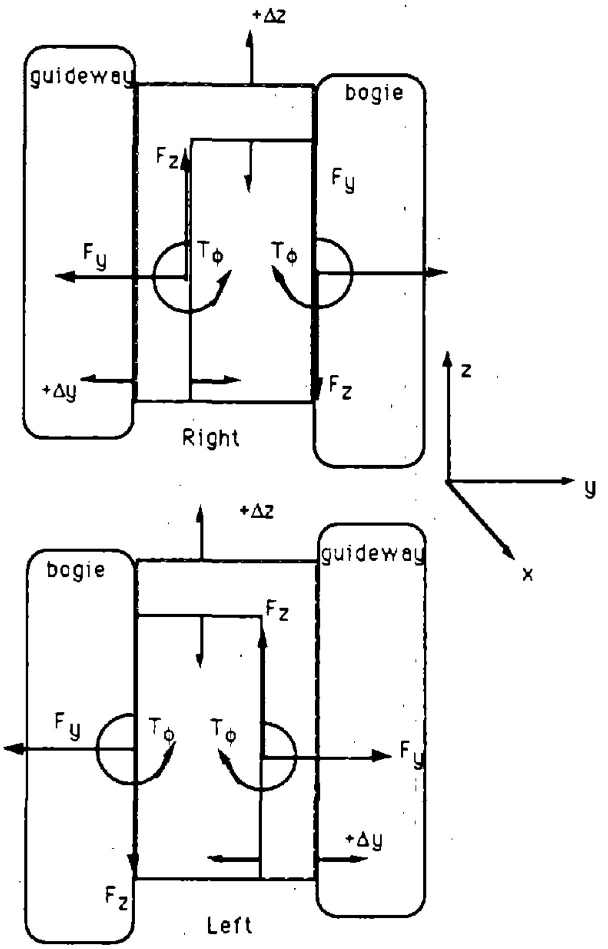

Figure 4.1.6. - Primary suspension model

$$\Delta x_{pil} = \begin{bmatrix} -y_{bi} - \phi_{bi} LZBP + y_{gi} \\ z_{bi} - z_{gi} + \frac{W_b}{2}\left(\phi_{bi} - \phi_{gi}\right) \\ -\phi_{bi} + \phi_{gi} \end{bmatrix} \tag{4.1.57}$$

Using transformation matrices, the primary deflections can be written as:

$$\Delta x_{p1l} = T^{x}_{b1-p1l} x_{b1} + T^{x}_{g1-p1l} x_{g1} \tag{4.1.58}$$

$$\Delta x_{p1r} = T^{x}_{b1-p1r} x_{b1} + T^{x}_{g1-p1r} x_{g1} \tag{4.1.59}$$

$$\Delta x_{p2l} = T^{x}_{b2-p2l} x_{b2} + T^{x}_{g2-p2l} x_{g2} \tag{4.1.60}$$

$$\Delta x_{p2r} = T^{x}_{b2-p2r} x_{b2} + T^{x}_{g2-p2r} x_{g2} \tag{4.1.61}$$

where

$\mathbf{x}_{g1}$ = the guideway position at the front bogie
$\mathbf{x}_{g2}$ = the guideway position at the rear bogie

The guideway position at each bogie[7] is specified by a vector:

$$\mathbf{x}_{gi} = \begin{bmatrix} y \\ z \\ \phi \end{bmatrix}_{gi} \qquad (4.1.62)$$

Combining the above equations yields an equation for the force due to a primary suspension element in terms of system states:

$$\mathbf{F}_{pi(l,r)} = \mathbf{K}_p \left(\mathbf{T}^x_{bi-pi(l,r)} \mathbf{x}_{bi} + \mathbf{T}^x_{gi-pi(l,r)} \mathbf{x}_{gi} \right) \qquad (4.1.63)$$

In this document, the primary suspension stiffnesses were considered to be free design parameters. We chose diagonal stiffness matrices (note that off-diagonal terms arise from the transformations) with zero rotational stiffness. Each translational stiffness terms is specified by a natural frequency:

$$\omega_n = \sqrt{\frac{4k_p}{m_t + 2m_b}} \qquad (4.1.64)$$

These frequencies are for mode shapes of combined train and bogie translation (vertical or lateral) with no secondary suspension deflection. While these are not necessarily actual modes of the system, they are easy to visualize and therefore useful for communicating suspension parameter values.

4.1.7. Aerodynamic Actuators

We considered two types of aerodynamic actuators in our research, wings mounted on the train and ground-effect flaps mounted on the bogies.

---

[7] Although the guideway position is not constant along the length of the bogie, we model the bogie as having zero-length. Thus, we ignore "finite length filtering" effects which tend to smooth high frequency (closely-spaced) guideway variations. Disregarding this effect makes our analysis slightly conservative. However, this conservatism is somewhat negated by our assumption of a two bogie vehicle: a train with many bogies will have a smoother ride than one with two bogies.

4.1.7.1. *Train-mounted Actuators*

Train-mounted actuators operate in "free-stream", and are modeled as winglets with one degree of freedom. The lift and induced drag for a flap in free-stream are given by:

$$F_{L_{flap}} = \frac{1}{2}\rho\ |V_{air}|^2 A_{flap} C_L(\alpha) \qquad (4.1.65)$$

$$F_{D_{flap}} = \frac{1}{2}\rho\ |V_{air}|^2 A_{flap} C_D(\alpha)\sin(\alpha) \qquad (4.1.66)$$

where

α = flap angle of attack
$C_L(\alpha)$ = coefficient of lift

In modeling the train dynamics, we considered only the lift component of the flap forces. The induced drag of the flaps is calculated to determine the drawbacks of aerodynamic control, but its effects on train accelerations are not considered[8].

The lift coefficient was obtained from conventional aerodynamic theory[9]. Since the resulting curve, shown in Figure 4.1.7, is nearly linear for small alpha's, a linear equation for $C_L(\alpha)$ results:

$$C_L(\alpha) \approx C_{L\alpha}\,\alpha \qquad (4.1.67)$$

where

$$C_{L\alpha} = \frac{\partial C_L}{\partial \alpha}(\alpha)\bigg|_{\alpha_0} \qquad (4.1.68)$$

The operating point that was linearized about was zero degrees, assuming that negative lift could be obtained for negative angles of attack.

---

[8] Since induced drag acts parallel to the velocity vector, drag forces act in a direction not included in our model. Induced drag also creates torques when the drag force is transformed to the train CG; but these torques are small compared to other torques on the vehicle. Also, the drag is in the same direction, regardless of the sign of the deflection of the aero-surface's angle. Therefore this effect cannot be included in a linear model.

[9] Borst, H.V.; Hoerner, S.F.,"Fluid-Dynamic Lift," published by Mrs. Liselotte Hoerner, Bricktown, NJ, 1975.

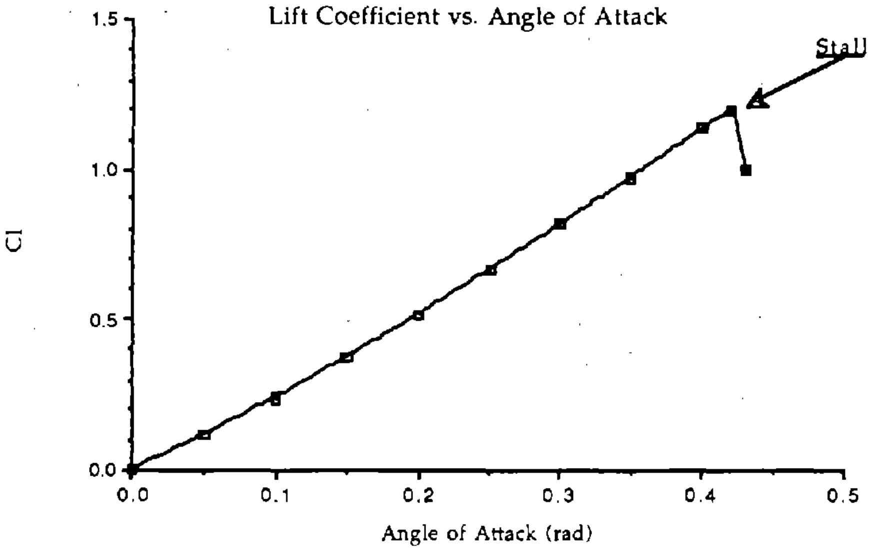

Figure 4.1.7 - Lift coefficient vs attack angle for train mounted wings

As in Section 4.1.3.2, we approximate $|V_{air}|$ as equal to the train's velocity. In addition, we ignore the effects of wind and vehicle rotation and, using a small angle approximation for α, model the lift force (normal to the wing) as perpendicular to the velocity vector. Thus, the final equation for the magnitude of the flap force is:

$$\left|\mathbf{F}_{\mathrm{flap}i}\right| = \frac{1}{2}\rho\ |V|^2 A_{\mathrm{flap}}\, C_{L\alpha}\, \alpha_{\mathrm{flap}i} \tag{4.1.69}$$

The direction of this force depends on the mounting point and orientation of the flap, so that

$$\mathbf{F}_{\mathrm{flap}i} = \begin{bmatrix} F_y \\ F_z \end{bmatrix}_{\mathrm{flap}i} = \mathbf{T}\left|F_{\mathrm{flap}i}\right| \tag{4.1.70}$$

The dynamics of the actuators controlling the flap angles are ignored so that each $\alpha_{\mathrm{flap}i}$ is assumed to be perfectly controllable.

In theory, a very large aerodynamic force can be obtained for relatively low actuator torque. The idea is that if the flap rotates about its center of pressure, the aerodynamic torques across the flap rotation joint are small compared to the forces generated by the flap. However, the actual force required in a hydraulic system which drives the wing can still be large, due to physical constraints and practical considerations. The dynamics of the system dictate a high actuator bandwidth (based upon Linear Quadratic Regulator (LQR) optimal control designs), so that actuator power requirements may become large depending on the flap moment of inertia.

The primary advantage of aerodynamic actuators is that forces can be applied with respect to an earth fixed reference frame.

Flap locations and parameters for each flap are described in Appendix A.

4.1.7.2. Ground-effect flaps

In the case of a channel guideway, any bogie-mounted aerodynamic actuator operates in "ground effect" due to the close proximity of the guideway. In this configuration, a flap is used in conjunction with a loose-fitting seal to trap air passing between the bogie and guideway, resulting in an area of high pressure and lift on the bogie. The pressure is non-linearly dependent on the gaps at the front and rear of the actuator. Since these gaps can be described in terms of flap angle (α) and the front air gap (ε), we choose these as the independent variables for determining coefficients of lift and induced drag. The resultant equations for lift and induced drag are:

$$F_{L_{gef}} = \frac{1}{2}\rho\ |V_{air}|^2 A_{gef}\, C_L(\alpha,\varepsilon) \qquad (4.1.71)$$

$$F_{D_{gef}} = \frac{1}{2}\rho\ |V_{air}|^2 A_{gef}\, C_D(\alpha,\varepsilon) \qquad (4.1.72)$$

where

A_{gef} = surface area of the ground-effect flap

Plots of lift coefficients as a function of the independent variables are shown in Figures 4.1.8-4.1.9.

Where applicable, the data were linearized via Taylor series approximations to yield simplified descriptions suitable for our analysis:

$$C_L \approx C_{L\alpha}(\alpha_0)\alpha + C_{L\varepsilon}(\varepsilon_0)\varepsilon \qquad (4.1.73)$$

$$C_D \approx C_{D\alpha}(\alpha_0)\alpha + C_{D\varepsilon}(\varepsilon_0)\varepsilon \qquad (4.1.74)$$

The front gap (ε) can be written in terms of the bogie and guideway positions as:

$$\varepsilon_{gefi} = \mathbf{T}^{x}_{bj-gefi}\,\mathbf{x}_{b1} + \mathbf{T}^{x}_{gj-gefi}\,\mathbf{x}_{g1} \qquad (4.1.75)$$

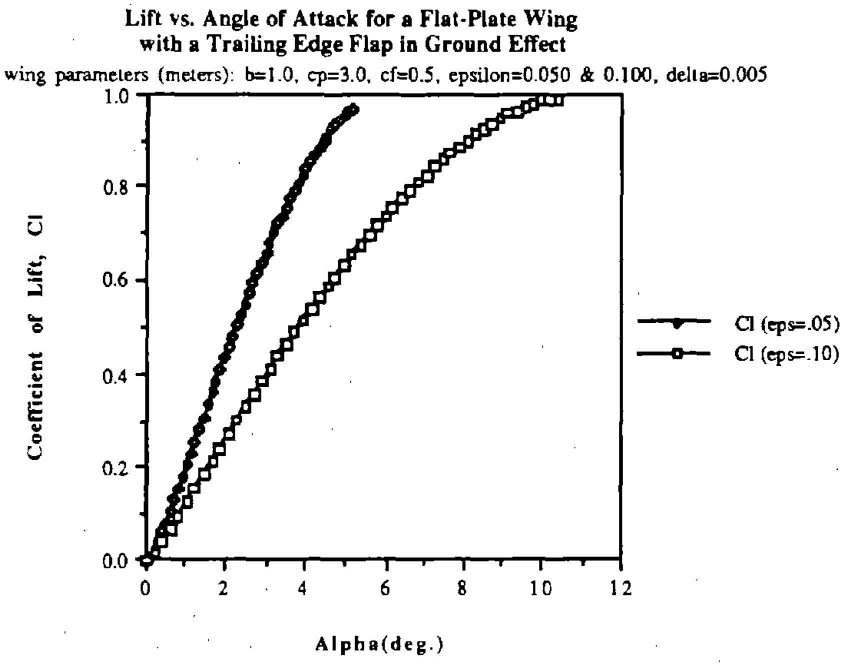

Figure 4.1.8 - Coefficient of lift versus angle of attack for a fixed air gap

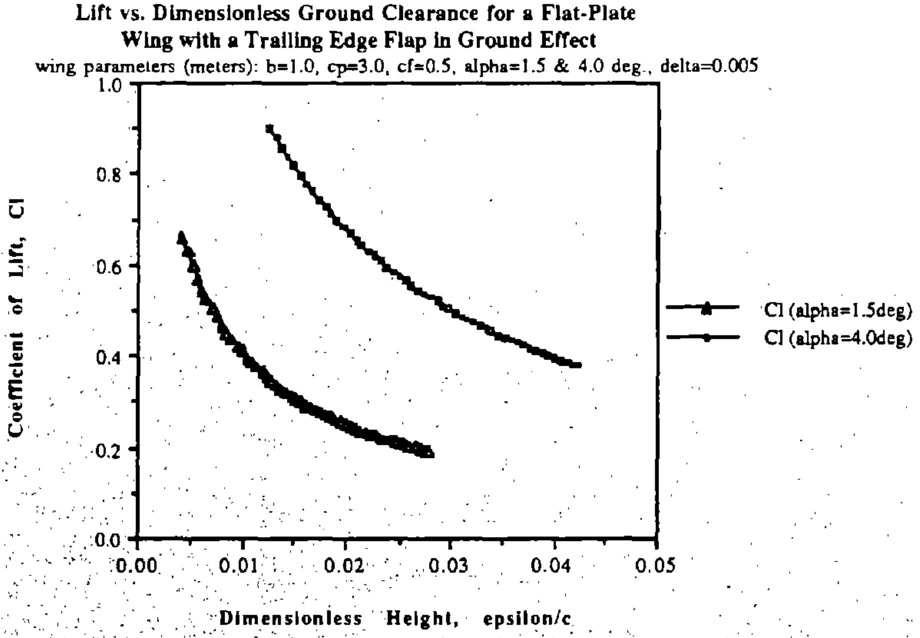

Figure 4.1.9 - Coefficient of lift versus dimensionless (relative) air gap for fixed angle of attack

Thus, the equation for magnitude of ground-effect flap force can be written as:

$$\left|\mathbf{F}_{gefi}\right| = \frac{1}{2}\rho\ |V|^2 A_{gefi}\Big(C_{L\alpha}(\alpha_0)\alpha_{gefi} + C_{L\varepsilon}(\varepsilon_0)\Big(\mathbf{T}^{x}_{bj-gefi}\,\mathbf{x}_{b1} + \mathbf{T}^{x}_{gj-gefi}\,\mathbf{x}_{g1}\Big)\Big) \quad (4.1.76)$$

To determine the coefficients in this equation, operating points (α_0, ε) must be chosen for each flap. The appropriate choice for each flap depends on how it is used.

Ground-effect flaps can exert positive forces in only one direction: outward between the bogie and the guideway. Thus, to achieve bi-directional changes in control force, each flap must be either operated about some non-zero steady-state angle of attack or operated as part of an opposing pair. For our work, we assumed four flaps per bogie: two on the bottom exerting force in the +Z direction; and two on opposite sides of the bogie exerting forces in the +Y and -Y directions. Figure 4.1.10 depicts the flap, including the two variables on which the force is dependent. (Details of the flap parameters can be found in Appendix A.)

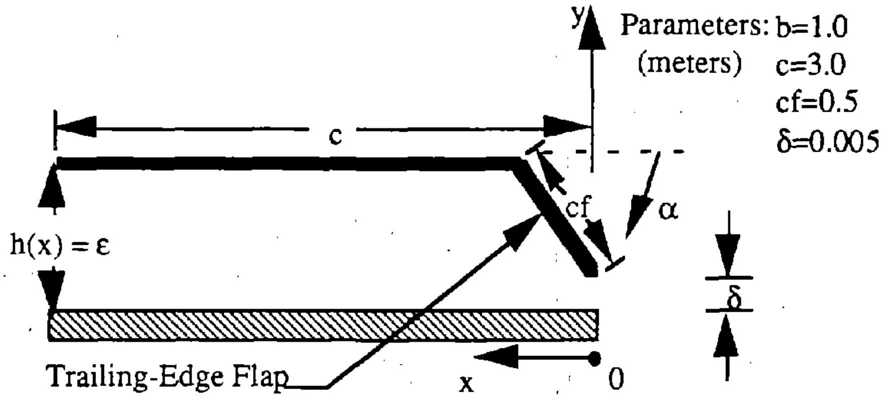

Figure 4.1.10 - Ground-effect flap

The bottom-mounted flaps are operated at a non-zero angle of attack to generate a non-zero DC lift. This enables the angle of attack to be decreased as well as increased, thus providing both positive and negative control forces. The nominal operating point for linearization of the bottom-mounted flaps is:

α_0 = static equilibrium deflection curve-fit through zero

ε_0 = nominal air gap

The side-mounted flaps work in concert to achieve both +Y and -Y forces. At a given moment, force in the direction desired is achieved by generating positive lift from the appropriate flap and setting the angle of attack for the other flap to zero. Therefore, force is applied against one side of the guideway and bogies at a time. The nominal operating point for linearization of the side-mounted flaps is:

α_0 = linearized curve-fit of equation through zero

ε_0 = nominal air gap

In addition, since the side-mounted flaps must work in pairs, with only one flap active at an instant, the force magnitude for each side-mounted flap is scaled by a factor of one-half.

The lift force versus angle of attack slope (holding the air gap fixed) must be determined so that it approximates the entire curve shown in Figure 4.1.8. This slope is all that characterizes this curve in the model, and it must be ensured that a control angle (not necessarily the actual angle of attack in the case of the bottom mounted flaps) of zero will result in zero force exerted on the train. In the case of the slope of the coefficient of lift vs. the air gap curve, the slope is all that is important, since any y-intercept will simply result in a slightly different operating height of the train: the force differential with changing air gap will not be affected.

An important note is that the portion of the ground-effect flap's force that is dependent on the air gap is modeled as an additional primary suspension stiffness, since it acts between the bogies and the guideway. This effect is described by the slope of the coefficient of lift versus the air gap curve. Thus this portion of the ground-effect flap's force is modeled as essentially an air spring in the primary suspension. As a result, this portion of the force is not controllable. Thus, its impact on system performance is not necessarily beneficial.

As for the train-mounted wings, the angle of attack for each ground-effect flap is assumed to be perfectly controllable. Unlike the wings, however, the ground-effect flaps can not pivot about the flap's center of pressure, so comparatively large actuator torques may be required to obtain the same forces, which act on the bogies rather than on the train. In addition, the dynamics of the ground-effect flap are highly nonlinear; thus a non-linear control scheme[10]

---

[10] Development of nonlinear control laws and the simulations required to test them is beyond the scope of the current research. Evaluation of the ground effect flaps via linear models and linear control laws is adequate for determining their potential benefit.

most likely will be needed for an actual system. Also, since the flaps are located in the air gap between the bogie and guideway, there is a larger chance that they may hit the guideway. These three concerns must be considered disadvantages of ground-effect flaps. Additionally, the ground-effect flaps exert forces on the bogies, rather than on the train; since we seek to reduce passenger accelerations, direct forces on the train are preferable. The advantages of ground-effect flaps are that they can generate comparatively large forces and can be designed to produce lateral control forces without greatly increasing tunnel size requirements.

4.1.8. Wind inputs

Since, for suspension performance, the worst-case wind is perpendicular to the vehicle, we model all winds as crosswinds. The crosswind is modeled as the sum of a random process and a DC value:

$$V_{wind} = \overline{V}_{wind} + V_{wind}(t) \tag{4.1.77}$$

where

$\overline{V}_{wind}$ = mean cross-wind velocity (steady state component of wind)

$V_{wind}(t)$ = time-varying wind component

The random component is modeled as a first-order Markov process with power-spectral-density:

$$\Phi_{wind}(\omega) = \frac{2\sigma_w^2 \nu}{\omega^2 + \nu^2} \tag{4.1.78}$$

where

Φ_{wind} = power spectral density of time-varying cross-wind

ν = break frequency of wind spectrum (rad/s)

σ_w = RMS of time-varying wind component (m/s)

ω = frequency (rad/s)

The break frequency (ν) depends on weather conditions and terrain features. We assumed a value of 1 (rad/s). σ_w and $\overline{V}_{wind}$ also depend on weather and terrain. We assumed a relationship between σ_w, $\overline{V}_{wind}$ and the peak wind:

$$(V_{wind})_{max} = \overline{V}_{wind} + 3\sigma_w \tag{4.1.79}$$

$$(V_{wind})_{min} = \overline{V}_{wind} + 3\sigma_w = 0 \tag{4.1.80}$$

Thus, the peak wind is equal to twice the mean wind, with a minimum wind speed of zero.

Several different levels of maximum wind were considered.

For our analysis, we desire a model for the time-varying wind in the form of a linear system driven by white noise. A linear system that has an output with the appropriate PSD (Power Spectral Density) is straightforward to derive. The PSD of the output of a linear system is given by:

$$\Phi_{wind}(\omega) = \Phi_{yy}(\omega) = g(j\omega)\, g(-j\omega)\, \Phi_{uu}(\omega) \qquad (4.1.81)$$

If we choose unfiltered white noise as the system input, its PSD is:

$$\Phi_{uu}(\omega) = 1 \qquad (4.1.82)$$

A system with the desired output is:

$$g(j\omega) = \frac{\sigma_w \sqrt{2\nu}}{j\omega + \nu} \qquad (4.1.83)$$

$$g(s) = \frac{\sigma_w \sqrt{2\nu}}{s + \nu} \qquad (4.1.84)$$

We use a state-space representation of this system for our covariance analysis, *i.e.*:

$$\dot{\mathbf{x}}_w = \mathbf{A}_w \mathbf{x}_w + \mathbf{B}_w \xi_w \qquad (4.1.85)$$

$$\mathbf{V}_{wind}(t) = \mathbf{C}_w\, \mathbf{x}_w \qquad (4.1.86)$$

where

ξ_w = white noise input to wind model (unit intensity)

The mean component of the wind is accounted for in the mean sideslip angle β_0 (see the wind force equations in Section 4.1.3.2). System responses to sharp discontinuities in the wind profile, such as might occur when the train exits a tunnel or passes a terrain feature, can be evaluated by employing appropriate time functions for $V_{wind}(t)$.

4.1.9. Guideway inputs

The guideway is modeled as a time-varying vector of positional and rotational inputs to the front and rear primary suspensions:

$$\mathbf{x}_{gi} = \begin{bmatrix} y \\ z \\ \phi \end{bmatrix}_{gi} \tag{4.1.87}$$

Since the guideway position is constant at a given point on the guideway, the input to the rear bogie is a time delay of the input to the front:

$$\mathbf{x}_{g1} = e^{-s\tau}\,\mathbf{x}_{g2} \tag{4.1.88}$$

where τ is the time it takes the train to travel the distance between the two bogies:

$$\tau = \frac{\mathrm{LXB1} + \mathrm{LXB2}}{\mathrm{V}}$$

To obtain a linear approximation of the time delay, we used a Pade approximation :

$$e^{-s\tau} \approx \frac{2 + (-s\tau) + \frac{(-s\tau)^2}{2!} + \cdots + \frac{(-s\tau)^n}{n!}}{2 + (s\tau) + \frac{(s\tau)^2}{2!} + \cdots + \frac{(s\tau)^n}{n!}} \tag{4.1.89}$$

where

n = the order of approximation

For our covariance analysis, a state-space form of equation 4.1.89 is used:

$$\dot{\mathbf{x}}_d = \mathbf{A}_d\,\mathbf{x}_d + \mathbf{B}_d\,\mathbf{x}_{g1} \tag{4.1.90}$$

$$\mathbf{x}_{g2} = \mathbf{C}_d\,\mathbf{x}_d + \mathbf{D}_d\,\mathbf{x}_{g1} \tag{4.1.91}$$

Guideway inputs to the front bogie are a sum of known inputs (curves, inclinations, *etc.*) and random guideway roughness:

$$\mathbf{x}_{g1} = \left(\mathbf{x}_{g1}\right)_{known} + \mathbf{x}_{g1}(t) \tag{4.1.92}$$

Known inputs are modeled by summing simple waveforms (steps, ramps, sinusoids), where a position-dependent guideway position, $\mathbf{x}_g(x)$, is transformed to a time-dependent input by:

$$x = V\,t \tag{4.1.93}$$

To describe random guideway roughness, we adapted a commonly applied model[11] which describes each roughness component as a power-spectral density function of the form:

$$\Phi_{\text{guideway}}(\omega) = \frac{A_r V}{\omega^2} \qquad (4.1.94)$$

where

A_r = roughness parameter

The appropriate roughness parameter is dependent on the manufacturing tolerances of the guideway. A discussion of roughness parameters used for our work is in Appendix B. Note that our present analysis excludes guideway flexibility and periodic guideway variations due to such factors as static guideway sag. In addition to this, none of the known inputs (curves, inclinations, etc.) are included for our analysis.

For our analysis, we desire a model of the guideway input in the form of a linear system driven by white noise. Derivation of the guideway model is similar to derivation of the wind model.

When driven by white noise, a linear system has the desired output statistics:

$$g(s) = \frac{\sqrt{A_r V}}{s} \qquad (4.1.95)$$

We use a state-space representation of this system:

$$\dot{\mathbf{x}}_{gm} = \mathbf{A}_{gm}\,\mathbf{x}_{gm} + \mathbf{B}_{gm}\,\xi_g \qquad (4.1.96)$$

$$\mathbf{x}_{g1}(t) = \mathbf{C}_{gm}\,\mathbf{x}_{gm} \qquad (4.1.97)$$

where

ξ_g = white noise input to guideway model

---

[11] Wormley, D.N.; Young, J.W., "Optimization of Linear Vehicle Suspensions Subjected to Simultaneous Guideway and External Force Disturbances," Journal of Dynamic Systems, Measurement, and Control: Transactions of the ASME, Paper No. 73-Aut-H, March 16,1973.

4.1.10. Forming the Complete Model

At this point, having presented models for all components of the vehicle-suspension system, we can form a complete model of the system. Combining equations yields the train accelerations in terms of the system inputs and the vehicle states as:

$$\ddot{\mathbf{x}}_t = \mathbf{I}_t^{-1} \cdot \begin{pmatrix} \left(\mathbf{T}^f_{s1\text{-}t}\,\mathbf{K}_s\,\mathbf{T}^x_{t\text{-}s1} + \mathbf{T}^f_{s2\text{-}t}\,\mathbf{K}_s\,\mathbf{T}^x_{t\text{-}s2} + \mathbf{T}^f_{aero\text{-}t}\,q\,A_t\,C_{y\beta}\,V\,\mathbf{T}^x_{t\text{-}\psi_t}\right)\mathbf{x}_t \\ +\left(\mathbf{T}^f_{s1\text{-}t}\,\mathbf{C}_s\,\mathbf{T}^x_{t\text{-}s1} + \mathbf{T}^f_{s2\text{-}t}\,\mathbf{C}_s\,\mathbf{T}^x_{t\text{-}s2}\right)\dot{\mathbf{x}}_t \\ +\mathbf{T}^f_{s1\text{-}t}\,\mathbf{K}_s\,\mathbf{T}^x_{b1\text{-}s1}\,\mathbf{x}_{b1} + \mathbf{T}^f_{s2\text{-}t}\,\mathbf{K}_s\,\mathbf{T}^x_{b2\text{-}s1}\,\mathbf{x}_{b2} \\ +\mathbf{T}^f_{s1\text{-}t}\,\mathbf{C}_s\,\mathbf{T}^x_{b1\text{-}s1}\,\dot{\mathbf{x}}_{b1} + \mathbf{T}^f_{s2\text{-}t}\,\mathbf{C}_s\,\mathbf{T}^x_{b2\text{-}s1}\,\dot{\mathbf{x}}_{b2} \\ +\mathbf{T}^f_{aero\text{-}t}\,q\,A_t\,C_{y\beta}\,V_{wind} + \mathbf{T}^f_{aero\text{-}t}\,q\,A_t\,C_\beta(\beta_0) \\ +\mathbf{T}^f_{s1\text{-}t}\mathbf{F}_{s1,act} + \mathbf{T}^f_{s2\text{-}t}\mathbf{F}_{s2,act} + \sum_i \mathbf{T}^f_{flapi-t}\,q\,A_{flapi}\,C_{y\alpha}\alpha_i \end{pmatrix} \qquad (4.1.98)$$

$$\ddot{\mathbf{x}}_{b1} = \mathbf{I}_{b1}^{-1} \cdot \begin{pmatrix} \mathbf{T}^f_{s1\text{-}b1}\,\mathbf{K}_s\,\mathbf{T}^x_{t\text{-}s1}\,\mathbf{x}_t + \mathbf{T}^f_{s1\text{-}b1}\,\mathbf{C}_s\,\mathbf{T}^x_{t\text{-}s1}\dot{\mathbf{x}}_t \\ +\left(\mathbf{T}^f_{s1\text{-}b1}\,\mathbf{K}_s\,\mathbf{T}^x_{b1\text{-}s1} + \sum_i \mathbf{T}^f_{gefi-b1}\,q\,A_{flapi}\,C_{y\varepsilon}\mathbf{T}^x_{b1\text{-}gefi}\right)\mathbf{x}_{b1} \\ +\mathbf{T}^f_{s1\text{-}b1}\,\mathbf{C}_s\,\mathbf{T}^x_{b1\text{-}s1}\,\dot{\mathbf{x}}_{b1} \\ +\sum_i \mathbf{T}^f_{gefi-b1}\,q\,A_{flapi}\,C_{y\varepsilon}\mathbf{T}^x_{g1\text{-}gefi}\,\mathbf{x}_{g1} \\ +\mathbf{T}^f_{s1\text{-}b1}\mathbf{F}_{s1,act} + \sum_i \mathbf{T}^f_{gefi-b1}\,q\,A_{flapi}\,C_{y\alpha}\alpha_{gefi} \end{pmatrix} \qquad (4.1.99)$$

$$\ddot{\mathbf{x}}_{b2} = \mathbf{I}_{b2}^{-1} \cdot \begin{pmatrix} \mathbf{T}^f_{s2\text{-}b2}\,\mathbf{K}_s\,\mathbf{T}^x_{t\text{-}s2}\,\mathbf{x}_t + \mathbf{T}^f_{s2\text{-}b2}\,\mathbf{C}_s\,\mathbf{T}^x_{t\text{-}s2}\dot{\mathbf{x}}_t \\ +\left(\mathbf{T}^f_{s2\text{-}b2}\,\mathbf{K}_s\,\mathbf{T}^x_{b2\text{-}s2} + \sum_i \mathbf{T}^f_{gefi-b2}\,q\,A_{flapi}\,C_{y\varepsilon}\mathbf{T}^x_{b2\text{-}gefi}\right)\mathbf{x}_{b2} \\ +\mathbf{T}^f_{s2\text{-}b2}\,\mathbf{C}_s\,\mathbf{T}^x_{b2\text{-}s2}\,\dot{\mathbf{x}}_{b2} \\ +\sum_i \mathbf{T}^f_{gefi-b2}\,q\,A_{flapi}\,C_{y\varepsilon}\mathbf{T}^x_{g2\text{-}gefi}\,\mathbf{x}_{g2} \\ +\mathbf{T}^f_{s2\text{-}b2}\mathbf{F}_{s2,act} + \sum_i \mathbf{T}^f_{gefi-b2}\,q\,A_{flapi}\,C_{y\alpha}\alpha_{gefi} \end{pmatrix} \qquad (4.1.100)$$

If we define a state vector **x**, control input vector **u**, and disturbance input vector **d**, a state-space equation for the system can be derived:

$$\dot{\mathbf{x}} = \mathbf{A}\,\mathbf{x} + \mathbf{B}_u\,\mathbf{u} + \mathbf{B}_d\,\mathbf{d} \tag{4.1.101}$$

where

$$\mathbf{x} = \begin{bmatrix} \mathbf{x}_t & \mathbf{x}_{b1} & \mathbf{x}_{b2} & \dot{\mathbf{x}}_t & \dot{\mathbf{x}}_{b1} & \dot{\mathbf{x}}_{b2} \end{bmatrix}^T \tag{4.1.102}$$

$$\mathbf{u} = \begin{bmatrix} \mathbf{F}_{s1,act} \\ \mathbf{F}_{s2,act} \\ \alpha_{flapi} \\ \vdots \\ \alpha_{gefi} \\ \vdots \end{bmatrix} \tag{4.1.103}$$

$$\mathbf{d} = \begin{bmatrix} \mathbf{x}_{g1} \\ \mathbf{x}_{g2} \\ V_{wind}(t) \\ \dfrac{\rho V^2}{2} A_t\, C_{y\beta}(\beta_0) \end{bmatrix} \tag{4.1.104}$$

Equations for system outputs of interest in terms of system states, disturbance inputs, and controls are:

$$\mathbf{z} = \mathbf{C}\,\mathbf{x} + \mathbf{D}_u\,\mathbf{u} + \mathbf{D}_d\,\mathbf{d} \tag{4.1.105}$$

The system outputs (z) are train accelerations and rotation rates, primary suspension air gap changes, and secondary suspension strokes.

A system model in the form of a linear system driven by white noise is desired for covariance analyses. To obtain such a model, we combine the equations above with control laws for the active secondary and active aerodynamic actuators and equations derived in Sections 4.1.8 and 4.1.9 for guideway and wind disturbance inputs.

The guideway model is added first to yield a new system model of the form:

$$\dot{\mathbf{x}} = \mathbf{A}\,\mathbf{x} + \mathbf{B}_u\,\mathbf{u} + \mathbf{B}_d\,\xi_g + \mathbf{L}\begin{bmatrix} V_{wind}(t) \\ \dfrac{\rho V^2}{2} A_t\, C_{y\beta}(\beta_0) \end{bmatrix} \tag{4.1.106}$$

$$\mathbf{y} = \mathbf{C}\,\mathbf{x} + \mathbf{D}_u\,\mathbf{u} + \mathbf{D}_d\begin{bmatrix} V_{wind}(t) \\ \dfrac{\rho V^2}{2} A_t\, C_{y\beta}(\beta_0) \end{bmatrix} \tag{4.1.107}$$

When driven by the white noise input, this system will have non-stationary random outputs due to the integrators in the guideway model. As a result, closed-form covariance analyses cannot be performed to determine system response to the random guideway and wind inputs.

This problem can be overcome by executing a change of variables for the entire vehicle-suspension system. First, observe that the integrator portion of the guideway model is present to determine the position of the guideway relative to some Earth-fixed reference frame. Since the output variables of interest (air gaps, secondary suspension strokes, etc.) do not depend on Earth-relative position, this part of the model is not needed. Thus, any state transformation that removes the integrator modes from the system model while retaining all other modes retains all the information required for our analysis. This can be performed because the integrator modes of the system are unobservable in the outputs of interest. We derived such a transformation:

$$\mathbf{x}' = \mathbf{T}\,\mathbf{x} \qquad (4.1.108)$$

where $\mathbf{x}'$ is the transformed state. This transformation was applied to redefine our system:

$$\dot{\mathbf{x}} = \mathbf{T}\mathbf{A}\mathbf{T}^{-1}\mathbf{x} + \mathbf{T}\mathbf{B}_u\mathbf{u} + \mathbf{T}\mathbf{B}_d\xi_g + \mathbf{T}\mathbf{L}\begin{bmatrix} V_{wind}(t) \\ \frac{\rho V^2}{2} A_t C_{y\beta}(\beta_0) \end{bmatrix} \qquad (4.1.109)$$

$$\mathbf{z} = \mathbf{C}\,\mathbf{T}\mathbf{x} + \mathbf{D}_u\mathbf{u} + \mathbf{D}_d\begin{bmatrix} V_{wind}(t) \\ \frac{\rho V^2}{2} A_t C_{y\beta}(\beta_0) \end{bmatrix} \qquad (4.1.110)$$

Note that, for convenience, the superscript (') has been dropped from the state vector in the above equations. Also for convenience, we redefine the system matrices as their transformed versions:

$$\mathbf{A} \leftarrow \mathbf{T}\,\mathbf{A}\,\mathbf{T}^{-1}$$

$$\mathbf{B}_u \leftarrow \mathbf{T}\,\mathbf{B}_u$$

$$\mathbf{B}_d \leftarrow \mathbf{T}\,\mathbf{B}_d$$

$$\mathbf{C} \leftarrow \mathbf{C}\,\mathbf{T}$$

We continue by introducing equations to describe the control inputs **u**. Full-state feedback is assumed, yielding an equation for the control inputs in terms of the states of the transformed system[12]:

$$\mathbf{u} = -\mathbf{G}\,\mathbf{x} \tag{4.1.111}$$

Note that the full-state feedback assumption implies availability of noise-free measurements of the system states, including the primary suspension air gaps and their changes in response to guideway position inputs. This is because our transformed states do not contain the absolute position of the guideway, so we only know the relative positions of each in terms of the air gap in each direction. Thus, when we perform feedback on these states, which of course must be controllable to do so, we assume that the air gap can be controlled by changing the position of the bogie and measuring perfectly the position of the guideway. Also observe that the dimensions of **u** and **G** depend on the specific actuator configuration chosen. For the case of an all-passive system, **u** and **G** are zero.

Defining the closed loop equations for A and C as:

$$\mathbf{A}_{cl} = \mathbf{A} - \mathbf{B}_u\,\mathbf{G} \tag{4.1.112}$$

$$\mathbf{C}_{cl} = \mathbf{C} - \mathbf{D}_u\,\mathbf{G} \tag{4.1.113}$$

yields:

$$\dot{\mathbf{x}} = \mathbf{A}_{cl}\,\mathbf{x} + \mathbf{B}_d\,\xi_g + \mathrm{L}\begin{bmatrix} V_{wind}(t) \\ \dfrac{\rho V^2}{2} A_t\, C_{y\beta}(\beta_0) \end{bmatrix} \tag{4.1.114}$$

$$\mathbf{z} = \mathbf{C}_{cl}\,\mathbf{x} + \mathbf{D}_d\begin{bmatrix} V_{wind}(t) \\ \dfrac{\rho V^2}{2} A_t\, C_{y\beta}(\beta_0) \end{bmatrix} \tag{4.1.115}$$

Finally, the model for the time-varying wind component is appended to yield the system equations used to calculate the output response:

---

[12] A description of how the gain matrix G is derived appears in Section 4.3.

$$\dot{\mathbf{x}} = \mathbf{A}_{cl}\,\mathbf{x} + \mathbf{B}_d \begin{bmatrix} \xi_g \\ \xi_w \end{bmatrix} + \mathbf{L}\left(\frac{\rho V^2}{2} A_\iota \, C_{y\beta}(\beta_0) \right) \qquad (4.1.116)$$

$$\mathbf{z} = \mathbf{C}_{cl}\,\mathbf{x} + \mathbf{D}_d \left(\frac{\rho V^2}{2} A_\iota \, C_{y\beta}(\beta_0) \right) \qquad (4.1.117)$$

The last term in these system equations is the force that results when the steady wind component ($\overline{\mathbf{V}}_{wind}$) is applied. We can solve for the response to this component separately, thus determining the DC components of the system outputs and the mean sideslip angle (β_0) used for system linearization. The aerodynamic stability derivative $C_{y\beta}(\beta)$ and center of pressure position (LXCP) are then determined as described in Section 4.1.3.2, and the steady wind term set to zero, yielding a linear system driven by white noise:

$$\dot{\mathbf{x}} = \mathbf{A}_{cl}\,\mathbf{x} + \mathbf{B}_d \begin{bmatrix} \xi_g \\ \xi_w \end{bmatrix} \qquad (4.1.118)$$

$$\mathbf{z} = \mathbf{C}_{cl}\,\mathbf{x} \qquad (4.1.119)$$

This describes the general treatment of aerodynamic inputs for the five degree-of-freedom model. The actual treatment of crosswind forces for the results of the study are described in the next section.

4.1.11 Subset of 5 DOF Model used for this Analysis

A subset of the five degree of freedom model consisting of the heave, sway (lateral), and roll directions of motion was used for the analysis results reported in Section 4.5. The desire was to analyze the motion in a cross-sectional plane, thus lending insight into the design of the vehicle/guideway interface. Because the sub-model essentially has no length for either the train or the bogies, the crosswind effects were dealt with slightly differently. First of all, the study was limited to high vehicle speeds, at or above 100 m/s, so that only small values of sideslip angle β were encountered. Thus a single linear term from equation 4.1.12 is adequate:

$$C_Y = C_{Y\beta}\,\beta$$

Also, since there was no yaw angle of the train in the model, there were no aerodynamic yaw stability effects that carried through to this subset of the model. The side force coefficient was obtained using data from Grunwald of NASA Langley. He measured data for a vehicle with three cross-sections: semi-circular, semi-circular with short vertical sides, and semi-circular with long vertical sides. Slender body theory tells us that the side force should be proportional to the height of the vehicle. Therefor it is logical to define a side force coefficient as follows:

$$C_Y = \frac{\text{Side Force}}{\frac{\pi}{2} H^2 q}$$

where q is the dynamic pressure as defined in Section 2. The reference area is a semicircle with a radius equal to the height of the train. This is the same as the area of the maximum cross-section area of Grunwald's semi-circular vehicle. Ruetenik has shown that if the data is replotted using the above definition, all three vehicle shapes give the same curve, which has a fairly linear slope. This slope is given by

$$C_{Y\beta} = 2.39 \text{ per radian at } \beta = 0$$

For this model, the disturbance and control inputs to the rear bogies were "slaved" to the those of the front bogies. In this way, the time delay and therefore the Pade approximation described earlier have been avoided.

Although there are aero-surfaces in ground effect mounted to the bogies that can exert forces in both the lateral and vertical directions, the aerodynamic wings mounted on the train can only exert forces in the vertical direction. The reason for this is that it was judged that there were practical problems arising from mounting vertical aero-surfaces that produce lateral forces on the train. Such surfaces would have to be located above the train because if they are placed in proximity to the train, their effectiveness is neutralized by aerodynamic interference with the train body. Even though a vertical surface mounted above the train body might be beneficial when actively controlled, it could become a liability if the active control fails, especially in the presence of crosswinds. Therefore, consideration of active aerodynamic control surfaces on the train was limited to horizontal surfaces that would produce vertical forces.

4.2. Analysis Methodology

4.2.1. Suspension Requirements

The maglev vehicle's suspension system is required to:

1) maintain the primary suspension air gaps (prevent the bogies from striking the guideway);
2) ensure that the secondary suspension stroke does not exceed stroke limits; and
3) maximize passenger comfort.

These performance requirements can be quantified in terms of the performance output vector **z**. As discussed in Section 4.1, the system outputs are driven by both a DC component due to steady wind and zero-mean random inputs (modeled as a vector of white noise) due to guideway roughness and time-varying winds. Thus, the components of the output vector **z** are each the sum of a steady component and a zero-mean, randomly varying component.

$$\mathbf{z}(t) = \bar{\mathbf{z}} + \tilde{\mathbf{z}}(t) \qquad (4.2.1)$$

where:

$\mathbf{z}(t)$ = performance output vector, including air gaps and secondary suspension strokes
$\bar{\mathbf{z}}$ = steady state, DC component of outputs
$\tilde{\mathbf{z}}(t)$ = time varying portion of outputs

The suspension requirements are written in terms of these two components.

4.2.1.1. *Air gap variations and secondary strokes*

The primary suspension air gap requirements are described by limits on the maximum primary suspension strokes:

$$\Delta \mathbf{x}_{pi(l,r)} < \left(\Delta \mathbf{x}_{pi(l,r)}\right)_{max} \qquad (4.2.2)$$

where:

$\Delta \mathbf{x}_{pi(l,r)}$ = change in primary air gap, on either the left or right side of the bogie

The limits on air gap variations are determined by the available nominal air gap between the bogies and the guideway, minus the gap used up by steady crosswinds. The resulting limits on peak air gap variations were assumed to be 10 cm in the vertical direction and 5 cm in the lateral direction.

The limit imposed on RMS variations of the primary air gap was:

$$\Delta\bar{x}_{pi(l,r)} + 5\sigma_{\Delta x_{pi(l,r)}} < \left(\Delta x_{pi(l,r)}\right)_{\max} \qquad (4.2.3)$$

where:

$\Delta\bar{x}_{pi(l,r)}$ = change in primary air gap, on either the left or right side of the bogie, due to DC input(s)

$\sigma_{\Delta x_{pi(l,r)}}$ = RMS variation in primary air gap, on either the left or right side of the bogie

At any given instant in time, there is a probability of 2.87×10^{-7} that the random component of the airgap will be greater than five times its RMS value. Therefore, we judge this criteria to be conservative.

The requirement of satisfying the secondary suspension stroke limits was quantified as:

$$\Delta x_{si} < \left(\Delta x_{si}\right)_{\max} \qquad (4.2.4)$$

where:

Δx_{si} = the change in the gap between the bogies and the train; *i.e.* the secondary suspension stroke

The criteria we used was:

$$\Delta\bar{x}_{si} + 3\sigma_{\Delta x_{si}} < \left(\Delta x_{si}\right)_{\max} \qquad (4.2.5)$$

where:

$\Delta\bar{x}_{si}$ = change in the gap between the bogies and the train due to DC input(s)

$\sigma_{\Delta x_{si}}$ = RMS variation in the gap between the bogies and the train

There is a probability of 0.00135 that the secondary stroke will be greater than this three sigma variation at any given instant in time. This less stringent criteria (three sigma versus five sigma peaks) was applied for the secondary suspension stroke because the (still rare) event of hitting the secondary suspension stops is not judged to be a critical failure of the suspension, as touchdown on the guideway is. (If the secondary suspension stroke limit is exceeded, the likely outcome is a slight "bump" felt in the passenger compartment as the suspension bottoms out). The maximum secondary suspension stroke was assumed to be 11 cm in both the vertical and lateral directions.

The contributions to the air gaps and secondary suspension strokes due to the steady crosswinds were neglected for this study. The purpose of this study is to compare the relative improvements of different type of active control systems over a passive system. Therefore, the exclusion of the steady state deflections of the suspension is acceptable because the exclusion is applied equally to all cases. The additional gap required to allow for deflections due to steady state winds will vary between different designs, and in this study it was desired to be as general as possible.

For the implementation of ground-effect flaps, the primary suspension airgap requirements are slightly different. The airgap variation limitations were more restrictive, since extra gap is required to accommodate the flaps. How this was done is described in Section 4.3.4.

4.2.1.2. Ride quality

Two measures of ride quality are commonly used for maglev vehicles, the ISO (International Standardization Organization) ride quality criteria and the Pepler ride quality criteria.[13] Both measures are dependent on train accelerations. In addition, the Pepler index includes the effects of roll and noise. Train accelerations and train rotation rates are variables in the output vector **z**.

The Pepler ride quality index is a scalar sum of statistics of system variables:

$$P.I. = 1.0 + 0.5\sigma_{\dot{\phi}} + 17\sigma_{\ddot{z}} + 17\sigma_{\ddot{y}} + 0.1(dB(N) - 65) \qquad (4.2.6)$$

where

$\sigma_{\dot{\phi}}$ = RMS passenger roll rate (deg/s)

$\sigma_{\ddot{z}}$ = RMS passenger acceleration in the Z direction (g's)

$\sigma_{\ddot{y}}$ = RMS passenger acceleration in the Y direction (g's)

dB(N) = passenger compartment noise level (decibels)

This research did not include the effect of noise on ride quality, so the formula used for computing the Pepler index was:

$$P.I. = 1.0 + 0.5\sigma_{\dot{\phi}} + 17\sigma_{\ddot{z}} + 17\sigma_{\ddot{y}} \qquad (4.2.7)$$

---

[13] Dunlap and Associates, Inc., "Development of Techniques and Data for Evaluating Ride Quality Volume II: Ride Quality Research," Report No. DOT-TSC-RSPD-77-1,II for U.S. Dept. of Transportation, February, 1978.

which depends only on RMS values of the system outputs.

The ISO ride quality criteria specifies limits on RMS vertical and lateral train accelerations in one-third octave bands over a specified range of frequencies (see the plots of system performance versus ISO 1 hour reduced comfort specifications in the results section). The limits are different for the lateral and vertical directions.

$$(\ddot{y}_t)_{rms} = \left\{ \int_{\omega_l}^{\omega_u} S_{\ddot{y}_t}(\omega) d\omega \right\}^{\frac{1}{2}} \tag{4.2.8}$$

Given each center frequency ω_c, the upper and lower bounds for the one third octave band are determined by:

$$\omega_u = \omega_c \exp\left(\frac{1}{6}\ln 2\right) = 1.122\,\omega_c \tag{4.2.9}$$

$$\omega_l = \omega_c \exp\left(-\frac{1}{6}\ln 2\right) = 0.891\,\omega_c \tag{4.2.10}$$

Note that the steady component of the system output vector does not contribute to either ride quality measure. Thus, only the time-varying portions of the system outputs affect ride quality, and only the system response to the white noise input needs to be considered in ride quality evaluations. Ride quality measures were calculated at the "worst seat in the train", typically a front or rear corner of the passenger compartment.

4.2.2 Calculations

As stated previously, the output variable **z** can be written as the sum of a DC (mean) component and a random, time-varying component.

$$\mathbf{z}(t) = \bar{\mathbf{z}} + \tilde{\mathbf{z}}(t) \tag{4.2.11}$$

The mean and random components of the output are calculated separately and then added to determine system performance. However, as mentioned in Section 4.2.1.1, only the time varying portion of the outputs was considered in this analysis.

4.2.2.1 *Determining the mean of the outputs*

We first set the time-varying disturbances to zero and solve the remaining non-linear equations. This requires the solution to:

$$\dot{\mathbf{x}} = \mathbf{A}\,\mathbf{x} + \mathbf{B}_{dc}\left(\frac{\rho}{2}|V|^2 C_y(\beta_0)\right) = 0 \tag{4.2.12}$$

$$\bar{\mathbf{z}} = \mathbf{C}\,\mathbf{x} + \mathbf{D}_{dc}\left(\frac{\rho}{2}|V|^2 C_y(\beta_0)\right) \tag{4.2.13}$$

for the mean sideslip angle (β_0) and the steady component of the system outputs ($\bar{\mathbf{z}}$). The resultant value for β_0 is then used to calculate the aerodynamic terms which depend on β (C_{yb}, LXCP). Dropping the steady disturbance term from the system equations then yields a system model that is linear and driven by white noise:

$$\dot{\mathbf{x}} = \mathbf{A}\,\mathbf{x} + \mathbf{B}_d\,\xi \tag{4.2.14}$$

$$\mathbf{z} = \mathbf{C}\,\mathbf{x} + \mathbf{D}_d\,\xi \tag{4.2.15}$$

These equations are used to calculate RMS values of the time-varying outputs ($\mathbf{z}(t)$). RMS values could be calculated in two ways: numerical integration of the transfer functions describing the PSD (Power Spectral Density), through a steady state covariance analysis which involves solution of Lyapunov equations.

4.2.2.2 *Determining RMS outputs via numerical integration*

RMS acceleration in a given frequency band can be calculated by numerically integrating the power-spectral density function over the desired range of frequencies:

$$(z)_{rms} = \left\{\int_{\omega_l}^{\omega_u} S_z(\omega)\,d\omega\right\}^{\frac{1}{2}} \tag{4.2.16}$$

Since the time-varying output is driven by two random inputs (guideway and wind), the RMS response to each input is calculated separately. (Although not explicitly described here, the system response to guideway disturbances in the vertical, lateral, and roll directions were computed individually, and then root sum squared. This was done to insure that there would be no phase correlation between these inputs.) The two results are combined to yield the total RMS system output:

$$(z)_{rms} = \sqrt{(z_g)^2_{rms} + (z_w)^2_{rms}} \qquad (4.2.17)$$

These components are given by:

$$\Phi_{z_g} = |G_g(j\omega)|^2 \Phi_{\xi_g}(\omega) \qquad (4.2.18)$$

$$\Phi_{z_w} = |G_w(j\omega)|^2 \Phi_{\xi_w}(\omega) \qquad (4.2.19)$$

where

$$G_g(j\omega) = C(j\omega I - A)^{-1} B_g + D_g \qquad (4.2.20)$$

$$G_w(j\omega) = C(j\omega I - A)^{-1} B_w + D_w \qquad (4.2.21)$$

and the input in each case is white noise:

$$\Phi_{\xi_g} = \Phi_{\xi_w} = 1 \qquad (4.2.22)$$

Integrating the PSD from 0 to infinity (or some frequency range that captures all the system's dynamics) yields the total RMS of the system outputs.

Note that if we use the form of the system that has wind and guideway positions as inputs, we can input the wind and guideway PSDs directly. The result of the RMS calculations is identical to results of the procedure described above, except that an exact description of the guideway time delay can be used:

$$\Phi_{z_g} = |G_{g1}(j\omega) + G_{g2}(j\omega)e^{-j\omega\tau}|^2 \Phi_g(\omega) \qquad (4.2.23)$$

By comparing RMS calculations from this representation to that which employs the Pade approximation of the time delay, the accuracy of the Pade approximation can be determined. We found no significant loss of accuracy in RMS calculations when a 10th order Pade approximation is used. Once again, the Pade approximation was not used in this analysis. It is mentioned only for completeness of the description of the model.

4.2.2.3 Determining RMS outputs analytically

Although generally the most accurate method, calculating RMS values via numerical integration of PSDs requires relatively large amounts of computation time. An alternate procedure is to calculate output covariances analytically via the solution of an appropriate

Lyapunov equation. This method requires much less computation than integration of PSDs, but necessitates a vehicle description in the form of a linear system driven by white noise.

For the linear system driven by white noise:

$$\dot{\mathbf{x}} = \mathbf{A}\mathbf{x} + \mathbf{B}_d \xi \tag{4.2.24}$$

$$\mathbf{z} = \mathbf{C}\mathbf{x} \tag{4.2.25}$$

the state covariance obeys the equation:

$$\dot{\Sigma}_{xx} = \mathbf{A}\Sigma_{xx} + \Sigma_{xx}\mathbf{A}^T + \mathbf{B}_d \Xi_{\xi\xi} \mathbf{B}_d^T \tag{4.2.26}$$

$$\Xi_{\xi\xi} = \mathbf{I} \tag{4.2.27}$$

where

$\Xi_{\xi\xi}$ = intensity matrix for the white noise inputs

Σ_{xx} = covariance matrix for the state vector $\mathbf{x}$

In steady-state, the covariance equation becomes:

$$0 = \mathbf{A}\Sigma_{xx} + \Sigma_{xx}\mathbf{A}^T + \mathbf{B}_d \mathbf{B}_d^T \tag{4.2.28}$$

which is a Lyapunov equation that can be solved for Σ_{xx}. The output covariance matrix, in terms of the state covariance matrix, is:

$$\Sigma_{zz} = \mathbf{C}\Sigma_{xx}\mathbf{C}^T \tag{4.2.29}$$

The RMS components of the output vector (z) is the square-root of the terms along the diagonal of Σ_{yy}.

The results obtained from both a Lyapunov analysis and direct integration of the PSDs were compared to verify the software tools developed for this research. Results can be obtained via either method; however, a covariance analysis was performed, both because it is guaranteed to be accurate[14], and because it is much faster on a computer.

---

[14] The accuracy of numerical integration is dependent on the frequency interval chosen, while solution of a lyaponov equation yields directly the state covariance.

4.3. Control Law Description

4.3.1 Background

Active control was applied to the vehicle through the use of so-called Linear Quadratic Optimal Control methods, using full state feedback. The suspension design criteria for the active system remain the same: minimize passenger accelerations without exceeding limits on air gap variations and secondary suspension strokes. The active suspension must meet these goals while maintaining reasonable actuator requirements.

In deriving the control law, we begin with the appropriate equations from Sub-Section 10 of Section 4.1:

$$\dot{\mathbf{x}} = \mathbf{T}\mathbf{A}\mathbf{T}^{-1}\mathbf{x} + \mathbf{T}\mathbf{B}_u\mathbf{u} + \mathbf{T}\mathbf{B}_d\xi_g + \mathbf{T}\mathbf{L}\begin{bmatrix} V_{wind}(t) \\ \frac{\rho V^2}{2} A_t C_{y\beta}(\beta_0) \end{bmatrix} \qquad (4.3.1)$$

$$\mathbf{z} = \mathbf{C}\,\mathbf{T}^{-1}\mathbf{x} + \mathbf{D}_u\mathbf{u} + \mathbf{D}_d\begin{bmatrix} V_{wind}(t) \\ \frac{\rho V^2}{2} A_t C_{y\beta}(\beta_0) \end{bmatrix} \qquad (4.3.2)$$

Because, under this study, we use the same control law for all wind conditions, it is appropriate to linearize the equations describing these conditions about the steady state side slip angle. In addition, since the time-varying wind ($V_{wind}(t)$) cannot be measured, it is excluded from the state vector for feedback purposes. The resultant system model used for designing the control law (the so-called "design plant model") is:

$$\dot{\mathbf{x}} = \mathbf{T}\mathbf{A}\mathbf{T}^{-1}\mathbf{x} + \mathbf{T}\mathbf{B}_u\mathbf{u} + \mathbf{T}\mathbf{B}_d\xi_g \qquad (4.3.3)$$

$$\mathbf{z} = \mathbf{C}\,\mathbf{T}^{-1}\mathbf{x} + \mathbf{D}_u\mathbf{u} \qquad (4.3.4)$$

4.3.2 Control Law Derivation

To apply state-feedback optimal control, three key assumptions must be made.

1) All of the model states[15] are available for feedback. (This assumes we can make noise-free measurements of all the model states.)

2) The system $[\mathbf{A}, \mathbf{B}_\mathbf{u}]$ is stabilizable. That is, all unstable modes of the system are controllable. Our system is open-loop stable, so this criteria is met.

3) The system $[\mathbf{A}, \mathbf{B}_\mathbf{u}]$ is detectable. That is, all unstable modes of the system are observable in the output. Again, since our system is open loop stable, this criteria is met.

Making these assumptions, we now apply so-called Linear Quadratic Optimal Control Theory to obtain a control law. The result is a control law for the system of the form:

$$\mathbf{u} = -\mathbf{G}\,\mathbf{x} \tag{4.3.5}$$

The gain matrix $\mathbf{G}$ is selected to minimize a quadratic cost function that includes both the performance variables of interest and the control effort, thereby giving an "optimum" trade-off between the actuator effort and the performance of the system. The cost function that is minimized is:

$$J = \lim_{T \to \infty} E\left\{ \int_0^T \left(\mathbf{z}(t)^T \mathbf{Q}\,\mathbf{z}(t) + \mathbf{u}(t)^T \mathbf{R}\,\mathbf{u}(t) \right) dt \right\} \tag{4.3.6}$$

where $\mathbf{Q}$ is a weighting matrix used to vary the relative importance of the system outputs and $\mathbf{R}$ is a weighting matrix applied to ensure that the gain matrix yields reasonable controls ($\mathbf{u}$). $\mathbf{z}$(t), the time varying portion of the performance variables, is described by:

$$\mathbf{z}(t) = \mathbf{C}\,\mathbf{x}(t) + \mathbf{D}_\mathrm{u}\,\mathbf{u}(t) \tag{4.3.7}$$

Thus, the cost function to be minimized becomes:

$$J = \lim_{T \to \infty} E\left\{ \int_0^T \left(\mathbf{x}(t)^T \mathbf{C}^T \mathbf{Q}\mathbf{C}\mathbf{x}(t) + 2\mathbf{x}(t)^T \mathbf{C}^T \mathbf{Q}\mathbf{D}_u \mathbf{u}(t) + \mathbf{u}(t)^T \left(\mathbf{D}_u{}^T \mathbf{Q}\mathbf{D}_u + \mathbf{R} \right) \mathbf{u}(t) \right) dt \right\} \tag{4.3.8}$$

The gain matrix $\mathbf{G}$ that minimizes this cost function is described by:

---

[15] The states in the design plant include the primary and secondary suspension gaps and the absolute velocities of the train and bogies. The wind model is not included, so wind measurements are not assumed available.

$$G = R^{-1}\left[D_u^T QC + B_u^T K\right] \tag{4.3.9}$$

with **K** determined from the solution to the following algebraic Riccati equation:

$$0 = \mathbf{KA} + \mathbf{A}^T \mathbf{K} + \mathbf{C}^T\mathbf{QC} - [\mathbf{KB}_u + \mathbf{C}^T \mathbf{QD}_u]\, \mathbf{R}^{-1} [\mathbf{B}_u{}^T \mathbf{K} + \mathbf{D}_u \mathbf{QC}] \tag{4.3.10}$$

Because of the use of output weighting, the normal robustness associated with LQR designs does not apply

4.3.3 Choice of Weights in Cost Function

The choice of the weighting matrices (**Q**, **R**) in the cost functional determines the relative performance of the system in terms of the output variables and the control effort. The weights were chosen with emphasis on the Pepler index, which includes the vertical and lateral accelerations and the roll rate. This minimization was performed while maintaining acceptable air gap variations and secondary suspension strokes.

Six different suspension systems were developed and compared. The first was an optimized passive system (the choice of suspension parameters is described in detail in Section 4.4). Active control was then applied to this optimized passive suspension, which served as a baseline for comparison with the active systems. The optimal control law described above was then applied to five different types of actuator configurations.

- a system with an active secondary suspension (hydraulic actuators acting between the bogie and the train).
- a system with a passive secondary and active aerodynamic flaps on the train.
- a system with both an active secondary and aerosurfaces on the train.
- a system with a passive secondary and active ground-effect flaps on the bogie.
- a system with both an active secondary and ground-effect flaps on the bogie.

The normal limits imposed on the air gap variations and secondary suspension strokes are described in Section 4.2.

The exception to the rule is the case of the aero-surfaces acting in ground-effect. In this case, the air gap variations were penalized more severely because the amount of controllable force available from the flaps is dependent on the nominal air gap minus five times the RMS air gap variations (*i.e.*, the available control angle before contact with the guideway occurs). If the subsequent gap is small, a large force might still be produced with a very small angular deflection of the flap, but it is difficult to accurately model this force in such a manner that it can be easily controlled (particularly not with a linear control system, as the equations are highly non-linear). The reason for this is simply that the control angle is the input that describes the forces (due to the ground-effect flaps) that are controllable. The forces due to the air gap are modeled as a linear stiffness in the primary suspension, as described in Section 4.1.7.2. Therefore, the air gap variations were limited (by penalizing them more severely) so that the control angle was as large as possible, while keeping in mind that there is a diminishing rate of return on reducing the airgap variations. (The angle of attack cannot be larger than the angle which would lead to contact with the guideway from the flap.) This trade-off was imposed manually by the engineer designing the control laws for the flaps.

4.3.4 Active Suspension Design Trade-offs

The use of optimal control laws in the implementation of an active secondary system using hydraulic actuators assures an optimum trade-off (in a linear quadratic sense) between the ride comfort and the suspension displacements. This was achieved by making the control weighting matrix R small compared to the performance variable weighting matrix Q, so that the cost functional would be dominated by the performance variables. This allowed the air gap variations and secondary suspension stroke lengths to be traded off against passenger accelerations.

Thus, no limitations were imposed on the forces applicable by the hydraulic actuators except to verify that the forces of the final system were obtainable with currently available hydraulic systems. Nevertheless, there is still a fundamental limitation in system performance because any force exerted on the train by the hydraulic actuator in an attempt to reduce passenger accelerations will also act on the bogie, tending to decrease the primary air gap. In the case of the aero-surfaces, a limitation on the available control force was imposed by limiting the RMS value of the flap or wing angle, having sized these actuators as described in Appendix A.

The primary advantage of the active aerodynamic surfaces mounted on the train is that forces can be applied between the train and an inertial reference frame. Thus, the forces act directly on the train, but do not directly act on the bogies. Because of this, passenger accelerations can be reduced with no deleterious effects on air gap variations. Crosswind forces that act on the train can be directly canceled, as can forces from the secondary suspension elements, whether passive or active, that are exerted on the train. This effectively allows the train to act as though it has more mass, thus emulating a system with a lower unsprung mass to total mass ratio, which results in both improved guideway tracking and reduced passenger accelerations.

The ground-effect flaps also exert forces with respect to an inertial reference frame. However, it is more advantageous to apply the forces directly to the train, rather than to the bogies, since it is primarily train accelerations that one wishes to minimize. When the aero-surfaces are mounted directly on the bogies, the guideway disturbances transmitted to the train can only be reduced by exerting a force directly on the bogie, which uses up additional air gap. Additionally, since the force produced by the ground-effect surfaces is partially dependent on the air gap itself, guideway irregularities transmit disturbances to the bogies through these aero-surfaces. This effect is captured in the model.

These trade-offs are reflected in the data in Section 4.5.

4.4. Optimization of Passive Suspension

4.4.1 Objective

The function of a secondary suspension system on a maglev vehicle is to provide good ride quality for the passengers while preventing vehicle touchdown on the guideway and keeping the secondary suspension stroke within practical limitations. There is also a trade-off between the primary and secondary suspension stiffnesses, which can be dependent on each other. There is generally a conflict between ride quality and guideway tracking in the choice of the primary suspension stiffnesses, since a stiffer primary suspension generally provides better tracking of the guideway, but at the expense of a larger transmission of guideway disturbances through to the passenger compartment. This is also a factor in the choice of the secondary suspension stiffness.

Also, a maglev vehicle must have both a lateral and vertical suspension. The guideway irregularities will be comparable in magnitude in both directions, since they are largely dependent on the accuracy of the alignment of the guideway's coils, and this alignment is not expected to be better in one direction than in another. In addition, the suspension must be designed to isolate passengers from crosswind disturbances as well as guideway irregularities. The aerodynamic effects on high speed vehicles are larger than those on slower vehicles because the higher speed results in a larger dynamic pressure, which is the driving factor in determining the crosswind disturbance force magnitude. There is a trade-off between the secondary suspension stiffness and the effects of the crosswinds and guideway disturbances. A stiffer suspension reduces the roll and yaw angles due to crosswinds, but again also increases the transmission of guideway position disturbances to the passengers.

The choice of primary suspension parameters used here is somewhat arbitrary, but values were chosen that are in the range expected for maglev vehicles. The vertical primary suspension natural frequency was set at 5 Hz, a value which is reasonable for an EDS (Electro Dynamic Suspension) system. It was less clear what the lateral primary suspension natural frequency should be, so it was chosen to be 3 Hz, a value which insures that the lateral accelerations, air gap variations, and secondary suspension strokes would all be minimized. With the primary suspension stiffnesses thus defined, we may proceed to optimizing the passive secondary suspension.

4.4.2 Choice of Parameters

The values chosen for the secondary suspension parameters are:

Vertical Natural Frequency = 0.8 Hz
Vertical Damping Ratio = 0.08
Lateral Natural Frequency = 1.2 Hz
Lateral Damping Ratio = 0.2
Swaybar Stiffness = 0 N-m/rad
Independent Roll Damping = 1.5e5 N-m-s/rad

These parameters will be further defined in the following text.

The plots in this section will be referenced in the following explanation for the choice of these suspension parameters. As shown in Figure 4.4.1, the vertical RMS accelerations increase as the vertical secondary suspension natural frequency increases. Thus, barring other factors, we would like the secondary suspension's vertical frequency as low as possible. However, we are limited in this by the vertical air gap variations, which decrease as the secondary frequency is increased (at least to a point). The secondary suspension stroke also decreases as the secondary frequency is increased, but levels out after about 1 Hz. The value chosen as the optimum trade-off point was 0.8 Hz, because at this point, the air gap variations are acceptably low, given the available air gap in most EDS systems (10 cm is assumed for this work). The maximum available air gap variation is not needed to operate with a 0.8 Hz suspension frequency, thus allowing for some variation in the frequency without driving the air gap to zero. This extra margin, which grants the design more robustness, was desired because the slope of the curve of the airgap variations versus secondary suspension frequency is fairly steep at that portion of the curve. Also, the secondary suspension stroke increases rapidly as the frequency is decreased below this value.

Next, the vertical secondary suspension's damping ratio must be chosen. This ratio is chosen to be 0.08 solely in the interest of minimizing the vertical accelerations. We are willing to accept the larger air gap variations and secondary suspension stroke requirements, since both are within acceptable limits at this point.

A similar trade-off among the various parameters applies in the lateral direction. More importance has been attached to the air gap in this direction, however, since crosswind gusts could potentially use up more of this gap. A lateral secondary suspension natural frequency of 1.2 Hz was chosen.

For the lateral damping ratio, the same criterion used in the vertical direction was applied: lateral accelerations were minimized at all costs. Thus the damping ratio was chosen to be 0.2.

It was next investigated whether or not to include additional roll stiffness and/or damping, since otherwise the primary stiffness and damping in roll depend mainly on the vertical stiffness and lateral distance between the vertical suspension elements. It was determined that there was no advantage to using a swaybar to add roll stiffness, so no swaybar was added. A swaybar is a device which increases the roll stiffness above the roll stiffness that results from the vertical and/or lateral suspension actuators. In contrast, it was found that increasing the roll damping could reduce the lateral accelerations, roll rate, and roll acceleration, which in turn affects both the vertical and lateral accelerations. A value for this "dampbar" of 1.5e5 N-m-s/rad was chosen to be the best trade-off between these parameters, primarily because this value minimizes the Peplar index.

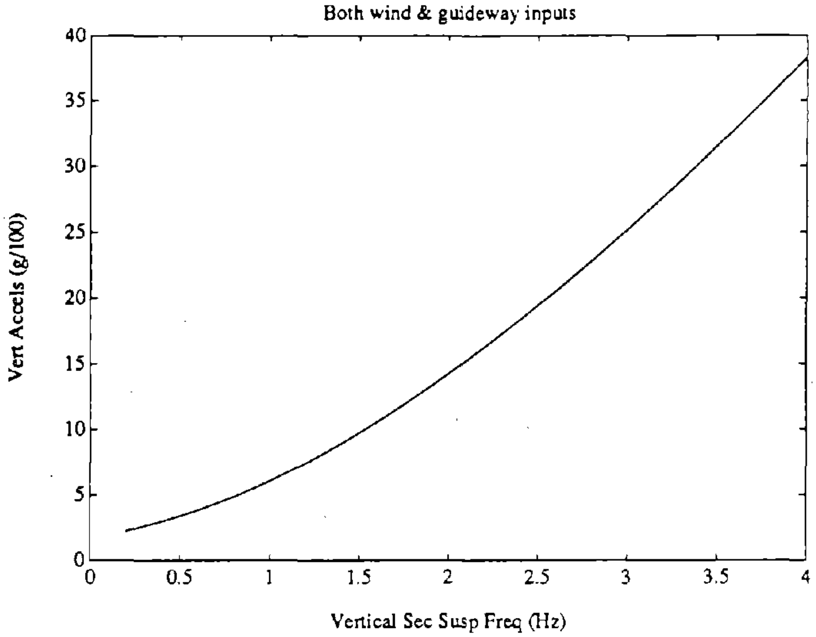

Figure 4.4.1 - Effect of vertical secondary suspension natural frequency on vertical accelerations

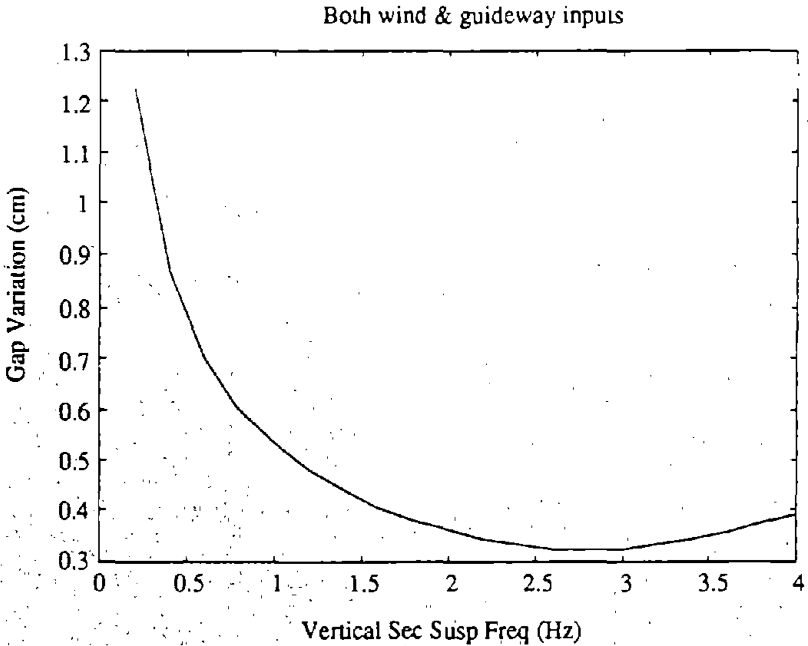

Figure 4.4.2 - Effect of vertical secondary suspension natural frequency on vertical air gap variations

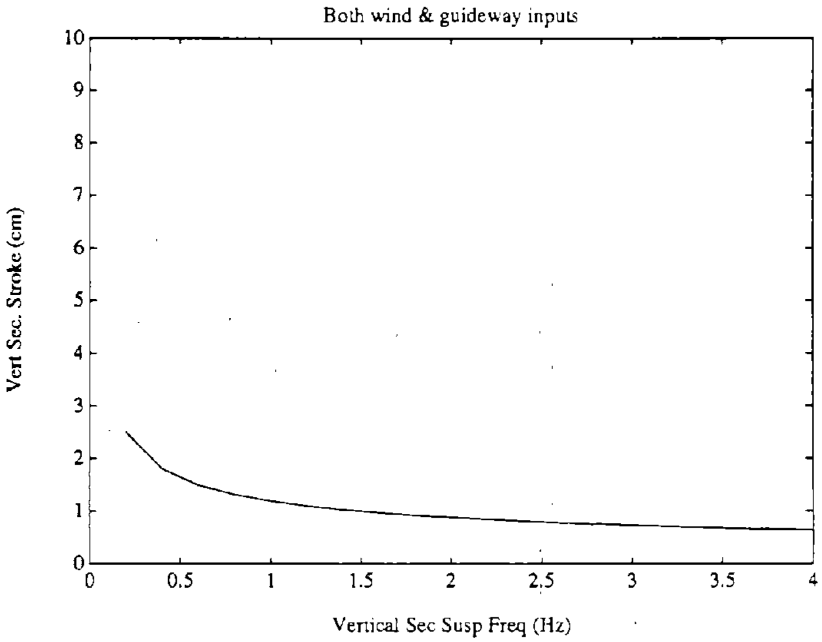

Figure 4.4.3 - Effect of vertical secondary suspension natural frequency on vertical secondary suspension strokes

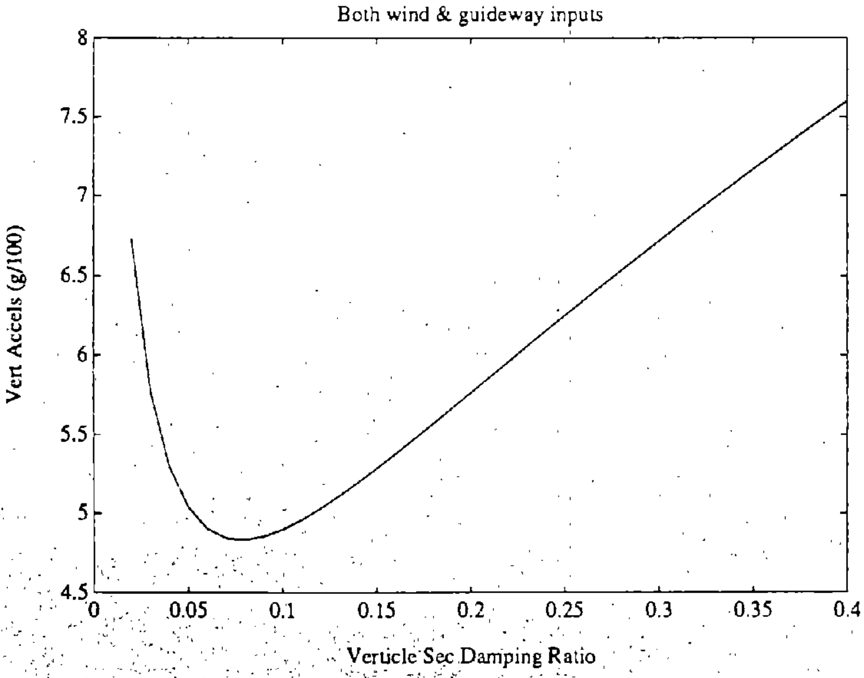

Figure 4.4.4 - Effect of vertical secondary suspension damping ratio on vertical accelerations

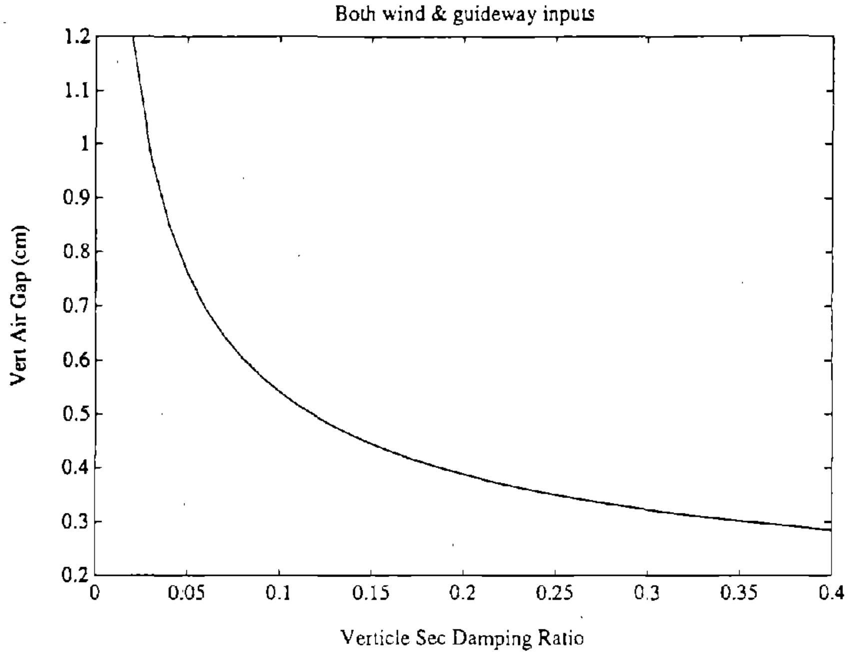

Figure 4.4.5 - Effect of vertical secondary suspension damping ratio on vertical air gap variations

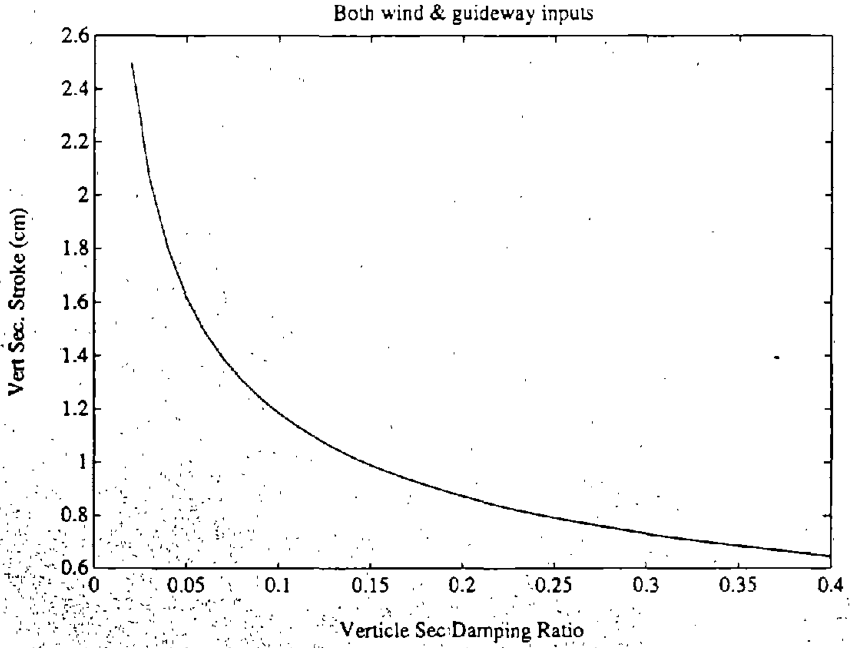

Figure 4.4.6 - Effect of vertical secondary suspension damping ratio on vertical secondary suspension strokes

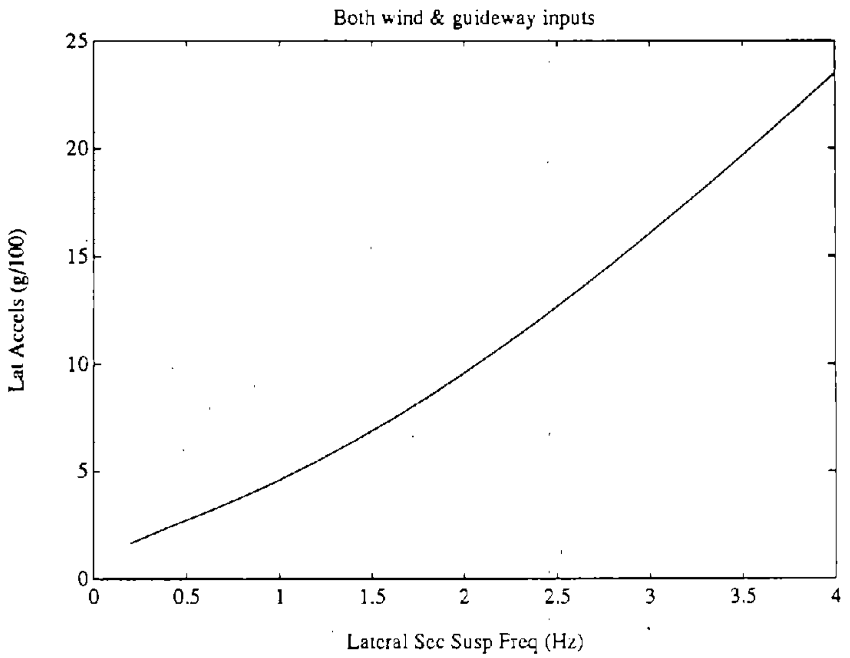

Figure 4.4.7 - Effect of lateral secondary suspension natural frequency on lateral accelerations

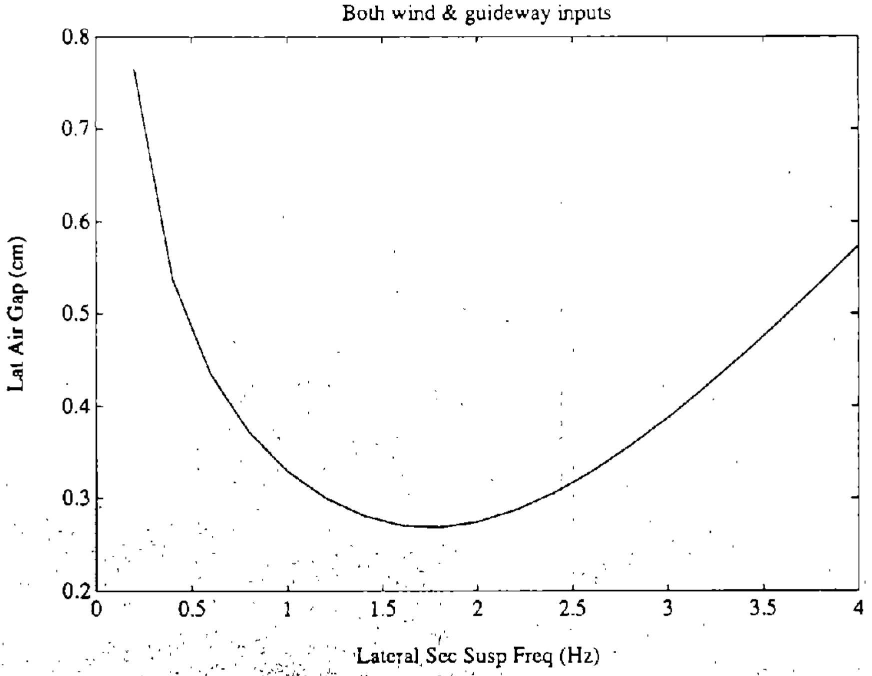

Figure 4.4.8 - Effect of lateral secondary suspension natural frequency on lateral air gap variations

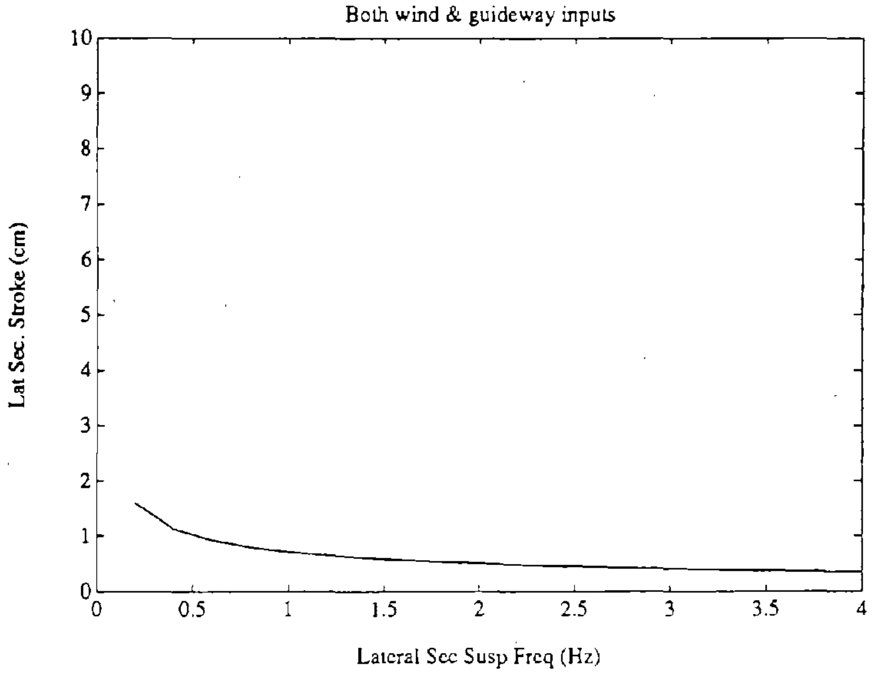

Figure 4.4.9 - Effect of lateral secondary suspension natural frequency on lateral secondary suspension strokes

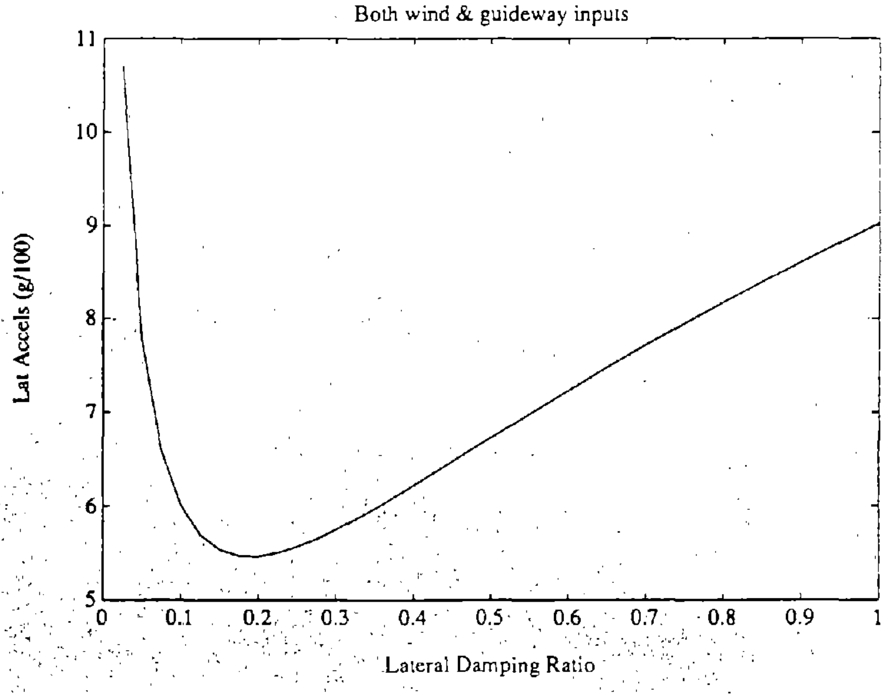

Figure 4.4.10 - Effect of lateral secondary suspension damping ratio on lateral accelerations

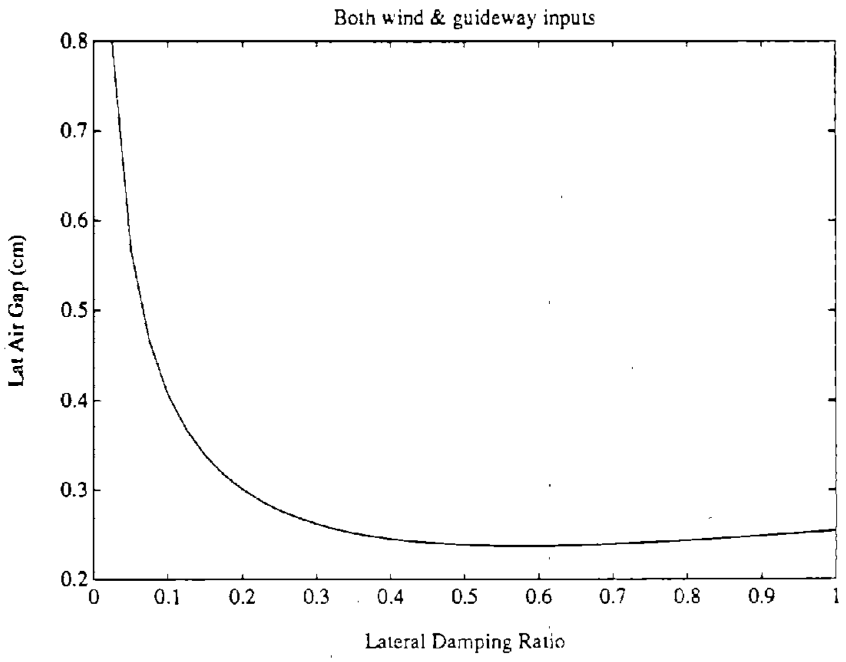

Figure 4.4.11 - Effect of lateral secondary suspension damping ratio on lateral air gap variations

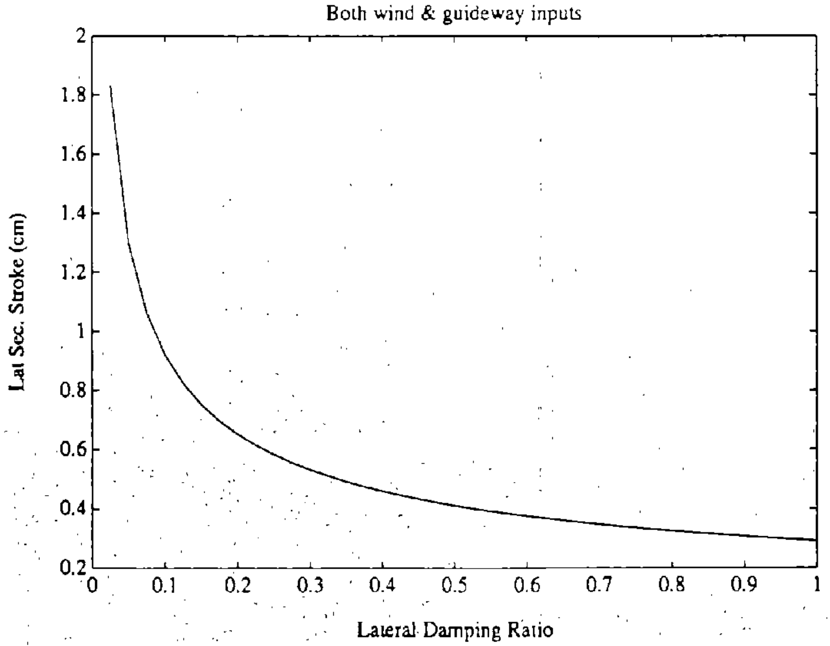

Figure 4.4.12 - Effect of lateral secondary suspension damping ratio on lateral secondary suspension strokes

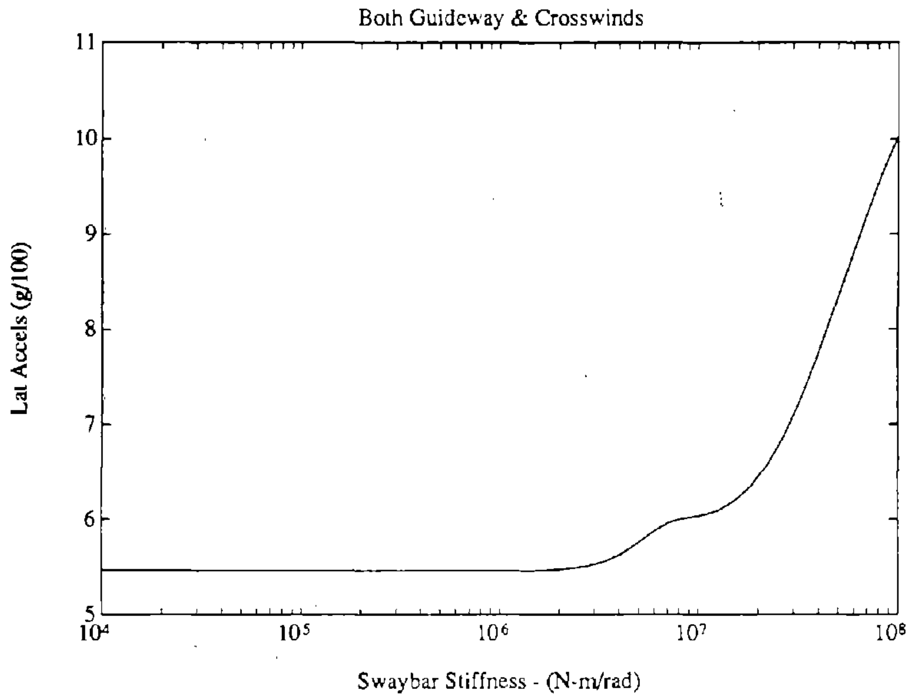

Figure 4.4.13 - Effect of auxiliary roll stiffness on lateral accelerations

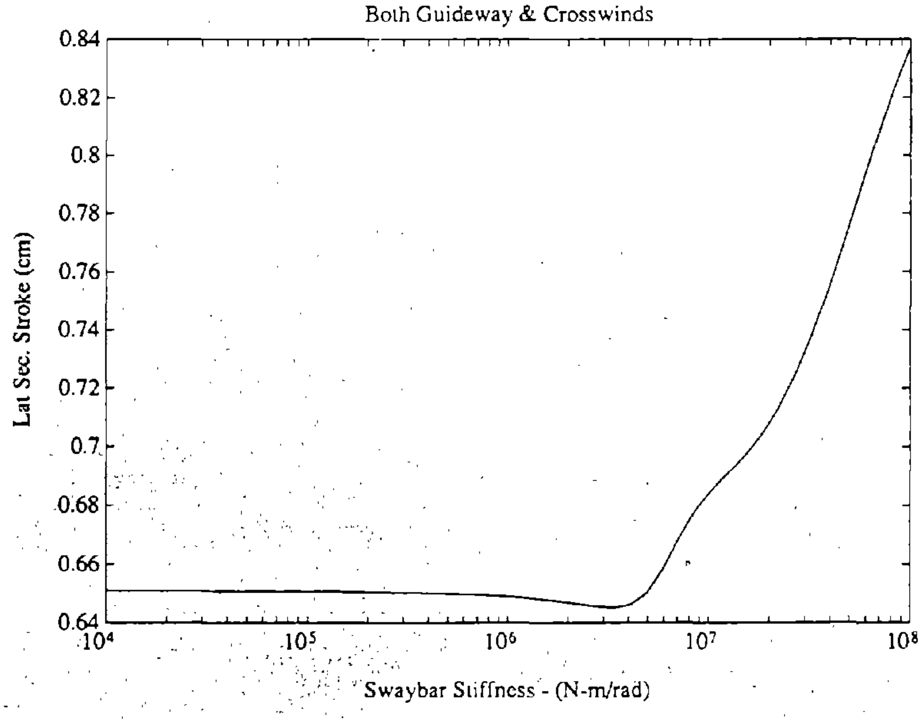

Figure 4.4.14 - Effect of auxiliary roll stiffness on lateral secondary suspension strokes

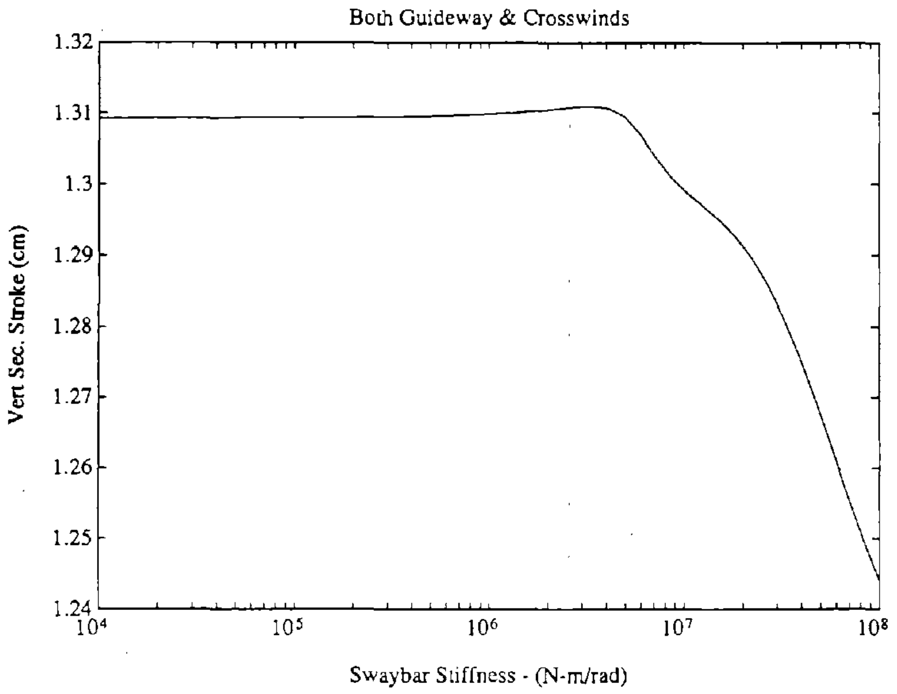

Figure 4.4.15 - Effect of auxiliary roll stiffness on vertical suspension stroke

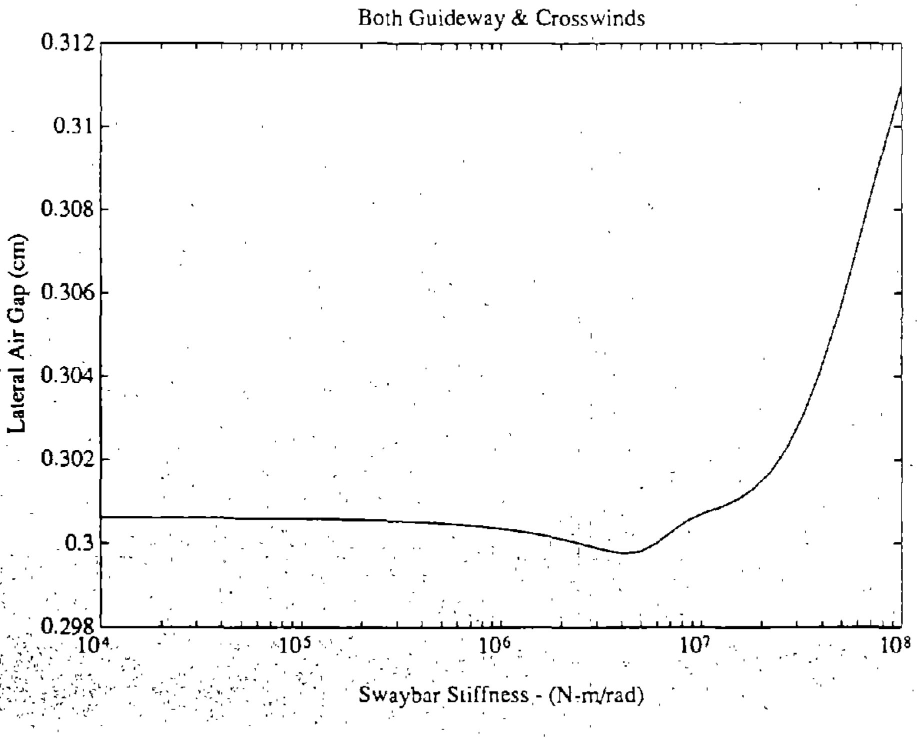

Figure 4.4.16 - Effect of auxiliary roll stiffness on lateral air gap variations

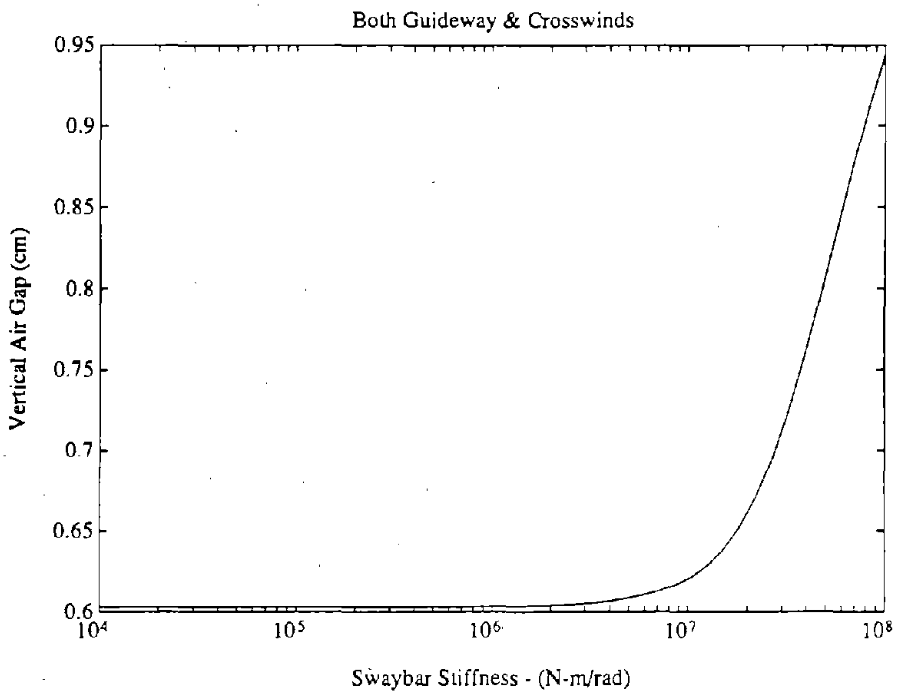

Figure 4.4.17 - Effect of auxiliary roll stiffness on vertical air gap variations

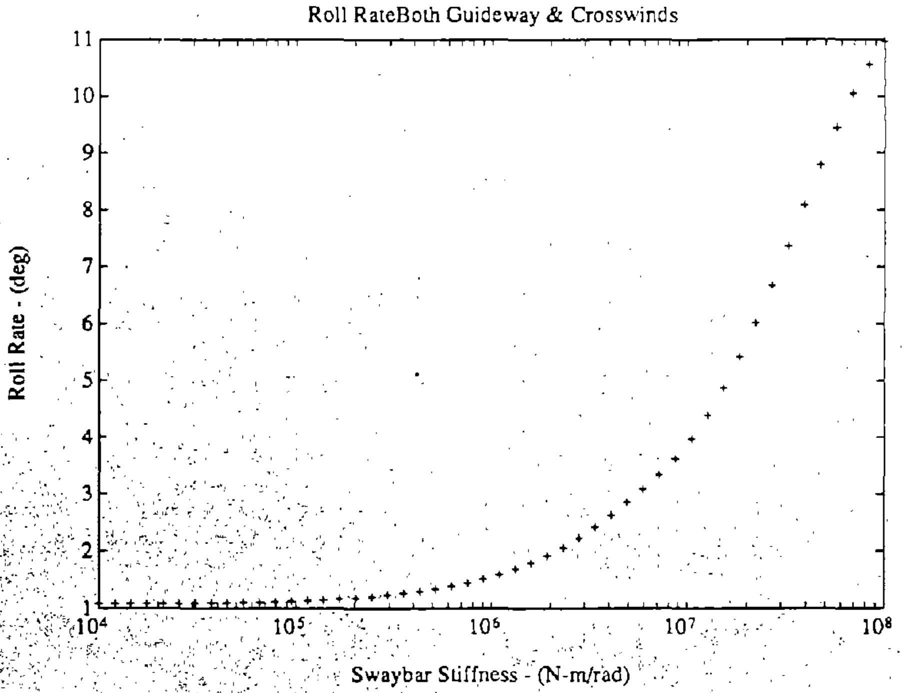

Figure 4.4.18 - Effect of auxiliary roll stiffness on roll rate

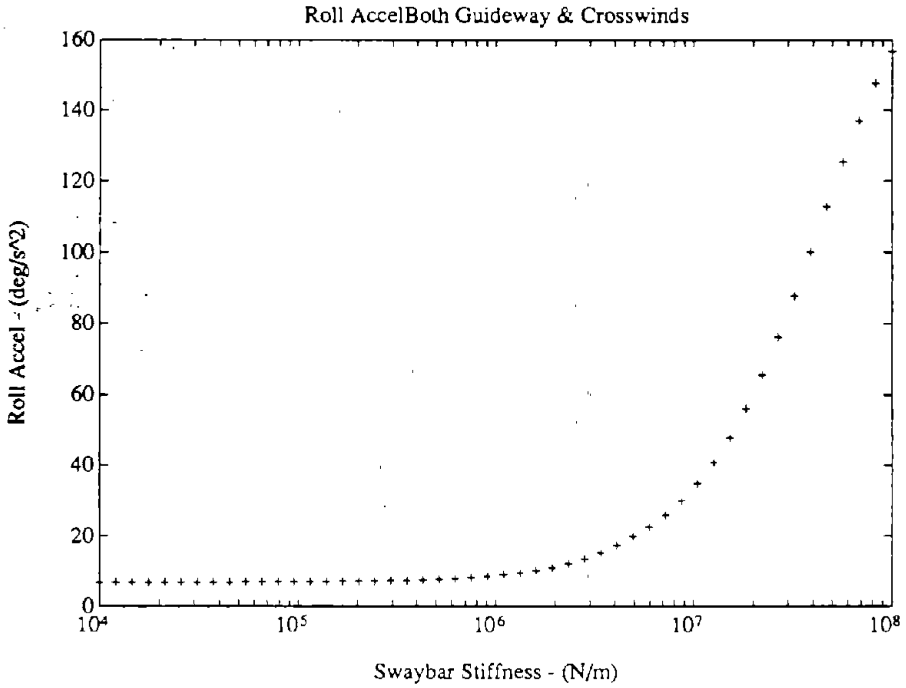

Figure 4.4.19 - Effect of auxiliary roll stiffness on roll accelerations

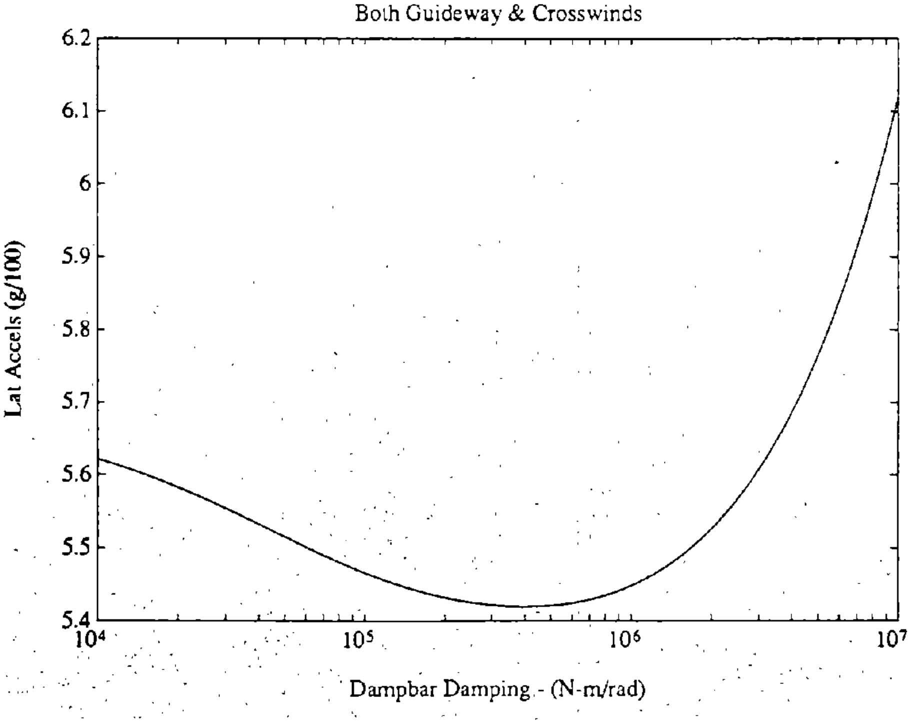

Figure 4.4.20 - Effect of auxiliary roll damping on lateral accelerations

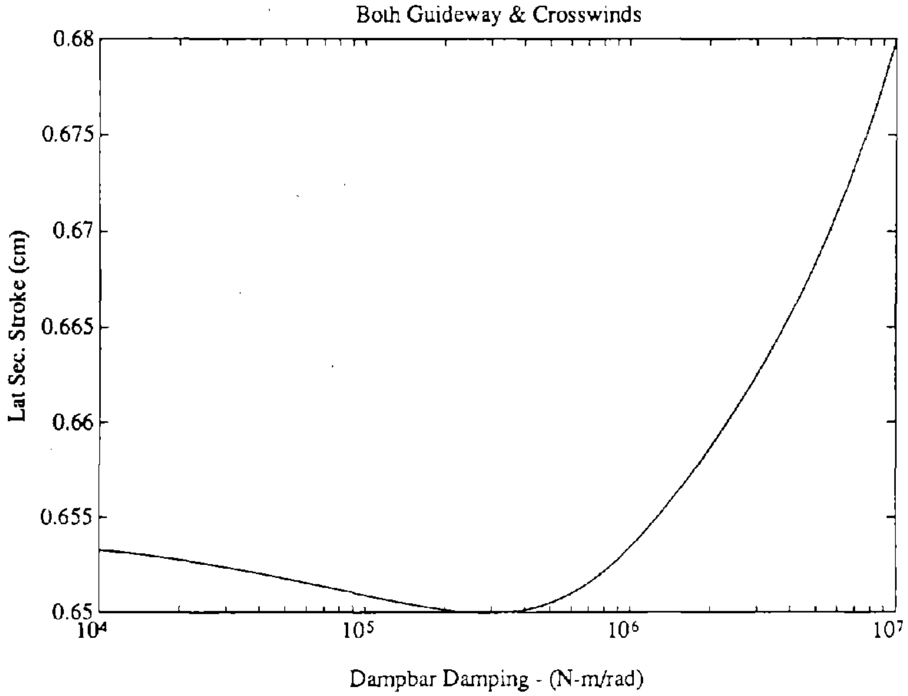

Figure 4.4.21 - Effect of auxiliary roll damping on lateral secondary suspension stroke

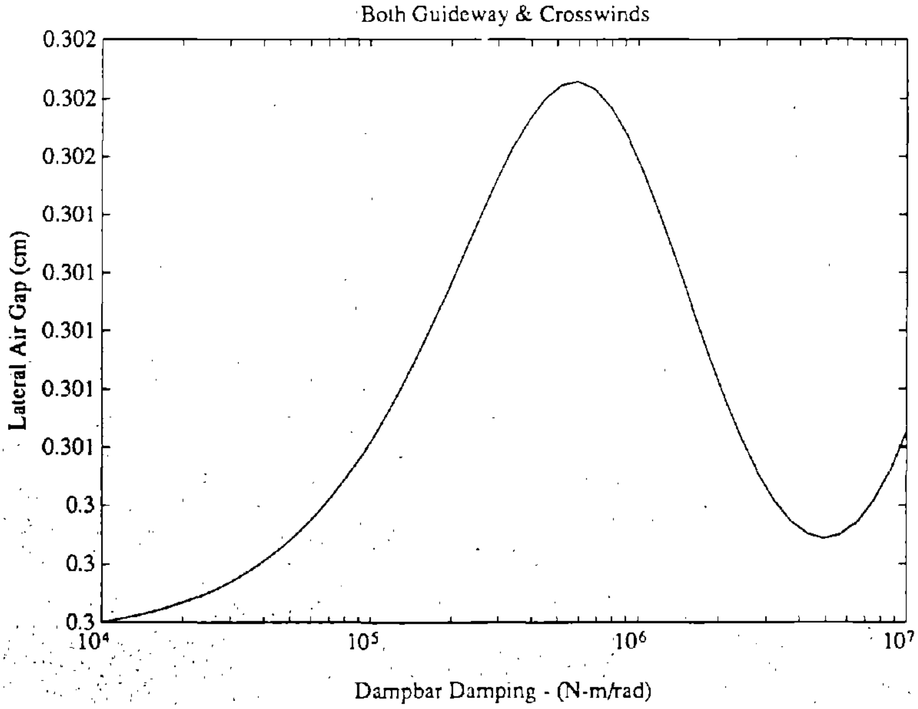

Figure 4.4.22 - Effect of auxiliary roll damping on lateral air gap variations

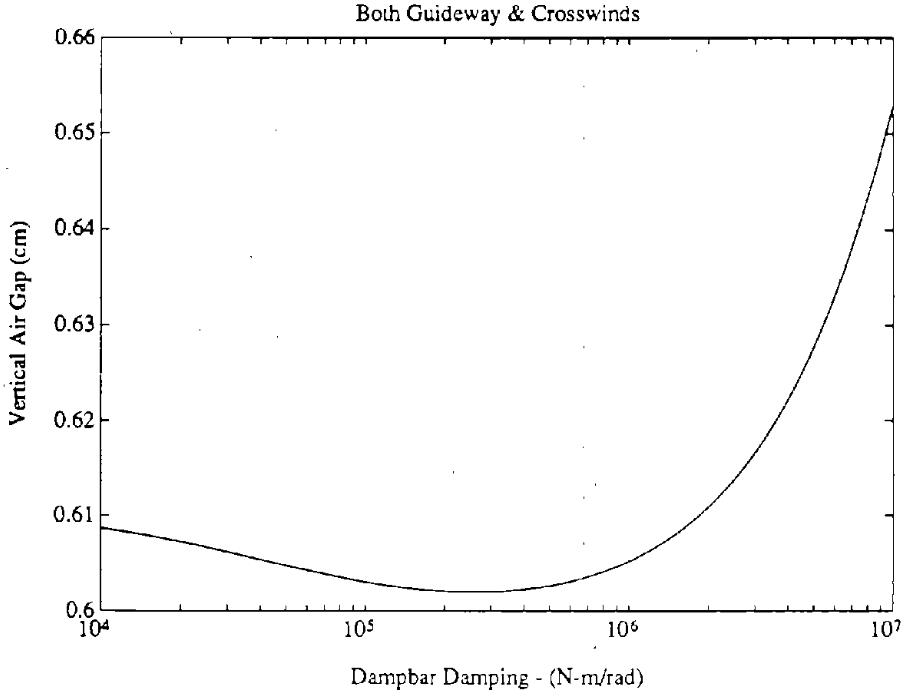

Figure 4.4.23 - Effect of auxiliary roll damping on vertical air gap variations

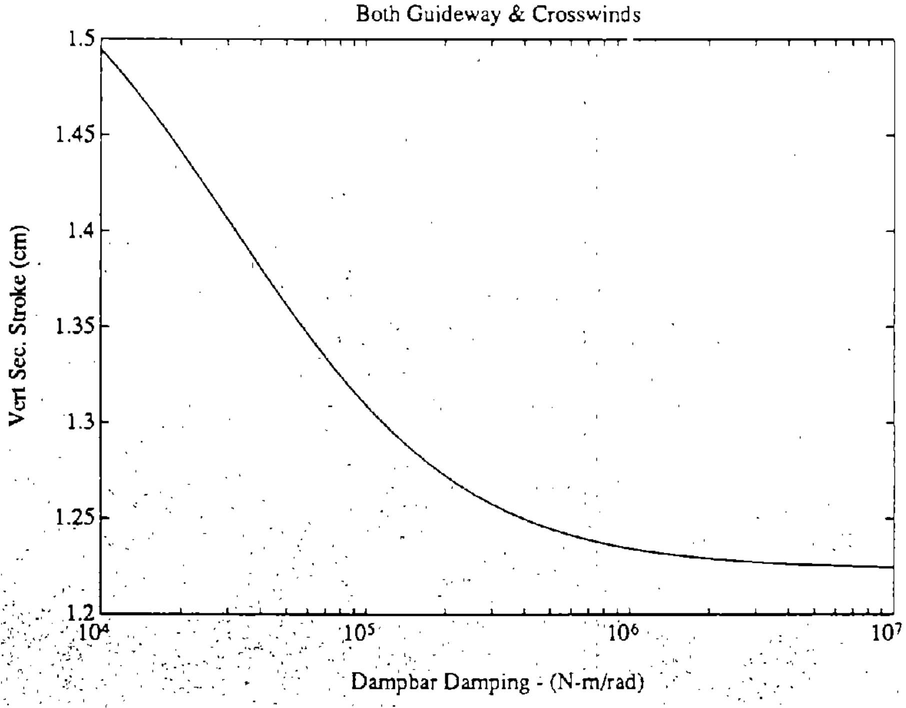

Figure 4.4.24 - Effect of auxiliary roll damping on vertical secondary suspension stroke

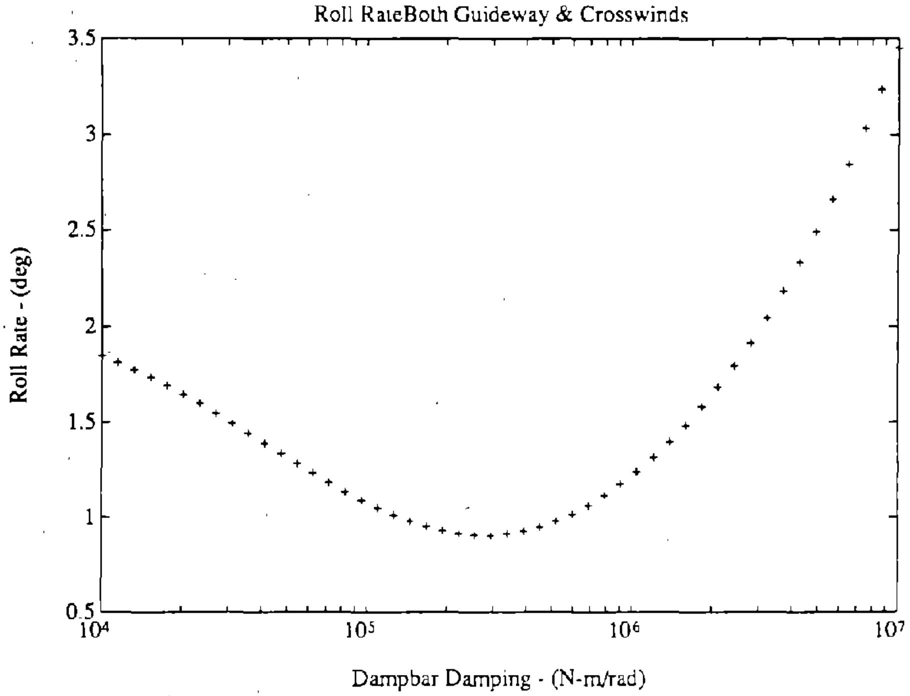

Figure 4.4.25 - Effect of auxiliary roll damping on roll rate

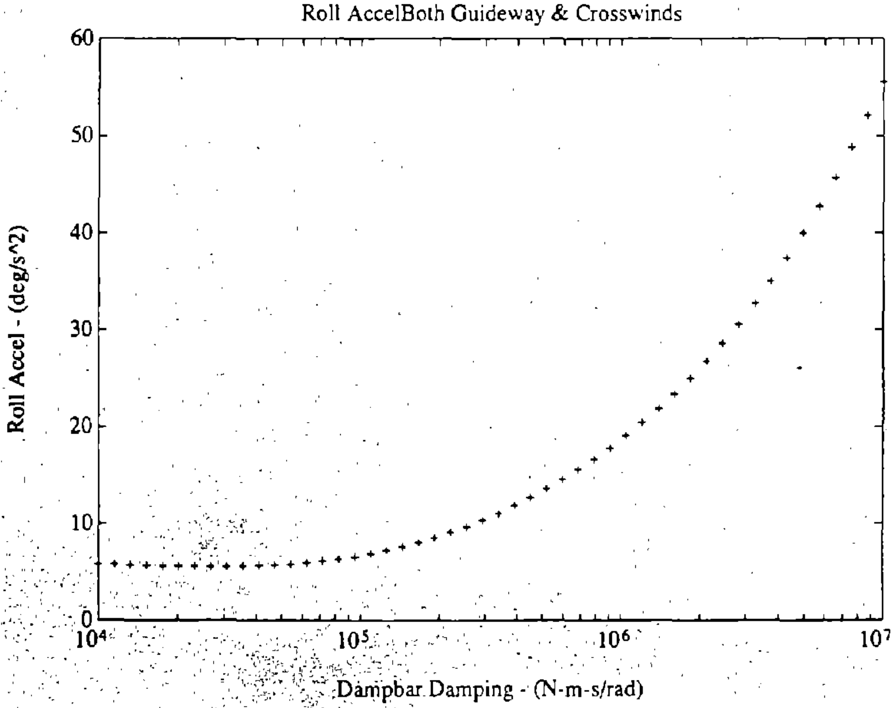

Figure 4.4.26 - Effect of auxiliary roll damping on roll accelerations

4.5. Results and Conclusions

The secondary suspension strokes and airgap variations in the vertical and lateral directions include the roll effects assuming that the farthest edge of the bogie that might contact either the guideway or the train is at the same location that the force of the primary or secondary suspension acts at. RMS output data for a vehicle speed of 100 m/s can be found in Appendix C.

The aerosurfaces in ground-effect are mounted on the bogies, while the aerodynamic wing surfaces are mounted on the train.

4.5.1 A Word on Nominal Air Gap

These results are for a roughness parameter A_r corresponding to welded steel rail. However, the results scale linearly with the square root of A_r, and therefore can be adjusted to account for a different guideway roughness. Using a rougher guideway to increase the air gap variations until all of the available nominal gap is utilized will also have the effect of increasing both the train accelerations and the secondary suspension strokes. Because of this, there is no direct benefit with a passive suspension in having a larger nominal air gap than what is needed to provide adequate clearance for the expected air gap variations. However, an active system can take advantage of a larger nominal airgap by using it up to improve ride quality, provided that this is the limiting factor in reducing train accelerations. (In some cases it may be the secondary suspension stroke length, rather than the air gap variation, which limits reductions of accelerations.)

4.5.1.1 RMS Outputs, Ground-Effect Surfaces on Bogies

Table 4.5.1 - Aerosurfaces in ground-effect on bogies, vehicle velocity = 150 m/s

V = 150 m/s Welded Rail RMS Wind = 10 mph	Passive Secondary	Active Hydraulic Secondary	Active Ground-Effect Aerosurfaces	Active Aero & Hydraulic Secondary
Y RMS Train Accels				
Guideway	5.44 g/100	1.48 g/100	3.79 g/100	0.09 g/100
Crosswinds	3.74 g/100	0.19 g/100	3.04 g/100	0.07 g/100
Combined	6.60 g/100	1.50 g/100	4.86 g/100	0.12 g/100
Z RMS Train Accels				
Guideway	4.95 g/100	1.32 g/100	3.83 g/100	0.05 g/100
Crosswinds	0.34 g/100	0.05 g/100	0.09 g/100	0.01 g/100
Combined	4.96 g/100	1.32 g/100	3.83 g/100	0.05 g/100
Y Actuator Effort (RMS)				
Guideway	N/A	28.66 KN	N/A	28.55 KN
Crosswinds		14.45 KN		17.82 KN
Combined		32.09 KN		33.66 KN
Z Actuator Effort (RMS)				
Guideway	N/A	19.56 KN	N/A	11.18 KN
Crosswinds		0.00 KN		0.00 KN
Combined		19.56 KN		11.18 KN
Roll Actuator Effort (RMS)				
Guideway	N/A	44.37 KN-m	N/A	15.55 KN-m
Crosswinds		5.35 KN-m		0.58 KN-m
Combined		44.69 KN-m		15.56 KN-m
Peplar Ride Comfort Index No.				
Guideway	3.25	1.52	2.69	1.06
Crosswinds	1.89	1.09	1.58	1.03
Combined	3.49	1.54	2.87	1.07
Y Aerosurface Deflection				
Guideway	N/A	N/A	1.19 Deg	1.36 Deg
Crosswinds			0.74 Deg	0.84 Deg
Combined			1.40 Deg	1.60 Deg

Z Aerosurface Deflection				
Guideway	N/A	N/A	1.56 Deg	1.64 Deg
Crosswinds			0.24 Deg	0.08 Deg
Combined			1.58 Deg	1.64 Deg
Y RMS Air Gap Variation				
Guideway	0.3009 cm	0.7845 cm	0.2303 cm	0.2043 cm
Crosswinds	0.1408 cm	0.1525 cm	0.1216 cm	0.1149 cm
Combined	0.3322 cm	0.7992 cm	0.2605 cm	0.2344 cm
Z RMS Air Gap Variation				
Guideway	0.6024 cm	1.5666 cm	0.3337 cm	0.2322 cm
Crosswinds	0.0359 cm	0.0411 cm	0.0179 cm	0.0269 cm
Combined	0.6034 cm	1.5671 cm	0.3342 cm	0.2337 cm
Y RMS Sec. Stroke				
Guideway	0.6504 cm	1.4996 cm	0.4962 cm	2.1936 cm
Crosswinds	1.1350 cm	0.7524 cm	1.0807 cm	3.4557 cm
Combined	1.3081 cm	1.6778 cm	1.1891 cm	4.0931 cm
Z RMS Sec. Stroke				
Guideway	1.2858 cm	3.3456 cm	1.1542 cm	2.9947 cm
Crosswinds	0.2616 cm	0.7361 cm	0.0660 cm	0.2198 cm
Combined	1.3121 cm	3.4256 cm	1.1561 cm	3.0028 cm
Roll Rate (RMS)				
Guideway	1.00 deg/s	0.08 deg/s	0.78 deg/s	0.08 deg/s
Crosswinds	0.39 deg/s	0.10 deg/s	0.10 deg/s	0.03 deg/s
Combined	1.04 deg/s	0.13 deg/s	0.79 deg/s	0.09 deg/s

4.5.1.2 RMS Outputs, Wings on Train Body

Table 4.5.2 - Wings on train, vehicle velocity = 150 m/s

V = 150 m/s Welded Rail RMS Wind = 10 mph	Passive Secondary	Active Hydraulic Secondary	Active Aerosurfaces	Active Aero & Hydraulic Secondary
Y RMS Train Accels				
Guideway	5.44 g/100	1.48 g/100	5.33 g/100	1.00 g/100
Crosswinds	3.74 g/100	0.19 g/100	3.70 g/100	0.13 g/100
Combined	6.60 g/100	1.50 g/100	6.49 g/100	1.01 g/100

Z RMS Train Accels				
Guideway	4.95 g/100	1.32 g/100	0.07 g/100	0.06 g/100
Crosswinds	0.34 g/100	0.05 g/100	0.19 g/100	0.13 g/100
Combined	4.96 g/100	1.32 g/100	0.20 g/100	0.14 g/100
Y Actuator Effort (RMS)				
Guideway	N/A	28.66 KN	N/A	25.96 KN
Crosswinds		14.45 KN		12.70 KN
Combined		32.09 KN		28.90 KN
Z Actuator Effort (RMS)				
Guideway	N/A	19.56 KN	N/A	8.31 KN
Crosswinds		0.00 KN		0.00 KN
Combined		19.56 KN		8.31 KN
Roll Actuator Effort (RMS)				
Guideway	N/A	44.37 KN-m	N/A	51.29 KN-m
Crosswinds		5.35 KN-m		6.74 KN-m
Combined		44.69 KN-m		51.73 KN-m
Peplar Ride Comfort Index No.				
Guideway	3.25	1.52	1.95	1.22
Crosswinds	1.89	1.09	1.75	1.12
Combined	3.49	1.54	2.23	1.28
Aerosurface Deflection				
Guideway	N/A	N/A	5.0 Deg	7.9 Deg
Crosswinds			1.3 Deg	1.2 Deg
Combined			5.2 Deg	8.0 Deg
Y RMS Air Gap Variation				
Guideway	0.3009 cm	0.7845 cm	0.3008 cm	0.7789 cm
Crosswinds	0.1408 cm	0.1525 cm	0.1408 cm	0.1522 cm
Combined	0.3322 cm	0.7992 cm	0.3321 cm	0.7936 cm
Z RMS Air Gap Variation				
Guideway	0.6024 cm	1.5666 cm	0.6115 cm	0.8477 cm
Crosswinds	0.0359 cm	0.0411 cm	0.0461 cm	0.0427 cm
Combined	0.6034 cm	1.5671 cm	0.6133 cm	0.8488 cm
Y RMS Sec. Stroke				
Guideway	0.6504 cm	1.4996 cm	0.6502 cm	1.4168 cm
Crosswinds	1.1350 cm	0.7524 cm	1.1349 cm	0.3042 cm
Combined	1.3081 cm	1.6778 cm	1.3080 cm	1.4491 cm

Z RMS Sec. Stroke				
Guideway	1.2858 cm	3.3456 cm	3.3993 cm	3.1556 cm
Crosswinds	0.2616 cm	0.7361 cm	1.4714 cm	0.0457 cm
Combined	1.3121 cm	3.4256 cm	3.7041 cm	3.1559 cm
Roll Rate (RMS)				
Guideway	1.00 deg/s	0.08 deg/s	0.06 deg/s	0.07 deg/s
Crosswinds	0.39 deg/s	0.10 deg/s	0.18 deg/s	0.00 deg/s
Combined	1.04 deg/s	0.13 deg/s	0.19 deg/s	0.07 deg/s

4.5.2 Discussion of RMS Results

It should be noted that the Pepler index numbers in these charts assume that the sound level within the train for the passengers will be less than 65 dB, so that there will not be any additions to the Pepler index due to noise.

4.5.2.1 Hydraulic Active System

Looking first at the hydraulic actuator active secondary suspension system, we note that the accelerations have been reduced to only 20-25% of those of the passive system, in both the vertical and lateral directions. The actuator forces required to achieve this improvement in performance may seem somewhat high, but a separate analysis has revealed that these forces are achievable at the bandwidths needed with a reasonably sized hydraulic system. The RMS values also correspond to less than 5% of the total vehicle's weight.

The Pepler index has been significantly reduced, and is not too far from the excellent ride quality rating of 1. The roll rate has also been reduced to nearly zero.

Note that the variables we have traded off to obtain this improvement in ride quality are the air gap variations, which have more than tripled in the vertical direction, and just about tripled in the lateral direction. The secondary suspension strokes have also increased in both directions. However, all of these suspension displacements are still within the bounds considered acceptable for a Maglev vehicle, based on literature on the subject, and Draper's experience with a design by the Bechtel consortium.

4.5.2.2 Actively Controlled Ground-Effect Surfaces on Bogies Alone

It is important to keep in mind that there were severe difficulties in modeling the ground-effect surfaces (as described in Section 4.1.7.2), so the difference between an actual implemented system's performance and the performance determined by the analysis with the model may be larger than for the other cases considered. It is still considered to be reasonably valid.

The roll rate cannot be controlled as well as any of the other active suspension configurations. This is important, since half of the roll rate in deg/s is added directly to the Peplar Index, which is an indication that passengers will find this type of motion very uncomfortable.

4.5.2.3 Active Aerosurface Elements on Train Alone

The aerosurfaces on the train are not effective at reducing the accelerations in the lateral direction because they can only apply forces to the vehicle in the vertical direction, as explained in Section 4.1.11. However, even in this direction, there is some improvement for the combined system over the purely hydraulic actuator active system.

In the vertical direction, the actively controlled aerosurfaces reduce the RMS accelerations tremendously, leaving them at less than one one-thousandth of a g. Also note that only 5 of the available 8 degrees of RMS deflection of the aerosurfaces are used up at the 150 m/s speed, indicating that there is more force available than can be used. The limiting factor in this case is the trade-off between accelerations, roll rate, and secondary suspension stroke limits, which can be seen to be quite high for this case. At the lower speed of 100 m/s, the limitation on the angular displacement of the control surfaces was reached before the secondary suspension stroke limits were. More control authority is available at the 150 m/s speed, because the aerodynamic forces vary with the square of the train's velocity.

Note that the air gap variations have not been increased significantly as they were for the active hydraulic suspension system. Instead, we are trading a larger secondary suspension stroke for lower accelerations in the vertical direction. Again, greatly reduced roll rate has been achieved. The roll rate is low for all cases because it is a significant contributor to the Peplar index, and thus must be kept low to get a good rating.

4.5.2.4 Combined Hydraulic and Aerosurface Control Elements

The combined system is able to achieve vertical acceleration levels as low as the aerosurface system alone, and lateral accelerations 25-30% less than the hydraulic system alone, and thus, has the best ride quality and lowest Peplar index of any of the configurations. The vertical air gap variations are larger than those of a passive system, but are not nearly as large as those for the hydraulic system alone. However, the secondary suspension strokes in both directions are as large as for the purely hydraulic system.

The Peplar index is higher for this system than for the combined system using ground-effect aerosurfaces on the bogies because the lateral accelerations cannot be reduced as much, since the wings mounted on the train cannot exert forces in the lateral direction.

4.5.2.5 Combined Ground-Effect Surfaces and Hydraulic Actuators

When the hydraulic actuators are combined with the ground-effect aerosurfaces, the accelerations can be reduced to the same low levels as the other combined case. Also, the roll rate can now be significantly reduced. And since there are aerosurface actuators in both the vertical and lateral directions, accelerations in both these directions can be effectively reduced, thus resulting in the lowest Peplar index rating of any of the cases. And this is achieved with lower air gap variations in both directions than the passive system. However, there is no benefit in terms of additional insurance against contact with the guideway, as the control surfaces are in these air gaps, and therefore use all of the available gap up, under the stochastic restrictions imposed. In addition, the secondary suspension strokes are larger for this system than for the passive design, by a factor of more than 2 in the vertical direction, and a factor of greater than 3 in the lateral direction.

4.5.3. One-Third Octave Analysis of Ride Quality

In order to compare the ride quality to the ISO one hour reduced comfort standards, the RMS accelerations in one-third octave bands were calculated as described in the analysis methodology section. The results so obtained are displayed in sections 4.5.3.2 - 4.5.3.6. One-third octave analysis data for a vehicle speed of 100 m/s can be found in Appendix D.

4.5.3.1 Discussion of One-third Octave RMS Acceleration Plots

For the passive suspension, there are two lightly damped resonant peaks in both the vertical and lateral directions. While both of these resonant frequencies are excited by the guideway inputs, only the lower frequency resonance is excited by the wind input. This is due to the different Power Spectral Density of the wind disturbance, as described in Appendix B. A more involved explanation and discussion of the modes can be found in Appendix E

The active suspension with hydraulic actuators reduces the impact of the disturbances at the lower resonant frequency, thereby revealing additional high frequency lightly damped resonances. It is clear that the ride quality has been significantly improved at all frequencies, since the curves of the RMS accelerations are farther below the one hour reduced comfort ISO criteria.

The active aerosurfaces in ground-effect (mounted on the bogies) do not significantly attenuate the lower frequency lightly damped resonant modes, or the high frequency mode in the vertical direction. However, in the lateral direction, the higher frequency mode is attenuated much more than the active system using only hydraulic elements. The active aerosurfaces in ground-effect are noticeably more effective at attenuating the disturbances due to winds than those due to the guideway disturbances.

The combined active system employing both aerosurfaces in ground-effect (mounted on the bogies) and hydraulic actuators provides an even greater overall reduction in RMS acceleration levels in both the lateral and vertical directions. There is only a slight rise in the accelerations at the higher natural frequency.

The active aerodynamic wing surfaces (mounted on the train) have no noticeable effect on the shape of the lateral RMS accelerations versus frequency curve, but do slightly reduce these accelerations. Thus there is a very poor response to crosswinds, which act in the lateral direction. In fact, the system violates the one hour reduced comfort level in the lateral direction when both inputs are included. However, in the vertical direction, the only direction in which these actuators can directly exert forces, the resonant peaks have been eliminated. The accelerations are also drastically reduced in magnitude across the spectrum.

The combined active system employing both aerodynamic wing surfaces (mounted on the train) and hydraulic actuators provides even greater reductions in the vertical RMS accelerations, making more high frequency modes visible. Note that these modes are visible in these plots because the accelerations at the frequencies around them have been reduced even further than in the other active systems. When both wind and guideway inputs are included, the curve of vertical RMS accelerations versus frequency is essentially straight with a fixed roll-off rate. This system's performance in the lateral direction is largely limited by the performance of the hydraulic actuators in this direction, and so retains the higher natural frequency (lateral) mode that the active system with hydraulic actuators has, as seen in the plots.

4.5.3.2 One-Third Octave RMS Accelerations for Optimized Passive Suspension

V = 150 m/s

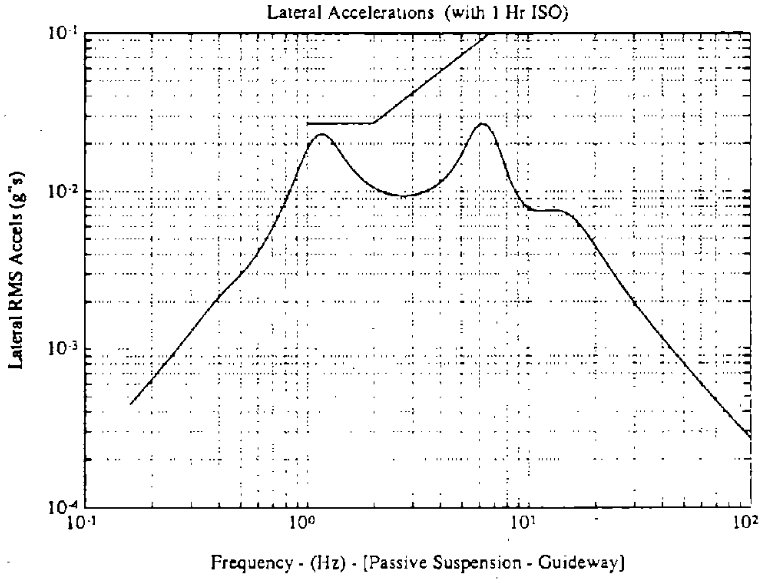

Figure 4.5.1 - Lateral 1/3 octave accelerations for passive suspension with guideway inputs only

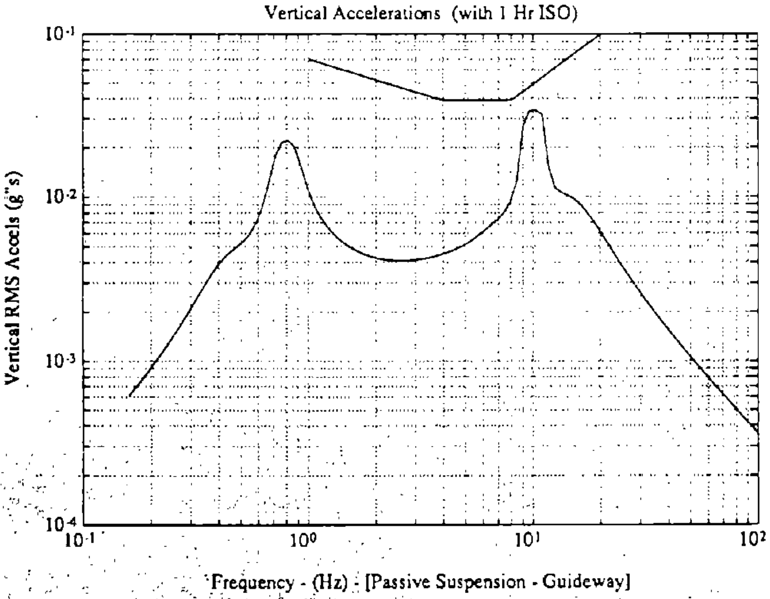

Figure 4.5.2 - Vertical 1/3 octave accelerations for passive suspension with guideway inputs only

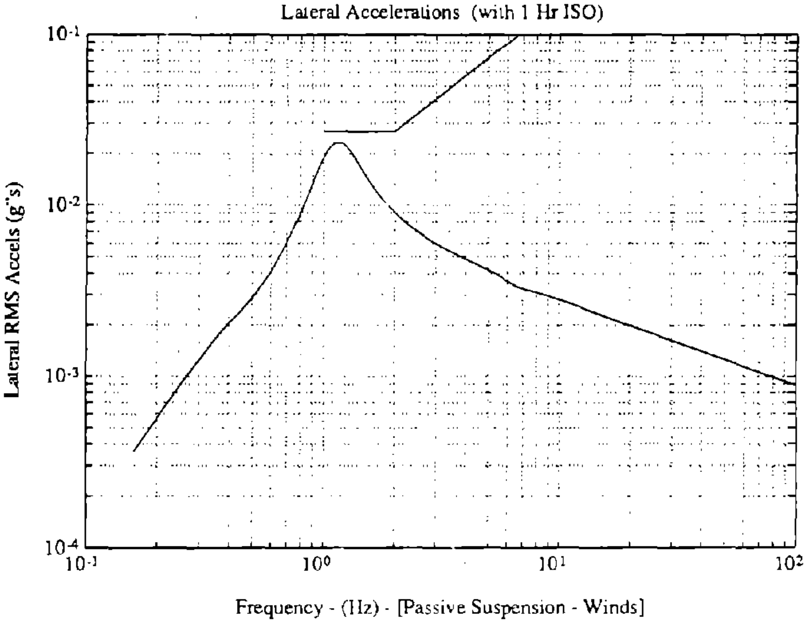

Figure 4.5.3 - Lateral 1/3 octave accelerations for passive suspension with wind inputs only

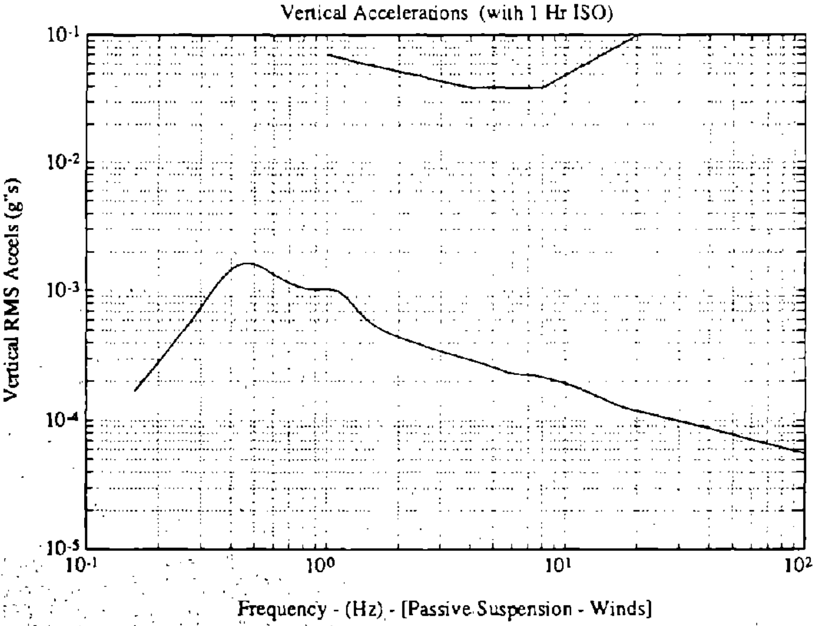

Figure 4.5.4 - Vertical 1/3 octave accelerations for passive suspension with wind inputs only

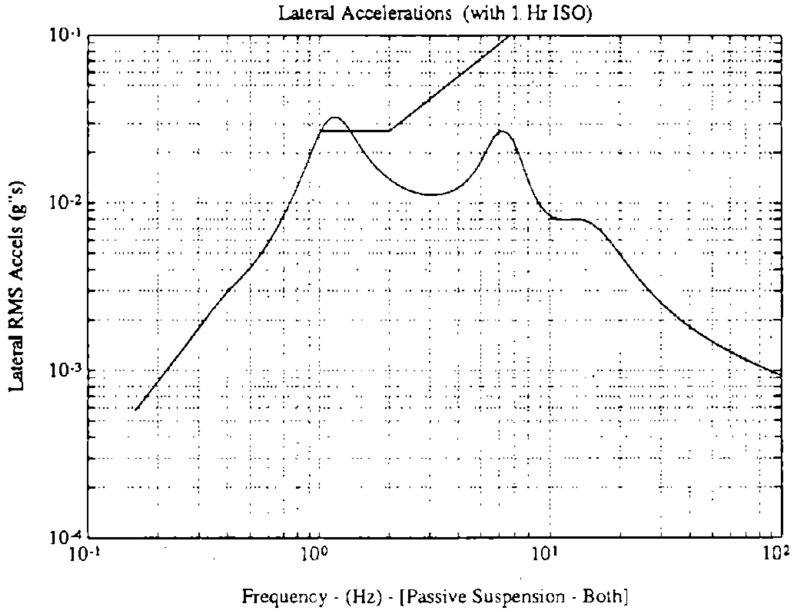

Figure 4.5.5 - Lateral 1/3 octave accelerations for passive suspension with both guideway and wind inputs

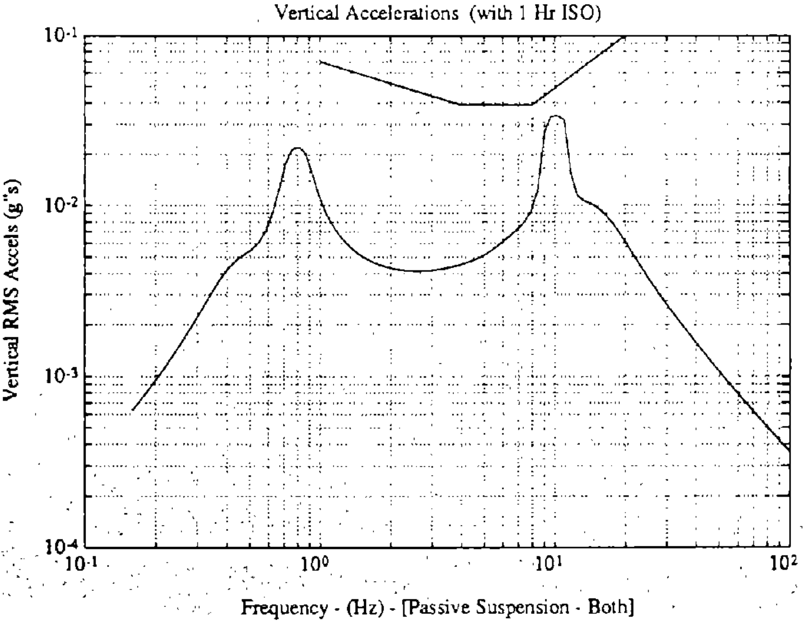

Figure 4.5.6 - Vertical 1/3 octave accelerations for passive suspension with both guideway and wind inputs

4.5.3.2 One-Third Octave RMS Accelerations for Active Hydraulic System

V = 150 m/s

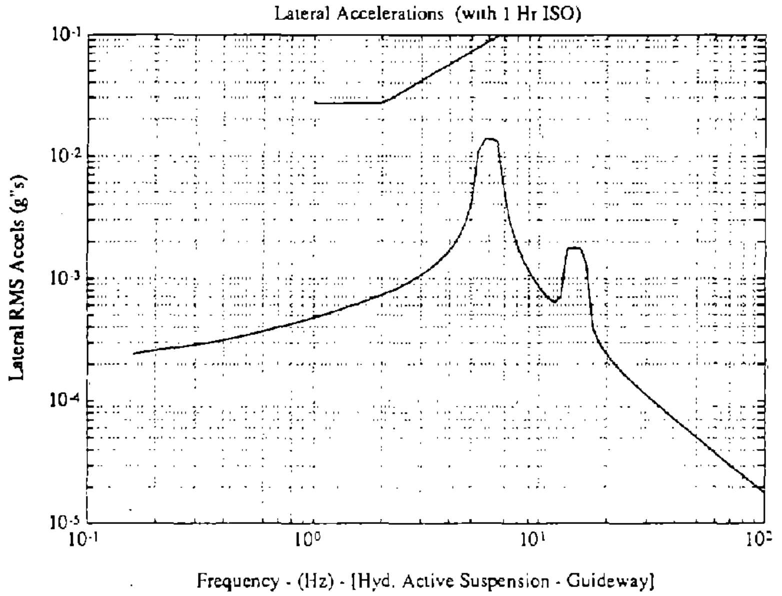

Figure 4.5.7 - Lateral 1/3 octave accelerations for active hydraulic suspension with guideway inputs only

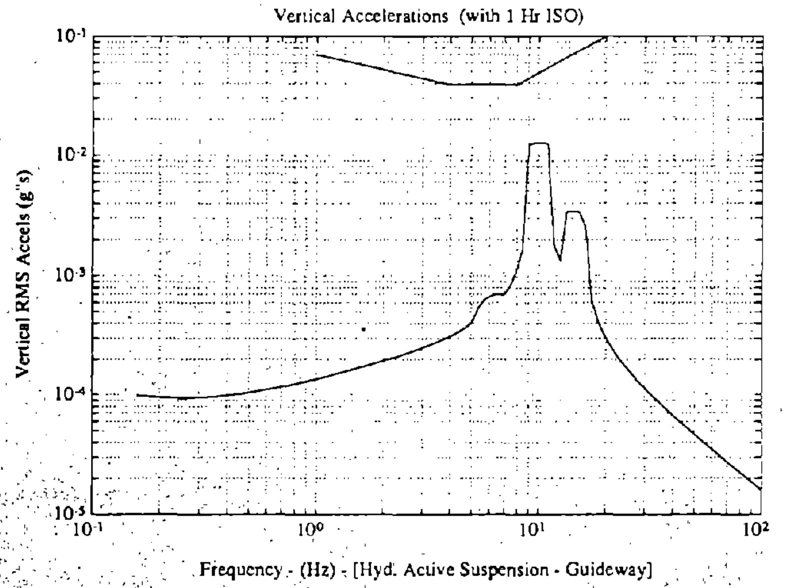

Figure 4.5.8 - Vertical 1/3 octave accelerations for active hydraulic suspension with guideway inputs only

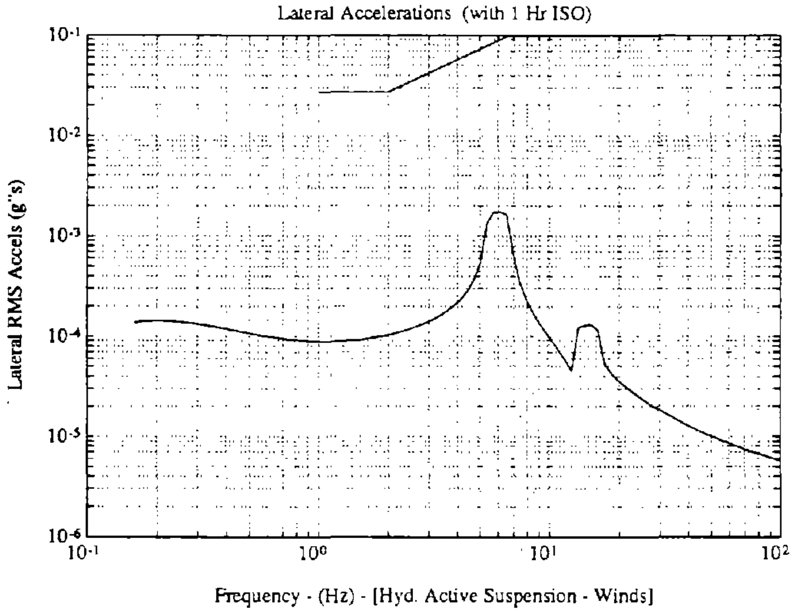

Figure 4.5.9 - Lateral 1/3 octave accelerations for active hydraulic suspension with wind inputs only

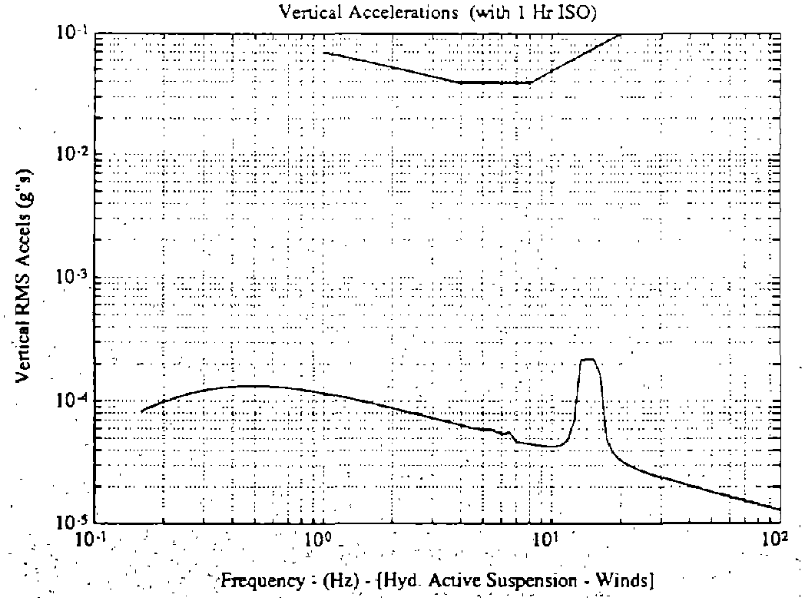

Figure 4.5.10 - Vertical 1/3 octave accelerations for active hydraulic suspension with wind inputs only

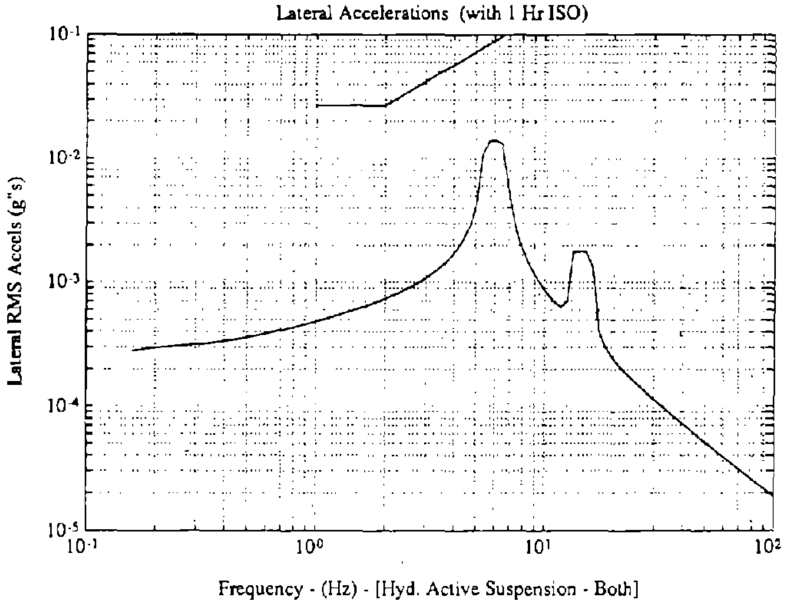

Figure 4.5.11 - Lateral 1/3 octave accelerations for active hydraulic suspension with both guideway and wind inputs

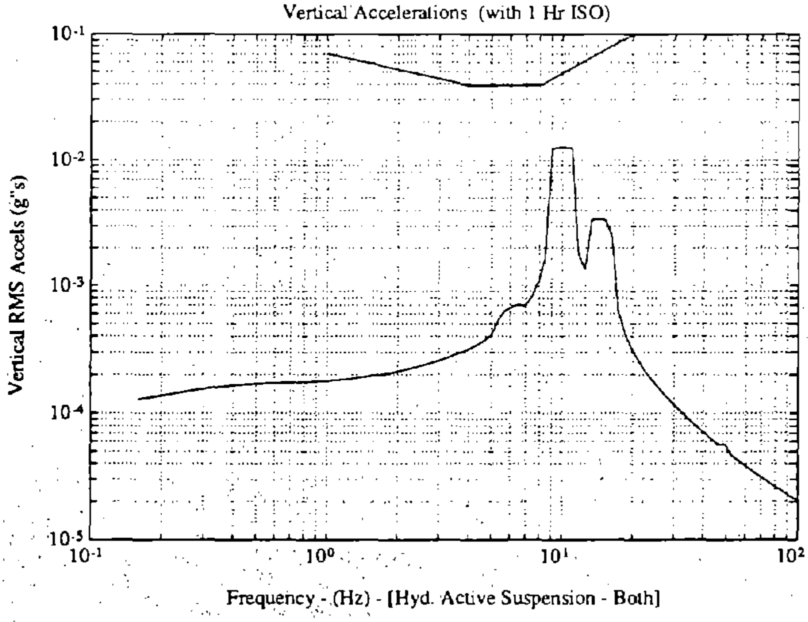

Figure 4.5.12 - Vertical 1/3 octave accelerations for active hydraulic suspension with both guideway and wind inputs

4.5.3.3 One-Third Octave RMS Accelerations for Ground-Effect Flaps on Bogies

V = 150 m/s

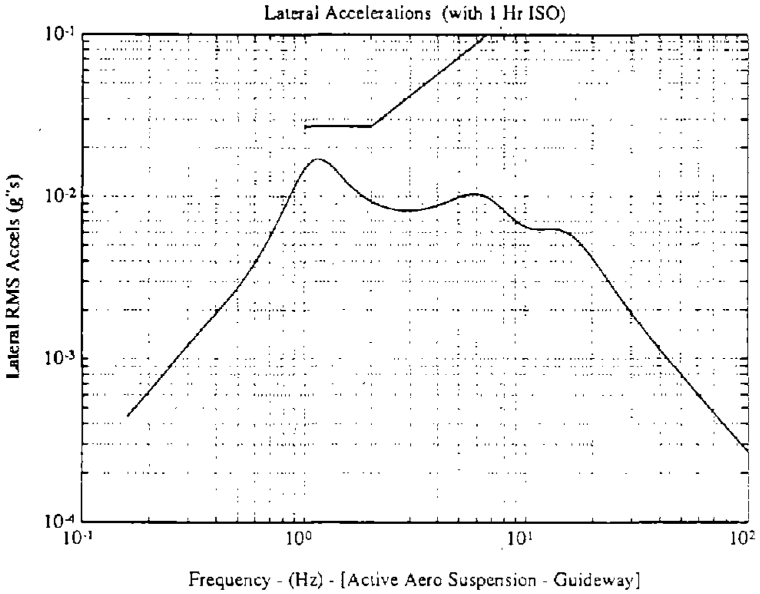

Figure 4.5.13 - Lateral 1/3 octave accelerations for active aerosurfaces in ground-effect with guideway inputs only

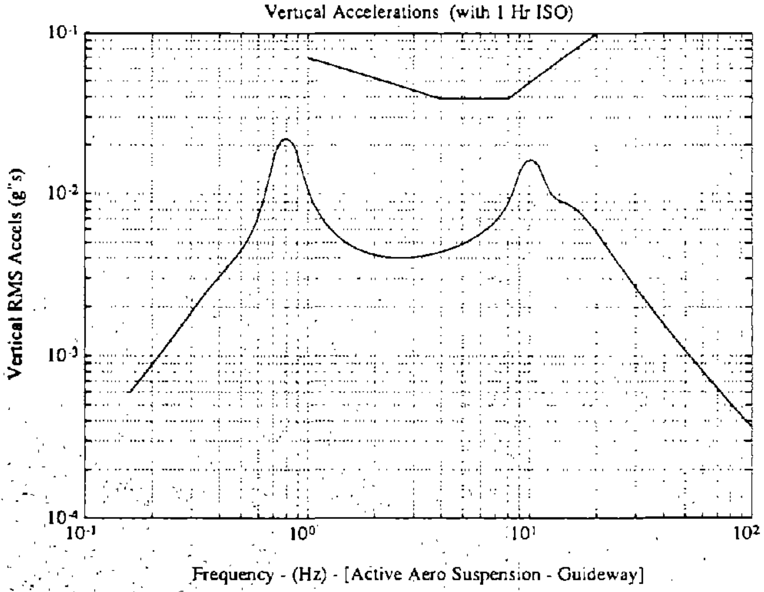

Figure 4.5.14 - Vertical 1/3 octave accelerations for active aerosurfaces in ground-effect with guideway inputs only

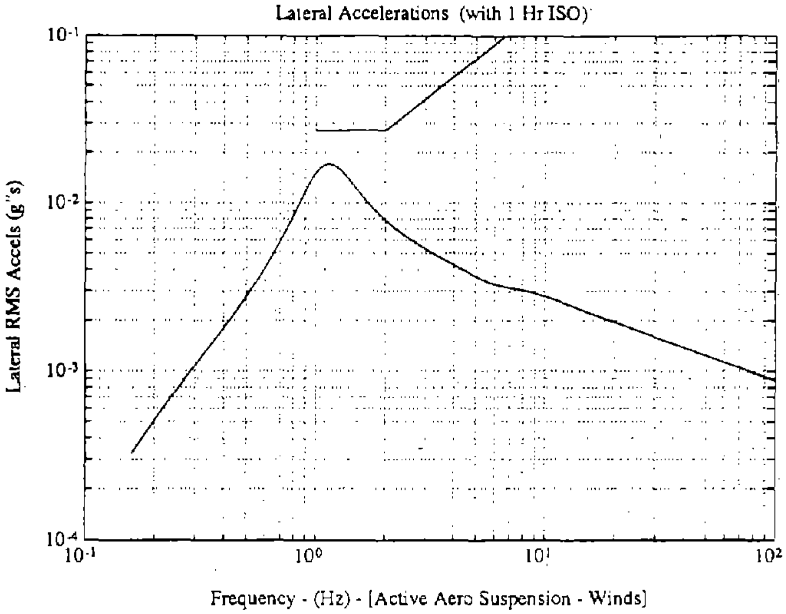

Figure 4.5.15 - Lateral 1/3 octave accelerations for active aerosurfaces in ground-effect with wind inputs only

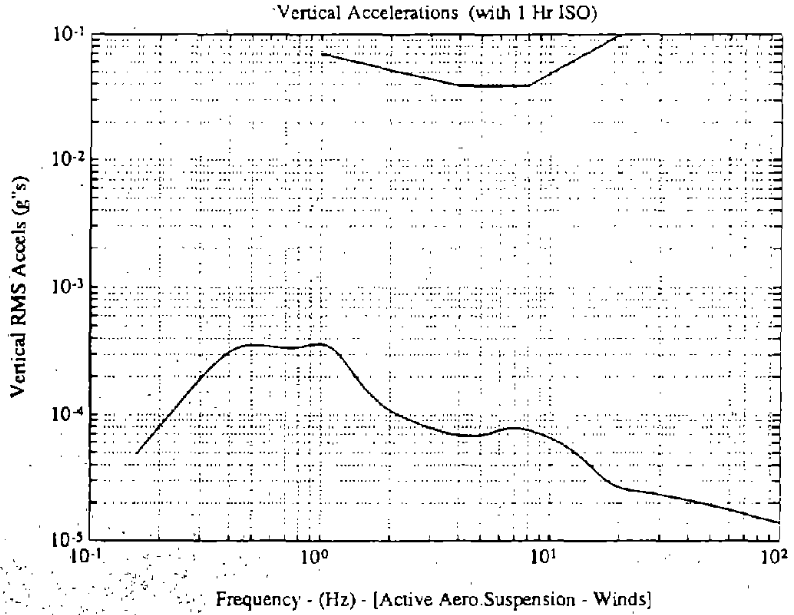

Figure 4.5.16 - Vertical 1/3 octave accelerations for active aerosurfaces in ground-effect with wind inputs only

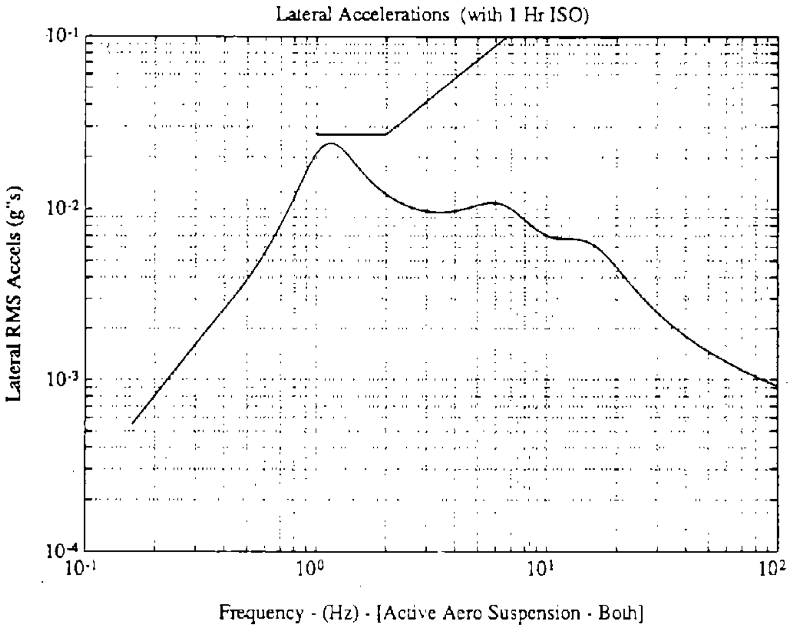

Figure 4.5.17 - Lateral 1/3 octave accelerations for active aerosurfaces in ground-effect with both guideway and wind inputs

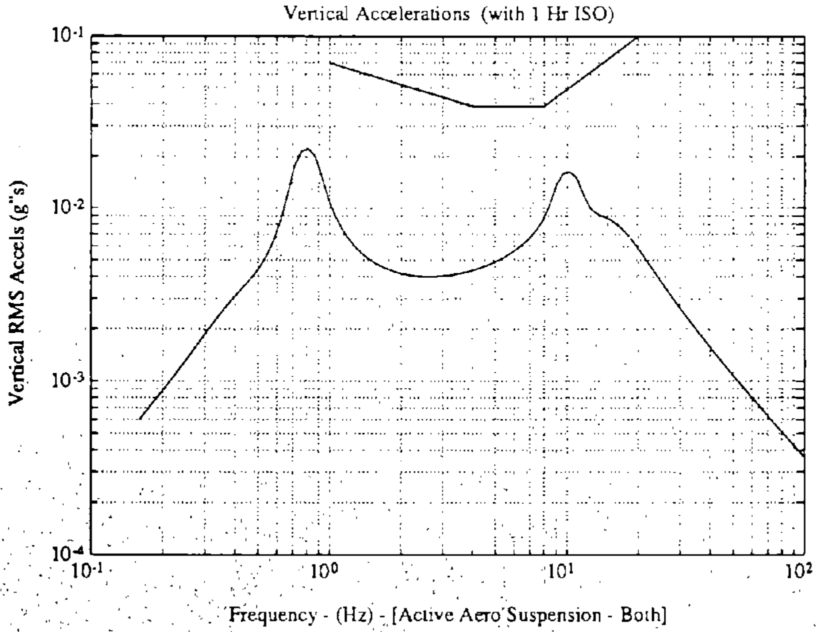

Figure 4.5.18 - Vertical 1/3 octave accelerations for active aerosurfaces in ground-effect with both guideway and wind inputs

4.5.3.4 One-Third Octave RMS Accelerations for Combination of Hydraulic Actuators and Ground-Effect Flaps on Bogies

V = 150 m/s

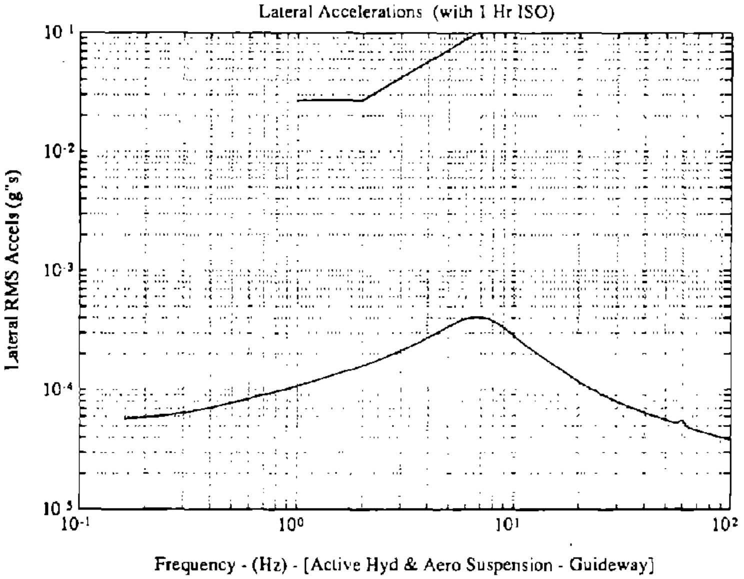

Figure 4.5.19 - Lateral 1/3 octave accelerations for active system with both hydraulic actuators and aerosurfaces in ground-effect with guideway inputs only

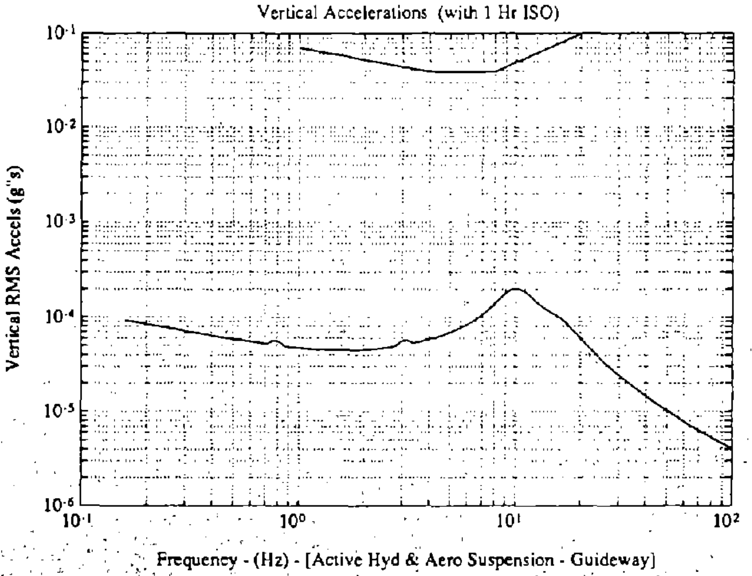

Figure 4.5.20 - Vertical 1/3 octave accelerations for active system with both hydraulic actuators and aerosurfaces in ground-effect with guideway inputs only

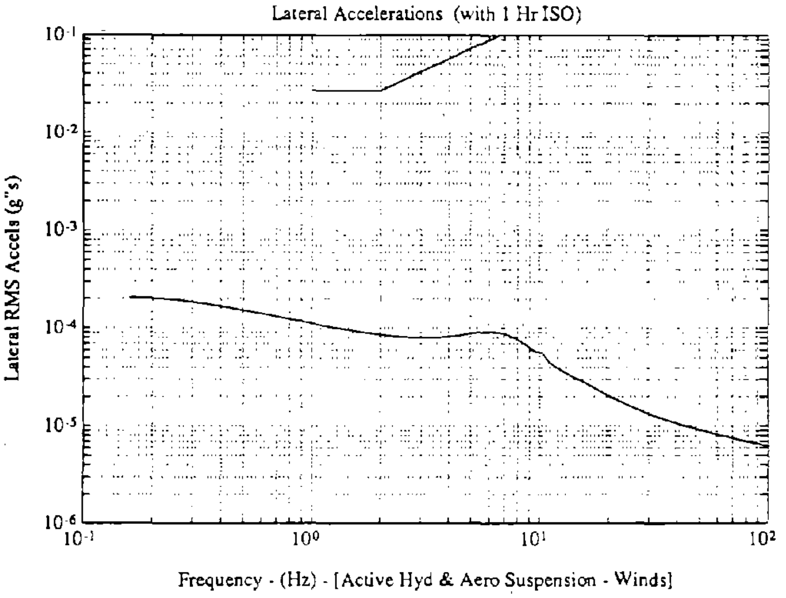

Figure 4.5.21 - Lateral 1/3 octave accelerations for active system with both hydraulic actuators and aerosurfaces in ground-effect with wind inputs only

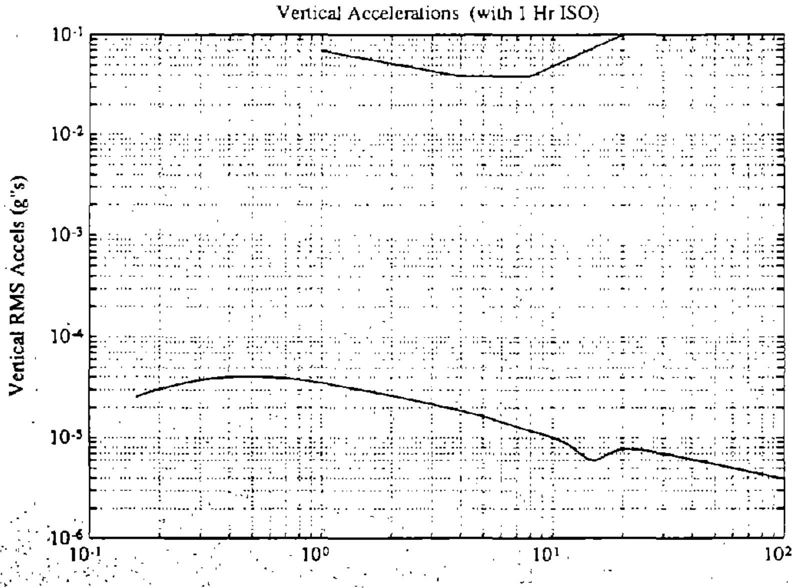

Figure 4.5.22 - Vertical 1/3 octave accelerations for active system with both hydraulic actuators and aerosurfaces in ground-effect with wind inputs only

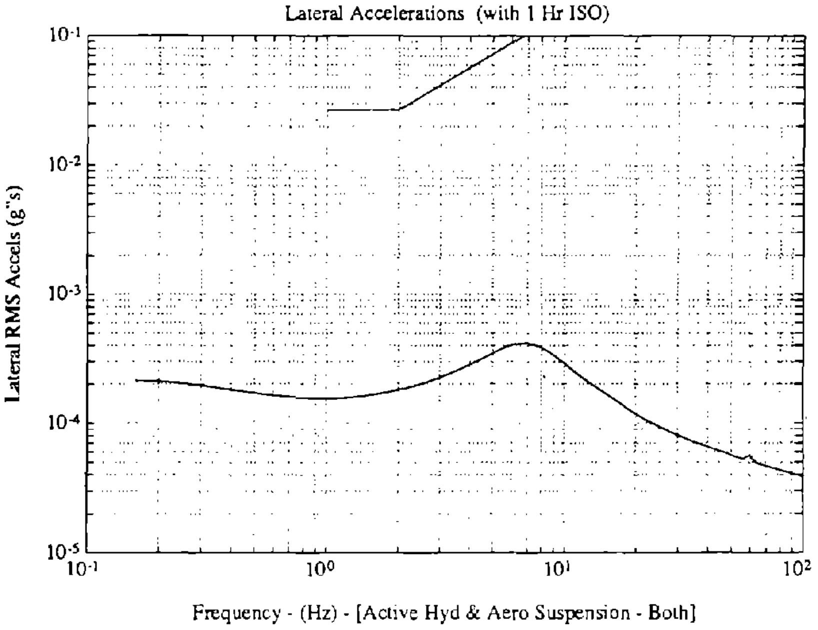

Figure 4.5.23 - Lateral 1/3 octave accelerations for active system with both hydraulic actuators and aerosurfaces in ground-effect with both guideway and wind inputs

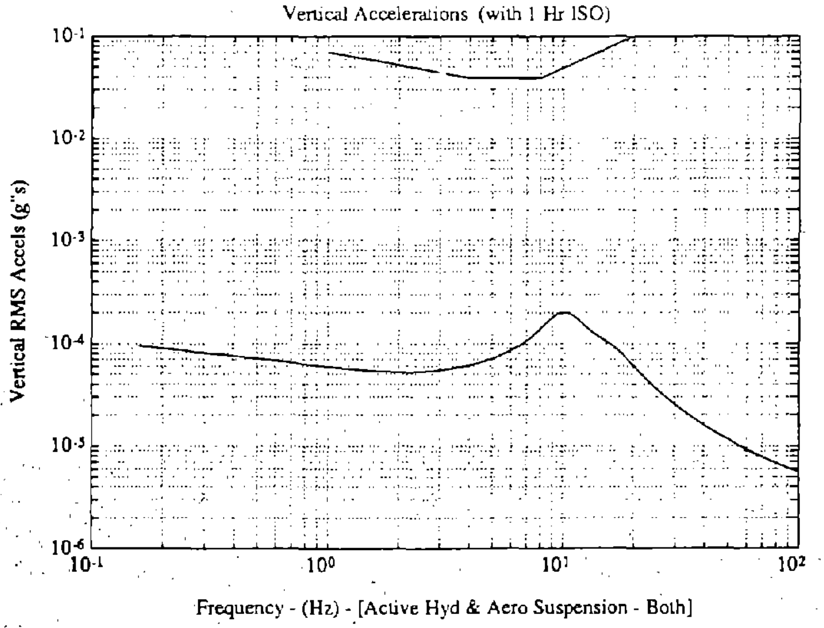

Figure 4.5.24 - Vertical 1/3 octave accelerations for active system with both hydraulic actuators and aerosurfaces in ground-effect with both guideway and wind inputs

4.5.3.5 *One-Third Octave RMS Accelerations for System with Active Wings on Train*

V = 150 m/s

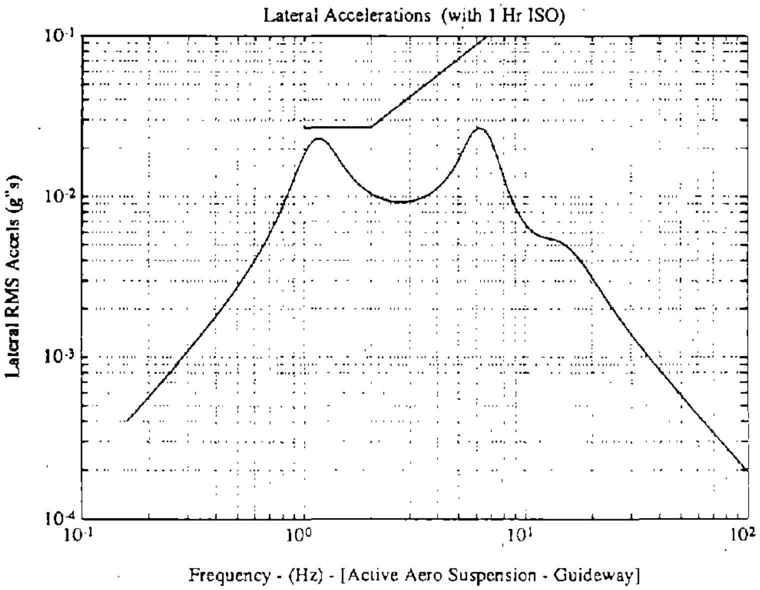

Figure 4.5.25 - Lateral 1/3 octave accelerations for active wings on train with guideway inputs only

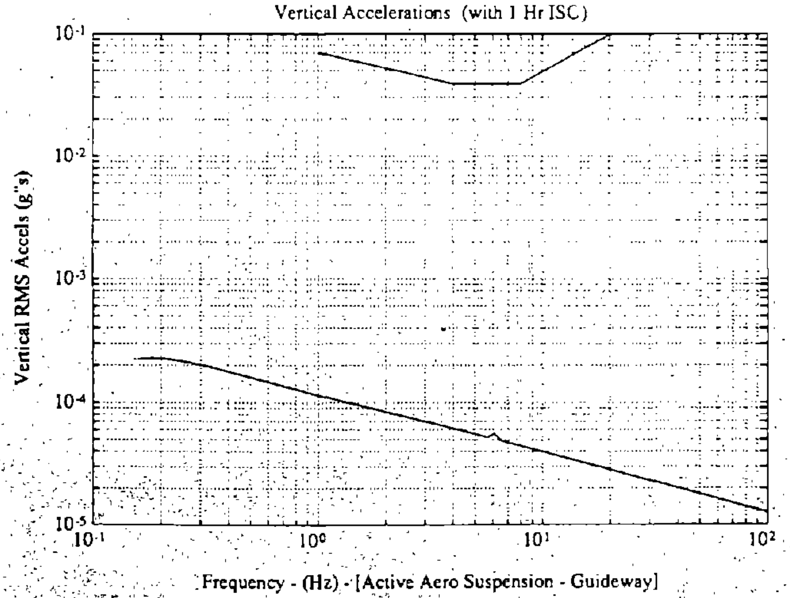

Figure 4.5.26 - Vertical 1/3 octave accelerations for active wings on train with guideway inputs only

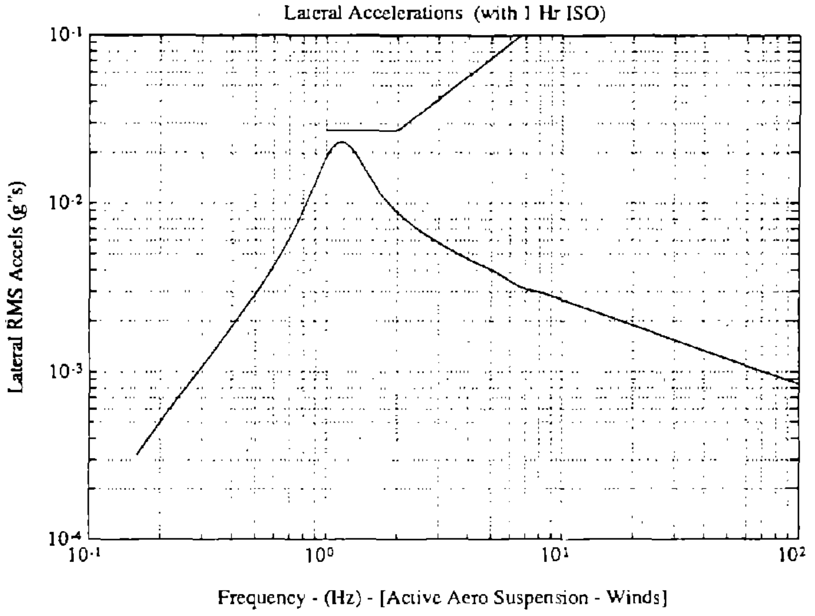

Figure 4.5.27 - Lateral 1/3 octave accelerations for active wings on train with wind inputs only

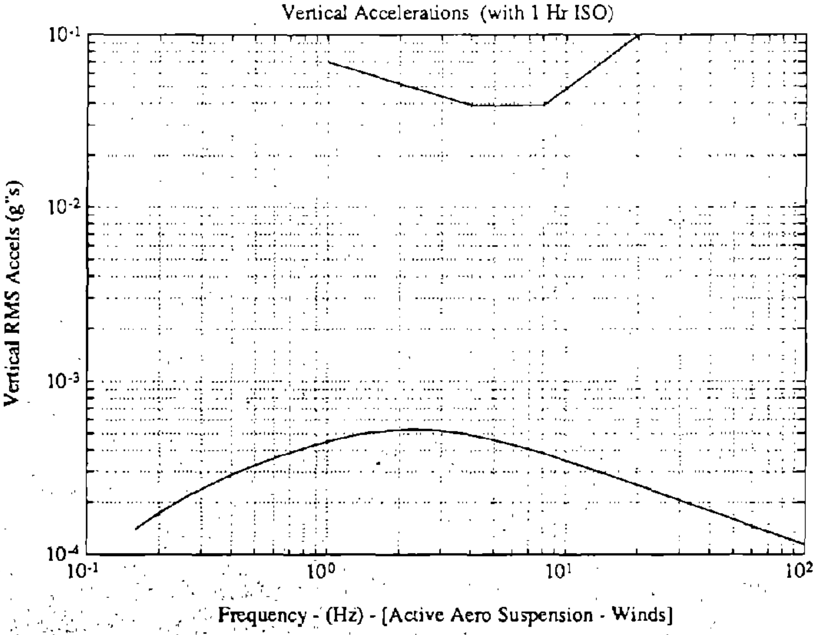

Figure 4.5.28 - Vertical 1/3 octave accelerations for active wings on train with wind inputs only

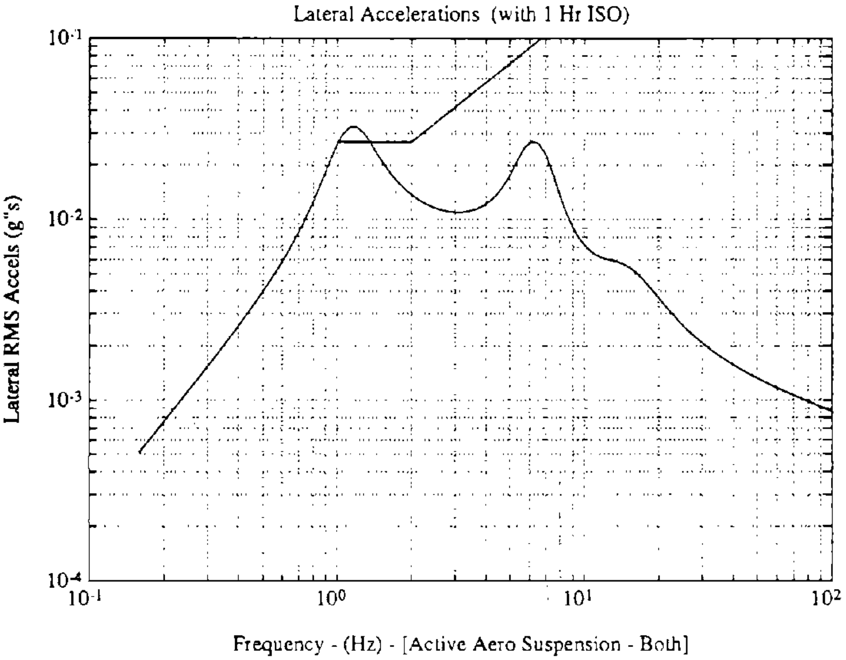

Figure 4.5.29 - Lateral 1/3 octave accelerations for active wings on train with both guideway and wind inputs

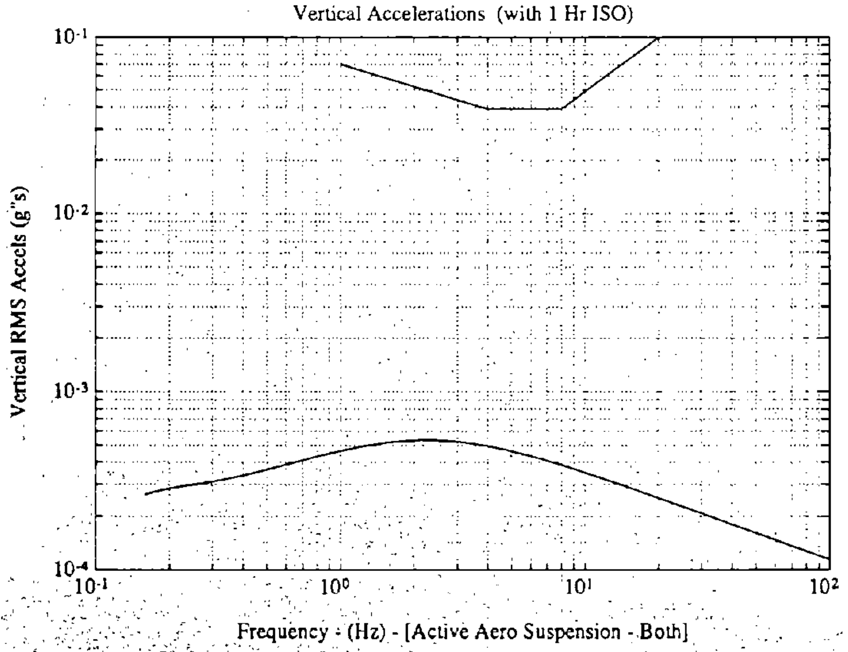

Figure 4.5.30 - Vertical 1/3 octave accelerations for active wings on train with both guideway and wind inputs

4.5.3.6 One-Third Octave RMS Accelerations for Active System with Hydraulic Actuators and Wings on Train

V = 150 m/s

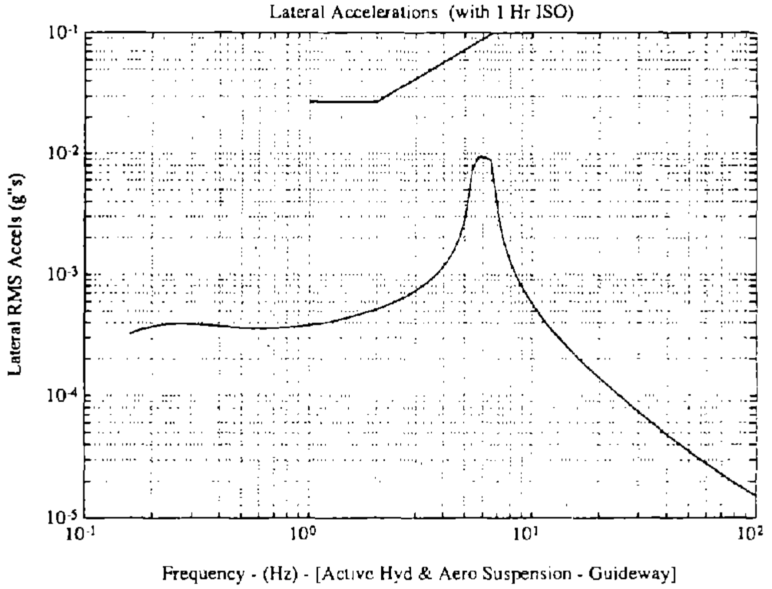

Figure 4.5.31 - Lateral 1/3 octave accelerations for active system with both hydraulic elements and wings on train with guideway inputs only

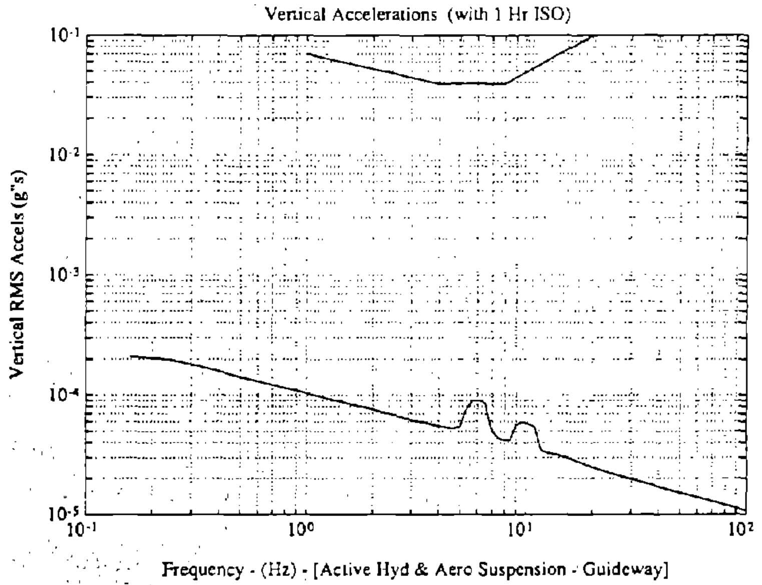

Figure 4.5.32 - Vertical 1/3 octave accelerations for active system with both hydraulic elements and wings on train with guideway inputs only

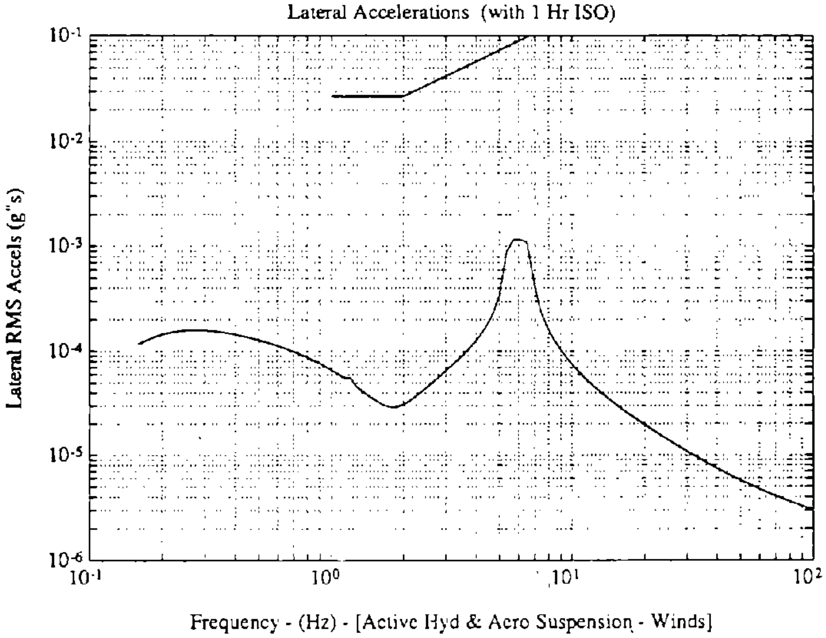

Figure 4.5.33 - Lateral 1/3 octave accelerations for active system with both hydraulic elements and wings on train with wind inputs only

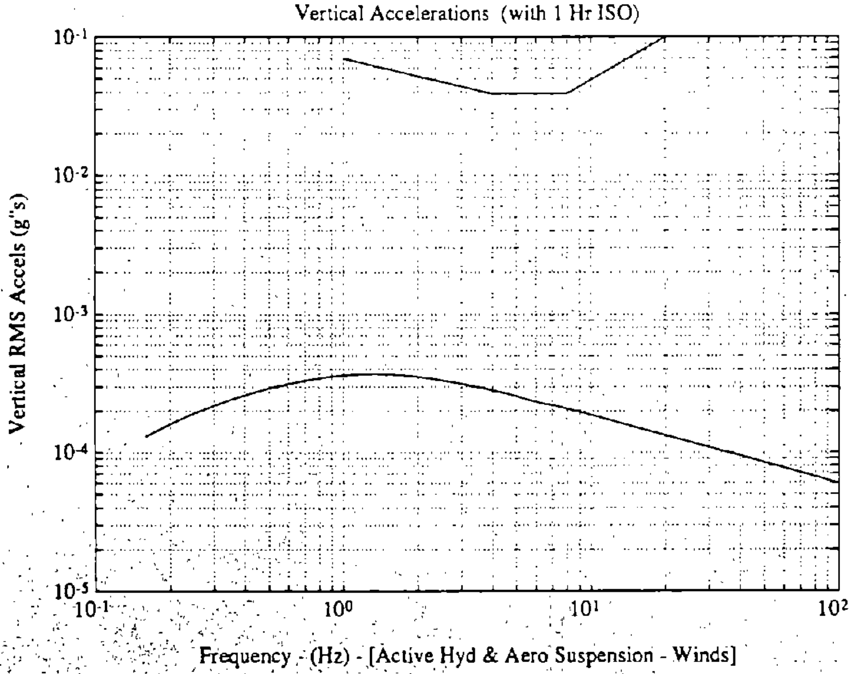

Figure 4.5.34 - Vertical 1/3 octave accelerations for active system with both hydraulic elements and wings on train with wind inputs only

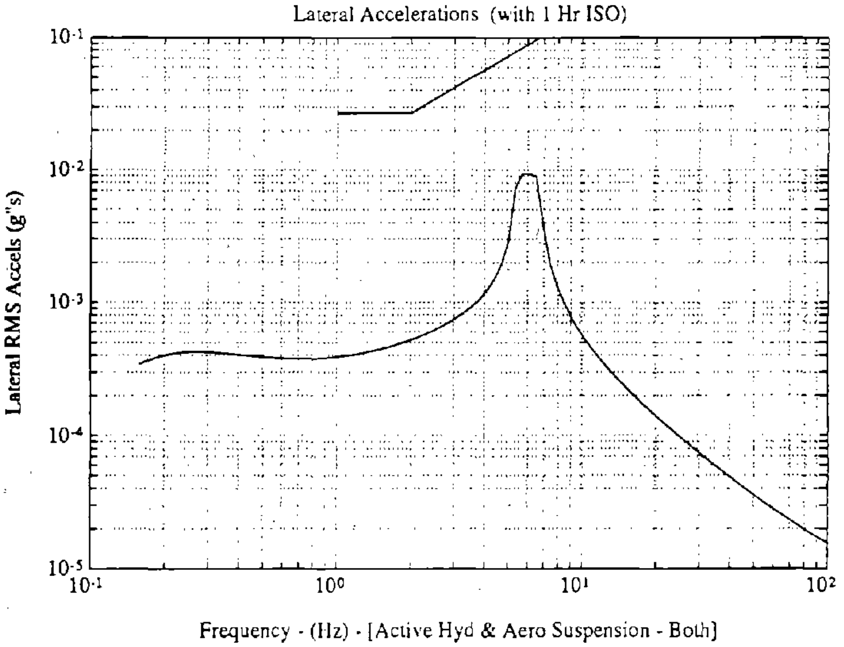

Figure 4.5.35 - Lateral 1/3 octave accelerations for active system with both hydraulic elements and wings on train with both guideway and wind inputs

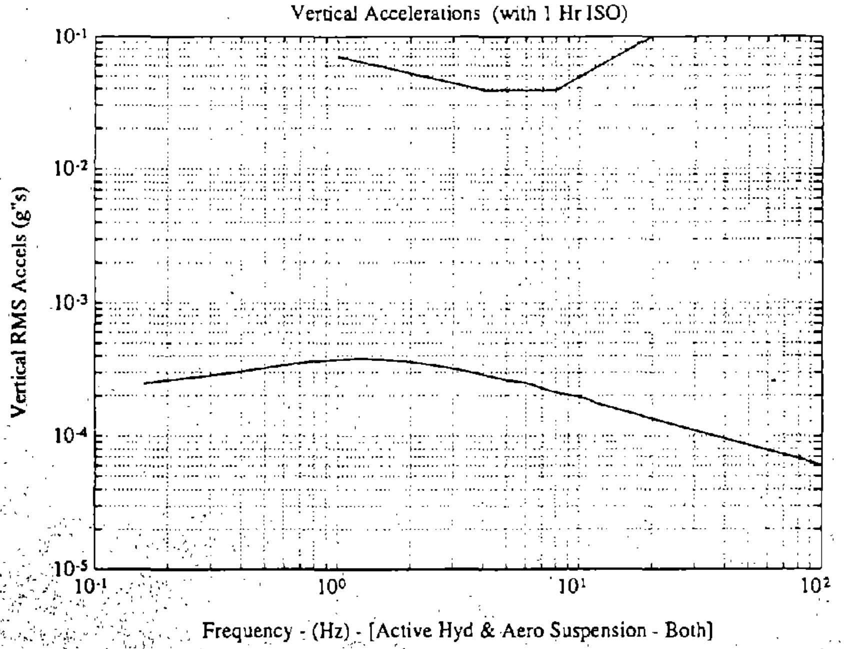

Figure 4.5.36 - Vertical 1/3 octave accelerations for active system with both hydraulic elements and wings on train with both guideway and wind inputs

4.5.4 Conclusions

In the vertical direction, the aerodynamic surfaces on the train are able to deliver ride quality nearly equal to the combined aerosurface and hydraulic element system, without introducing significantly larger air gap variations. Therefore, provided that surfaces large enough to provide sufficient control effort at the operating speed can be implemented, this type of control appears to be the most promising. It would be most preferable to have lateral aerosurface actuators as well, but if these are not physically implementable, as is assumed to be the case for this study, then the combination of lateral hydraulic actuators and vertical force aerosurfaces may be the best available option.

The main pitfall of this control system is its high control bandwidth requirement, due to the high natural frequency of the mode involving bogie oscillation under the train body. While frequency weighting may be introduced to limit the bandwidth, the fact that a lightly damped resonant peak might then lie above the system bandwidth could impact the system's performance significantly. Further study is required to determine the performance of a control system with frequency dependent weights used to limit this bandwidth.

APPENDIX A

TRAIN PARAMETERS

Speeds Evaluated

V = 100 m/s
V = 150 m/s

Vehicle Dimensions

Train width = 3.6576 m

Train height = 4 m

Bogie width = 1.5 m

Bogie height = 0.75 m

Mass Parameters

Total Mass	= 60 000 kg
Mass Ratio	= 0.25

where the mass ratio is defined as the unsprung mass over the total mass

I_{train} (roll)	= 1.1e5 kg-m^2
I_{train} (pitch)	= not used for this analysis
I_{train} (yaw)	= not used for this analysis
I_{bogies} (roll)	= 1.758e3 kg-m^2 (per bogie, assuming two bogies total)

Distances

lateral distance from train c.g. to average passenger's heart = 1.564 m
vertical distance from train c.g. up to average passenger's heart = 0.386 m

longitudinal distance between train c.g. and each bogie, assuming two bogie system equivalent to six bogie design (= LXB1 = LXB2) = 10 m

distance from train c.g. up to assumed roll center of secondary suspension (= LZTS) = 0.0 m
vertical distance from bogie c.g. up to assumed roll center of secondary suspension (= LZBS) = 0.400 m

vertical distance from bogie c.g. down to point of force application by primary suspension

(= LZBP) = 0.025 m

lateral distance between the two points on the bogie that are subjected to lift forces

(= W_g) = 1.400 m

vertical distance from train c.g. up to center of pressure for crosswind forces

(= LZCP) = 0.10 m

Active Wings mounted on Train

lift versus angle of attack for aerodynamic wing control surfaces

(= clavf1 = clavf2) = 0.049 CL/deg

where CL stands for coefficient of lift

width of each aero-dynamic control surface (= widvf = widvr) = 1.12 m

geometric aspect ratio for each aero-dynamic control surface = 0.8

lateral distance between center of pressure of each aero-dynamic control surface and train c.g. (= wingsepvf = wingsepvr) = 2.389 m

Active Aero-surfaces in Ground-Effect mounted on Bogies

lift versus angle of attack for aerodynamic control surfaces in ground-effect exerting lateral forces (= clalf1 = clalf2) = 0.225 CL/deg

lift versus angle of attack for aerodynamic control surfaces in ground-effect exerting vertical forces (= clavf1 = clavf2) = 0.1338 CL/deg

width of each aero-dynamic control surface (= widvf = widvr) = 1.0 m

geometric aspect ratio for each aero-dynamic control surface = 0.2857

slope of lift coefficient versus change in air gap (lateral) = 16.055

slope of lift coefficient versus change in air gap (vertical) = 4.2857

The aero-surfaces in ground effect on the bogies were assumed to exert forces at the same point as the primary suspension magnets.

APPENDIX B

DESCRIPTION OF STOCHASTIC INPUT PARAMETERS

Guideway Stochastic Model

$$\Phi_{guideway}(\omega) = \frac{A_r v}{\omega^2} \qquad \text{B.1}$$

$\Phi_{guideway}$ = Power Spectral Density of Guideway Irregularities

A_r = Roughness Parameter

v = Train Velocity

A roughness parameter A_r corresponding to welded steel rail was used in defining the guideway PSD, which was then used to form a linear system driven by a white noise input to describe the guideway position variations. While our guideway will not be welded steel rail and its roughness as seen by the train will be dominated by the alignment of the guideway's coils, the PSD of the guideway is expected to be similar. In other words, the stochastics should be the same for both cases, so the use of a roughness parameter corresponding to welded steel rail is valid. However, the results of this analysis can be applied generally, knowing the equivalent roughness parameter of the actual guideway. The results scale linearly with the square root of the roughness parameter.

The same roughness was assumed in both the vertical and lateral directions. The roughness parameter used to model the guideway roll variations was determined by comparing our situation to railroad measures of this parameter.[1] Again, the stochastics were assumed to be similar for a Maglev guideway, and so the relationship between cross-level[2] and profile[3] for rail of class 4 to 6 was determined. This relation was then assumed to apply equally to the Maglev guideway, and an angular roll disturbance was computed based on the roughness in the vertical direction. A guideway width of 1.2 meters was used for this calculation.

---

[1] Garg, Vijay K.; Dukkipati, Rao V., "Dynamics of Railway Vehicle Systems," Academic Press, 1984.

[2] The difference between the elevation of two rails (railroad terminology)

[3] vertical surface profile is the average elevation of the two rails (railroad terminology)

The resulting roughness parameters were:

A_r(vertical) $= 2\pi \times 6.1\pi \times 10^{-8}$
A_r(lateral) $= 2\pi \times 6.1\pi \times 10^{-8}$
A_r(roll) $= 2\pi \times 6.1\pi \times 10^{-8}/(1.75\text{x}1.2)$

Wind Stochastic Model

$$\Phi_{wind}(\omega) = \frac{2\sigma_w^2 \nu}{\omega^2 + \nu^2} \qquad \text{B.2}$$

Φ_{wind} = Power Spectral Density of Wind

ν = break frequency of wind spectrum (rad/s)

σ_w = rms wind (m/s)

ω = frequency (rad/s)

where Power Spectral Density is defined as:

$$\Phi\ (\omega) = \frac{2\sigma_w^2 \nu}{\omega^2 + \nu^2} = \int_{-\infty}^{+\infty} \underbrace{\sigma_w^2 e^{-\nu\omega|\tau|}}_{\psi(\tau)} e^{-j\omega\tau} d\tau \qquad \text{B.3}$$

with $\psi(\tau)$ = the Auto-Correlation Function for the disturbance

The guideway and wind models described in this report are developed using this relationship between Power Spectral Densities and Auto-Correlation Functions.

Using this definition for Power Spectral Density, $A_r = 2\pi \times 6.1\pi \times 10^{-8}$ for welded steel rail

Note the extra 2π factor multiplying the roughness parameter which is found elsewhere[4] for welded steel rail. This factor is needed to account for the different definition of the

---

[4] Wormley, D.N.; Young, J.W., "Optimization of Linear Vehicle Suspensions Subjected to Simultaneous Guideway and External Force Disturbances," Journal of Dynamic Systems, Measurement, and Control: Transactions of the ASME, Paper No. 73-Aut-H, March 16,1973.

(cont.)

relationship between Power Spectral Density and Auto-Correlation Function found in those other places.

Figures B.1 and B.2 show the PSD's of the guideway and wind, respectively. Although the wind spectrum is shown as a force, the shape of the curve is the same as that for wind velocity, which was used as the input for the final analysis. Also, although the PSD for the guideway shown is for smooth highway, the shape is identical to that for welded steel rail.

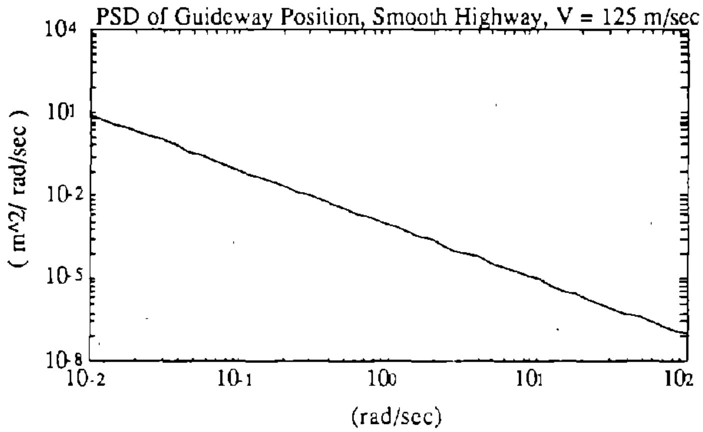

Figure B.1 - PSD of guideway disturbance

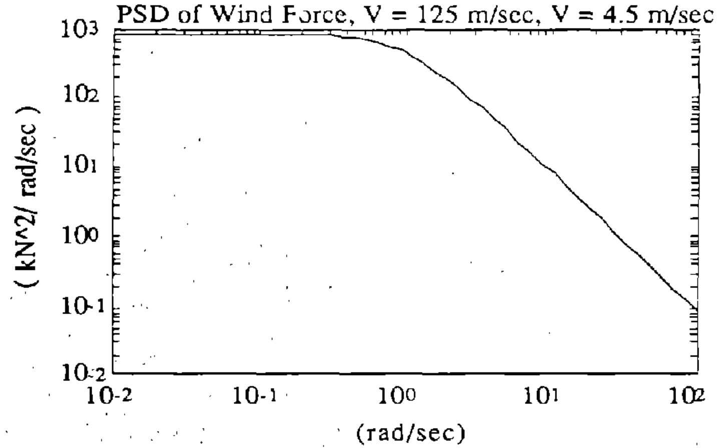

Figure B.2 - PSD of wind disturbance

APPENDIX C

RMS VALUES OF OUTPUTS FOR 100 m/s VEHICLE SPEED

This appendix contains the RMS outputs for the variables of interest for a train speed of 100 m/s.

Table C.1 - Wings in Ground Effect on Bogies, Vehicle Velocity = 100 m/s

V = 100 m/s Welded Rail RMS Wind = 10 mph	Passive Secondary	Active Hydraulic Secondary	Active Ground-Effect Aero-Surfaces	Active Aero & Hydraulic Secondary
RMS Y Train Accels				
Guideway	4.44 g/100	1.00 g/100	3.38 g/100	0.10 g/100
Crosswinds	2.49 g/100	0.11 g/100	2.18 g/100	0.08 g/100
Combined	5.10 g/100	1.01 g/100	4.02 g/100	0.11 g/100
RMS Z Train Accels				
Guideway	4.04 g/100	0.83 g/100	3.29 g/100	0.02 g/100
Crosswinds	0.23 g/100	0.03 g/100	0.07 g/100	0.02 g/100
Combined	4.05 g/100	0.83 g/100	3.29 g/100	0.03 g/100
Y Actuator Effort (RMS)				
Guideway	N/A	26.58 KN	N/A	24.56 KN
Crosswinds		8.90 KN		29.68 KN
Combined		28.03 KN		38.52 KN
Z Actuator Effort (RMS)				
Guideway	N/A	20.51 KN	N/A	11.19 KN
Crosswinds		0.00 KN		0.00 KN
Combined		20.51 KN		11.19 KN
Roll Actuator Effort (RMS)				
Guideway	N/A	35.56 KN-m	N/A	20.35 KN-m
Crosswinds		3.86 KN-m		1.59 KN-m
Combined		35.77 KN-m		20.41 KN-m
Peplar Ride Comfort Index No.				
Guideway	2.84	1.35	2.49	1.04
Crosswinds	1.59	1.08	1.42	1.02
Combined	2.97	1.37	2.60	1.05

Y Aero-Surface RMS Deflection				
Guideway	N/A	N/A	1.36 Deg	1.38 Deg
Crosswinds			0.63 Deg	0.20 Deg
Combined			1.49 Deg	1.40 Deg
Z Aero-Surface Deflection				
Guideway	N/A	N/A	1.56 Deg	1.57 Deg
Crosswinds			0.31 Deg	0.03 Deg
Combined			1.59 Deg	1.57 Deg
Y RMS Air Gap Variation				
Guideway	0.2457 cm	0.7764 cm	0.1899 cm	0.2520 cm
Crosswinds	0.0939 cm	0.1111 cm	0.0848 cm	0.0808 cm
Combined	0.2630 cm	0.7844 cm	0.2080 cm	0.2646 cm
Z RMS Air Gap Variation				
Guideway	0.4918 cm	1.6802 cm	0.3225 cm	0.3533 cm
Crosswinds	0.0239 cm	0.0286 cm	0.0158 cm	0.0186 cm
Combined	0.4924 cm	1.6805 cm	0.3228 cm	0.3538 cm
Y RMS Sec. Stroke				
Guideway	0.5311 cm	1.3064 cm	0.4427 cm	1.8343 cm
Crosswinds	0.7567 cm	0.3405 cm	0.7324 cm	2.3031 cm
Combined	0.9244 cm	1.3500 cm	0.8558 cm	2.9444 cm
Z RMS Sec. Stroke				
Guideway	1.0498 cm	2.6081 cm	0.9688 cm	3.3385 cm
Crosswinds	0.1744 cm	0.5571 cm	0.0475 cm	0.2558 cm
Combined	1.0642 cm	2.6669 cm	0.9699 cm	3.3482 cm
Roll Rate (RMS)				
Guideway	0.79 deg/s	0.08 deg/s	0.72 deg/s	0.04 deg/s
Crosswinds	0.26 deg/s	0.10 deg/s	0.08 deg/s	0.02 deg/s
Combined	0.83 deg/s	0.12 deg/s	0.72 deg/s	0.05 deg/s

Table C.2 - Winglets on Train, Vehicle Velocity = 100 m/s

V = 100 m/s Welded Rail RMS Wind = 10 mph	Passive Secondary	Active Hydraulic Secondary	Active Aero-Surfaces	Active Aero & Hydraulic Secondary

RMS Y Train Accels				
Guideway	4.44 g/100	1.00 g/100	4.35 g/100	0.76 g/100
Crosswinds	2.49 g/100	0.11 g/100	2.48 g/100	0.08 g/100
Combined	5.10 g/100	1.01 g/100	5.01 g/100	0.76 g/100
RMS Z Train Accels				
Guideway	4.04 g/100	0.83 g/100	0.09 g/100	0.05 g/100
Crosswinds	0.23 g/100	0.03 g/100	0.05 g/100	0.06 g/100
Combined	4.05 g/100	0.83 g/100	0.10 g/100	0.07 g/100
Y Actuator Effort (RMS)				
Guideway	N/A	26.58 KN	N/A	27.62 KN
Crosswinds		8.90 KN		12.23 KN
Combined		28.03 KN		30.21 KN
Z Actuator Effort (RMS)				
Guideway	N/A	20.51 KN	N/A	19.03 KN
Crosswinds		0.00 KN		0.00 KN
Combined		20.51 KN		19.03 KN
Roll Actuator Effort (RMS)				
Guideway	N/A	35.56 KN-m	N/A	29.73 KN-m
Crosswinds		3.86 KN-m		4.73 KN-m
Combined		35.77 KN-m		30.10 KN-m
Peplar Ride Comfort Index No.				
Guideway	2.84	1.35	1.79	1.17
Crosswinds	1.59	1.08	1.48	1.07
Combined	2.97	1.37	1.93	1.20
Z Aero-Surface RMS Deflection				
Guideway	N/A	N/A	8.0 Deg	7.9 Deg
Crosswinds			1.1 Deg	0.8 Deg
Combined			8.0 Deg	7.9 Deg
Y RMS Air Gap Variation				
Guideway	0.2457 cm	0.7764 cm	0.2456 cm	0.7893 cm
Crosswinds	0.0939 cm	0.1111 cm	0.0939 cm	0.1119 cm
Combined	0.2630 cm	0.7844 cm	0.2630 cm	0.7972 cm
Z RMS Air Gap Variation				
Guideway	0.4918 cm	1.6802 cm	0.4966 cm	1.5044 cm
Crosswinds	0.0239 cm	0.0286 cm	0.0217 cm	0.0260 cm
Combined	0.4924 cm	1.6805 cm	0.4970 cm	1.5046 cm

Y RMS Sec. Stroke				
Guideway	0.5311 cm	1.3064 cm	0.5309 cm	1.5285 cm
Crosswinds	0.7567 cm	0.3405 cm	0.7567 cm	0.7958 cm
Combined	0.9244 cm	1.3500 cm	0.9244 cm	1.7233 cm
Z RMS Sec. Stroke				
Guideway	1.0498 cm	2.6081 cm	1.9786 cm	2.9550 cm
Crosswinds	0.1744 cm	0.5571 cm	0.5096 cm	0.7084 cm
Combined	1.0642 cm	2.6669 cm	2.0432 cm	3.0387 cm
Roll Rate (RMS)				
Guideway	0.79 deg/s	0.08 deg/s	0.07 deg/s	0.06 deg/s
Crosswinds	0.26 deg/s	0.10 deg/s	0.09 deg/s	0.09 deg/s
Combined	0.83 deg/s	0.12 deg/s	0.11 deg/s	0.11 deg/s

APPENDIX D

ONE-THIRD OCTAVE RMS ACCELERATION PLOTS @ 100 m/s

D.1 Optimized Passive Suspension

V = 100 m/s

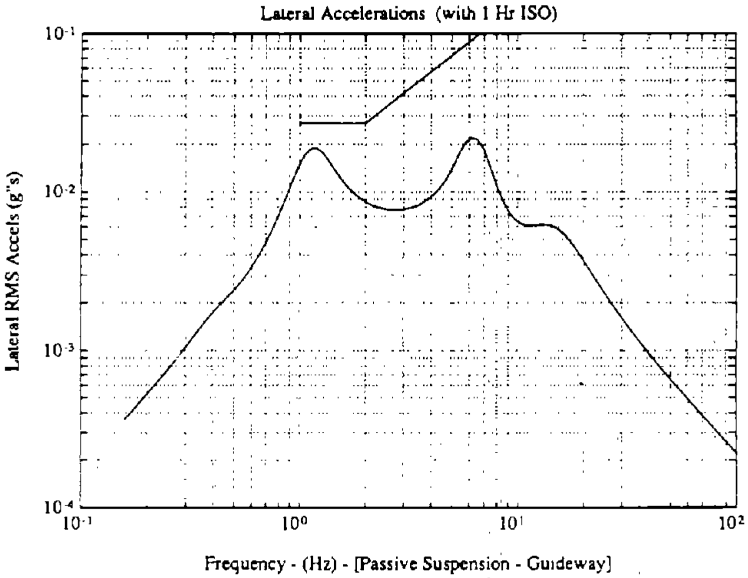

Figure D.1 - Lateral 1/3 octave accelerations for passive suspension with guideway inputs only

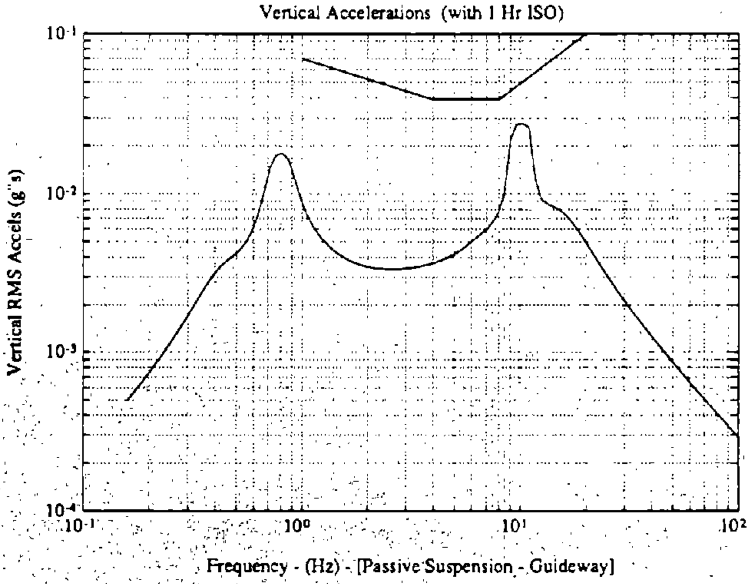

Figure D.2 - Vertical 1/3 octave accelerations for passive suspension with guideway inputs only

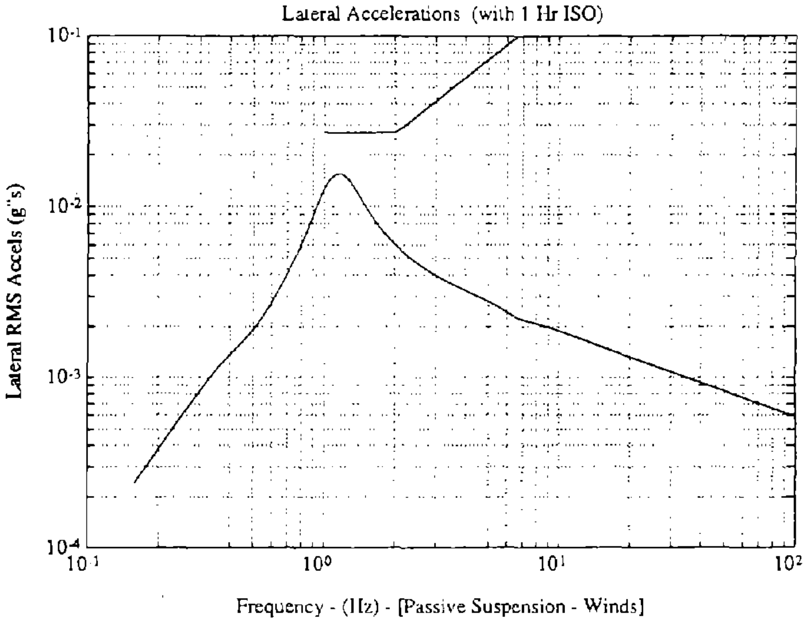

Figure D.3 - Lateral 1/3 octave accelerations for passive suspension with wind inputs only

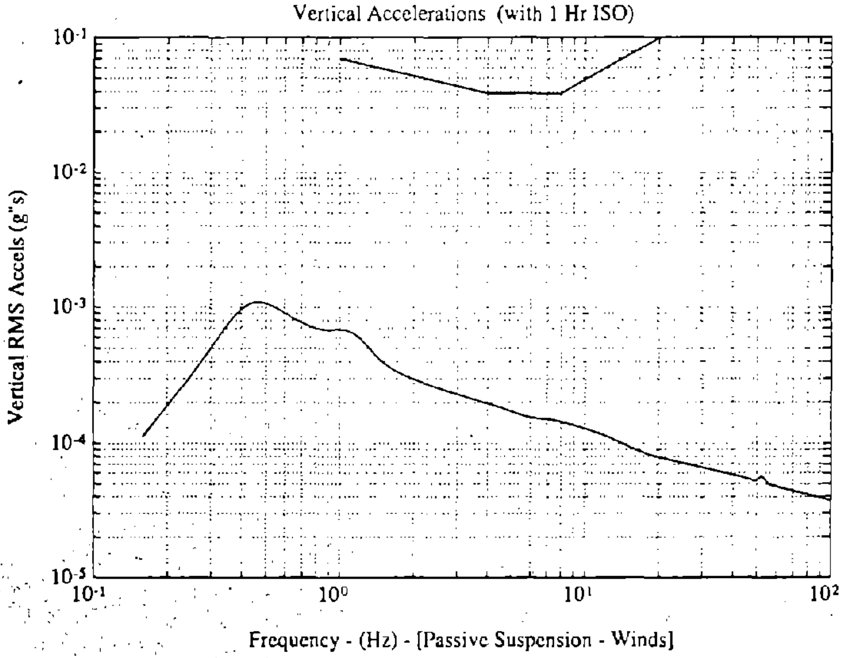

Figure D.4 - Vertical 1/3 octave accelerations for passive suspension with wind inputs only

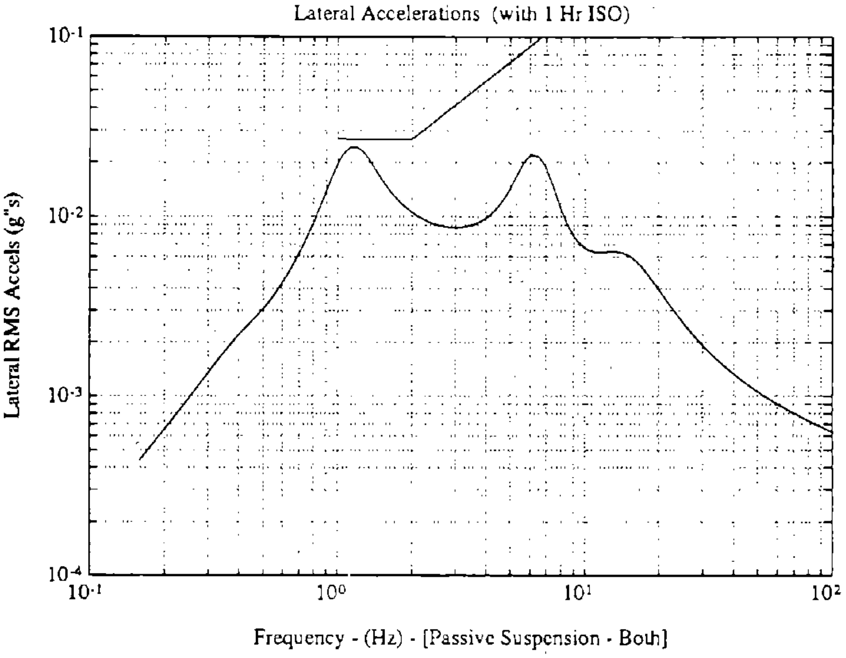

Figure D.5 - Lateral 1/3 octave accelerations for passive suspension with both guideway and wind inputs

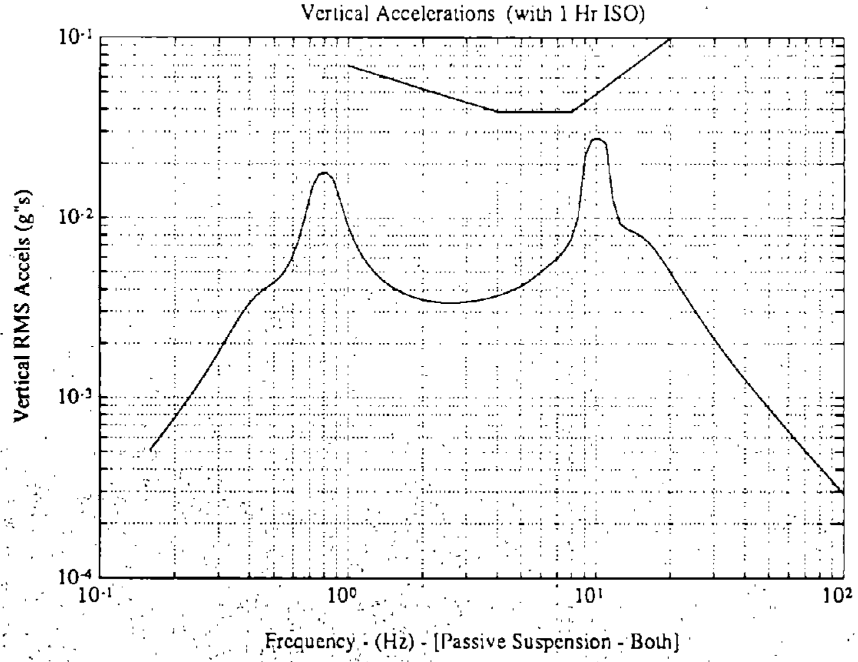

Figure D.6 - Vertical 1/3 octave accelerations for passive suspension with both guideway and wind inputs

D.2 Active Hydraulic Secondary Suspension

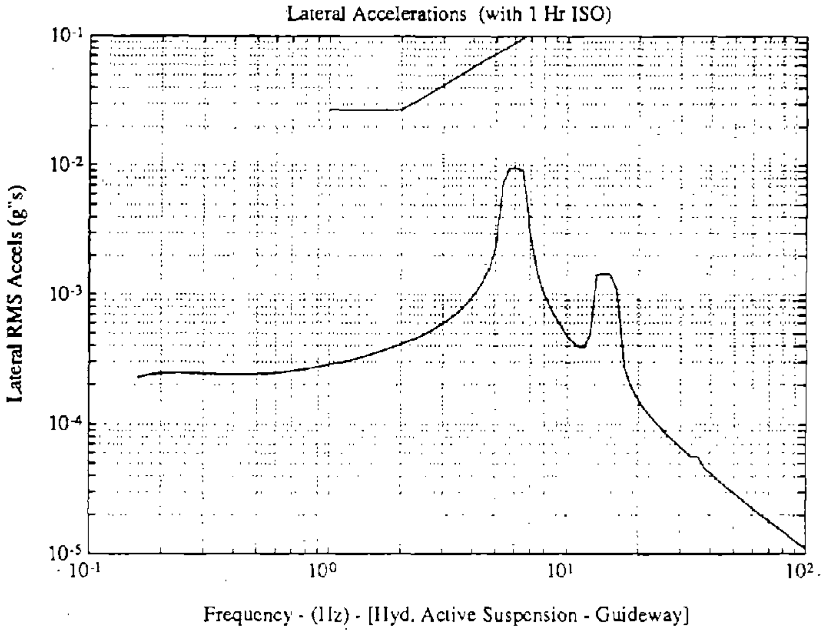

Figure D.7 - Lateral 1/3 octave accelerations for active hydraulic suspension with guideway inputs only

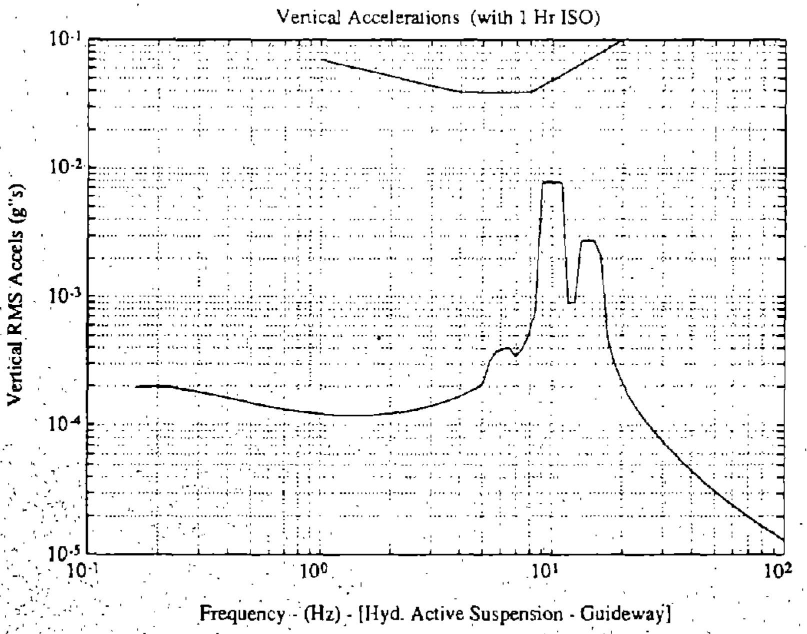

Figure D.8 - Vertical 1/3 octave accelerations for active hydraulic suspension with guideway inputs only

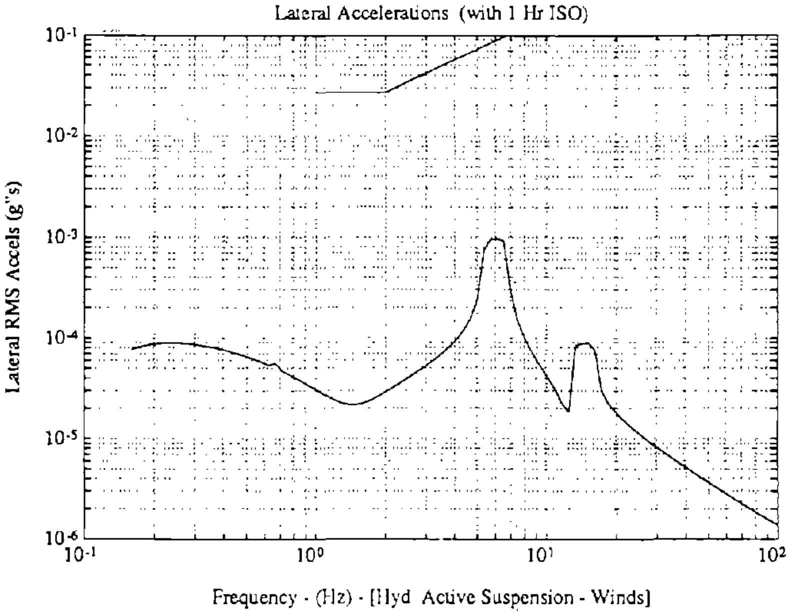

Figure D.9 - Lateral 1/3 octave accelerations for active hydraulic suspension with wind inputs only

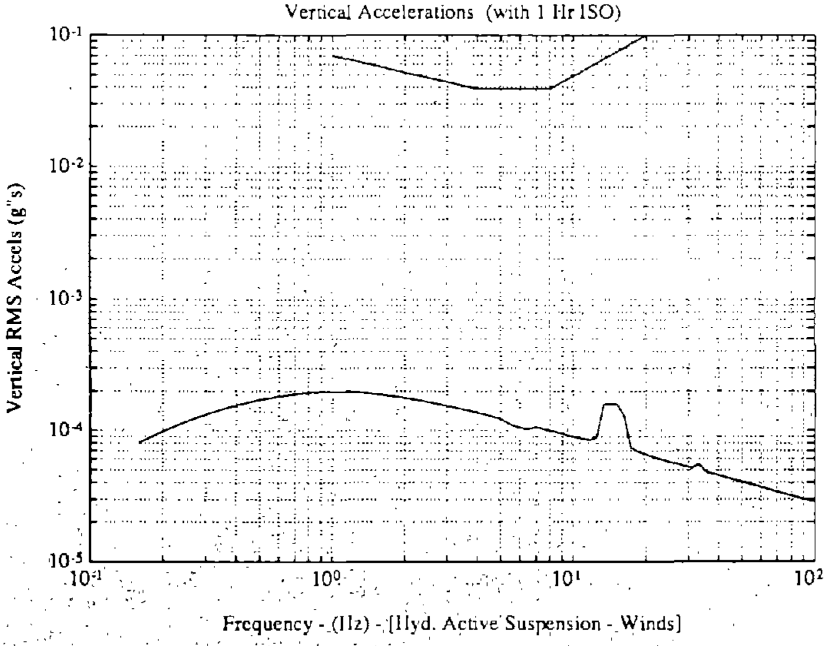

Figure D.10 - Vertical 1/3 octave accelerations for active hydraulic suspension with wind inputs only

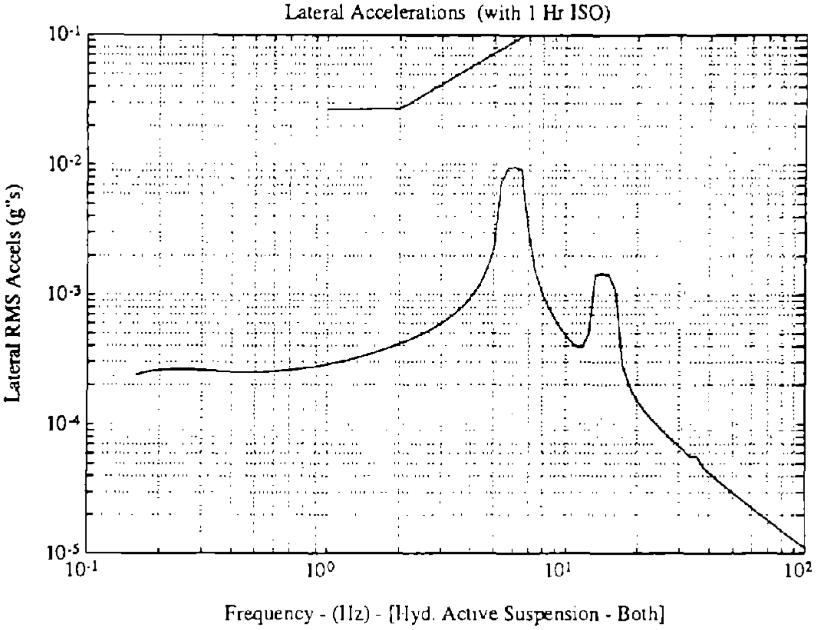

Figure D.11 - Lateral 1/3 octave accelerations for active hydraulic suspension with both guideway and wind inputs

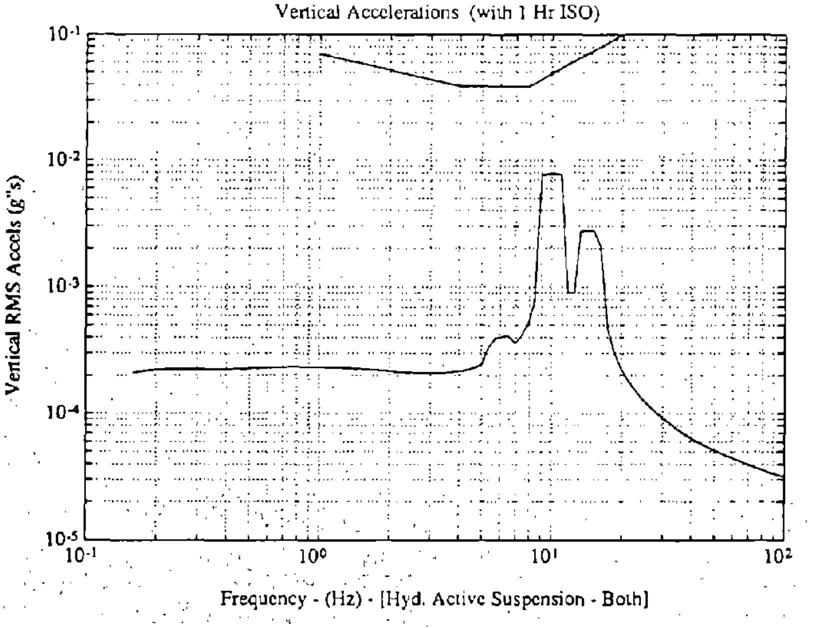

Figure D.12 - Vertical 1/3 octave accelerations for active hydraulic suspension with both guideway and wind inputs

D.2 Active Aero-Surfaces in Ground-Effect acting on Bogies

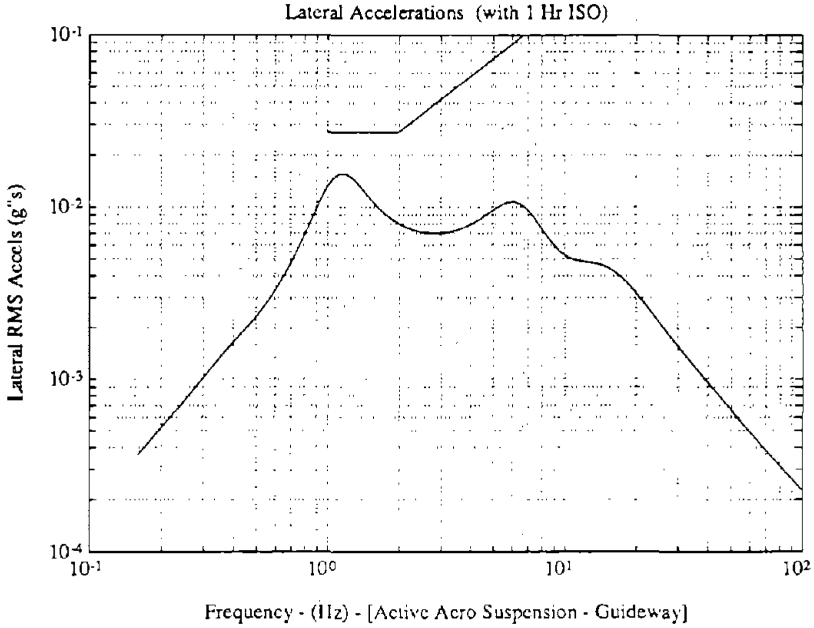

Figure D.13 - Lateral 1/3 octave accelerations for active aero-surfaces in ground-effect with guideway inputs only

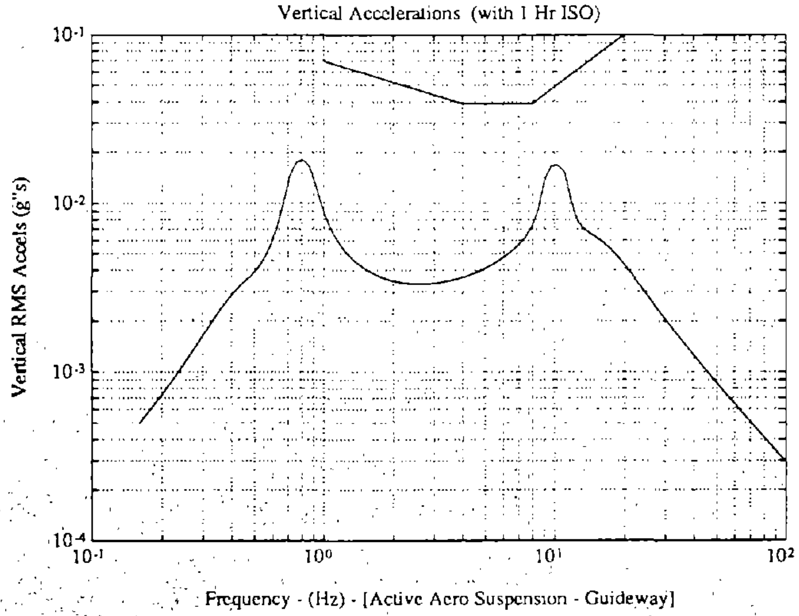

Figure D.14 - Vertical 1/3 octave accelerations for active aero-surfaces in ground-effect with guideway inputs only

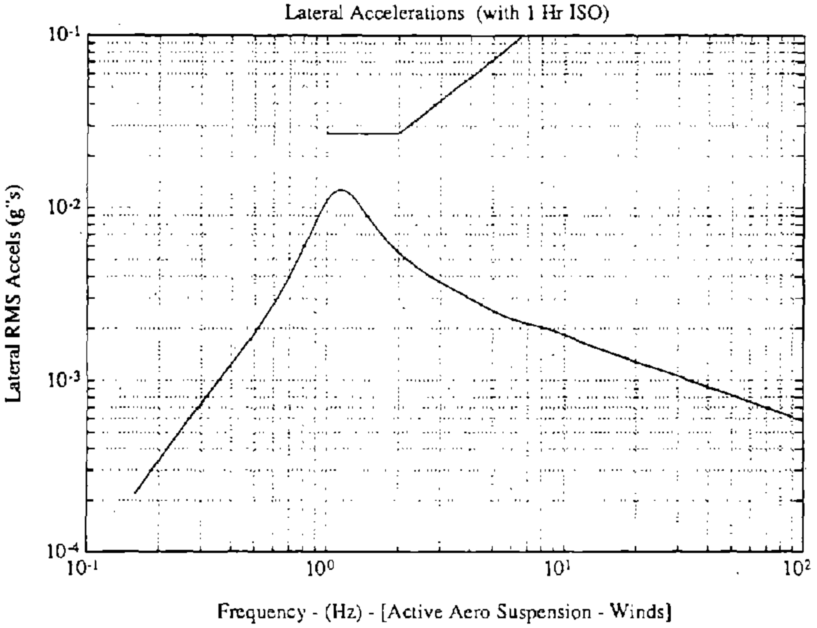

Figure D.15 - Lateral 1/3 octave accelerations for active aero-surfaces in ground-effect with wind inputs only

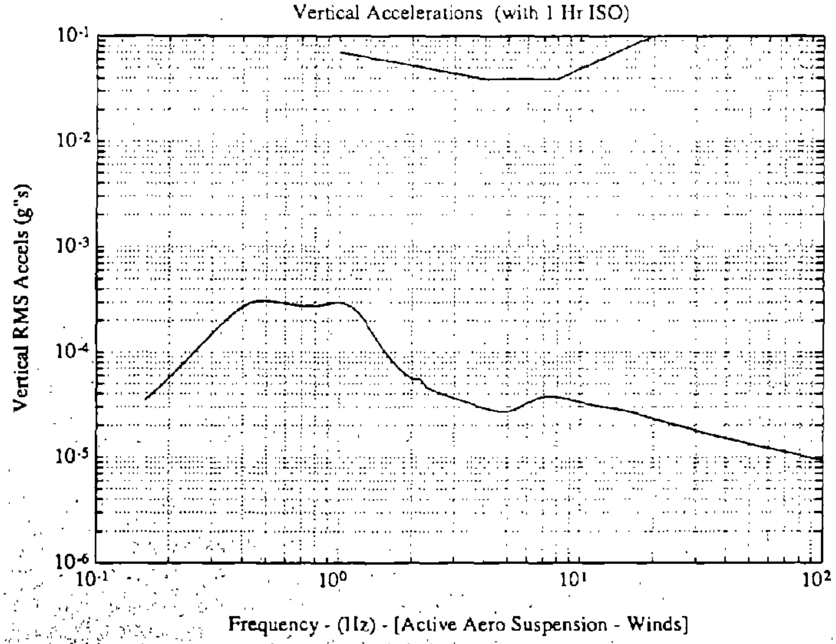

Figure D.16 - Vertical 1/3 octave accelerations for active aero-surfaces in ground-effect with wind inputs only

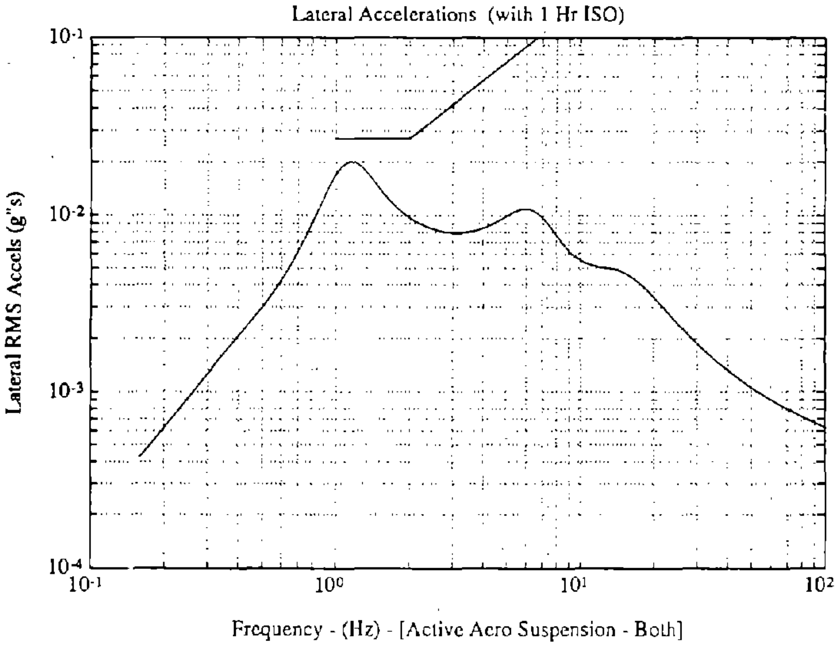

Figure D.17 - Lateral 1/3 octave accelerations for active aero-surfaces in ground-effect with both guideway and wind inputs

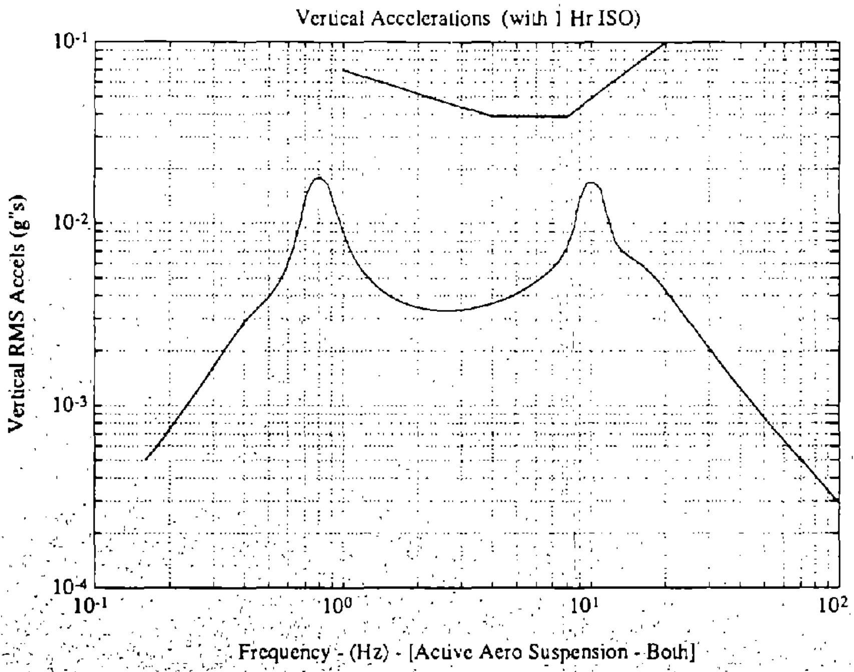

Figure D.18 - Vertical 1/3 octave accelerations for active aero-surfaces in ground-effect with both guideway and wind inputs

D.2 Active Secondary Suspension with both Hydraulic Actuators and Aero-Surfaces in Ground-Effect acting on Bogies

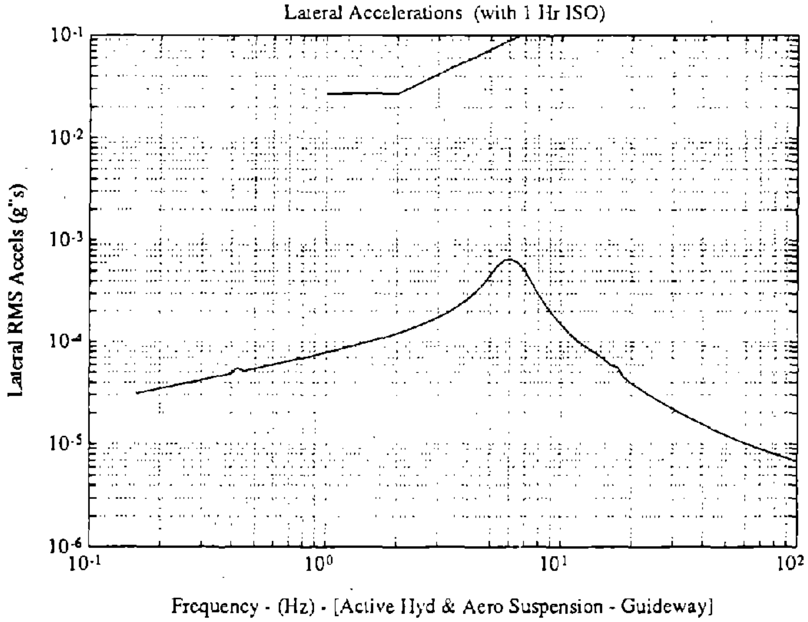

Figure D.19 - Lateral 1/3 octave accelerations for active system with both hydraulic actuators and aero-surfaces in ground-effect with guideway inputs only

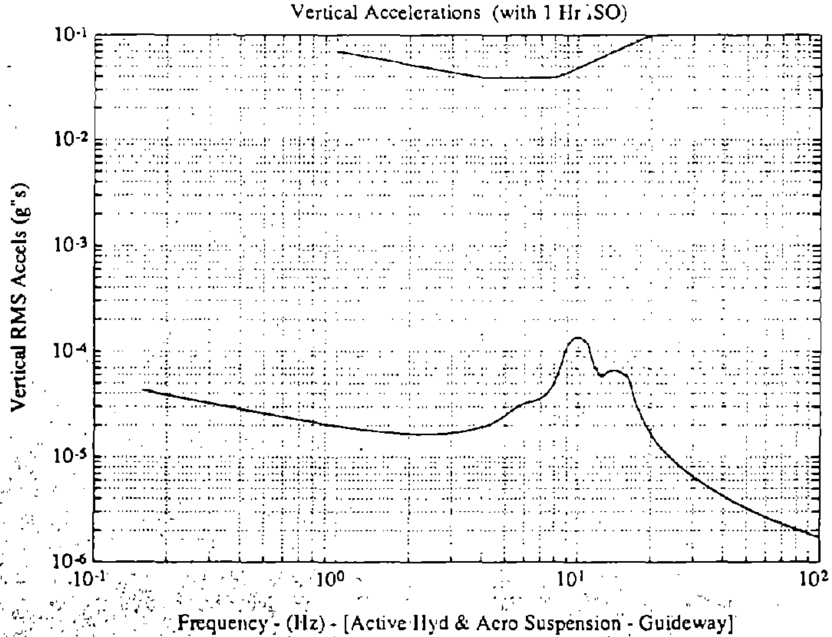

Figure D.20 - Vertical 1/3 octave accelerations for active system with both hydraulic actuators and aero-surfaces in ground-effect with guideway inputs only

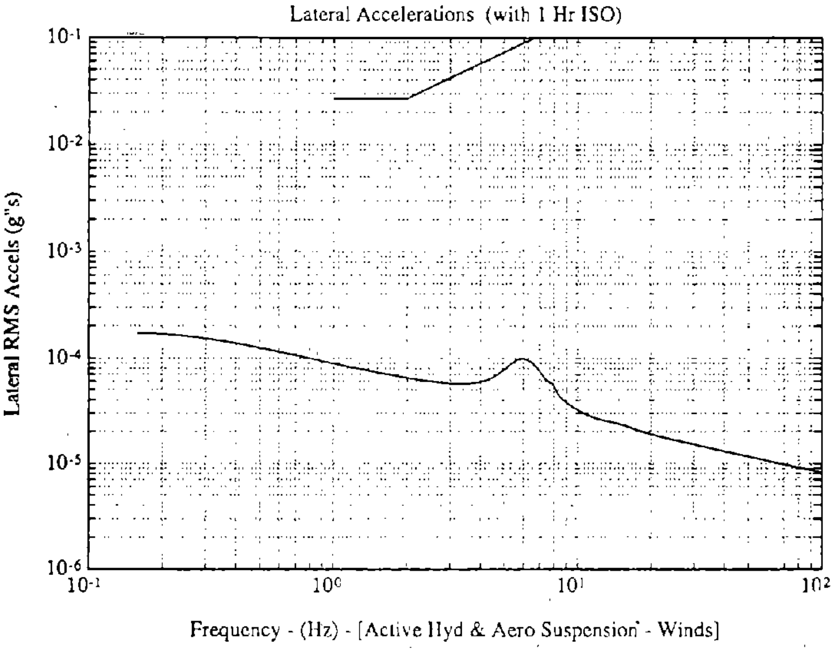

Figure D.21 - Lateral 1/3 octave accelerations for active system with both hydraulic actuators and aero-surfaces in ground-effect with wind inputs only

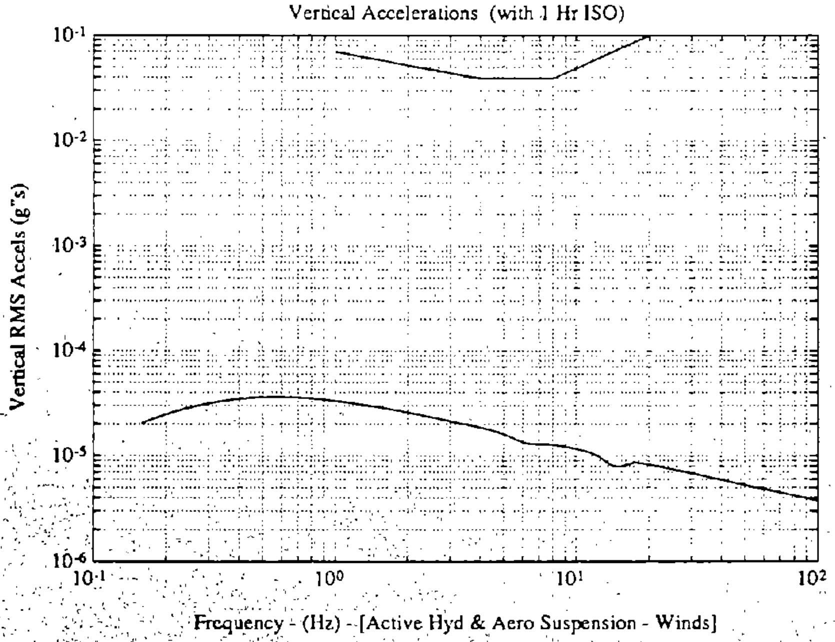

Figure D.22 - Vertical 1/3 octave accelerations for active system with both hydraulic actuators and aero-surfaces in ground-effect with wind inputs only

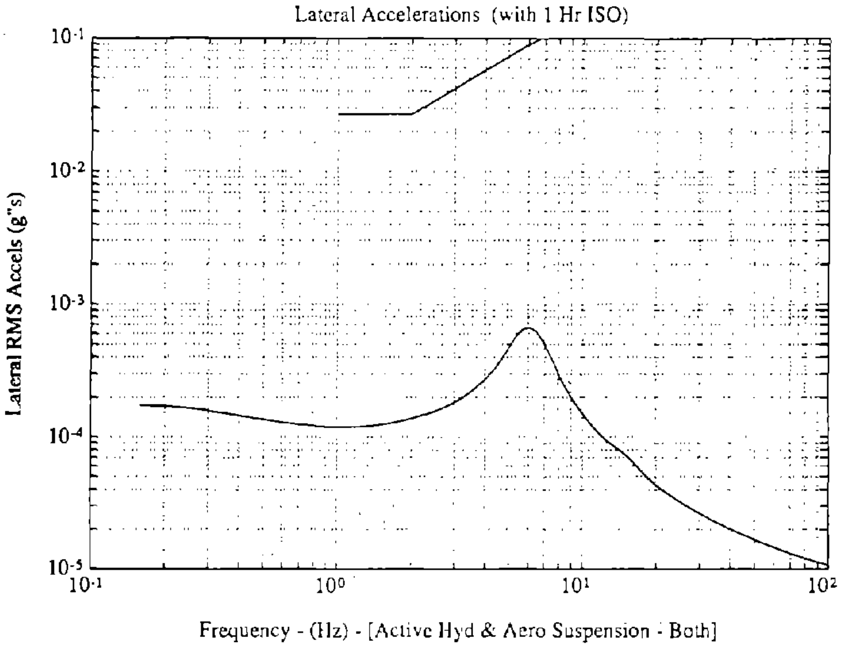

Figure D.23 - Lateral 1/3 octave accelerations for active system with both hydraulic actuators and aero-surfaces in ground-effect with both guideway and wind inputs

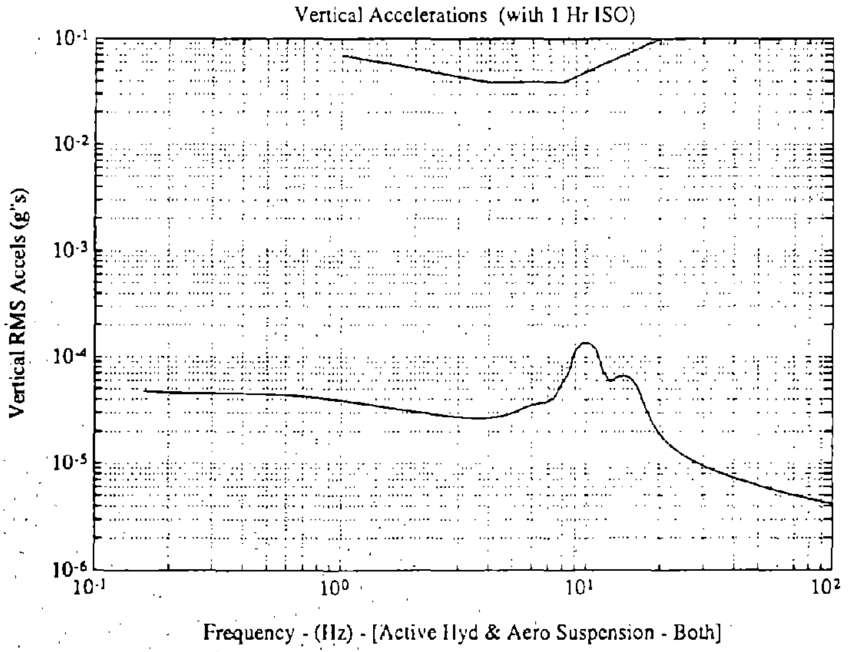

Figure D.24 - Vertical 1/3 octave accelerations for active system with both hydraulic actuators and aero-surfaces in ground-effect with both guideway and wind inputs

D.5 System with Active Wings on Train

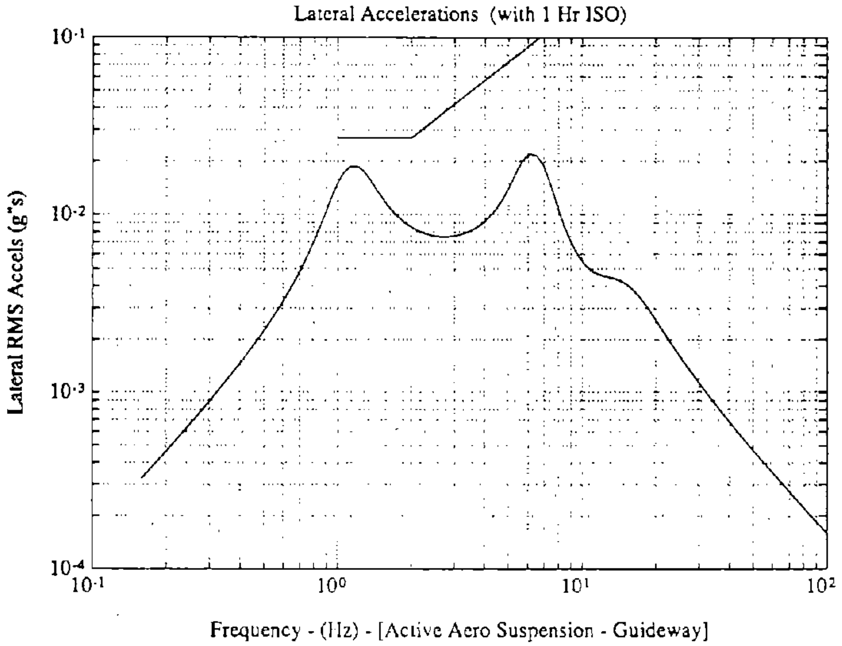

Figure D.25 - Lateral 1/3 octave accelerations for active wings on train with guideway inputs only

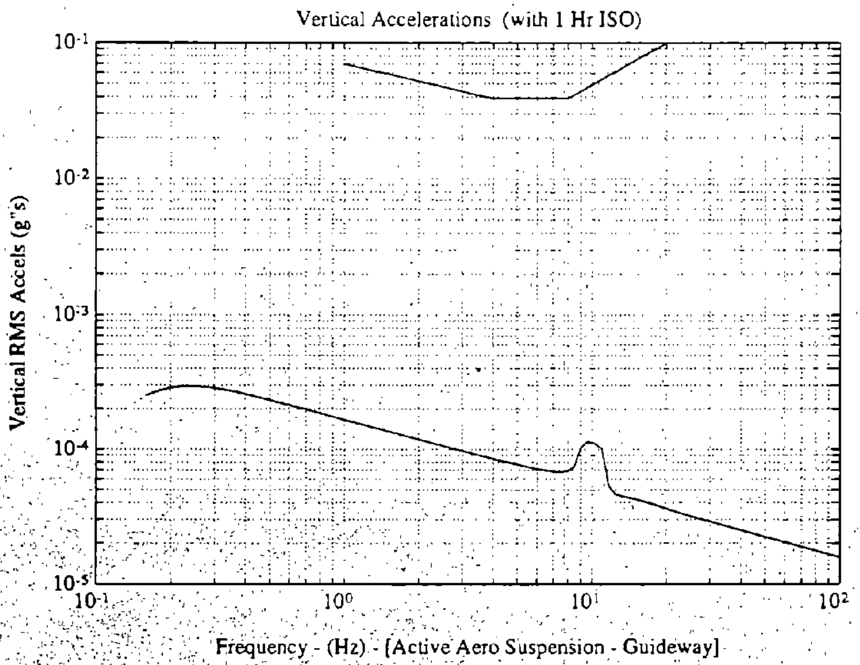

Figure D.26 - Vertical 1/3 octave accelerations for active wings on train with guideway inputs only

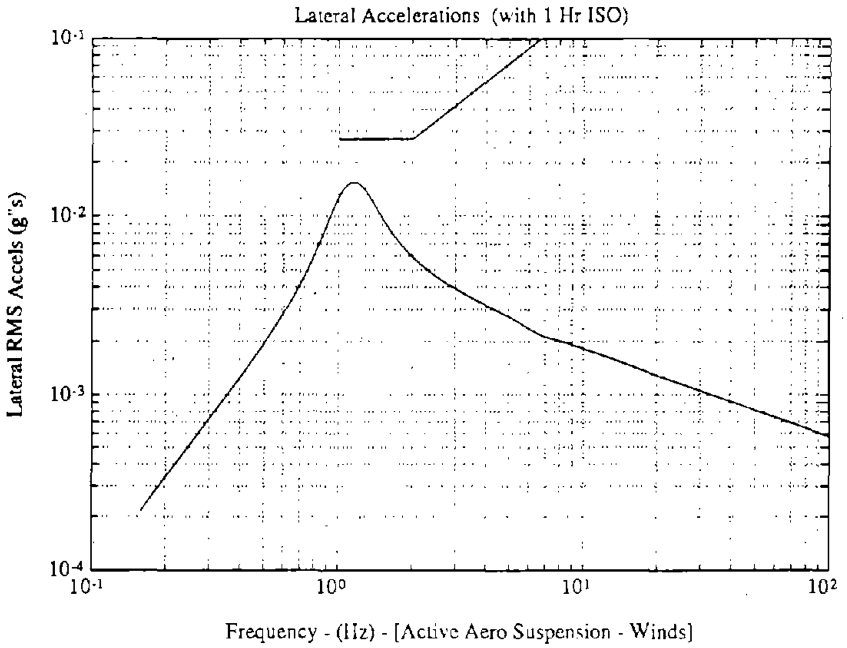

Figure D.27 - Lateral 1/3 octave accelerations for active wings on train with wind inputs only

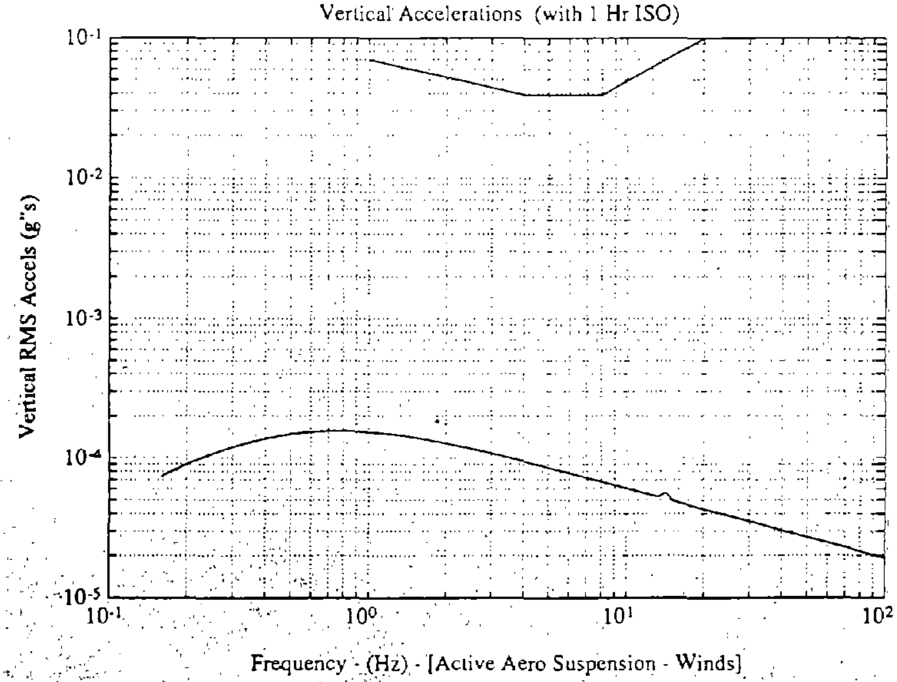

Figure D.28 - Vertical 1/3 octave accelerations for active wings on train with wind inputs only

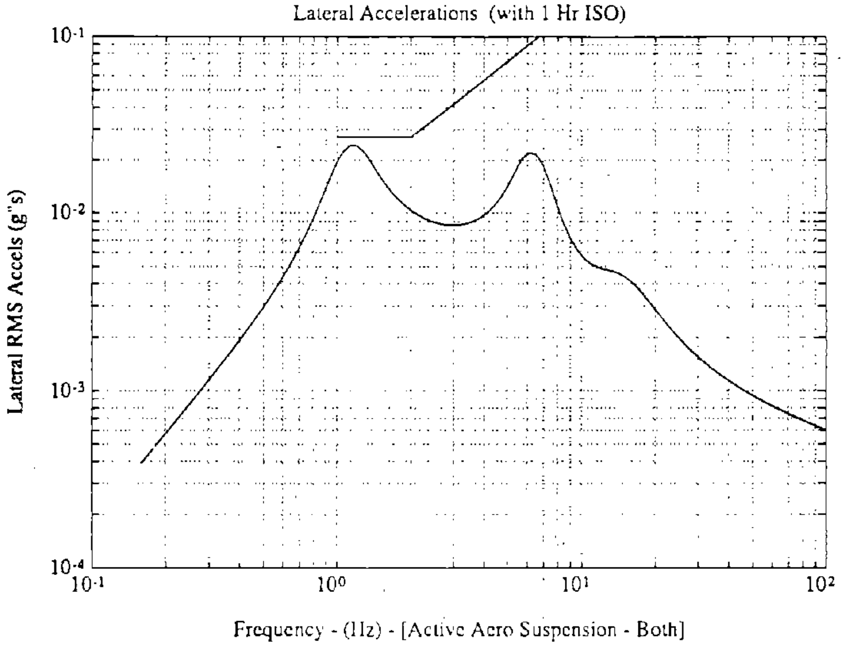

Figure D.29 - Lateral 1/3 octave accelerations for active wings on train with both guideway and wind inputs

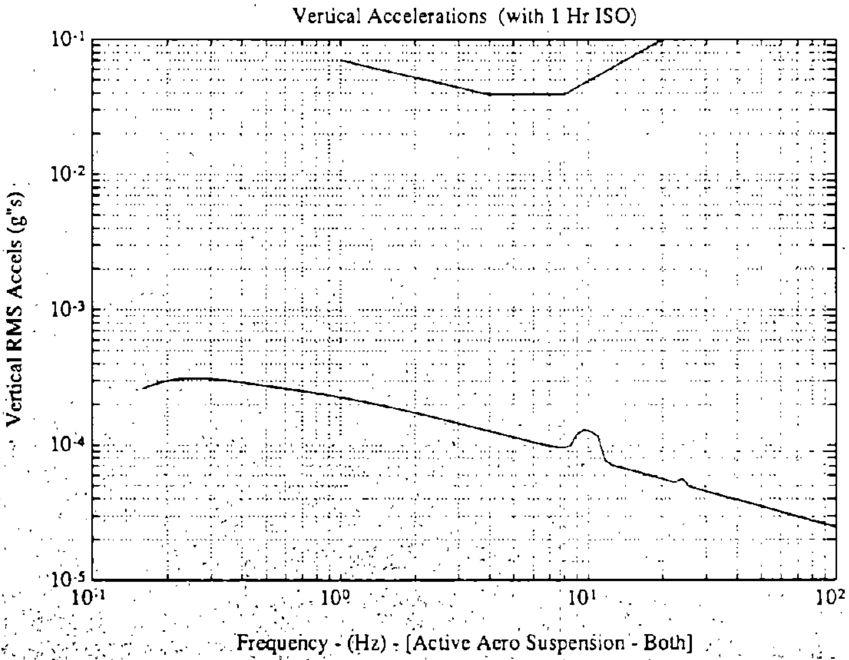

Figure D.30 - Vertical 1/3 octave accelerations for active wings on train with both guideway and wind inputs

D.6 Active System with Hydraulic Actuators andWings on Train

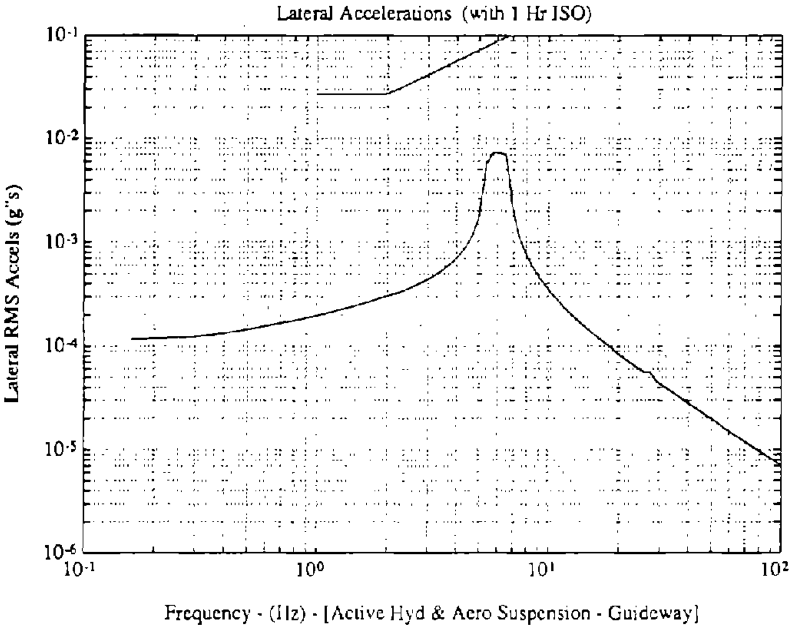

Figure D.31 - Lateral 1/3 octave accelerations for active system with both hydraulic elements and wings on train with guideway inputs only

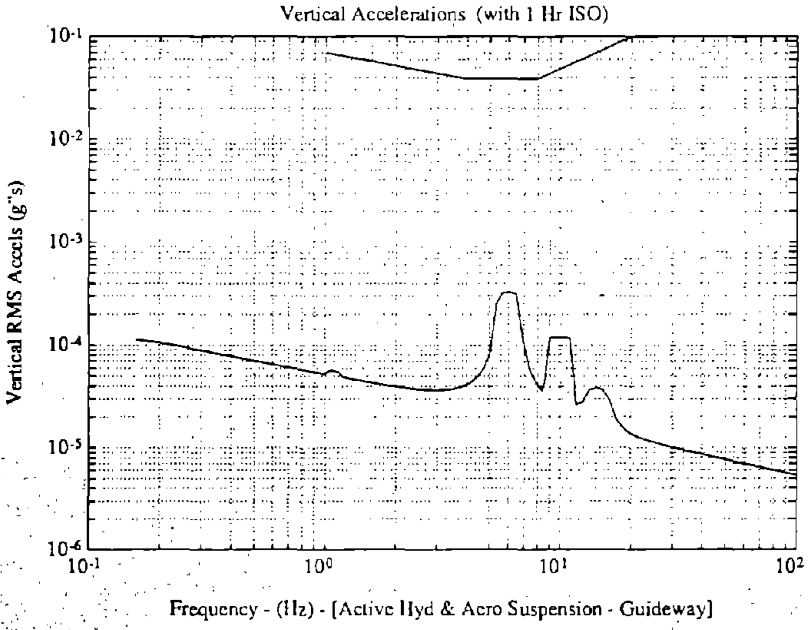

Figure D.32 - Vertical 1/3 octave accelerations for active system with both hydraulic elements and wings on train with guideway inputs only

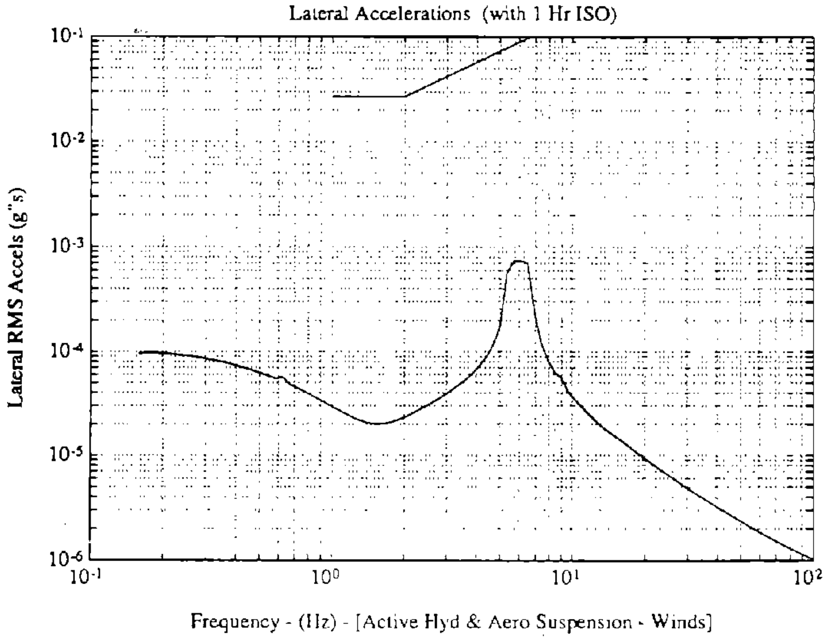

Figure D.33 - Lateral 1/3 octave accelerations for active system with both hydraulic elements and wings on train with wind inputs only

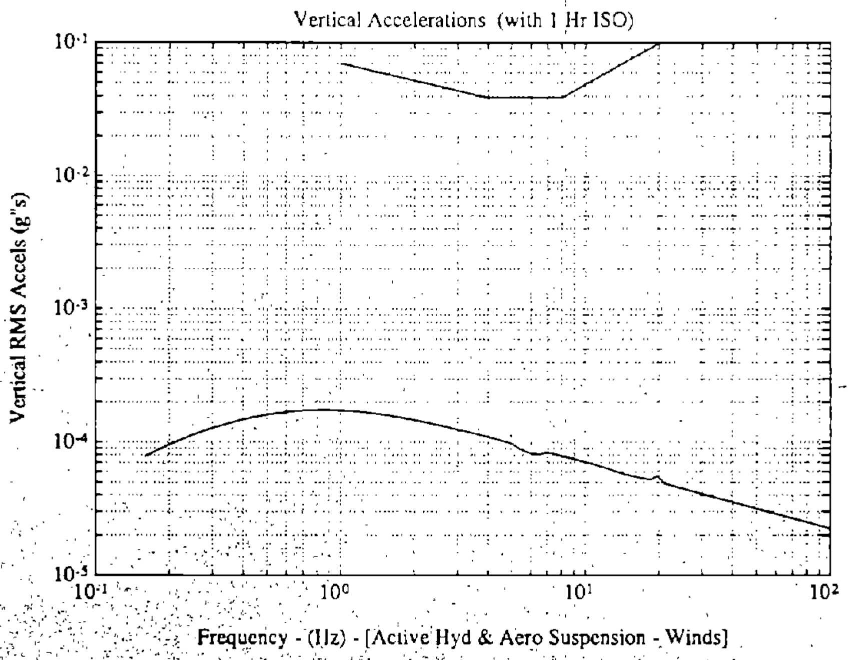

Figure D.34 - Vertical 1/3 octave accelerations for active system with both hydraulic elements and wings on train with wind inputs only

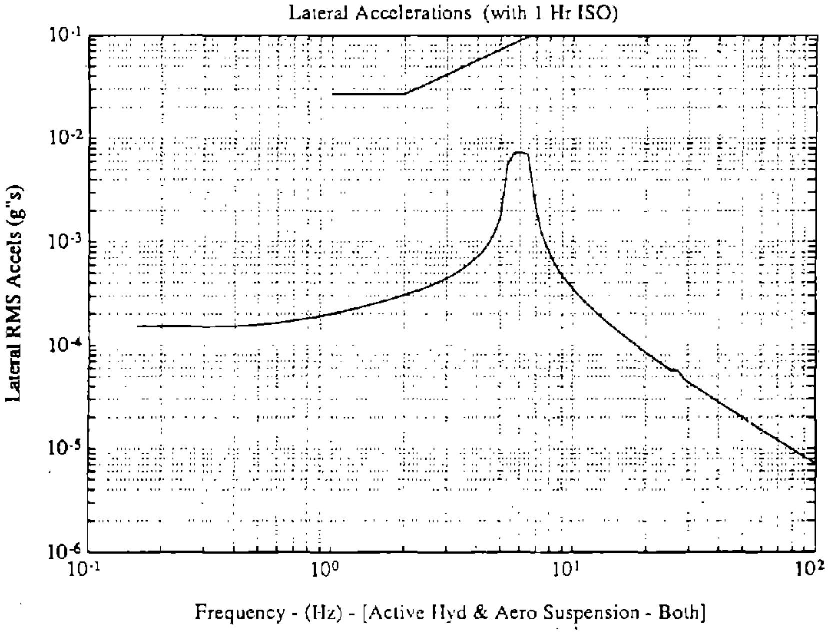

Figure D.35 - Lateral 1/3 octave accelerations for active system with both hydraulic elements and wings on train with both guideway and wind inputs

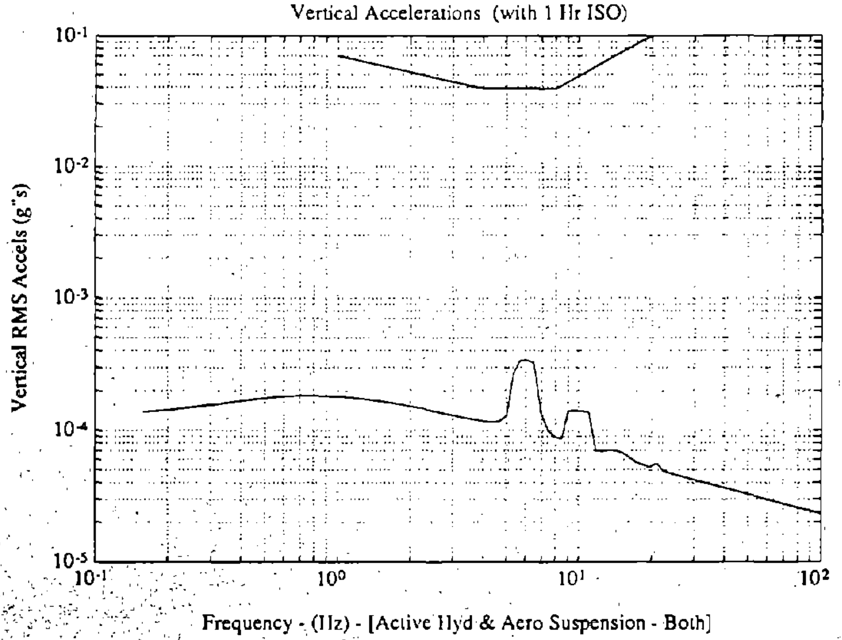

Figure D.36 - Vertical 1/3 octave accelerations for active system with both hydraulic elements and wings on train with both guideway and wind inputs

APPENDIX E

PREVIOUSLY RELEASED MEMO COVERING MODE DESCRIPTION

555 Technology Square, Cambridge, Massachusetts 02139
Mail Station 4C
Telephone (617) 258-2426

To: Maglev Community

From: Steve Mark, Draper Lab Fellow, Advanced Control Systems Group

Date: March 13, 1992

Subject: Choice of suspension stiffness for Maglev vehicles

Introduction

The purpose of this memo is to present a recent discovery that has developed from our Maglev train suspension research. I believe this finding to be in contradiction with what most people in the Maglev community previously believed to be correct. What we have found is that increasing the primary suspension stiffness above about 2.5 Hz does not improve the tracking of the bogie on the guideway. Instead, for secondary suspension damping ratios less than 0.2, the bogie's guideway tracking is slightly poorer. Since most of the primary suspension system designs up to this point have had natural frequencies above 2.5 Hz, the question is whether the benefits of such a stiff primary suspension outweigh the penalties. This memo will present the penalties of an overly stiff primary suspension, and dispel the myth that the stiffer the primary suspension, the more closely the bogie will track the guideway surface.

Background

Figure 1 is a drawing of the Maglev train suspension model we are currently using. The suspension parameters used also appear below.

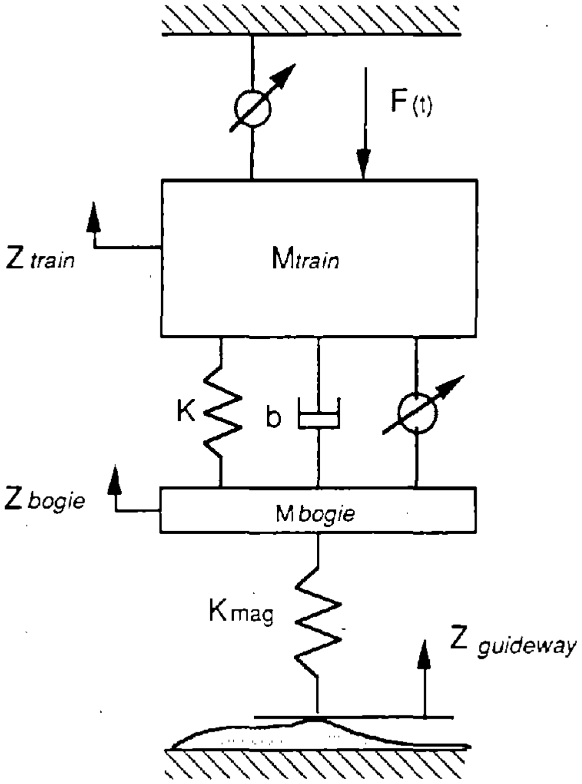

Figure 1: One-dimensional suspension model

The suspension parameters used in our model are:

Total mass = 64 tonne
Train mass = 48 tonne
Bogie mass = 16 tonne
Primary nat. freq = 2.5 Hz
Secondary nat. freq = 1.0 Hz
Secondary damping ratio = 0.2

The wind input is modeled as a first order Markov process, with a break frequency at 1 rad/sec. The guideway disturbance is modelled as a random input with power spectral density $A_g V/w^2$, where A_g is a roughness parameter, V is train forward velocity, and w is the frequency of the disturbance.

Using the equations of motion of the system, I will explain this increase in the airgap variation that occurs with increasing primary suspension frequency above 2.5 Hz. Then I will present data that supports my reasoning. Figure 2 depicts the two fundamental modes of a 1-

dimensional Maglev vehicle suspension system. These modes are obtained from the eigenvectors that correspond to the eigenvalues of the system's "A" matrix.

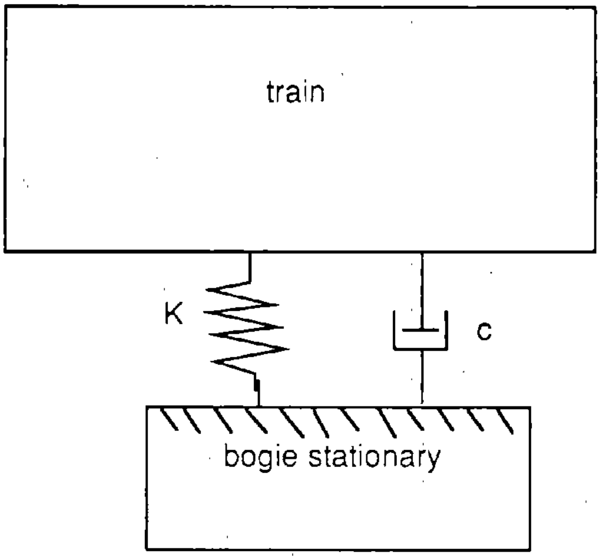

Mode 1 - train moves above stationary bogie

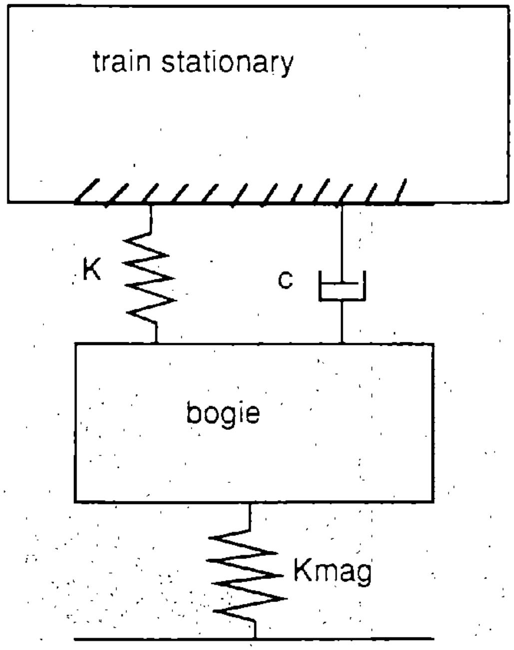

Mode 2 - bogie moves below stationary train

Figure 2: Modes of the system

Mode 1 corresponds to motion dominated by oscillation of the train on top of the bogie. Mode 2 corresponds to oscillation of the bogie between the guideway and the train. Mode 2 has a higher natural frequency, as defined below. These modes are only approximations of the actual motions, but are still fairly accurate. What I mean by this is that while the train might not be completely stationary in mode 2, the magnitude of train motion is small in comparison to the magnitude of bogie motion. The equations governing these fundamental modes are:

mode 1

$$s^2 + \frac{c}{m_t}s + \frac{K}{m_t}$$

$$\omega_{n1}=\sqrt{\frac{K}{m_t}} \qquad \xi_1=\frac{c}{2}\sqrt{\frac{1}{Km_t}}$$

mode 2

$$s^2 + \frac{c}{m_b} + \frac{K + K_{mag}}{m_b}$$

$$\omega_{n2}=\sqrt{\frac{K+ K_{mag}}{m_b}} \qquad \xi_2=\frac{c}{2}\sqrt{\frac{1}{(K + K_{mag})m_b}}$$

Problem Definition

The strange behavior to be explained is that the bogie tracks the guideway more poorly (i.e.. with greater RMS airgap variation) as the primary suspension is made stiffer. This is only true when the primary suspension frequency is above 2.5 Hz, and the damping ratio of the secondary suspension is close to 0.1, where the primary suspension natural frequency is defined as:

$$\omega_{\mathrm{primary}} = \sqrt{\frac{K_{\mathrm{mag}}}{m_t + m_b}}$$

Please note that this is not the natural frequency of either of the two modes of the system. Below 2.5 Hz, as the primary suspension stiffness is reduced, the bogie tracking worsens. The fact that the tracking would begin to worsen again when increasing the primary suspension natural frequency beyond 2.5 Hz may seem unusual, since we would expect that an infinitely stiff primary would result in perfect guideway tracking by the bogie.

Analytical Analysis

Because the poorer bogie tracking of the guideway is a result of the coupling between the modes, the unexpected behavior of the system cannot be explained by the two simple, decoupled equations given above. One might first be inclined to think that the effect is due to the fact that the damping ratio of mode 2 increases as the magnetic stiffness is reduced, without any effects on the other mode. This change in the damping ratio can be seen directly from the equation for the damping ratio for mode 2, knowing that the damping term "c" in the characteristic equation for that mode is held constant. However, increasing the natural frequency of the system described by mode 2 while holding the damping term "c" constant will not produce the increased airgap variation at high frequencies observed in the Maglev train simulations. This was verified in a separate simulation of the decoupled mode.

The transfer function relating airgap variations to guideway displacements is:

$$\frac{X_{air}}{X_g} = \frac{\frac{K + K_{mag}}{m_b}}{\left(s^2 + \frac{c}{m_b}s + \frac{K + K_{mag}}{m_b}\right) - \left(\frac{c}{m_b}s\left(\frac{\frac{c}{m_t}s + \frac{K}{m_t}}{s^2 + \frac{c}{m_t}s + \frac{K}{m_t}}\right)\right.} - 1$$

We can see that if we substitute s=jw, where w is the natural frequency of either of the two decoupled modes, into the above equation, a resonance occurs. The magnitudes of the peaks at these resonances are large because both modes are very lightly damped.

Following are the equations obtained when a value of jw, corresponding to each of the modes is plugged into the above equation. These equations give the value of the maximum singular value at each of these frequencies.

case 1: natural frequency of mode 1

$$\frac{X_{air}}{X_g} = \frac{\frac{K + K_{mag}}{m_b}}{\left(\frac{K}{m_t} + j\frac{c}{m_b}\sqrt{\frac{K}{m_t}} + \frac{K + K_{mag}}{m_b}\right) - \left(j\frac{c}{m_b}\sqrt{\frac{K}{m_t}} + \frac{K}{m_t}\right)} - 1$$

case 2: natural frequency of mode 2

$$\frac{X_{air}}{X_g} = \frac{\frac{K + K_{mag}}{m_b}}{\left(j\frac{c}{m_b}\sqrt{\frac{K + K_{mag}}{m_b}}\right) - \left(j\frac{c}{m_b}\sqrt{\frac{K + K_{mag}}{m_b}}\left(\frac{\frac{jc}{m_t}\sqrt{\frac{K + K_{mag}}{m_b}} + \frac{K}{m_t}}{\frac{K + K_{mag}}{m_b} + \frac{jc}{m_t}\sqrt{\frac{K + K_{mag}}{m_b}} + \frac{K}{m_t}}\right)\right.} - 1$$

Call w1 the natural frequency of mode 1, and w2 the natural frequency of mode 2. Then when Kmag is increased, the airgap peak at w1 decreases, while the peak at w2 increases. This is graphically depicted in Figure 3, which shows singular value plots for systems with three different values of primary stiffness: at, below, and above the "optimal" 2.5 Hz. This plot is for the case of 0.1 damping ratio for the secondary.

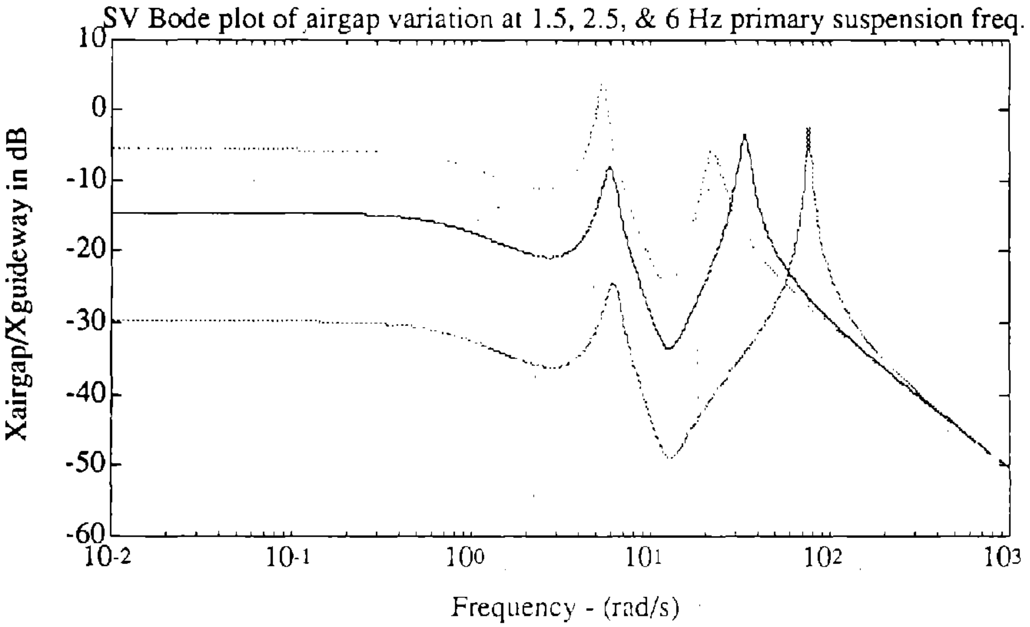

Figure 3: Singular Value plots at three different Primary Suspension Frequencies - in order from top to bottom at the left, 1.0 Hz, 2.5 Hz, and 6 Hz Primary Frequency

The reason that a 2.5 Hz primary suspension natural frequency gives the lowest RMS variation of the airgap is that at this frequency the total area under the singular value bode plots is a minimum. If the primary suspension natural frequency is either above or below 2.5 Hz, the area under one of the two peaks increases more than the area under the other peak decreases. This explains why the airgap RMS variation increases as the primary suspension stiffness is increased beyond 2.5 Hz: the peak in the singular value bode plot at the resonance of mode 2 increases more than the peak at the resonance of mode 1 decreases, resulting in a slight net increase. Figures 4 and 5 are plots of the singular values for the 2.5 and 6 Hz primary suspension natural frequency cases. These plots have a non-logarithmic frequency axis, so it is easier to see that there is more area under the curve in figure 5 that under the curve in figure 4. This area has a direct correspondence with the rms airgap variation.

Numerical Analysis & Suspension Design

I will now provide an explanation for the choice of primary and secondary suspension parameters given earlier. This will be supplemented with data that supports my conclusions.

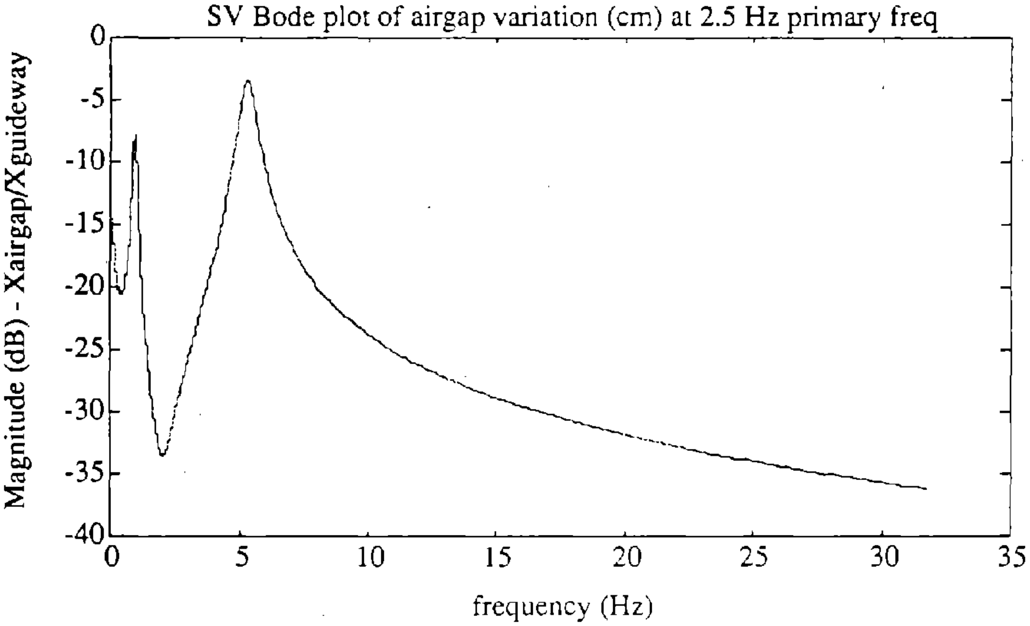

Figure 4: Airgap SV plot at 2.5 Hz primary with non-logarithmic frequency axis

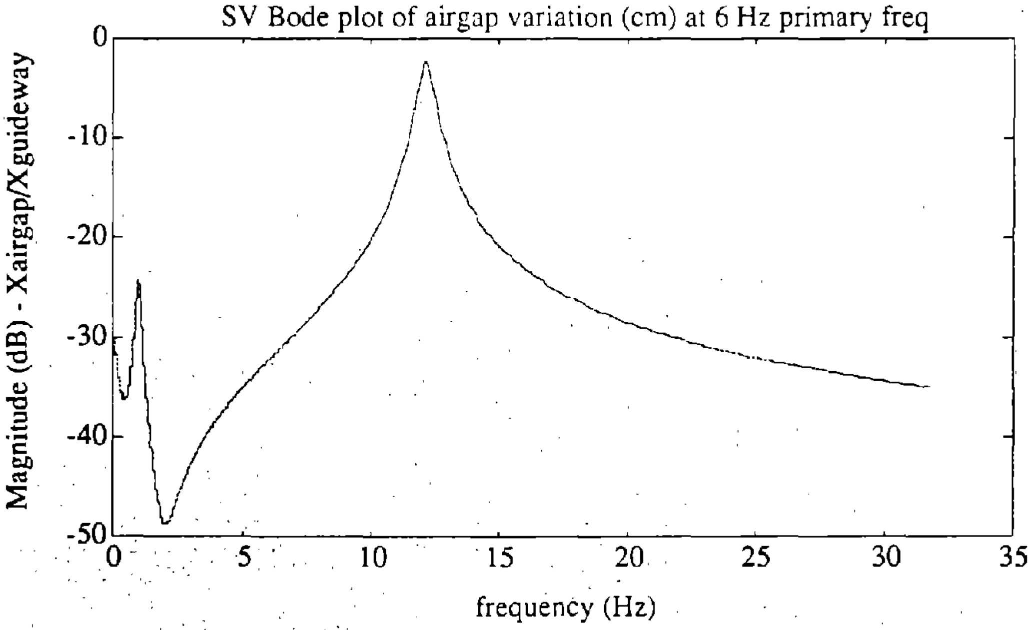

Figure 5: Airgap SV plot at 6 Hz primary with non-logarithmic frequency axis

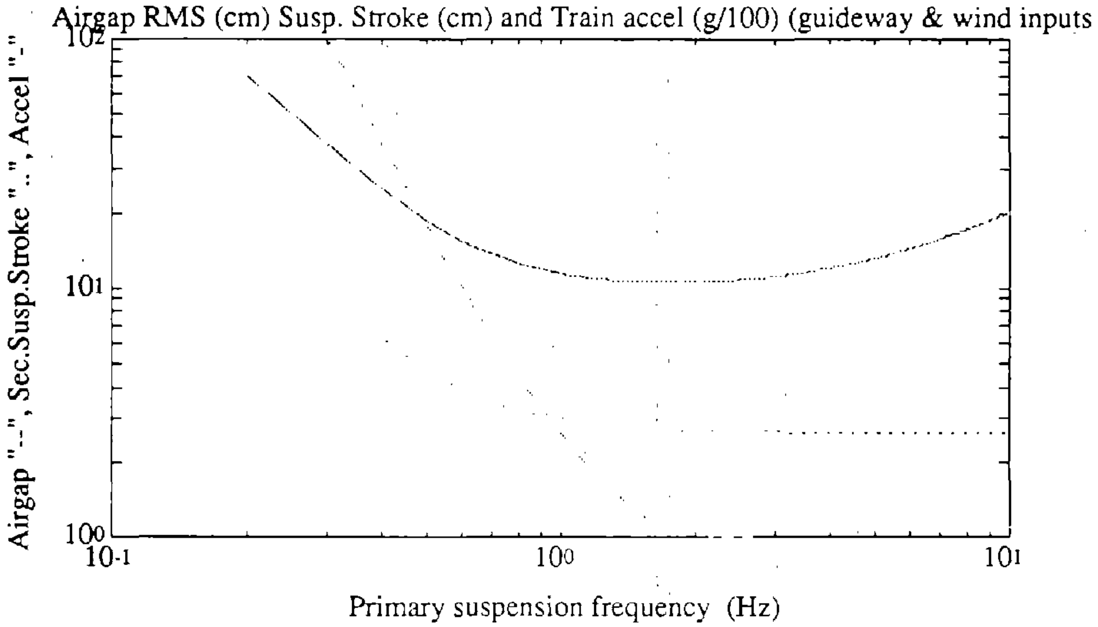

Figure 6: Effect of primary frequency on variables of interest

Figure 6 is a graph of airgap variation, secondary suspension stroke variation, and acceleration of the train, all expressed as RMS values, vs. primary suspension frequency. In this plot,

$$\xi_{sec} = \frac{c}{2}\sqrt{\frac{1}{Km_t}} = 0.1,$$

which by our definition is both the damping ratio of mode 1 and the damping ratio of the secondary suspension. Also,

$$\omega_{sec} = \sqrt{\frac{K}{m_t}} = 1.0\ \text{Hz},$$

which is the secondary suspension natural frequency. Both guideway and wind disturbance inputs have been included in the evaluation of the RMS values plotted on this graph.

The exclusion of the wind inputs would not alter the basic result that this memo is presenting. However, including both wind and guideway inputs in the model when creating these graphs justifies the use of said plots for choosing the suspension parameters, since we have accounted for all known inputs. When both wind and guideway inputs are included, the model is intended to represent lateral dynamics, since the wind inputs are crosswinds.

It can be seen in Figure 6 that the lowest airgap variation occurs at about 2.5 Hz. At this frequency, the acceleration curve is nearly at its lowest point. Although the RMS accelerations are not quite at their minimum, they are very close to this value. Further, the secondary suspension stroke required at 2.5 Hz is almost as low as achievable. Therefore, we conclude from this graph alone that the primary suspension frequency should be 2.5 Hz when using these secondary suspension parameters. We will check this conclusion against other graphs as well.

One may question the validity of varying the primary suspension stiffness while leaving the secondary suspension stiffness constant. The reason this was done can be seen by looking at the governing equations of mode 1. Any decrease in the stiffness of this mode will decrease the accelerations of the train, but will simultaneously increase the required suspension stroke.

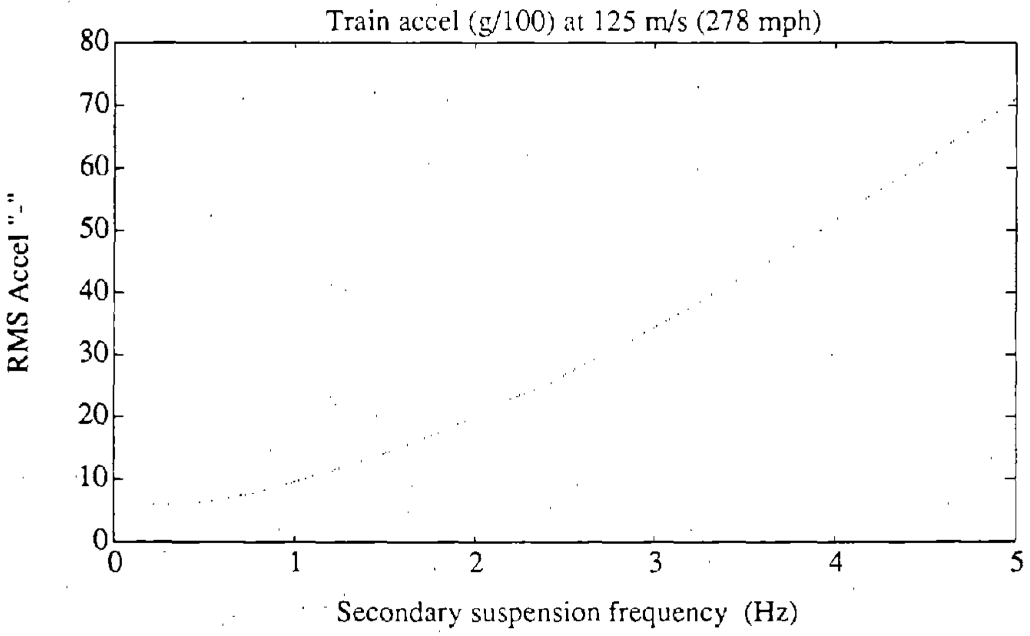

Figure 7: Train Acceleration vs Secondary Suspension Frequency

Graphs of the data support this conclusion. The secondary suspension stiffness cannot be decreased to improve the ride quality, as suggested by Figure 7 (a plot of train acceleration vs secondary suspension frequency). If this were done, the secondary suspension stroke would become larger than practical, as can be seen in the plot of secondary suspension stroke vs secondary suspension frequency in Figure 8.

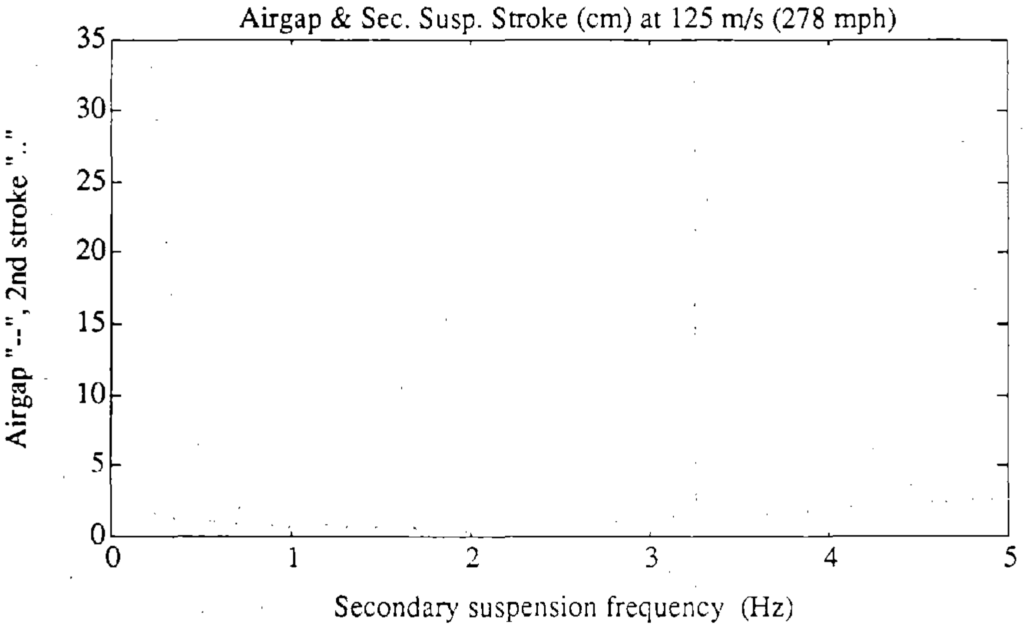

Figure 8: Airgap & Suspension Stroke vs. Secondary Suspension Frequency

Suspension Design Criteria Summary

The final recommended suspension parameters are:

Total mass = 64 tonne
Train mass = 48 tonne
Bogie mass = 16 tonne
Primary nat. freq = 2.5 Hz
Secondary nat. freq = 1.0 Hz
Secondary damping ratio = 0.2

A summary of the logic behind choosing the suspension parameters is as follows:

1). The secondary suspension stiffness is chosen on the premise that the allowable secondary suspension stroke will be 10 cm. Therefore, we designed the system to have an RMS variation of 3 cm.

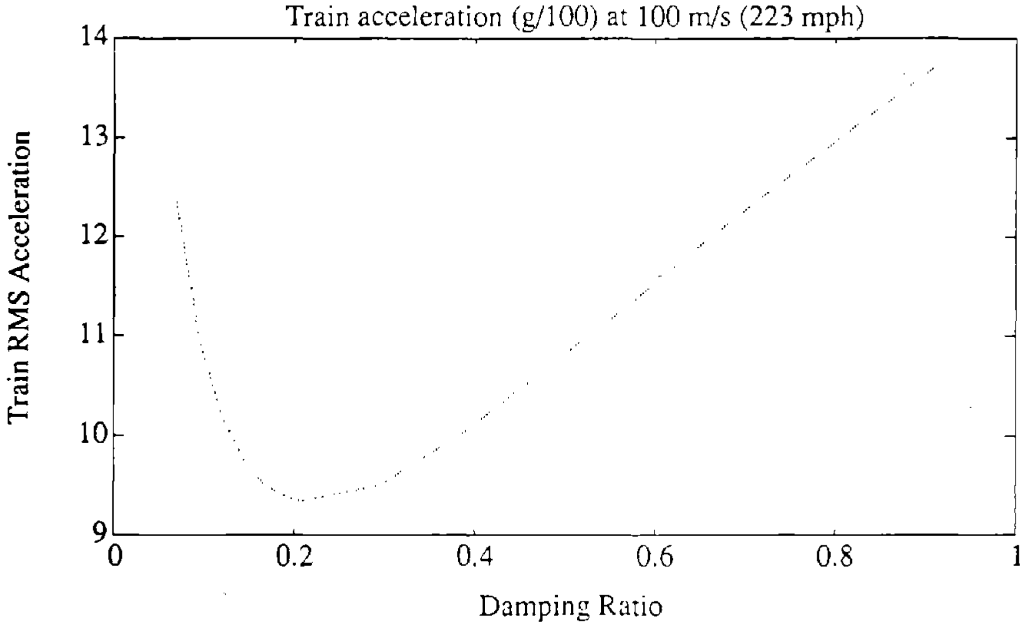

Figure 9: Train RMS Acceleration vs Secondary Suspension Frequency
damping ratio

2) Figure 9 shows a plot of the train acceleration vs the damping ratio. For this plot, the primary suspension frequency was set at 2.5 Hz. It is apparent from this graph that we wish to have a damping ratio for the secondary suspension of about 0.2. Use of this value will minimize the train accelerations, thus giving the best ride quality. This damping ratio is not ideal for either airgap variation or secondary suspension stroke, but it does not put them at unacceptable levels. Also, when the primary natural frequency is 6 Hz, the "preferred" damping ratio is 0.1, which is why the first plots in this memo are for a system with that value.

3) Figure 10 shows that with a secondary suspension damping ratio of 0.2, a primary suspension natural frequency of 2.5 Hz will still minimize airgap variations.

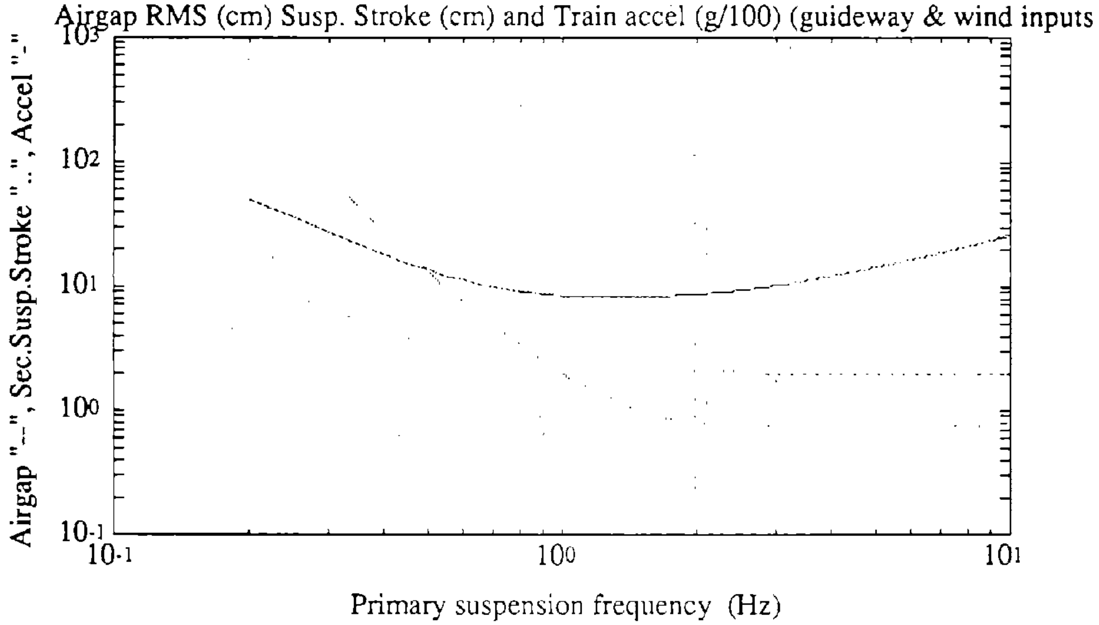

Figure 10: Variables of interest vs Primary suspension frequency

The RMS acceleration curve is farther from its minimum when the airgap variation is at the minimum, but not by a large amount. In any event, we still would prefer to keep the primary suspension natural frequency at 2.5 Hz (rather than higher) to minimize accelerations, since increasing the primary suspension natural frequency beyond 2.5 Hz will not improve the airgap. Note that the RMS airgap variations do not increase at higher primary natural frequencies because the additional damping introduced has decreased the peaks of the resonances at the frequencies of the two modes of the system. Indeed, the minimum airgap variation has actually been reduced by the higher damping ratio. Thus the changes to the primary and secondary suspensions complement each other: the increased damping ratio of the secondary reduces both the airgap variations and the train accelerations. Now all of the suspension parameters have been chosen.

It is worthy to note that if the damping ratio of the secondary suspension were higher, around .707, the strange behavior is not present. This is because the oscillations at the resonant frequencies are not as large, because they are more highly damped. This is shown in both figures 11 and 12.

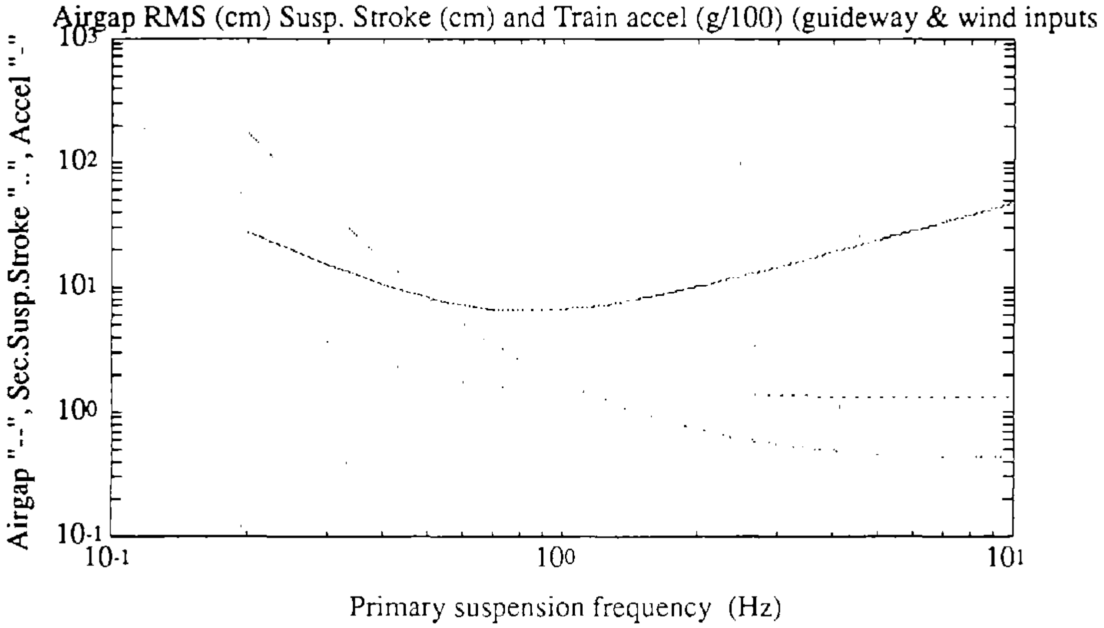

Figure 11: Variables of Interest vs Primary Suspension Frequency with damping ratio of Secondary Suspension = 0.707

However, note that with a damping ratio of .707, the primary suspension frequency at which the minimum train RMS acceleration occurs is at about 1 Hz. Meanwhile, the primary suspension frequency at which the minimum airgap variation occurs is up at 5-6 Hz, where the train accelerations are much higher. This mismatching of desirable primary natural frequencies for airgap and train acceleration minimization is one reason to keep the damping ratio at 0.2 or less. Remember that we already desire to do this to keep the train accelerations low. Thus we have more than one reason to keep the damping ratio low. A damping ratio no larger than 0.2 is desired.

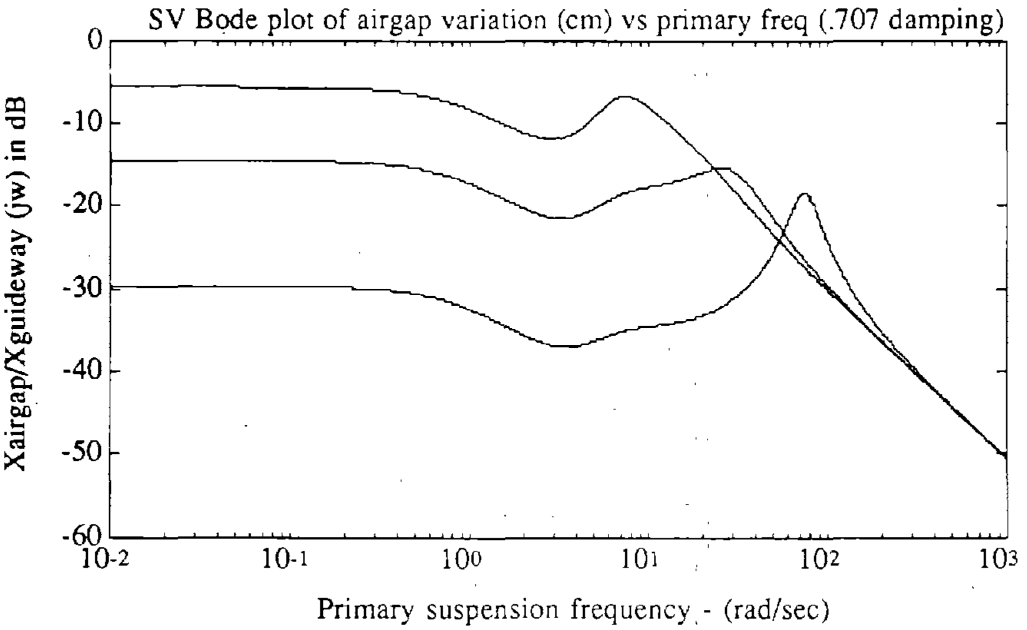

Figure 12: Comparison of Singular Values vs frequency for three different primary suspension frequencies. For this plot, the damping ratio of the secondary suspension was set at .707.

To reiterate, the tracking does not become significantly worse as the primary frequency is increased beyond 2.5 Hz, but the ride quality suffers for no gain, unless magnetic suspension efficiency gains are significant.

Conclusions/Recommendations

As a final note, changing from a 3.52 Hz primary, 1.0 Hz, 0.1 damping ratio secondary suspension to a 2.5 Hz primary, 1.0 Hz, 0.2 damping ratio secondary suspension yields a 20% reduction in train accelerations, a 25% reduction in the secondary suspension stroke required, and a 27% reduction in the airgap variation for a passive system using the roughness parameter corresponding to smooth highway.

The bottom line is: to achieve the best tracking possible, the primary natural frequency should be set to about 2.5 Hz, because a suspension any stiffer than this will degrade the ride quality with no improvement in airgap variations. This conclusion is based on the assumptions that the airgap variations are not too large, AC losses in the superconductors are not a problem, and that we have a passive suspension. If an active suspension is implemented to control the airgap or the train accelerations, then reducing the size of the disturbances at the high frequency of mode 2 may become an important consideration. In this case, the results of this memo may not apply.

APPENDIX F

1-DIMENSIONAL ANALYSIS RESULTS

This Appendix contains a very brief summary of the initial 1-dimensional results obtained for this research.

In Figures F.1 and F.2, the Pepler index was computed only including the vertical accelerations, and so should not be compared to other Pepler index numbers found in this document.

Table F.1 - Model parameters

Vehicle mass, M	60,000 kg
Train mass/Bogie mass	10/1
Primary suspension	6 Hz
Vehicle height, H_v	4 m
Frontal area, A_c	12.3 m^2
Air-gap	5 cm
Susp. stroke-length	±10 cm
C_D	0.30
$C_{y\beta}$	2.43 (1/rad)

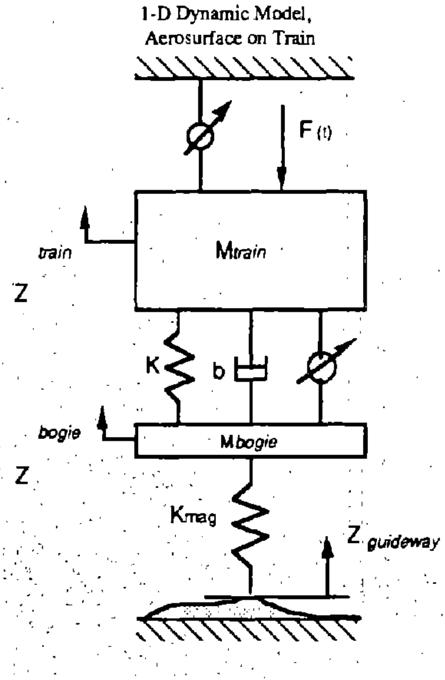

Figure F.1 - 1-D model

Table F.2 - 1-D results for welded steel rail guideway roughness

V= 125 m/sec Welded Rail RMS wind = 10 mph	Passive suspension	System with active secondary suspension	System with aerosurface on train	System with active secondary suspension and aerosurface on train
Train accel. (g's/100)				
guideway	5.6 RMS	2.2 RMS	4.5 RMS	0.1 RMS
crosswind	4.3 RMS	0.1 RMS	1.2 RMS	0.1 RMS
total	7.1 RMS	2.2 RMS	4.7 RMS	0.1 RMS
Ride comfort (Peplar)				
guideway	2.0	1.4	1.8	1.02
crosswind	1.7	1.01	1.2	1.01
total	2.2	1.4	1.8	1.02
Peak aerodynamic drag (kW)	4800	4800	5150	5150
Actuator force (kN)	-	47.8 RMS		27.8 RMS
Aeroflap deflection (deg)	-	-	5.0 RMS	5.0 RMS

Table F.3 - 1-D results for smooth highway guideway roughness

V= 125 m/sec Smooth Highway RMS wind = 10 mph	Passive suspension	System with active secondary suspension	System with aerosurface on train	System with active secondary suspension and aerosurface on train
Train accel. (g's/100)				
guideway	13.8 RMS	8.6 RMS	11.8 RMS	6.4 RMS
crosswind	4.3 RMS	0.1 RMS	1.9 RMS	0.1 RMS
total	14.4 RMS	8.6 RMS	11.9 RMS	6.4 RMS
Ride comfort (Peplar)				
guideway	3.3	2.5	3.0	2.1
crosswind	1.7	1.02	1.3	1.02
total	3.4	2.5	3.0	2.1
Peak aerodynamic drag (kW)	4800	4800	5150	5150
Actuator force (kN)	-	55.5 RMS bandwidth ~1 Hz		52.6 RMS bandwidth ~1 Hz
Aeroflap deflection (deg)	-	-	5.0 RMS bandwidth ~ 0.2 Hz	5.0 RMS bandwidth ~ 0.2 Hz

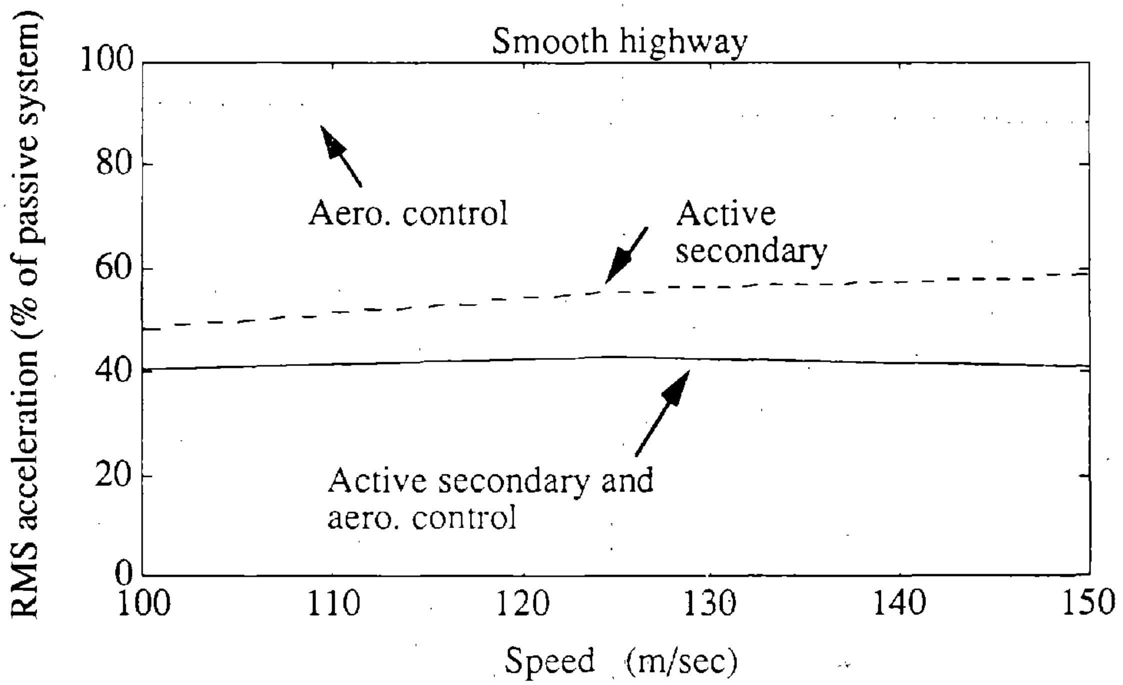

Figure F.2 - Effect of speed on performance

REFERENCES

1. Anderson, J.D. Jr., Fundamentals of Aerodynamics, McGraw-Hill Book Company, New York, 1984.

2. Ashill, P.R.,'On the Minimum Induced Drag of Ground Effect Wings', Aeronautical Quarterly, Vol. XXI , Aug. 1970.

3. Ashley, Holt, and Landahl, Martin, Aerodynamics of Wings and Bodies, Dover Publications, Inc., New York 1985.

4. Barrows, T.M., 'Fluid, Magnetic, and Mechanical Suspension Concepts for High Speed Ground Transportation', Technology Review, Winter 1975.

5. Barrows, T.M., 'Analytical Studies of the Lift and Roll Stability of a Ram Air Cushion Vehicle', PB 219820, December 1972.

6. Barrows, T.M., et.al., 'The Use of Aerodynamic Lift for Application to High Speed Ground Transportation', PB 197 242, 1970.

7. Barrows, T.M., and Widnall, S.E., 'Optimum Lift-Drag Ratio for a Ram Wing Tube Vehicle', AIAA Journal, Vol. 8, p.491, 1970.

8. Barrows, T.M., and Widnall, S.E., 'The Aerodynamics of Ram Wing Vehicles for Application to High Speed Ground Transportation', AIAA Paper No. 70-142, Jan. 1970.

9. Batchelor, G.K., An Introduction to Fluid Machanics, Cambridge University Press, New York, 1990.

10. Boccadoro, Y., 'Towing Tank Tests on a Ram Wing in a Rectangular Guideway', FRA-RT-73-34, (PB 210 743), 1973.

11. Borst, Henry V., The Aerodynamics of the Unconventional Air Vehicle of A. Lippisch , H.V. Borst and Associates, Wayne, Pennsylvania, 1980.

12. Carson, .H., 'Experimental Observations of the Two-Dimensional, Power-Augmented Ram Wing Operated Statically Over Water', DTNSRDC ASED 372, March 1977.

13. Carson, B.H., 'The Theory of Lift for the Power Augmented Ram Wing', U.S. Naval Academy, EW Rep't. 3-77, March 1977.

14. Carter, Arthur W., 'Effect of Ground Proximity on the Aerodynamic Characteristics of Aspect-Ratio-1 Airfoils With and Without End Plates', NASA TN D-970, Oct. 1961.

15. Colton, Russel F., 'The Pressure Distribution on the Lower Side of an Arbitrary Wing Section in Ground Proximity', Collins Radio Report, 1963-64.

16. Cornish, J.J. III, 'Some Consideration of Automobile Lift and Drag', SAE Paper 948B, Jan. 1965.

17. Curtiss, H.C. Jr., 'The Aerodynamics of Tracked Ram Air Cushion Vehicles- Static Lateral/Directional Characteristic's, Princeton Univ. MAE Tech. Rept. 1427, under contract to U.S. DOT, Feb. 1979.

18. Curtiss, H.C., and Putman, W.F., 'Experimental Investigation of Aerodynamic Characteristics of a Tracked Ram Air Cushion Vehicle', U.S. Dep't. of Transportation Report No. DOT-TSC-OST-78-1, PB277674, Jan. 1978.

19. Curtiss, H.C., et.al., 'Further Experimental and Theoretical Studies of the Aerodynamics of Tracked Ram Air Cushion Vehicles', DOT-TSC-OST- , Feb. 1979.

20. Curtiss, H.C., et.al., 'The Aerodynamics of Tracked Ram Air Cushion Vehicles- Effects of Pitch Attitude and Upper Surface Flow', Princeton Univ. MAE Tech. Rept. 1426, also Dep't. of Transportation Report DOT-TSC-RSPA-79-17, 1979.

21. Dau, Karl, and Davis, James M., 'Characteristics of a Rectangular Wing With a Peripheral Jet in Ground Effect', Part I and II, Univ. of Toronto, Inst. of Aerophysics, UTIA Tech. Notes No. 56 59, 1961 1962.

22. deDecker, R. William, 'Ground Interference on the Lift of a Wing', Feb.2, 1961.

23. Durand, William F., ed., <u>Aerodynamic Theory</u> , Julius Springer, Berlin, 1935.

24. Etkin, Bernard, <u>Dynamics of Atmospheric Flight</u> , Wiley and Sons, 1972.

25. Fink, M.P., and Lastinger, J.L., 'Aerodynamic Characteristics of Low-Aspect-Ratio Wings in Close Proximity to the Ground', NASA TN D-926, July 1961.

26. Foshag, William F., 'Literature Search and Comprehensive Bibliography of Wing in Ground Effect and Related Phenomena', David Taylor Model Basin, Dep't. of the Navy, Report 2179, March 1966.

27. Fraize, W.E., and Barrows, T.M., 'The Tracked Ram Air Cushion Vehicle TRACV)', MITRE Corp. Report HTR-6554, Nov. 1973.

28. Fujita, T., et.al., 'Vortex Recirculation Lift for Ground Effect Machines', Vehicle Research Corp. Rept. 17, Pasadena, Calif., Dec.1963.

29. Gallington, Miller, and Smith, "The Ram Wing Surface Effect Vehicle," <u>Hovering Craft and Hydrofoil</u>, Vol. 11, No.5, February 1972.

30. Gallington, Roger W., 'Sudden Deceleration of a Free Jet at the Entrance of a Channel', DTNSRDC Rep't. ASED 350, Bethesda, Hd., Jan. 1976.

31. Gallington, Roger W., 'Vortex Shedding from the Ram Wing Vehicle', Dep't. of Aeronautics, USAF Academy, Report DFAN TR 73-6, Aug.1973.

32. Gallington, R.W., and Chaplin, H.., 'Theory of Power Augmented Ram Lift at Zero Forward Speed', DTNSRDC Rep't. ASED 365, Feb. 1976.

33. Gallington, R.W., et.al.-, 'The Ram-Wing Surface Effect Vehicle: Comparison of One-Dimentional Theory with Wind-Tunnel and Free Flight Result', Frank J. Seiler Research Lab Report No. SRL- TR-71-0012, USAF Academy, 1971.

34. Garg, D.P. and Barrows, T.M. 'Modelling and Dynamic Response of Maglev Vehicles Subjected to Crosswind Gusts', Journal of Dynamic Systems, Measurement and Control, Vol. 103, Sept. 1981.

35. Glauert, H., Element of Aerofoil and Airscrew Theory, Cambridge, at the University Pre1937.

36. Hammitt, A.G., The Aerodynamics of High Speed Transportation Western Periodical Co., North Hollywood, Calif., 1973.

37. Hazen, Michael R., 'A Wind Tunnel Investigation for the Aerodynamic Characteristic of a Tracked Ram Air Cushion Vehicle', MSE the MAE Dep't., Princeton Univ., May 1975.

38. Hoerner, S.F., Fluid-Dynamic Drag , published by the author, 1958.

39. Hoerner, S.F., and Borst, H.V., Fluid-Dynamic Lift, Hoerner Fluid Dynamic, P.O. Box 342, Brick Town, N.J. 08723, 1975.

40. Hughes, N.J.S., 'Two-Dimentional Constant Velocity Duct', ARC RH 2089, London, 1944.

41. Hullender, D.A., 'Minimum Vehicle-Guideway Clearance Based on a Contact Frequency Criterion', ASME J. of Dynamic System, Measurement, and Control, June 1974.

42. Kaario, T.J., 'Process for Eliminating Friction Between a Surface Vehicle and the Surface', Finish patent No. 18630, 1935.

43. Kida, T., and Miyai, Y., 'Minimum Induced Drag of Non-Planar Ground Effect Wings with Small Tip Clearance', Aeronautical Quarterly, Feb. 1974.

44. Krause, Fred H., 'Evaluation of a Power-Augmented-Ram Wing Operating Free in Heave and Pitch over Water', DTNSRDC Rep't. ASED 385, Aug. 1977.

45. Krause, F.H., et.al., 'The Current Level of Power-Augmented-Ram Wing Technology', AIAA Paper 8-752, 1978. Also in DTNSRDC-78067.

46. Kumar, .E., 'Some Stability Problems of Ground Effect Wing Vehicles in Forward Motion', Aeronautical Quarterly, Vol. XXIII, Feb. 1972.

47. Lane, William H., and Wells, W.R., 'Stability Design Criteria for Surface Effects Aircraft', AFFDLFGC-TM-76-5, April 1977.

48. Lee, Su-Dah; 'A Theoretical Investigation of the Aerodynamic Characteristics of a Tracked Ram Air Cushion Vehicle', Princeton Univ. AMS Report No. 1255-T, Dec. 1975.

49. Lippisch, A.M., United States patents on WIGs numbered 3,190,582; 3,627,235; 3,661,111; 3,830,179: and 3,830,448.

50. Lissaman, P.B.S., 'Aerodynamic Characteristics of Jet-Flapped Airfoil in Ground Effect', Vehicle Research Corp. Rep't. 18, Pasadena, Calif., Dec. 1964.

51. Ludvigsen, K.E., 'The Time Tunnel- A Historical Survey of Automobile Aerodynamics', SAE 700035, 1970.

52. McCabe, E.F. Jr., 'Assessment of Load Alleviation Device Installed on a Power-Augmented-Ram Wing over Irregular Wave', DTNSRDC Report ASED 383, Aug. 1977.

53. McLeavy, R., ed., Jane's Surface Skimmers , Franklin Watts Inc., New York, Various ed.s up to 1981.

54. Miller, M.P., and Schott, G.J., 'Energy Efficiency of Current Intercity Passenger Transportation Modes', AIAA Paper 75-314.

55. Mittal, Ram K., 'Energy Intensity of Intercity Passenger Rail', DOT/RSPD/DPB/50-78/7, Dec. 1977.

56. 'Parametric and Conceptual Design Study of Aircraft Wing-In-Ground Effect (WIG) Vehicles', Advanced Naval Vehicles Concepts Evaluation (ANVCE), Preliminary Draft Submittal, Report No. 76020-30, Lockheed-Georgia, March 1977.

57. Parvez, Shabbir Ahmed, 'A Study of the Lateral Dynamics of Tracked Ram Air Cushion Vehicle', Princeton University, MAE Dep't., masters thesis 1452-T, Aug. 1979.

58. Peppin, J, 'The Study of a Ram Wing in a Trough', M.S. Thesis, M.I.T., 1970.

59. Pierson, J., and Helgesen, J., 'Tracked Air Cushion Research Vehicle Aerodynamic Analysis', Report No. FRA-RT-72-32, PB 212469, 1971.

60. Raymond, Arthur E., 'Ground Influence on Aerofoils', NACA TN 67, Dec. 1921.

61. Rice, Richard R., 'Energy Efficiencies of the Transport Systems', SAE Paper 730066, 1973.

62. Rousseau, David, 'Analysis of Empirically Determined Aerodynamic and Ram Coefficients for a Power-Augmented-Ram Wing-In-Ground Effect', DTNSRDC Rep't. ASED 396, Oct. 1977.

63. Rousseau, David G., and Gallington, R.W., 'Performance Prediction Method for a Wing-In-Ground Effect Vehicle With Blowing Under the Wing', DTNSRDC Rep't. ASED 379, March 1977.

64. Rousseau, Pierre, Histoire de la Vitesse, Paris, 1942.

65. J. Ray Ruetenik, et.al., 'Development of Methods for Predicting Airloads on TACV configurations Due to Strong Crosswind Gusts', DOT TSC 171-1. PB-229 995. 27 March 1972.

66. Schaeffer, R.L., and Fink, M.D., 'Evaluation of Airfoil Section Characteristics in Ground Effect', David Taylor Model Basin Technical Note AL2, Oct. 1965.

67. Schlichting, H., Boundary-Layer Theory, 6th ed., McGraw-Hill, New York, 1968.

68. Serebrisky, Y.M., and Biachuev, S.A., 'Wind-Tunnel Investigation of the Horizontal Motion of a Wing Near the Ground', NACA TM 1095, Russian Report 1939.

69. Smithey,W.J.H., et.al., 'Effect of Turbulent Jet Mixing on the Static Lift Performance of a Power-Augmented-Ram Wing', DTNSRDC Report ASED 389, Sept. 1977.

70. Sovran,G., et.al., ed.s, 'Aerodynamic Drag Mechanisms of Bluff Bodies and Road Vehicles', Plenum Press, N.Y., 1978.71. Staufenbiel, Rolf, 'Some Nonlinear Effects in Stability and Control of Wing-in-Ground Effect Vehicles', Journal of Aircraft, Aug. 1978.

72. Stephens, H.S., ed., 'Advance in Road Vehicle Aerodynamics 1973, published by BHRA Fluid Engineering, Cranfield Bedford MK43 OAJ England, 1973.

73. Strand, T., et.al., 'Performance Theory for High Speed Ground Effect Machines, Vehicle Research Corp. Report 11, Pasadena, Calif., June 1961.

74. Sugiyama, Y., 'Aerodynamic Characteristics of a Rectangular Wing With a Tip Clearance in a Channel', ASME Journal of Applied Mechanics, Dec. 1977.

75. Sweet, L.M., Luhrs, R., and Curtiss, H.C., 'Two-Dimensional Dynamics of Tracked Ram Air Cushion Vehicles with Fixed and Variable Winglets', MAE Dep't., Princeton Univ., 1978-79; and ASME Publication 7g-WA/DSC-11.

76. 'Symposium... Where Does All The Power Go?', Parts I through V, SAE Preprints 779 through 783, June 1956.

77. 'Theories on Wing Lift Near the Ground- a Survey', Paper presented at Detroit Section Meeting, I.A.S., June 1, 1961, G.M. Styling Staff.

78. Tracked Hovercraft Ltd., 'A Cost Comparison of Three Tracked Air Cushion Vehicle Configurations', Rep't. FRA-RT-71-68, PB 197501, 1970.

79. Tuck, E.O., 'A Nonlinear Unsteady One-Dimensional Theory for Wings in Extreme Ground Effect', J. Fluid Mechanics, vol. 98, pt. 1, pp.33-47, 1980.

80. VonKarman, Th., and Sears, W.R., 'Airfoil Theory for Non-Uniform Motion', J. of the Aeronautical Sciences, Vol. 5, No. 10, Aug. 1938.

81. White, Herbert E., 'Wind-Tunnel Tests of a Low-Aspect-Ratio Wing in Close Proximity to the Ground', David Taylor Model Basin, Aero Rep't. 1056, June 1963.

82. Widnall, S.E., and Barrows, T.M., 'An Analytical Solution for Two- and Three-Dimensional Wings in Ground Effect', MIT Fluid Dynamics Research Lab Report No. 69-1, June 1969; and J. of Fluid Mechanics, vol. 41, p. 769.

83. 'Wing-in-Ground Effect', by Gallington and Kirkpatrick, in 'Air Vehicle Concepts, Advanced Naval Vehicles Concepts Evaluation', 1st Interim Evaluation Seminar, Annapolis, Md., 1976.

84. 'Wing-in-Ground Effect (WIG)', Advanced Naval Vehicle Concepts Study Evaluation, Naval Air Development Center Contract No. N62269-76-C-0465, Lockheed-Georgia, Marietta, Georgia, March 15,1976.

85. Wong, J.Y., Theory of Ground Vehicles, Wiley, New York, 1978.

86. Woolard, H.W., 'Slender-Body Aerodynamics for High-Speed Ground Vehicles', AIAA Paper No. 70-139, Jan. 1970.

87. "Assessment of the Potential for Magnetic Levitation Transportation Systems in the United States", Supplement to the Report to Congress, Federal Railroad Administration, June 1990.

88. Matsunuma, S. , et al., "A Study of the Characteristics of the Aerodynamics of the Magnetically Levitated Transportation System (Maglev)", 11th International Conference on Magnetically Levitated Systems and Linear Drives: Maglev '89, Yokohama, Japan, July 7-11, 1989, pp.275-280.

89. Broad Agency Announcement No.90-1, Appendix A, Federal Railroad Administration, Sept. 1990.

90. Perkins, C.D. and Hage, R.E., Airplane Performance, Stability, and Control, John Wiley and Sons, New York, 1949, p 97.

91. Peters, J.L., "Aerodynamics of Very High Speed Trains and Maglev Vehicles", Int. J. of Vehicle Design, Special Publication SP3, 1983

92. Carl E. Hanson, Harris Miller Miller and Hanson, private correspondence.